

Combustion Theory

CEFRC Summer School

Princeton

June 28th - July 2nd, 2010

Norbert Peters¹

RWTH Aachen University

¹Copyright ©2010 by N. Peters. This material is the property of N. Peters. It is not to be sold, reproduced or distributed without the prior written permission of the owner.

Contents

Introduction	5
1 Thermodynamics of Combustion Systems	8
1.1 Mole Fractions and Mass Fractions	8
1.2 The Mole Fraction	9
1.2.1 The Mass Fraction	9
1.2.2 The Mass Fraction of Elements	10
1.2.3 The Partial Molar Density	10
1.2.4 The Partial Density	11
1.2.5 The Thermal Equation of State	11
1.2.6 Stoichiometry	12
1.2.7 The Mixture Fraction	14
2 Adiabatic Flame Temperature and Chemical Equilibrium	18
2.1 Chemical Equilibrium	31
2.1.1 The Chemical Potential and the Law of Mass Action	31
2.2 An Example: Equilibrium Calculation of the H ₂ -Air System	33
2.3 The Heterogeneous Equilibrium	35
Bibliography	39
3 Fluid Dynamics and Balance Equations for Reacting Flows	40
3.1 Balance Equations	40
3.2 Mass Balance	42
3.3 Momentum Balance	43
3.4 Kinetic Energy Balance	44

3.5 Potential Energy Balance	44
3.6 Total and Internal Energy and Enthalpy Balance	44
3.7 Transport Processes	45
3.8 Different Forms of the Energy Equation	47
3.9 Balance Equations for Element Mass Fractions	49
Bibliography	51
4 Laminar Premixed Flame Configuration	53
4.1 The Laminar Burning Velocity	53
4.2 Governing Equations for Steady Premixed Flames, Numerical Calculations and Experimental Data	57
4.3 A Field Equation Describing the Flame Position	61
4.4 Flame Stretch	63
4.5 Flame Front Instability	65
Bibliography	73
5 The Thermal Flame Theory	75
5.1 Premixed Flames Based on One-step Asymptotics	75
5.2 Flame Thickness and Flame Time	80
6 Asymptotic Structure of Four-Step Premixed Stoichiometric Methane Flames	84
6.1 The Four-Step Model for Methane-Air Flames	85
6.2 The Asymptotic Structure	90
6.3 An Analytic Expression for the Burning Velocity	95
6.4 Relation to the Activation Energy of the One-step Model	96
6.5 Analytic Approximations of Burning Velocities for Lean CH ₄ , C ₂ H ₆ , C ₂ H ₄ , C ₂ H ₂ , and C ₃ H ₈ Flames	98
Bibliography	103
7 Flame Extinction and Flammability Limits	104
7.1 Lean Flammability Limits of Hydrocarbon Flames	104
7.2 Extinction of a Plane Flame by Volumetric Heat Loss	106
Bibliography	112
8 Laminar Diffusion Flames: Basic Theory	113

8.1	Flamelet Structure of a Diffusion Flame	114
8.2	The Planar Counterflow Diffusion Flame	117
8.3	Steady State Combustion and Quenching of Diffusion Flames with One-Step Chemistry	120
8.4	Time and Length Scales in Diffusion Flames	125
8.5	Diffusion Flame Structure of Methane-Air Flames	128
	Bibliography	131
9	Laminar Diffusion Flame Configurations:	132
9.1	Diffusion Flames in a Stagnation Point Boundary Layer: The Tsuji Flame	132
9.2	The Round Laminar Diffusion Flame	137
9.3	Single Droplet Combustion	141
	Bibliography	148
10	Turbulent Combustion: The State of the Art	149
10.1	What is Specific about Turbulence with Combustion?	149
10.2	Statistical Description of Turbulent Flows	151
10.3	Navier-Stokes Equations and Turbulence Models	154
10.4	Two-Point Velocity Correlations and Turbulent Scales	156
10.5	Balance Equations for Reactive Scalars	161
10.6	Moment Methods for Reactive Scalars	162
10.7	Dissipation and Scalar Transport of Non-Reacting Scalars	163
10.8	The Eddy Break Up and the Eddy Dissipation Model	165
10.9	The Pdf Transport Equation Model	166
10.10	The Laminar Flamelet Concept	168
10.11	The BML-Model and the Coherent Flamelet Model	169
10.12	Combustion Models used in Large Eddy Simulation	170
10.13	Modeling the Scalar Dissipation Rate	173
10.14	LES of Real Combustion Devices	177
	Bibliography	179
11	Premixed Turbulent Combustion: The Regime Diagram	184
11.1	Regimes in Premixed Turbulent Combustion	184

11.2 Regimes in Premixed Combustion LES	194
Bibliography	198
12 The Level Set Approach for Turbulent Premixed Combustion	200
12.1 The Level Set Approach for the Thin Reaction Zones Regime	205
12.2 A Common Level Set Equation for Both Regimes	208
12.3 Modeling Premixed Turbulent Combustion Based on the Level Set Approach	210
12.4 Equations for the Mean and the Variance of G	214
Bibliography	218
13 The Turbulent Burning Velocity	221
13.1 The Turbulent Burning Velocity	221
13.2 A Model Equation for the Flame Surface Area Ratio	226
Bibliography	235
14 Non-Premixed Turbulent Combustion: The Flamelet Concept	238
14.1 The Presumed Shape Pdf Approach	240
14.2 The Round Turbulent Jet Diffusion Flame	242
14.3 Experimental Data from Turbulent Jet Diffusion Flames	247
14.4 Laminar Flamelet Equations for Nonpremixed Combustion	251
Bibliography	259
15 Applications in Internal Combustion Engines	262
15.1 Spray-Guided Spark-Ignition Combustion	262
15.2 Injection-Rate Shaping in Diesel Engine Combustion	274
Bibliography	285

Introduction

This text is a reduced English version of the material prepared for my combustion class at the RWTH Aachen Technical University. It is intended as an introduction to the fundamentals of combustion science with the aim to supply the basic notions and equations for more detailed numerical investigations. With modern computational tools and facilities numerical calculations with large codes aiming to predict the performance of combustion devices such as furnaces, reciprocative engines and gas turbines are feasible. Whether they will partly or fully replace experimental investigations will largely depend on the reliability of the combustion models used. While there is a large scientific community concerned with Computational Fluid Dynamics and the improvement of turbulence models, the know-how in combustion modeling seems to be restricted to specialists. The reason for this is the complexity of the subject which requires advanced knowledge in thermodynamics, chemical kinetics and fluid mechanics. At the interface of these disciplines combustion emerges as a science which is able to predict rather than to merely describe experimentally observed phenomena. In order to classify combustion phenomena it has been useful to introduce two types of situations with respect to mixing: Premixed and non-premixed combustion. For laminar flames issuing from a tube burner these two models of combustion are shown in Fig. 1. If fuel and air are already mixed within the tube, as in the case of a Bunsen burner, and the gas is ignited downstream, a premixed flame front will propagate towards the burner until it finds its steady state position in the form of the well-known Bunsen cone. The fundamental quantity which describes this mode of combustion is the laminar burning velocity. It is the velocity at which the flame front propagates normal to itself into the unburned mixture. For the steady state Bunsen cone the burning velocity therefore must be equal to the flow velocity v_n normal to the flame front. Behind the flame front yet unburnt intermediates as CO and H₂ will mix with the air entrained from outside and lead to post flame oxidation and radiation. The other mode of combustion is that in a diffusion flame. Here no air is mixed with the fuel within the tube of the burner. This may be achieved but

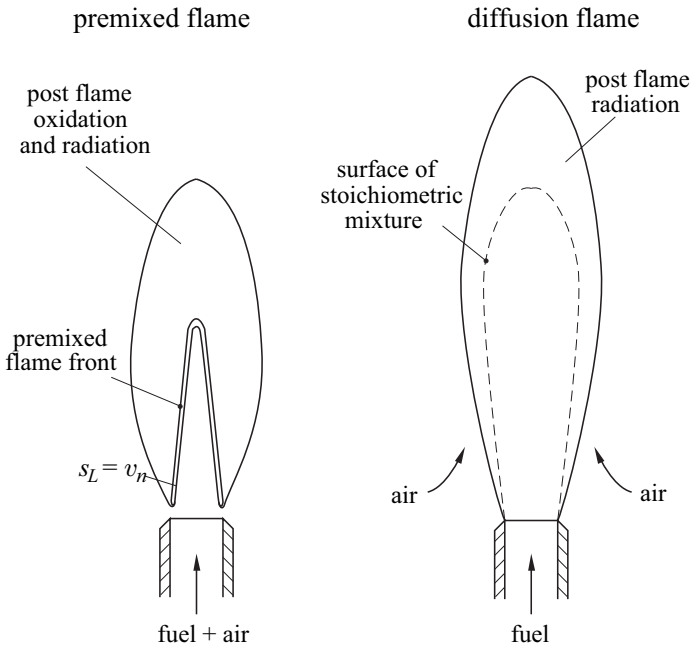


Figure 1: Different modes of laminar combustion

using a simply tube or by closing the air inlet in a Bunsen burner. Then only fuel issues from the tube as shown in the second picture in Fig. 1. It mixes with the surrounding air by convection and diffusion during combustion. Optimal conditions for combustion are restricted to the vicinity of the surface of stoichiometric mixture. This is the surface where fuel and air are locally mixed in a proportion that allows both to be entirely consumed. This will lead to the highest flame temperature and, due to the temperature sensitivity of the chemical reactions, to the fastest reaction rates. Since in most cases combustion is much faster than diffusion the latter is the rate limiting step that controls the entire process. This is the reason why those flames, where the reactants are initially non-premixed, are called diffusion flames. Premixed flames appear with a blue to bluish-green color, while diffusion flames radiate in a bright yellow color. The blue color of premixed flames is due to chemiluminescence of some excited species (C_2 and CH radicals), while the yellow color of diffusion flames is caused by radiating soot particles which dominate over the chemiluminescence that is also present in at the base of a diffusion flame. Close to the burner there appears blue layer since the local residence time is too short for soot particles to be formed. This leads to the conclusion that the color of a flame is characteristic for the available residence time rather than the mode

of mixing. Premixed Flames are used whenever intense combustion is required within a small volume. This is the case in household appliances and spark ignition engines. In such an engine a premixed turbulent flame front propagates from the spark through the combustion chamber until the entire mixture is burnt. An example for non-premixed combustion are Diesel engines, where a liquid fuel spray is injected into the compressed hot air within the cylinder. It rapidly evaporates and mixes with the air and then auto-ignition under partly premixed conditions. The final stage at combustion occurs under non-premixed conditions. Finally, large combustion devices such as furnaces, operate under non-premixed conditions because premixing of large volumes of fuel and air would represent a serious safety hazard.

The classification of combustion phenomena into premixed and non-premixed combustion is used throughout this text. After an introduction into the basic thermodynamics of combustion systems in Lecture 1, a simplified calculation of the adiabatic flame temperature and an approximate calculation of equilibrium constants is presented in Lecture 2. The balance equations of fluid dynamics are presented shortly in Lecture 3, laminar premixed flames are treated in Lecture 4-7 and laminar diffusion flames in Lectures 8 and 9. Then an introduction into turbulent combustion is given in Lecture 10. Premixed turbulent combustion is presented in terms of the regime diagram in Lecture 11, the level set approach and the turbulent burning velocity is presented in Lectures 12 and 13, while non-premixed turbulent combustion is treated in Lecture 14. Finally, in Lecture 15 applications in engines closes the text. In preparing these lectures and the text I have enjoyed the support from many of my students and friends. I am particular indebted to Bernd Binniger for cross-reading the manuscript and for the preparation of many of the figures. I could also rely on the efficiency of Sonja Engels in preparing the manuscript.

Lecture 1

Thermodynamics of Combustion Systems

Combustion is a mass and energy conversion process during which chemical bond energy is transformed to thermal energy. The fuel reacts with the oxygen of the air to form products such as carbon dioxide and water which have a lower enthalpy of formation or reference enthalpy than the reactants. The details of the reaction mechanism that leads from the reactants to the products will be presented by other lectures of this summer school. In this lecture we will only consider the initial and the final state of a homogeneous system and use the classical balance laws of thermodynamics. This global view is much simpler and leads in Lecture 2 to some useful results such as the adiabatic flame temperature. We will first present definitions of concentrations and other thermodynamic variables and present the mass and energy balance for multicomponent systems.

1.1 Mole Fractions and Mass Fractions

When chemical species react with each other to form other species, their basic constituents, the chemical elements are conserved. The particular atom defining the element, a C atom within a CH₄ molecule, for example, will be found within the CO₂ molecule after combustion is completed. In order to describe the chemical transformation between species quantitatively, we need to introduce definitions for concentrations. Since different descriptions are being used in the combustion

literature, it is useful to present these first and to relate them to each other.

1.2 The Mole Fraction

We consider a multi-component system with k different chemical species that contains a large number of molecules. Then $6.0236 \cdot 10^{23}$ molecules are defined as one mole. The number of moles of species i denoted by n_i and its sum is the total number of moles n_s

$$n_s = \sum_{i=1}^k n_i. \quad (1.1)$$

The mole fraction of species i is now defined

$$X_i \equiv \frac{n_i}{n_s}, \quad i = 1, 2, \dots, k. \quad (1.2)$$

1.2.1 The Mass Fraction

The mass m_i of all molecules of species i is related to its number of moles by

$$m_i = W_i n_i, \quad i = 1, 2, \dots, k, \quad (1.3)$$

where W_i is the molecular weight of species i . For some important species in combustion W_i is given in Tab. 2.1. The total mass of all molecules in the mixture is

$$m = \sum_{i=1}^k m_i. \quad (1.4)$$

The mass fraction of species i is now defined

$$Y_i = \frac{m_i}{m}, \quad i = 1, 2, \dots, k. \quad (1.5)$$

Defining the mean molecular weight W by

$$m = W n_s \quad (1.6)$$

one obtains the relation between mole fractions and mass fractions as

$$Y_i = \frac{W_i}{W} X_i, \quad i = 1, 2, \dots, k. \quad (1.7)$$

The mean molecular weight may be calculated if either the mole fractions or the mass fractions are known

$$W = \sum_{i=1}^k W_i X_i = \left[\sum_{i=1}^k \frac{Y_i}{W_i} \right]^{-1}. \quad (1.8)$$

1.2.2 The Mass Fraction of Elements

In addition, the mass fraction of elements is very useful in combustion. While the mass of the species changes due to chemical reactions, the mass of the elements is conserved. We denote by m_j the mass of all atoms of element j contained in all molecules of the system. If a_{ij} is the number of atoms of element j in a molecule of species i and W_j is the molecular weight of that atom, the mass of all atoms j in the system is

$$m_j = \sum_{i=1}^k \frac{a_{ij} W_j}{W_i} m_i, \quad j = 1, 2, \dots, k_e, \quad (1.9)$$

where k_e is the total number of elements in the system. The mass fraction of element j is then

$$Z_j = \frac{m_j}{m} = \sum_{i=1}^k \frac{a_{ij} W_j}{W_i} Y_i = \frac{W_j}{W} \sum_{i=1}^k a_{ij} X_i, \quad j = 1, 2, \dots, k_e, \quad (1.10)$$

Notice that no meaningful definition for the mole fraction of elements can be given because only the mass of the elements is conserved. From the definitions above it follows that

$$\sum_{i=1}^k X_i = 1, \quad \sum_{i=1}^k Y_i = 1, \quad \sum_{j=1}^{k_e} Z_j = 1. \quad (1.11)$$

1.2.3 The Partial Molar Density

An additional variable defining a concentration, that is frequently used in chemical kinetics, is the number of moles per unit volume or partial molar density

$$[X_i] = \frac{n_i}{V}, \quad i = 1, 2, \dots, k, \quad (1.12)$$

where V is the volume of the system. The molar density of the system is then

$$\frac{n_s}{V} = \sum_{i=1}^k [X_i]. \quad (1.13)$$

1.2.4 The Partial Density

The density and the partial density are defined

$$\rho = \frac{m}{V}, \quad \rho_i = \frac{m_i}{V} = \rho Y_i, \quad i = 1, 2, \dots, k. \quad (1.14)$$

The partial molar density is related to the partial density and the mass fraction by

$$[X_i] = \frac{\rho_i}{W_i} = \frac{\rho Y_i}{W_i}, \quad i = 1, 2, \dots, k. \quad (1.15)$$

1.2.5 The Thermal Equation of State

In most combustion systems of technical interest the law of ideal gases is valid. Even for high pressure combustion this is a sufficiently accurate approximation because the temperatures are typically also very high. In a mixture of ideal gases the molecules of species i exert on the surrounding walls of the vessel the partial pressure p_i

$$p_i = \frac{n_i \mathcal{R}T}{V} = [X_i] \mathcal{R}T = \frac{\rho Y_i}{W_i} \mathcal{R}T, \quad i = 1, 2, \dots, k. \quad (1.16)$$

Here \mathcal{R} is the universal gas constant equal to 8.3143 J/mol/K. Dalton's law states that for an ideal gas the total pressure is equal to the sum of the partial pressures. This leads to the thermal equation of state for a mixture of ideal gases

$$p = \sum_{i=1}^k p_i = n_s \frac{\mathcal{R}T}{V} = \frac{\rho \mathcal{R}T}{W}, \quad (1.17)$$

where Eqs. (1.6) and (1.14) have been used. From Eqs. (1.16), (1.17), and (1.2) it follows that the partial pressure is equal to the total pressure times the mole fraction

$$p_i = p X_i, \quad i = 1, 2, \dots, k. \quad (1.18)$$

Furthermore, defining the partial volume by

$$V_i = \frac{n_i \mathcal{R}T}{p}, \quad i = 1, 2, \dots, k, \quad (1.19)$$

it follows that an equivalent relation exists for the partial volume

$$V_i = V X_i, \quad i = 1, 2, \dots, k. \quad (1.20)$$

1.2.6 Stoichiometry

Equations describing chemical reactions such as



or



are based on the principle of element conservation during reaction and define the stoichiometric coefficients ν'_i of the reactant i on the left hand side and ν''_i of the product i on the right hand side. The first example above corresponds to a global reaction while the second one, where the equal sign is replaced by arrows, denotes an elementary reaction that takes place with a finite reaction rate (conf. Lecture 2). Formally a reaction equation may be cast into the form

$$\sum_{i=1}^k \nu'_i M_i = \sum_{i=1}^k \nu''_i M_i \quad (1.23)$$

where M_i stands for the chemical symbol of species i . The net stoichiometric coefficient

$$\nu_i = \nu''_i - \nu'_i, \quad i = 1, 2, \dots, k \quad (1.24)$$

is positive for products and negative for reactants. A system of r elementary reactions may formally then be written

$$\sum_{i=1}^k \nu_{il} M_i = 0, \quad l = 1, 2, \dots, r \quad (1.25)$$

where ν_{il} is the net stoichiometric coefficient of species i in reaction l .

The stoichiometry defined by the reaction equation relates the molar production or consumption

of species to each other. The change of the number of moles of species i to that of species 1 is

$$\frac{dn_i}{\nu_i} = \frac{dn_1}{\nu_1}, \quad i = 2, \dots, k. \quad (1.26)$$

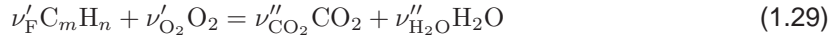
With Eq. (1.3) the relation between the partial masses is

$$\frac{dm_i}{\nu_i W_i} = \frac{dm_1}{\nu_1 W_1}, \quad i = 2, \dots, k. \quad (1.27)$$

Since the total mass in the system is independent of the chemical reaction (while the total number of moles is not), the relation between mass fractions is

$$\frac{dY_i}{\nu_i W_i} = \frac{dY_1}{\nu_1 W_1}, \quad i = 2, \dots, k. \quad (1.28)$$

A fuel-air mixture is called stoichiometric, if the fuel-to-oxygen ratio is such that both are entirely consumed when combustion to CO_2 and H_2O is completed. For example, the global reaction describing the combustion of a single component hydrocarbon fuel C_mH_n (subscript F) is



the stoichiometric coefficients are

$$\nu_F = 1, \quad \nu'_{\text{O}_2} = m + \frac{n}{4}, \quad \nu''_{\text{CO}_2} = m, \quad \nu''_{\text{H}_2\text{O}} = \frac{n}{2} \quad (1.30)$$

where ν'_F may be chosen arbitrarily to unity. Stoichiometric mixture requires that the ratio of the number of moles of fuel and oxidizer in the unburnt mixture is equal to the ratio of the stoichiometric coefficients

$$\left. \frac{n_{\text{O}_2,u}}{n_{\text{F},u}} \right|_{st} = \frac{\nu'_{\text{O}_2}}{\nu'_F} \quad (1.31)$$

or in terms of mass fractions

$$\left. \frac{Y_{\text{O}_2,u}}{Y_{\text{F},u}} \right|_{st} = \frac{\nu'_{\text{O}_2} W_{\text{O}_2}}{\nu'_F W_{\text{F}}} = \nu, \quad (1.32)$$

where ν is called the stoichiometric mass ratio. Then fuel and oxidizer are both consumed when combustion is completed. Integrating Eq. (1.28) with $i = \text{O}_2$, $1 = \text{F}$ between the initial unburnt

state (subscript u) and any later state leads to

$$\frac{Y_{O_2} - Y_{O_{2,u}}}{\nu'_{O_2} W_{O_2}} = \frac{Y_F - Y_{F,u}}{\nu'_F W_F}. \quad (1.33)$$

This may be written as

$$\nu Y_F - Y_{O_2} = \nu Y_{F,u} - Y_{O_{2,u}}. \quad (1.34)$$

For a stoichiometric mixture fuel and oxygen are completely consumed at the end of combustion, $Y_F = Y_{O_2} = 0$. Introducing this into Eqs. (1.34), (1.32) is recovered.

1.2.7 The Mixture Fraction

The mixture fraction is an extremely useful variable in combustion, in particular for diffusion flames (Lectures 9, 10, 12, and 13). Here we present it first for a homogeneous system. In a two-feed system, where a fuel stream (subscript 1) with mass flux m_1 is mixed with an oxidizer stream (subscript 2) with mass flux m_2 , the mixture fraction represents the mass fraction of the fuel stream in the mixture

$$Z = \frac{m_1}{m_1 + m_2}. \quad (1.35)$$

Both fuel and oxidizer streams may contain inerts such as nitrogen. The mass fraction $Y_{F,u}$ of the fuel in the mixture is proportional to the mass fraction in the original fuel stream, so

$$Y_{F,u} = Y_{F,1} Z \quad (1.36)$$

where $Y_{F,1}$ denotes the mass fraction of fuel in the fuel stream. Similarly, since $1 - Z$ represents the mass fraction of the oxidizer stream in the mixture, one obtains for the mass fraction of oxygen in the mixture

$$Y_{O_{2,u}} = Y_{O_{2,2}}(1 - Z), \quad (1.37)$$

where $Y_{O_{2,2}}$ represents the mass fraction of oxygen in the oxidizer stream ($Y_{O_{2,2}} = 0.232$ for air). Introducing Eqs. (1.36) and (1.37) into Eq. (1.34) one obtains the mixture fraction as a variable that couples the mass fractions of the fuel and the oxygen

$$Z = \frac{\nu Y_F - Y_{O_2} + Y_{O_{2,2}}}{\nu Y_{F,1} + Y_{O_{2,2}}}. \quad (1.38)$$

For a stoichiometric mixture one obtains with $\nu Y_F = Y_{O_2}$ the stoichiometric mixture fraction

$$Z_{st} = \frac{Y_{O_2,2}}{\nu Y_{F,1} + Y_{O_2,2}} \quad (1.39)$$

If $Z < Z_{st}$ fuel is deficient and the mixture is called fuel lean. Then, combustion terminates when all the fuel is consumed, $Y_{F,b} = 0$ in the burnt gas (subscript b). The remaining oxygen mass fraction in the burnt gas is calculated from Eq. (1.38) as

$$Y_{O_2,b} = Y_{O_2,2} \left(1 - \frac{Z}{Z_{st}}\right), \quad Z \leq Z_{st} \quad (1.40)$$

where Eq. (1.39) was used. Similarly, if $Z > Z_{st}$ oxygen is deficient and the mixture is called fuel rich. Combustion then terminates when all the oxygen is consumed, $Y_{O_2,b} = 0$, leading to

$$Y_{F,b} = Y_{F,1} \frac{Z - Z_{st}}{1 - Z_{st}}, \quad Z \geq Z_{st}. \quad (1.41)$$

For the hydrocarbon fuel considered above the element mass fractions in the unburnt mixture are

$$Z_C = m \frac{W_C}{W_F} Y_{F,u}, \quad Z_H = n \frac{W_H}{W_F} Y_{F,u}, \quad Z_O = Y_{O_2,u} \quad (1.42)$$

or

$$\frac{Z_C}{mW_C} = \frac{Z_H}{nW_H} = \frac{Y_{F,u}}{\nu'_F W_F}. \quad (1.43)$$

For a stoichiometric mixture where

$$\frac{Y_{O_2,u}}{\nu'_{O_2} W_{O_2}} = \frac{Y_{F,u}}{\nu'_F W_F} \quad (1.44)$$

it follows that the combination

$$\beta = \frac{Z_C}{mW_C} + \frac{Z_H}{nW_H} - 2 \frac{Z_O}{\nu'_{O_2} W_{O_2}} \quad (1.45)$$

vanishes. Normalizing this such that the variable $Z = 1$ in the fuel stream and $Z = 0$ in the oxidizer stream, one obtains Bilger's definition

$$Z = \frac{\beta - \beta_2}{\beta_1 - \beta_2} \quad (1.46)$$

or

$$Z = \frac{Z_C/(mW_C) + Z_H/(nW_H) + 2(Y_{O_2,u} - Z_O)/(\nu'_{O_2} W_{O_2})}{Z_{C,1}/(mW_C) + Z_{H,1}/(nW_H) + 2Y_{O_2,u}/(\nu'_{O_2} W_{O_2})}. \quad (1.47)$$

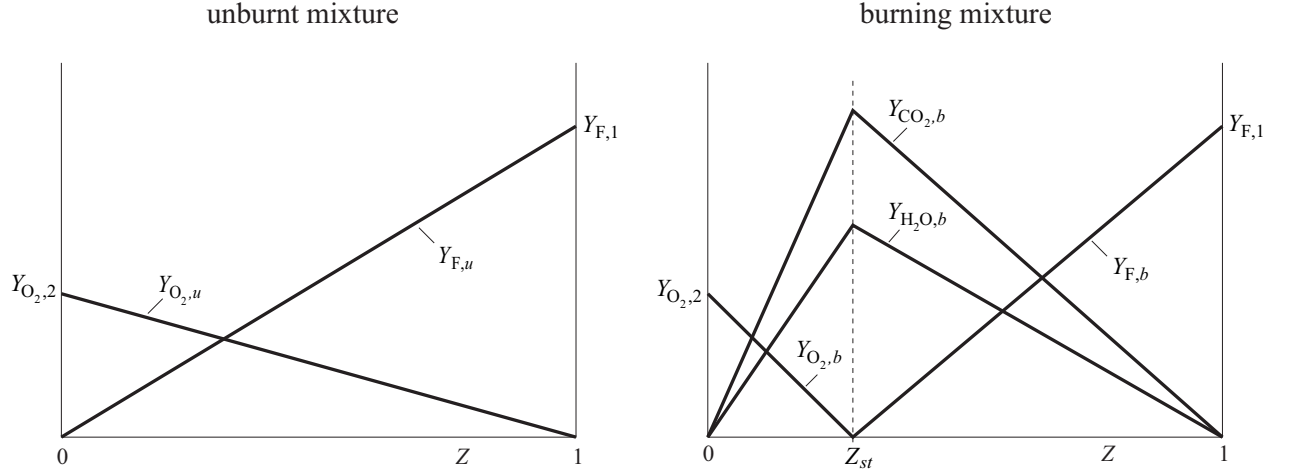


Figure 1.1: Profiles of Y_F , Y_{O_2} , Y_{CO_2} and Y_{H_2O} in the unburnt and burning gas

Because elements are conserved during combustion, the element mass fractions calculated from Eq. (1.10) do not change. For the burnt gas they are

$$Z_C = m \frac{W_C}{W_F} Y_{F,b} + \frac{W_C}{W_{CO_2}} Y_{CO_2,b} \quad (1.48)$$

$$Z_H = n \frac{W_H}{W_F} Y_{F,b} + 2 \frac{W_H}{W_{H_2O}} Y_{H_2O,b} \quad (1.49)$$

$$Z_O = 2 \frac{W_O}{W_{O_2}} Y_{O_2,b} + 2 \frac{W_O}{W_{CO_2}} Y_{CO_2,b} + \frac{W_O}{W_{H_2O} Y_{H_2O,b}}. \quad (1.50)$$

This leads with Eq. (1.36) and $Y_{F,b} = 0$ for $Z \leq Z_{st}$ and Eq. (1.38) for $Z \geq Z_{st}$ to piecewise linear relations of the product mass fractions in terms of Z

$$Z \leq Z_{st} : \quad Y_{CO_2,b} = Y_{CO_2,st} \frac{Z}{Z_{st}}, \quad Y_{H_2O,b} = Y_{H_2O,st} \frac{Z}{Z_{st}} \quad (1.51)$$

$$Z \geq Z_{st} : \quad Y_{CO_2,b} = Y_{CO_2,st} \frac{1-Z}{1-Z_{st}}, \quad Y_{H_2O,b} = Y_{H_2O,st} \frac{1-Z}{1-Z_{st}}. \quad (1.52)$$

where

$$Y_{CO_2,st} = Y_{F,1} Z_{st} \frac{m W_{CO_2}}{W_F} \quad (1.53)$$

Profiles of Y_F and Y_{O_2} in the unburnt and in the burnt gas and product profiles are shown in Fig. 1.1. The fuel-air equivalence ratio is the ratio of fuel-air ratio in the unburnt to that of a stoichiometric mixture

$$\phi = \frac{Y_{F,u}/Y_{O_2,u}}{(Y_{F,u}/Y_{O_2,u})_{st}} = \frac{\nu Y_{F,u}}{Y_{O_2,u}}. \quad (1.54)$$

Introducing Eqs. (1.36) and (1.37) into Eq. (1.38) leads with Eq. (1.39) to a unique relation between the equivalence ratio and the mixture fraction

$$\phi = \frac{Z}{1-Z} \frac{(1-Z_{st})}{Z_{st}}. \quad (1.55)$$

This relation is also valid for multicomponent fuels (conf. Exercise 1.1). It illustrates that the mixture fraction is simply another expression for the local equivalence ratio.

Exercise 1.1

The element mass fractions $Z_{H,F}$, $Z_{C,F}$ of a mixture of hydrocarbons and its mean molecular weight W are assumed to be known. Determine its stoichiometric mixture fraction in air!

Lecture 2

Adiabatic Flame Temperature and Chemical Equilibrium

The first law of thermodynamics describes the balance between different forms of energy and thereby defines the internal energy.

$$du + pdv = dh - vdp = \delta q + \delta w_R \quad (2.1)$$

Here δq is the heat transfer from the surroundings, δw_R is the frictional work, du is the change of internal energy and pdv is the work due to volumetric changes, where $v = 1/\rho$ is the specific volume¹. The specific enthalpy h is related to the specific inner energy u by

$$h = u + pv, \quad (2.2)$$

which for an ideal gas also reads

$$h = u + \frac{\mathcal{R}T}{W}. \quad (2.3)$$

In a multicomponent system, the specific internal energy and specific enthalpy are the mass

¹The different notation of infinitesimal quantities in Eq. (2.1) is chosen to discriminate between variables of state like internal energy, enthalpy, pressure and volume, which have a total differential written d , whereas heat and work are process dependent quantities, of which infinitesimal small amounts are indicated with a δ . This perfectly corresponds to the difference in notation of integrals such as $u_2 - u_1 = \int_1^2 du$ and $q_{12} = \int_1^2 \delta q!$

weighted sums of the specific quantities of all species

$$u = \sum_{i=1}^k Y_i u_i, \quad h = \sum_{i=1}^k Y_i h_i. \quad (2.4)$$

For an ideal gas the partial specific enthalpy is related to the partial specific internal energy by

$$h_i = u_i + \frac{\mathcal{R}T}{W_i}, \quad i = 1, 2, \dots, k \quad (2.5)$$

and both depend only on temperature. The temperature dependence of the partial specific enthalpy is given by

$$h_i = h_{i,\text{ref}} + \int_{T_{\text{ref}}}^T c_{pi} dT, \quad i = 1, 2, \dots, k \quad (2.6)$$

Here c_{pi} is the specific heat capacity at constant pressure and $h_{i,\text{ref}}$ is the reference enthalpy at the reference temperature T_{ref} . This temperature may be arbitrarily chosen, most frequently $T_{\text{ref}} = 0 \text{ K}$ or $T_{\text{ref}} = 298.15 \text{ K}$ are being used. The partial molar enthalpy is

$$H_i = W_i h_i, \quad i = 1, 2, \dots, k, \quad (2.7)$$

and its temperature dependence is

$$H_i = H_{i,\text{ref}} + \int_{T_{\text{ref}}}^T C_{pi} dT, \quad i = 1, 2, \dots, k, \quad (2.8)$$

where the molar heat capacity at constant pressure is

$$C_{pi} = W_i c_{pi}, \quad i = 1, 2, \dots, k. \quad (2.9)$$

In a multicomponent system, the specific heat capacity at constant pressure of the mixture is

$$c_p = \int_{i=1}^k Y_i c_{pi}. \quad (2.10)$$

In Tab. 2.1 the molar reference enthalpies at $T_{\text{ref}} = 298.15 \text{ K}$ of a number of species are listed. It should be noted that the reference enthalpies of H_2 , O_2 , N_2 , and solid carbon were chosen as zero, because they represent the chemical elements. Reference enthalpies of combustion products such as CO_2 and H_2O are typically negative. The temperature dependence of C_{pi} , H_i

and S_i may be calculated from the NASA polynomials Tab. 2.2

Tab. 2.1, Legend see page 22

Nr.	species	M_i kg/kmol	$H_{i,\text{ref}}$ kJ/mol	$S_{i,\text{ref}}$ kJ/(molK)	$\pi_{A,i}$	$\pi_{B,i}$
1	H°	1.008	217.986	114.470	-1.2261	1.9977
2	HNO°	31.016	99.579	220.438	-1.0110	4.3160
3	OH°	17.008	39.463	183.367	3.3965	2.9596
4	HO_2°	33.008	20.920	227.358	-1.1510	4.3160
5	H_2	2.016	0.000	130.423	-2.4889	2.8856
6	H_2O	18.016	-241.826	188.493	-1.6437	3.8228
7	H_2O_2	34.016	-136.105	233.178	-8.4782	5.7218
8	N°	14.008	472.645	153.054	5.8661	1.9977
9	NO	30.008	90.290	210.442	5.3476	3.1569
10	NO_2	46.008	33.095	239.785	-1.1988	4.7106
11	N_2	28.016	0.000	191.300	3.6670	3.0582
12	N_2O	44.016	82.048	219.777	-5.3523	4.9819
13	O°	16.000	249.194	160.728	6.8561	1.9977
14	O_2	32.000	0.000	204.848	4.1730	3.2309
15	O_3	48.000	142.674	238.216	-3.3620	5.0313
16	NH°	15.016	331.372	180.949	3.0865	2.9596
17	NH_2°	16.024	168.615	188.522	-1.9835	3.8721
18	NH_3	17.032	-46.191	192.137	-8.2828	4.8833
19	N_2H_2	30.032	212.965	218.362	-8.9795	5.4752
20	$\text{N}_2\text{H}_3^\circ$	31.040	153.971	228.513	-17.5062	6.9796
21	$\text{N}_2\text{H}_4^\circ$	32.048	95.186	236.651	-25.3185	8.3608
22	C°	12.011	715.003	157.853	6.4461	1.9977
23	CH°	13.019	594.128	182.723	2.4421	3.0829
24	HCN°	27.027	130.540	201.631	-5.3642	4.6367
25	HCNO	43.027	-116.733	238.048	-10.1563	6.0671
26	HCO°	29.019	-12.133	224.421	-10.2313	4.2667
27	CH_2°	14.027	385.220	180.882	-5.6013	4.2667

Continuation see next page

Continuation of Tab. 2.1

Nr.	species	M_i kg/kmol	$H_{i,\text{ref}}$ kJ/mol	$S_{i,\text{ref}}$ kJ/(molK)	$\pi_{A,i}$	$\pi_{B,i}$
28	CH ₂ O	30.027	-115.896	218.496	-8.5350	5.4012
29	CH ₃ [°]	15.035	145.686	193.899	-10.7155	5.3026
30	CH ₂ OH [°]	31.035	-58.576	227.426	-15.3630	6.6590
31	CH ₄	16.043	-74.873	185.987	-17.6257	6.1658
32	CH ₃ OH	32.043	-200.581	240.212	-18.7088	7.3989
33	CO	28.011	-110.529	197.343	4.0573	3.1075
34	CO ₂	44.011	-393.522	213.317	-5.2380	4.8586
35	CN [°]	26.019	456.056	202.334	4.6673	3.1075
36	C ₂ [°]	24.022	832.616	198.978	1.9146	3.5268
37	C ₂ H [°]	25.030	476.976	207.238	-4.6242	4.6367
38	C ₂ H ₂	26.038	226.731	200.849	-15.3457	6.1658
39	C ₂ H ₃ [°]	27.046	279.910	227.861	-17.0316	6.9056
40	CH ₃ CO [°]	43.046	-25.104	259.165	-24.2225	8.5334
41	C ₂ H ₄	28.054	52.283	219.468	-26.1999	8.1141
42	CH ₃ COH [°]	44.054	-165.979	264.061	-30.7962	9.6679
43	C ₂ H ₅ [°]	29.062	110.299	228.183	-32.8633	9.2980
44	C ₂ H ₆	30.070	-84.667	228.781	-40.4718	10.4571
45	C ₃ H ₈	44.097	-103.847	269.529	-63.8077	14.7978
46	C ₄ H ₂ [°]	50.060	465.679	250.437	-34.0792	10.0379
47	C ₄ H ₃ [°]	51.068	455.847	273.424	-36.6848	10.8271
48	C ₄ H ₈	56.108	16.903	295.298	-72.9970	16.7215
49	C ₄ H ₁₀	58.124	-134.516	304.850	-86.8641	19.0399
50	C ₅ H ₁₀	70.135	-35.941	325.281	-96.9383	20.9882
51	C ₅ H ₁₂	72.151	-160.247	332.858	-110.2702	23.3312
52	C ₆ H ₁₂	84.152	-59.622	350.087	-123.2381	25.5016
53	C ₆ H ₁₄	86.178	-185.560	380.497	-137.3228	28.2638
54	C ₇ H ₁₄	98.189	-72.132	389.217	-147.4583	29.6956
55	C ₇ H ₁₆	100.205	-197.652	404.773	-162.6188	32.6045
56	C ₈ H ₁₆	112.216	-135.821	418.705	-173.7077	34.5776

Continuation see next page

Continuation of Tab. 2.1

Nr.	species	M_i kg/kmol	$H_{i,\text{ref}}$ kJ/mol	$S_{i,\text{ref}}$ kJ/(molK)	$\pi_{A,i}$	$\pi_{B,i}$
57	C_8H_{18}	114.232	-223.676	430.826	-191.8158	37.6111
58	$\text{C}_2\text{H}_4\text{O}$	44.054	-51.003	243.044	-34.3705	9.7912
59	HNO_3	63.016	-134.306	266.425	-19.5553	9.7912
60	He	4.003	0.000	125.800	-	-
61	Ar	39.944	0.000	154.599	-	-
62	C_{solid}	12.011	0.000	0.000	-9.975	1.719

Table 2.1: Molecular data for some important species in combustion at $T_{\text{ref}} = 298.15 \text{ K}$. Superscripts \circ denote chemical radicals.)

$$\begin{aligned} \frac{C_{p_i}}{\mathcal{R}} &= a_1 + a_2 \frac{T}{\text{K}} + a_3 \frac{(T/\text{K})^2}{2} + a_4 \frac{(T/\text{K})^3}{3} + a_5 \frac{(T/\text{K})^4}{4} \\ \frac{H_i}{\mathcal{R} T} &= a_1 + a_2 \frac{T}{\text{K}} + a_3 \frac{(T/\text{K})^2}{2} + a_4 \frac{(T/\text{K})^3}{3} + a_5 \frac{(T/\text{K})^4}{4} + a_6 \frac{(T/\text{K})^5}{5} + \frac{a_7}{T/\text{K}} \quad (2.11) \\ \frac{S_i}{\mathcal{R}} &= a_1 \ln(T/\text{K}) + a_2 \frac{T}{\text{K}} + a_3 \frac{(T/\text{K})^2}{2} + a_4 \frac{(T/\text{K})^3}{3} + a_5 \frac{(T/\text{K})^4}{4} + a_7 + \ln(p/p_0). \end{aligned}$$

Let us consider the first law for an adiabatic system ($\delta q = 0$) at constant pressure ($\text{d}p = 0$) and neglect the work done by friction ($\delta w_R = 0$). From Eq. (2.1) we then have $\text{d}h = 0$ which may be integrated from the unburnt to the burnt state as

$$h_u = h_b \quad (2.12)$$

or

$$\sum_{i=1}^k Y_{i,u} h_{i,u} = \sum_{i=1}^k Y_{i,b} h_{i,b}. \quad (2.13)$$

Tab. 2.2, NASA Polynomials for two temperature ranges and standard pressure $p = 1$ atm

H₂	temperature range:	$1000 < T < 5000$	
		$a_1 = +0.29914234E+01$	$a_2 = +0.70006441E-03$
		$a_3 = -0.56338287E-07$	$a_4 = -0.92315782E - 11$
		$a_5 = +0.15827518E-14$	$a_6 = -0.83503399E+03$
		$a_7 = -0.13551102E+01$	
	temperature range:	$300 < T < 1000$	
		$a_1 = +0.32981243E+01$	$a_2 = +0.82494417E-03$
		$a_3 = -0.81430153E-06$	$a_4 = -0.94754343E - 10$
		$a_5 = +0.41348722E-12$	$a_6 = -0.10125209E+04$
		$a_7 = +0.32940941E+01$	
O₂	temperature range:	$1000 < T < 5000$	
		$a_1 = +0.36975782E+01$	$a_2 = +0.61351969E-03$
		$a_3 = -0.12588419E-06$	$a_4 = +0.17752815E - 10$
		$a_5 = -0.11364353E-14$	$a_6 = -0.12339302E+04$
		$a_7 = +0.31891656E+01$	
	temperature range:	$300 < T < 1000$	
		$a_1 = +0.32129364E+01$	$a_2 = +0.11274863E-02$
		$a_3 = -0.57561505E-06$	$a_4 = +0.13138772E - 08$
		$a_5 = -0.87685539E-12$	$a_6 = -0.10052490E+04$
		$a_7 = +0.60347376E+01$	
N₂	temperature range:	$1000 < T < 5000$	
		$a_1 = +0.29266400E+01$	$a_2 = +0.14879767E-02$
		$a_3 = -0.56847608E-06$	$a_4 = +0.10097038E - 09$
		$a_5 = -0.67533513E-14$	$a_6 = -0.92279767E+03$
		$a_7 = +0.59805279E+01$	
	temperature range:	$300 < T < 1000$	
		$a_1 = +0.32986769E+01$	$a_2 = +0.14082404E-02$
		$a_3 = -0.39632223E-05$	$a_4 = +0.56415153E - 08$
		$a_5 = -0.24448549E-11$	$a_6 = -0.10208999E+04$
		$a_7 = +0.39503722E+01$	

Continuation next page

Continuation Tab. 2.2, NASA Polynomials for two temperature ranges and standard pressure $p = 1 \text{ atm}$

CO	temperature range: $1000 < T < 5000$
	$a_1 = +0.30250781E+01$ $a_2 = +0.14426885E-02$ $a_3 = -0.56308278E-06$ $a_4 = +0.10185813E - 09$ $a_5 = -0.69109515E-14$ $a_6 = -0.14268349E+05$ $a_7 = +0.61082177E+01$
CO₂	temperature range: $300 < T < 1000$
	$a_1 = +0.32624516E+01$ $a_2 = +0.15119408E-02$ $a_3 = -0.38817552E-05$ $a_4 = +0.55819442E - 08$ $a_5 = -0.24749512E-11$ $a_6 = -0.14310539E+05$ $a_7 = +0.48488969E+01$
H₂O	temperature range: $1000 < T < 5000$
	$a_1 = +0.44536228E+01$ $a_2 = +0.31401687E-02$ $a_3 = -0.12784105E-05$ $a_4 = +0.23939967E - 09$ $a_5 = -0.16690332E-13$ $a_6 = -0.48966961E+05$ $a_7 = -0.95539588E+00$
H₂O	temperature range: $300 < T < 1000$
	$a_1 = +0.22757246E+01$ $a_2 = +0.99220723E-02$ $a_3 = -0.10409113E-04$ $a_4 = +0.68666868E - 08$ $a_5 = -0.21172801E-11$ $a_6 = -0.48373141E+05$ $a_7 = +0.10188488E+02$

Continuation next page

Continuation Tab. 2.2, NASA Polynomials for two temperature ranges and standard pressure $p = 1 \text{ atm}$

CH₄	temperature range:	$1000 < T < 5000$	
	$a_1 = +0.16834788E+01$	$a_2 = +0.10237235E-01$	$a_3 = -0.38751286E-05$
	$a_5 = -0.45034231E-13$	$a_6 = -0.10080787E+05$	$a_4 = +0.67855849E-09$
			$a_7 = +0.96233949E+01$
	temperature range:	$300 < T < 1000$	
	$a_1 = +0.77874148E+00$	$a_2 = +0.17476683E-01$	$a_3 = -0.27834090E-04$
	$a_5 = -0.12239307E-10$	$a_6 = -0.98252285E+04$	$a_4 = +0.30497080E-07$
			$a_7 = +0.13722195E+02$
C₃OH	temperature range:	$1000 < T < 5000$	
	$a_1 = +0.36012593E+01$	$a_2 = +0.10243223E-01$	$a_3 = -0.35999217E-05$
	$a_5 = -0.33912719E-13$	$a_6 = -0.25997155E+05$	$a_4 = +0.57251951E-09$
			$a_7 = +0.47056025E+01$
	temperature range:	$300 < T < 1000$	
	$a_1 = +0.57153948E+01$	$a_2 = -0.15230920E-01$	$a_3 = +0.65244182E-04$
	$a_5 = +0.26135383E-10$	$a_6 = -0.25642765E+05$	$a_4 = -0.71080873E-07$
			$a_7 = -0.15040970E+01$
C₂H₆	temperature range:	$1000 < T < 5000$	
	$a_1 = +0.48259382E+01$	$a_2 = +0.13840429E-01$	$a_3 = -0.45572588E-05$
	$a_5 = -0.35981614E-13$	$a_6 = -0.12717793E+05$	$a_4 = +0.67249672E-09$
			$a_7 = -0.52395067E+01$
	temperature range:	$300 < T < 1000$	
	$a_1 = +0.14625387E+01$	$a_2 = +0.15494667E-01$	$a_3 = +0.57805073E-05$
	$a_5 = +0.45862671E-11$	$a_6 = -0.11239176E+05$	$a_4 = -0.12578319E-07$
			$a_7 = +0.14432295E+02$

Continuation next page

Continuation Tab. 2.2, NASA Polynomials for two temperature ranges and standard pressure $p = 1$ atm

C₂H₄	temperature range:	$1000 < T < 5000$
$a_1 = +0.35284188E+01$	$a_2 = +0.11485184E-01$	$a_3 = -0.44183853E-05$
$a_5 = -0.52668485E-13$	$a_6 = +0.44282886E+04$	$a_7 = +0.22303891E+01$
temperature range:	$300 < T < 1000$	
$a_1 = -0.86148798E+00$	$a_2 = +0.27961628E-01$	$a_3 = -0.33886772E-04$
$a_5 = -0.97378789E-11$	$a_6 = +0.55730459E+04$	$a_7 = +0.24211487E+02$
C₂H₂	temperature range:	$1000 < T < 5000$
$a_1 = +0.44367704E+01$	$a_2 = +0.53760391E-02$	$a_3 = -0.19128167E-05$
$a_5 = -0.21567095E-13$	$a_6 = +0.25667664E+05$	$a_7 = -0.28003383E+01$
temperature range:	$300 < T < 1000$	
$a_1 = +0.20135622E+01$	$a_2 = +0.15190446E-01$	$a_3 = -0.16163189E-04$
$a_5 = -0.19127460E-11$	$a_6 = +0.26124443E+05$	$a_7 = +0.88053779E+01$
C₃H₈	temperature range:	$1000 < T < 5000$
$a_1 = +0.75252171E+01$	$a_2 = +0.18890340E-01$	$a_3 = -0.62839244E-05$
$a_5 = -0.48124099E-13$	$a_6 = -0.16464547E+05$	$a_7 = -0.17843903E+02$
temperature range:	$300 < T < 1000$	
$a_1 = +0.89692080E+00$	$a_2 = +0.26689861E-01$	$a_3 = +0.54314251E-05$
$a_5 = +0.92433301E-11$	$a_6 = -0.13954918E+05$	$a_7 = +0.19355331E+02$

Continuation next page

Continuation Tab. 2.2

C₇H₁₆	temperature range:	$1000 < T < 5000$
$a_1 = +0.22818893E+02$	$a_2 = +0.32543454E-01$	$a_3 = -0.11120041E-04$
$a_5 = -0.96212101E-13$	$a_6 = -0.33678738E+05$	$a_7 = -0.94335007E+02$
temperature range:	300 < T < 1000	
$a_1 = +0.30149546E+01$	$a_2 = +0.54457203E-01$	$a_3 = +0.21812681E-04$
$a_5 = +0.20808730E-10$	$a_6 = -0.26003379E+05$	$a_7 = +0.17508575E+02$

Table 2.2: NASA polynomials for two temperature ranges and standard pressure $p = 1$ atm.

With the temperature dependence of the specific enthalpy Eq. (2.6) this may be written as

$$\sum_{i=1}^k (Y_{i,u} - Y_{i,b}) h_{i,\text{ref}} = \int_{T_{\text{ref}}}^{T_b} c_{p,b} dT - \int_{T_{\text{ref}}}^{T_u} c_{p,u} dT. \quad (2.14)$$

Here the specific heat capacities are those of the mixture, to be calculated with the mass fractions of the burnt and unburnt gases, respectively

$$c_{p,b} = \sum_{i=1}^k Y_{i,b} c_{pi}(T), \quad c_{p,u} = \sum_{i=1}^k Y_{i,u} c_{pi}(T). \quad (2.15)$$

For a one-step global reaction the left hand side of Eq. (2.14) may be calculated by integrating Eq. (1.28) as

$$Y_{i,u} - Y_{i,b} = (Y_{F,u} - Y_{F,b}) \frac{\nu_i W_i}{\nu_F W_F}, \quad i = 1, 2, \dots, k, \quad (2.16)$$

such that

$$\sum_{i=1}^k (Y_{i,u} - Y_{i,b}) h_{i,\text{ref}} = \frac{(Y_{F,u} - Y_{F,b})}{\nu_F W_F} \sum_{i=1}^k \nu_i W_i h_{i,\text{ref}}. \quad (2.17)$$

Here it is convenient to define the heat of combustion as

$$Q = - \sum_{i=1}^k \nu_i W_i h_i = - \sum_{i=1}^k \nu_i H_i. \quad (2.18)$$

This quantity changes very little with temperature and is often set equal to

$$Q_{\text{ref}} = - \sum_{i=1}^k \nu_i H_{i,\text{ref}} \quad (2.19)$$

For simplicity, let us set $T_u = T_{\text{ref}}$ and assume $c_{p,b}$ to be approximately constant. For combustion in air, the contribution of nitrogen is dominant in calculating $c_{p,b}$. At temperatures around 2000 K its specific heat is approximately 1.30 kJ/kg/K. The value of c_{pi} is somewhat larger for CO₂ and somewhat smaller for O₂ while that for H₂O is twice as large. A first approximation for the specific heat of the burnt gas for lean and stoichiometric mixtures is then $c_p = 1.40$ kJ/kg/K. Assuming c_p constant and $Q = Q_{\text{ref}}$, the adiabatic flame temperature for a lean mixture ($Y_{F,b} = 0$) is calculated from Eqs. (2.14) and (2.17) with $\nu_F = -\nu'_F$ as

$$T_b - T_u = \frac{Q_{\text{ref}} Y_{F,u}}{c_p \nu'_F W_F}. \quad (2.20)$$

For a rich mixture Eq. (2.16) must be replaced by

$$Y_{i,u} - Y_{i,b} = (Y_{\text{O}_2,u} - Y_{\text{O}_2,b}) \frac{\nu_i W_i}{\nu_{\text{O}_2} W_{\text{O}_2}}, \quad i = 1, 2, \dots, k \quad (2.21)$$

and one obtains similarly for complete consumption of the oxygen ($Y_{\text{O}_2,b} = 0$)

$$T_b - T_u = \frac{Q_{\text{ref}} Y_{\text{O}_2,u}}{c_p \nu'_{\text{O}_2} W_{\text{O}_2}}. \quad (2.22)$$

Eqs. (2.20) and (2.22) may be expressed in terms of the mixture fraction by introducing Eqs. (1.36) and (1.37) and by specifying the temperature of the unburnt mixture by

$$T_u(Z) = T_2 - Z(T_2 - T_1), \quad (2.23)$$

where T_2 is the temperature of the oxidizer stream and T_1 that of the fuel stream. Equation Eq. (2.23) describes mixing of the two streams with c_p assumed to be constant. Equations Eqs. (2.20) and (2.22) then take the form

$$\begin{aligned} T_b(Z) &= T_u(Z) + \frac{Q_{\text{ref}} Y_{\text{F},1}}{c_p \nu'_{\text{F}} W_{\text{F}}} Z, \quad Z \leq Z_{st}, \\ T_b(Z) &= T_u(Z) + \frac{Q_{\text{ref}} Y_{\text{O}_2,2}}{c_p \nu'_{\text{O}_2} W_{\text{O}_2}} (1 - Z) \quad Z \geq Z_{st}. \end{aligned} \quad (2.24)$$

The adiabatic temperature is plotted over mixture fraction in Fig. 2.1. The maximum temperature at $Z = Z_{st}$ is calculated from either one of Eq. (2.24) as

$$\begin{aligned} T_{st} &= T_u(Z_{st}) + \frac{Y_{\text{F},1} Z_{st} Q_{\text{ref}}}{c_p \nu'_{\text{F}} W_{\text{F}}} \\ &= T_u(Z_{st}) + \frac{Y_{\text{O}_2,2} (1 - Z_{st}) Q_{\text{ref}}}{c_p \nu'_{\text{O}_2} W_{\text{O}_2}}. \end{aligned} \quad (2.25)$$

For the combustion of a pure fuel ($Y_{\text{F},1} = 1$) in air ($Y_{\text{O}_2,2} = 0.232$) with $T_{u,st} = 300$ K values for T_{st} are given in Tab. 2.3 using $c_p = 1.4$ kJ/kg/K.

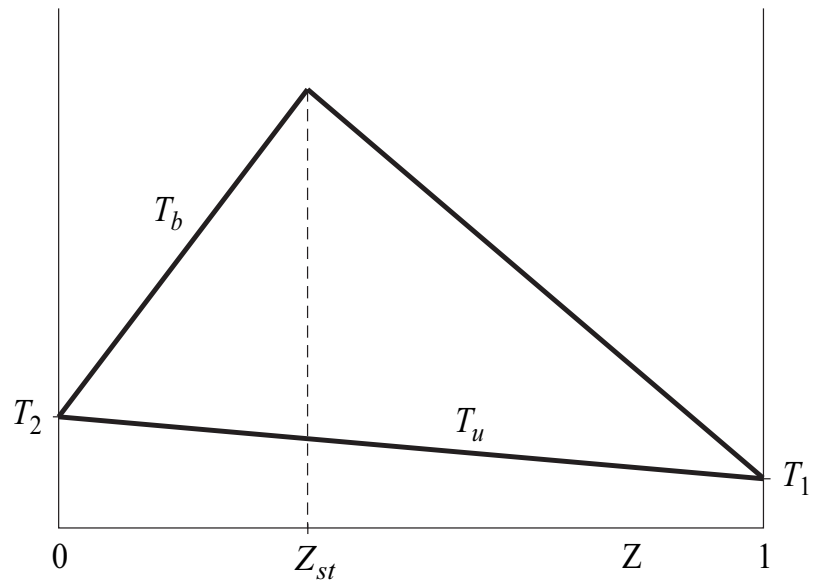


Figure 2.1: The adiabatic temperature over mixture fraction

Fuel	Z_{st}	T_{st} [K]
CH ₄	0.05496	2263.3
C ₂ H ₆	0.05864	2288.8
C ₂ H ₄	0.06349	2438.5
C ₂ H ₂	0.07021	2686.7
C ₃ H ₈	0.06010	2289.7

Table 2.3: Stoichiometric mixture fractions and stoichiometric flame temperatures for some hydrocarbon-air mixtures.

2.1 Chemical Equilibrium

From the standpoint of thermodynamics, the assumption of complete combustion is an approximation because it disregards the possibility of dissociation of combustion products. A more general formulation is the assumption of chemical equilibrium. In that context complete combustion represents the limit of an infinite equilibrium constant as will be shown below. Both approximations, chemical equilibrium and complete combustion, are valid in the limit of infinitely fast reaction rates only, a condition which will seldom be valid in combustion systems. We will consider finite rate chemical kinetics in Lecture 2. Only for hydrogen diffusion flames complete chemical equilibrium is a good approximation, while for hydrocarbon diffusion flames finite kinetic rates are needed. In the latter the fast chemistry assumption overpredicts the formation of intermediates such as CO and H₂ due to the dissociation of fuel on the rich side by large amounts. Nevertheless, since the equilibrium assumption represents an exact thermodynamic limit, it shall be considered here.

2.1.1 The Chemical Potential and the Law of Mass Action

Differently from the enthalpy, the partial molar entropy of a chemical species in a mixture of ideal gases depends on the partial pressure

$$S_i = S_i^0 - \mathcal{R} \ln \frac{p_i}{p_0}, \quad i = 1, 2, \dots, k, \quad (2.26)$$

where $p_0 = 1 \text{ atm}$ and

$$S_i^0 = S_{i,\text{ref}}^0 + \int_{T_{\text{ref}}}^T \frac{C_{p_i}}{T} dT, \quad i = 1, 2, \dots, k \quad (2.27)$$

depends only on temperature. Values for the reference entropy $S_{i,\text{ref}}$ are also listed in Tab. 2.1. The partial molar entropy may now be used to define the chemical potential

$$\mu_i = H_i - TS_i = \mu_i^0 + \mathcal{R}T \ln \frac{p_i}{p_0}, \quad i = 1, 2, \dots, k, \quad (2.28)$$

where

$$\mu_i^0 = H_{i,\text{ref}} - TS_{i,\text{ref}}^0 + \int_{T_{\text{ref}}}^T C_{p_i} dT - T \int_{T_{\text{ref}}}^T \frac{C_{p_i}}{T} dT, \quad i = 1, 2, \dots, k \quad (2.29)$$

is the chemical potential at 1 atm. As it is shown in standard textbooks of thermodynamics the condition for chemical equilibrium for the l -th reaction is given by

$$\sum_{i=1}^k \nu_{il} \mu_i = 0, \quad l = 1, 2, \dots, r. \quad (2.30)$$

Using Eq. (2.28) in Eq. (2.30) leads to

$$-\sum_{i=1}^k \nu_{il} \mu_i^0 = \mathcal{R}T \ln \prod_{i=1}^k \left(\frac{p_i}{p_0}\right)^{\nu_{il}}, \quad l = 1, 2, \dots, r. \quad (2.31)$$

Defining the equilibrium constant K_{pl} by

$$\mathcal{R}T \ln K_{pl} = -\sum_{i=1}^k \nu_{il} \mu_i^0, \quad l = 1, 2, \dots, r \quad (2.32)$$

one obtains the law of mass action

$$\prod_{i=1}^k \left(\frac{p_i}{p_0}\right)^{\nu_{il}} = K_{pl}(T), \quad l = 1, 2, \dots, r. \quad (2.33)$$

An approximation of equilibrium constants may be derived by introducing the quantity

$$\pi_i = \frac{H_{i,\text{ref}} - \mu_i^0}{\mathcal{R}T} = \frac{S_{i,\text{ref}}^0}{\mathcal{R}} + \int_{T_{\text{ref}}}^T \frac{C_{p_i}}{\mathcal{R}T} dT - \frac{1}{\mathcal{R}T} \int_{T_{\text{ref}}}^T C_{p_i} dT, \quad i = 1, 2, \dots, k. \quad (2.34)$$

For constant C_{p_i} the second term in this expression would yield a logarithm of the temperature, while the last term does not vary much if $T \gg T_{\text{ref}}$. Therefore $\pi_i(T)$ may be approximated by

$$\pi_i(T) = \pi_{iA} + \pi_{iB} \ln T, \quad i = 1, 2, \dots, k. \quad (2.35)$$

Introducing this into Eq. (2.32) one obtains

$$K_{pl} = B_{pl} T^{n_{pl}} \exp\left(\frac{Q_{l,\text{ref}}}{\mathcal{R}T}\right), \quad l = 1, 2, \dots, r, \quad (2.36)$$

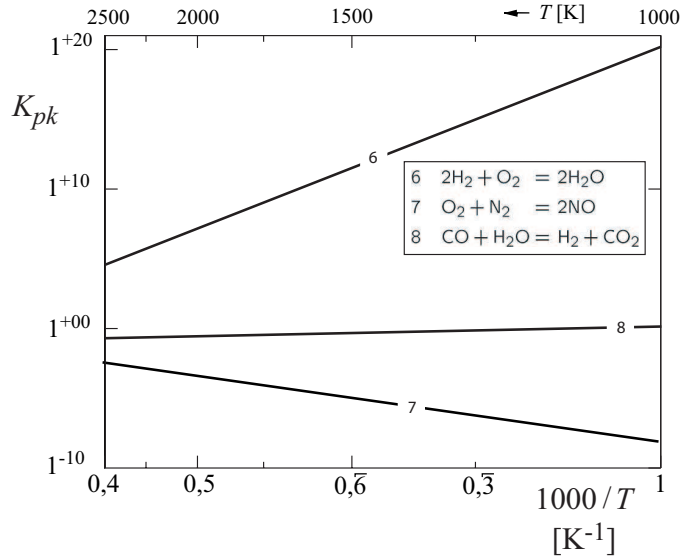


Figure 2.2: Equilibrium constants of the elementary and global reactions $2\text{H}_2 + \text{O}_2 = 2\text{H}_2\text{O}$, $\text{O}_2 + \text{N}_2 = 2\text{NO}$ and $\text{CO} + \text{H}_2\text{O} = \text{H}_2 + \text{CO}_2$.

where Eq. (2.19) was used and

$$B_{pl} = \exp\left(\sum_{i=1}^k \nu_{il} \pi_{iA}\right), \quad n_{pl} = \sum_{i=1}^k \nu_{il} \pi_{iB}, \quad l = 1, 2, \dots, r. \quad (2.37)$$

Values for π_{iA} and π_{iB} are also listed in Tab. 2.1. They were obtained by linear interpolation in terms of $\ln T$ for the values given in the JANAF-Tables [1] at $T = 300\text{ K}$ and $T = 2000\text{ K}$. In Fig. 2.2 equilibrium constants for the reactions $2\text{H}_2 + \text{O}_2 = 2\text{H}_2\text{O}$, $\text{O}_2 + \text{N}_2 = 2\text{NO}$ and $\text{CO} + \text{H}_2\text{O} = \text{H}_2 + \text{CO}_2$ are plotted.

2.2 An Example: Equilibrium Calculation of the H_2 -Air System

Using the law of mass action one obtains for the reaction



the relation between partial pressures

$$p_{\text{H}_2}^2 p_{\text{O}_2} = p_{\text{H}_2\text{O}}^2 K_{p1} \cdot p_{\text{O}}, \quad (2.39)$$

where

$$K_{p1} = 0.0835 T^{-1.3565} \exp(58171/T) \quad (2.40)$$

was approximated using Eqs. (2.36) and (2.37) the values from Tab. 2.1. Introducing the definition

$$\Gamma_i = \frac{Y_i}{W_i}, \quad i = 1, 2, \dots, k \quad (2.41)$$

the partial pressures are written with Eq. (1.18) as

$$p_i = p X_i = p \Gamma_i W, \quad i = 1, 2, \dots, k, \quad (2.42)$$

where the mean molecular weight is

$$W = (\Gamma_{\text{H}_2} + \Gamma_{\text{O}_2} + \Gamma_{\text{H}_2\text{O}} + \Gamma_{\text{N}_2})^{-1}. \quad (2.43)$$

Furthermore, we need to consider the element mass balance. The element mass fractions of the unburnt mixture are

$$Z_{\text{H}} = Y_{\text{F},1} Z, \quad Z_{\text{O}} = Y_{\text{O}_2,2}(1 - Z), \quad Z_{\text{N}} = Y_{\text{N}_2,2}(1 - Z). \quad (2.44)$$

These are equal to those in the equilibrium gas where

$$\begin{aligned} \frac{Z_{\text{H}}}{W_{\text{H}}} &= 2\Gamma_{\text{H}_2,b} + 2\Gamma_{\text{H}_2\text{O},b} \\ \frac{Z_{\text{O}}}{W_{\text{O}}} &= 2\Gamma_{\text{O}_2,b} + \Gamma_{\text{H}_2\text{O},b}, \end{aligned} \quad (2.45)$$

while Z_{N} remains unchanged. Combining Eqs. (2.39)-(2.45) leads to the following nonlinear equation for $\Gamma_{\text{H}_2\text{O},b}$

$$\begin{aligned} f(\Gamma_{\text{H}_2\text{O},b}) &\equiv \left(\Gamma_{\text{H}_2\text{O},b} - \frac{Z_{\text{H}}}{2W_{\text{H}}} \right)^2 \left(\frac{Z_{\text{O}}}{W_{\text{O}}} - \Gamma_{\text{H}_2\text{O},b} \right) \\ &\quad - \frac{\Gamma_{\text{H}_2\text{O},b}^2}{K_{p1}^2 p} \left(\frac{Z_{\text{H}}}{W_{\text{H}}} + \frac{Z_{\text{O}}}{W_{\text{O}}} + 2\Gamma_{\text{N}_2} - \Gamma_{\text{H}_2\text{O},b} \right) = 0. \end{aligned} \quad (2.46)$$

This equation has one root between $\Gamma_{\text{H}_2\text{O},b} = 0$ and the maximum values $\Gamma_{\text{H}_2\text{O},b} = Z_{\text{H}}/2W_{\text{H}}$ and $\Gamma_{\text{H}_2\text{O},b} = Z_{\text{O}}/W_{\text{O}}$ which correspond to complete combustion for lean and rich conditions in the limit $K_{p1} \rightarrow \infty$, respectively. The solution, which is a function of the temperature, may be found by successively bracketing the solution within this range. The temperature is then calculated by employing a Newton iteration on Eq. (2.12) leading to the equation

$$f_T(T) = h_u - \sum_{i=1}^k Y_{i,b} h_{i,\text{ref}} - \int_{T_{\text{ref}}}^T C_{p_b} dT. \quad (2.47)$$

The iteration converges readily following

$$T = T^i + \frac{f_T(T^i)}{C_{p_b}(T^i)}, \quad (2.48)$$

where i is the iteration index. The solution is shown in Fig. 2.3 for a hydrogen-air flame as a function of the mixture fraction for $T_u = 300$ K. Tab. 2.4 shows equilibrium mass fractions of H_2 , O_2 and H_2O at $p = 1$ bar and $p = 10$ bar at different temperatures.

Equilibrium temperature profiles for lean methane, acetylene and propane flames as a function of the equivalence ratio for $T_u = 300$ K are shown in Fig. 2.4.

2.3 The Heterogeneous Equilibrium

A reaction is called heterogeneous, if it occurs for instance at the gas-to-solid interface, while gas phase reactions are called homogeneous. Since the chemical potential of the solid is independent

T [K]	p [bar]	Y_{H_2}	Y_{O_2}	$Y_{\text{H}_2\text{O}}$
2000	1	0.0006	0.0049	0.9945
3000	1	0.0172	0.1364	0.8464
4000	1	0.0653	0.5180	0.4167
2000	10	0.0002	0.0022	0.9974
3000	10	0.0084	0.0664	0.9252
4000	10	0.0394	0.3127	0.6478

Table 2.4: Equilibrium compositions of the $\text{H}_2/\text{O}_2/\text{H}_2\text{O}$ system for several temperatures and pressures.

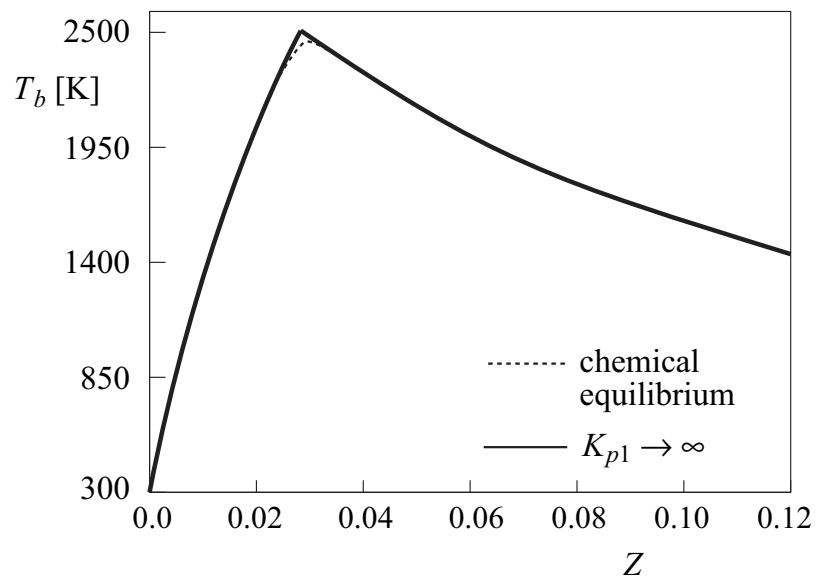


Figure 2.3: Equilibrium flame temperature for a hydrogen-air flame.

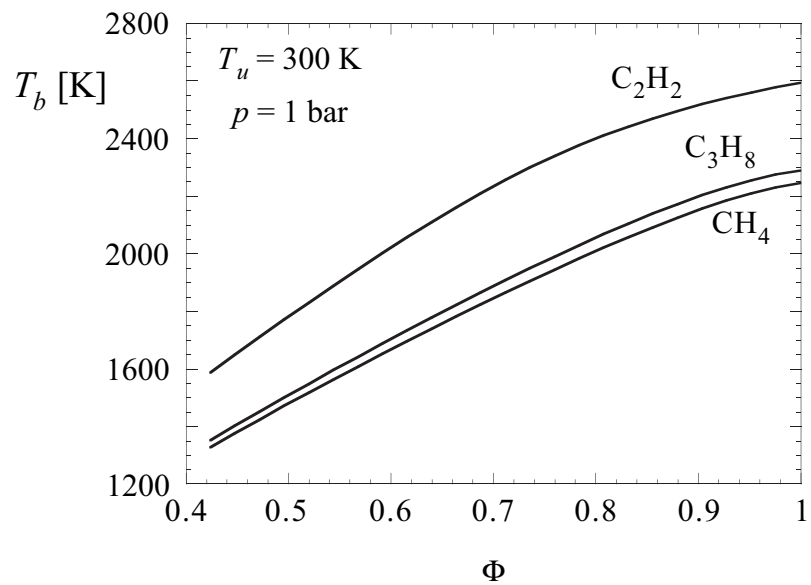


Figure 2.4: Adiabatic flame temperatures for lean methane, acetylene and propane flames as a function of the equivalence ratio for $T_u = 300$ K.

of pressure

$$\mu_i = \mu_i^0 = H_{i,\text{ref}} - TS_{i,\text{ref}} + \int_{T_{\text{ref}}}^T C_{p,i} dT - T \int_{T_{\text{ref}}}^T \frac{C_{p,i}}{T} dT, \quad i = 1, 2, \dots, k \quad (2.49)$$

only the partial pressures of the gaseous components will appear in the law of mass action. As an example consider the reaction of solid carbon $\text{C}_s + \text{O}_2 = \text{CO}_2$. Then the ratio of partial pressures of CO_2 and O_2 becomes

$$\frac{p_{\text{CO}_2}}{p_{\text{O}_2}} = \exp\left(\frac{\mu_{\text{CO}_2}^0 - \mu_{\text{C}_s}^0 - \mu_{\text{O}_2}^0}{\mathcal{R}T}\right) = K_p. \quad (2.50)$$

Here the molar enthalpy $H_{\text{C}_s,\text{ref}}$ of solid carbon is zero per definition while $\pi_{A,\text{C}_s} = -9.979$ and $\pi_{B,\text{C}_s} = 1.719$.

Example 2.1

Calculate the equilibrium mole fraction of NO in air at $T = 1000$ K and $T = 1500$ K by assuming that the mole fractions of O_2 ($X_{\text{O}_2} = 0.21$) and N_2 ($X_{\text{N}_2} = 0.79$) remain unchanged.

Solution

The equilibrium constant of the reaction



is with the values in Tab. 2.1

$$K_p(T) = 17.38 T^{0.0247} \exp(-21719/T) \quad (2.52)$$

For the partial pressure of NO one has

$$p_{\text{NO}} = (p_{\text{N}_2} p_{\text{O}_2} K_p)^{1/2} \quad (2.53)$$

Neglecting the consumption of N_2 and O_2 as a first approximation, their partial pressures may be approximated with Eq. (1.18) as $p_{\text{N}_2} = 0.79 p$, $p_{\text{O}_2} = 0.21 p$ in air. The equilibrium mole fraction of

NO is then

$$X_{\text{NO}} = 1.7 T^{0.01235} \exp(-10856/T). \quad (2.54)$$

At $T = 1000 \text{ K}$ one obtains 38 ppv (*parts per volume* = $X_i \cdot 10^{-6}$) and at $T = 1500 \text{ K}$ 230 ppv. This indicates that at high temperatures equilibrium NO-levels exceed by far those that are accepted by modern emission standards which are around 100 ppv or lower. Equilibrium considerations therefore suggest that in low temperature exhaust gases NO is above the equilibrium value and can be removed by catalysts.

Bibliography

[1] Janaf Tables. <http://www.me.berkeley.edu/gri-mech>.

Lecture 3

Fluid Dynamics and Balance Equations for Reacting Flows

The basic equations for calculating combustion processes in the gas phase are the equations of continuum mechanics. They include in addition to balance equations for mass and momentum those for the energy and the chemical species. Associated with the release of thermal energy and the increase in temperature is a local decrease in density which in turn affects the momentum balance. Therefore, all these equations are closely coupled to each other. Nevertheless, in deriving these equations we will try to point out how they can be simplified and partially uncoupled under certain assumptions.

3.1 Balance Equations

Let us consider a general quality per unit volume $f(x, t)$. Its integral over the finite volume V , with the time-independent boundary A is given by

$$F(t) = \int_V f(x, t) dV. \quad (3.1)$$

The temporal change of F

$$\frac{\partial F}{\partial t} = \int_V \frac{\partial f}{\partial t} dV \quad (3.2)$$

is then due to the following three effects (cf. Fig. 3.1):

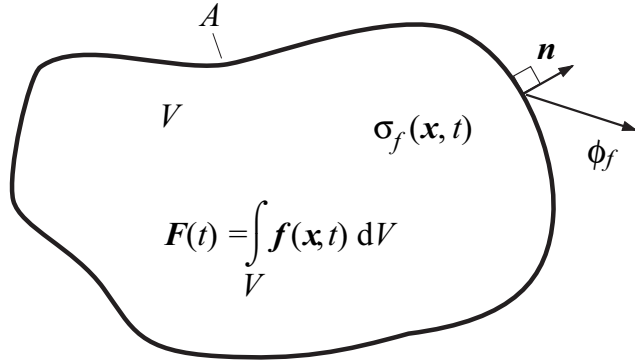


Figure 3.1: A time-independent control volume V for a balance quality $F(t)$. The scalar product between the surface flux ϕ_f and the normal vector n determines the outflow through the surface A , a source s_f the rate of production of the balance quality.

1. by the flux ϕ_f across the boundary A . This flux may be due to convection or molecular transport. By integration over the boundary A we obtain the net contribution

$$-\int_A \phi_f \cdot n \, dA, \quad (3.3)$$

which is negative, if the normal vector is assumed to direct outwards.

2. by a local source σ_f within the volume. This is an essential production of partial mass by chemical reactions. Integrating the source term over the volume leads to

$$\int_V \sigma_f \, dV; \quad (3.4)$$

3. by an external induced source s . Examples are the gravitational force or thermal radiation. Integration of s_f over the volume yields

$$\int_V s_f \, dV. \quad (3.5)$$

We therefore have the balance equation

$$\int_V \frac{\partial f}{\partial t} \, dV = - \int_A \phi_f \cdot n \, dA + \int_V (\sigma_f + s_f) \, dV \quad (3.6)$$

Changing the integral over the boundary A into a volume integral using Gauss' theorem

$$\int_A \phi_f \cdot \mathbf{n} \, dA = \int_V \operatorname{div} \phi_f \, dV \quad (3.7)$$

and realizing that the balance must be independent of the volume, we obtain the general balance equation in differential form

$$\frac{\partial f}{\partial t} = -\operatorname{div} \phi_f + \sigma_f + s_f. \quad (3.8)$$

3.2 Mass Balance

Set the partial mass per unit volume $\rho_i = \rho Y_i = f$. The partial mass flux across the boundary is $\rho_i v_i = \phi_f$, where v_i is called the diffusion velocity. Summation over all components yields the mass flow

$$\rho \mathbf{v} = \sum_{i=1}^k \rho_i v_i, \quad (3.9)$$

where \mathbf{v} is the mass average velocity. The difference between v_i defines the diffusion flux

$$v_i - \mathbf{v} = \frac{\mathbf{j}_i}{\rho_i}, \quad (3.10)$$

where the sum satisfies

$$\sum_{i=1}^k \mathbf{j}_i = \mathbf{0}. \quad (3.11)$$

Setting the chemical source term

$$\sigma_f = \dot{m}_i = W_i \sum_{l=1}^r \nu_{il} \omega_l \quad (3.12)$$

one obtains the equation for the partial density

$$\frac{\partial \rho_i}{\partial t} = -\operatorname{div} (\rho_i \mathbf{v}_i) + \dot{m}_i, \quad i = 1, 2, \dots, k. \quad (3.13)$$

The summation over i leads to the continuity equation

$$\frac{\partial \rho}{\partial t} = -\operatorname{div} (\rho \mathbf{v}). \quad (3.14)$$

Introducing the total derivative of a quantity \mathcal{A}

$$\frac{D\mathcal{A}}{Dt} = \frac{\partial \mathcal{A}}{\partial t} + \mathbf{v} \cdot \mathbf{grad} \mathcal{A}, \quad (3.15)$$

a combination with the continuity equation yields

$$\rho \frac{D\mathcal{A}}{Dt} = \frac{\partial(\rho\mathcal{A})}{\partial t} + \mathbf{div} (\rho\mathbf{v}\mathcal{A}). \quad (3.16)$$

Then Eq. (3.13) may also be written using Eq. (3.10)

$$\rho \frac{DY_i}{Dt} = -\mathbf{div} \mathbf{j}_i + \dot{m}_i, \quad i = 1, 2, \dots, k. \quad (3.17)$$

Here \dot{m}_i is the chemical source term defined by

$$\dot{m}_i = M_i \sum_{l=1}^r \nu_{il} \omega_l, \quad (3.18)$$

where ω_l are the chemical reaction rates.

3.3 Momentum Balance

Set the momentum per unit volume $\rho\mathbf{v} = \mathbf{f}$. The momentum flux is the sum of the convective momentum in flow $\rho\mathbf{v}\mathbf{v}$ and the stress tensor

$$\mathbf{P} = p\mathbf{I} + \boldsymbol{\tau} \quad (3.19)$$

where \mathbf{I} is the unit tensor and $\boldsymbol{\tau}$ is the viscous stress tensor. Therefore $\rho\mathbf{v}\mathbf{v} + \mathbf{P} = \phi_f$. There is no local source of momentum, but the gravitational force from outside $s_f = \rho\mathbf{g}$ where \mathbf{g} denotes the constant of gravity. The momentum equation then reads

$$\frac{\partial(\rho\mathbf{v})}{\partial t} = -\mathbf{div} (\rho\mathbf{v}\mathbf{v} + \mathbf{P}) + \rho\mathbf{g} \quad (3.20)$$

or with Eq. (3.16) for $\mathcal{A} \equiv \mathbf{v}$

$$\rho \frac{D\mathbf{v}}{Dt} = -\mathbf{grad} p - \mathbf{div} \boldsymbol{\tau} + \rho\mathbf{g}. \quad (3.21)$$

3.4 Kinetic Energy Balance

The scalar product of the momentum equation Eq. (3.20) with \mathbf{v} provides the balance for the kinetic energy

$$\frac{1}{2} \frac{\partial}{\partial t} (\rho v^2) = -\mathbf{div} (\mathbf{P} \cdot \mathbf{v} + \frac{1}{2} \mathbf{v} \rho v^2) + \mathbf{P} : \mathbf{grad} \mathbf{v} + \rho \mathbf{g} \cdot \mathbf{v}, \quad (3.22)$$

where $v^2 = \mathbf{v} \cdot \mathbf{v}$.

3.5 Potential Energy Balance

The gravitational force may be written as the derivative of the time-independent potential

$$\mathbf{g} = -\mathbf{grad} \psi, \quad \frac{\partial \psi}{\partial t} = 0. \quad (3.23)$$

Then with the continuity equation Eq. (3.14) the balance for the potential energy is

$$\frac{\partial(\rho\psi)}{\partial t} = -\mathbf{div} (\rho \mathbf{v} \psi) - \rho \mathbf{g} \cdot \mathbf{v}. \quad (3.24)$$

3.6 Total and Internal Energy and Enthalpy Balance

The first law of thermodynamics states that the total energy must be conserved, such that the local source $\sigma_f = 0$. We set $\rho e = f$, where the total energy per unit mass is

$$e = u + \frac{1}{2} v^2 + \psi. \quad (3.25)$$

This defines the internal energy introduced in Eq. (2.1). The total energy flux $\phi_f \equiv j_e$ is

$$j_e = \rho e \mathbf{v} + \mathbf{P} \cdot \mathbf{v} + j_q \quad (3.26)$$

which defines the total heat flux j_q . The externally induced source due to radiation is $\dot{q}_R = s_f$.

Then the total energy balance

$$\frac{\partial(\rho e)}{\partial t} = -\mathbf{div} j_e + \dot{q}_R \quad (3.27)$$

may be used to derive an equation for the internal energy

$$\frac{\partial(\rho u)}{\partial t} = -\mathbf{div}(\rho v u + \mathbf{j}_q) - \mathbf{P} : \mathbf{grad} \mathbf{v} + \dot{q}_R. \quad (3.28)$$

Using Eq. (3.16) this may be written with the total derivative

$$\rho \frac{Du}{Dt} = -\mathbf{div} \mathbf{j}_q - p \mathbf{div} \mathbf{v} - \boldsymbol{\tau} : \mathbf{grad} \mathbf{v} + \dot{q}_R. \quad (3.29)$$

With the continuity equation Eq. (3.14) we may substitute $\mathbf{div} \mathbf{v}$ by $\rho \frac{D}{Dt}(\frac{1}{\rho})$ and may write the balance in the form

$$\underbrace{\frac{Du}{Dt}}_{\propto du} + \underbrace{p \frac{D}{Dt}(\frac{1}{\rho})}_{\propto pdv} = \underbrace{\frac{1}{\rho} [-\mathbf{div} \mathbf{j}_q + \dot{q}_R]}_{\propto \delta q} - \underbrace{\frac{1}{\rho} \boldsymbol{\tau} : \mathbf{grad} \mathbf{v}}_{\propto \delta w_R} \quad (3.30)$$

to illustrate the equivalence with the first law introduced in a global thermodynamic balance in Eq. (2.1). With $h = u + p/\rho$ the enthalpy balance equation reads

$$\rho \frac{Dh}{Dt} = \frac{Dp}{Dt} = -\mathbf{div} \mathbf{j}_q - \boldsymbol{\tau} : \mathbf{grad} \mathbf{v} + \dot{q}_R. \quad (3.31)$$

3.7 Transport Processes

In its most general form Newton's law states that the viscous stress tensor is proportional to the symmetric, trace-free part of the velocity gradient, more specifically

$$\boldsymbol{\tau} = -\mu \left(2[\mathbf{grad} \mathbf{v}]^{\text{sym}} - \frac{2}{3} \mathbf{div} \mathbf{v} \mathbf{I} \right). \quad (3.32)$$

Here the suffix ^{sym} denotes that only the symmetric part is taken and the second term in the parenthesis subtracts the trace elements from the tensor. Newton's law thereby defines the dynamic viscosity. Similarly Fick's law states that the diffusion flux is proportional to the concentration gradient. Due to thermodiffusion it is also proportional to the temperature gradient. The most general form for multicomponent diffusion is written as

$$\mathbf{j}_i = \frac{W_i}{W} \sum_{\substack{j=1 \\ j \neq i}}^k \rho \mathcal{D}_{ij} W_j \mathbf{grad} X_j - \frac{D_i^T}{T} \mathbf{grad} T, \quad i = 1, 2, \dots, k. \quad (3.33)$$

For most combustion processes thermodiffusion can safely be neglected. For a binary mixture Eq. (3.33) then reduces to

$$\mathbf{j}_i = -\rho D_{ij} \mathbf{grad} Y_i \quad (3.34)$$

where $D_{ij} = D_{ji}$ is the binary diffusion coefficient. For multicomponent mixtures, where one component occurs in large amounts, as for the combustion in air where nitrogen is abundant, all other species may be treated as trace species and Eq. (3.34) with the binary diffusion coefficient with respect to the abundant component may be used as an approximation

$$\mathbf{j}_i = -\rho D_i \mathbf{grad} Y_i, \quad D_i = D_{i,N_2}. \quad (3.35)$$

A generalization for an effective diffusion coefficient D_i to be used for the minor species in Eq. (3.35) is

$$D_i = \frac{\sum_{\substack{i=1 \\ i \neq j}}^k X_i}{\sum_{\substack{j=1 \\ j \neq i}}^k X_j / D_{ij}}. \quad (3.36)$$

Note that the use of Eq. (3.35) does not satisfy the condition Eq. (3.11). Finally, Fourier's law of thermal conductivity states that the heat flux should be proportional to the negative temperature gradient. The heat flux \mathbf{j}_q includes the effect of partial enthalpy transport by diffusion and is written

$$\mathbf{j}_q = -\lambda \mathbf{grad} T + \sum_{i=1}^k h_i \mathbf{j}_i \quad (3.37)$$

which defines the thermal conductivity λ . In Eq. (3.37) the Dufour heat flux has been neglected. Transport coefficients for single components can be calculated on the basis of the theory of rarefied gases [1].

3.8 Different Forms of the Energy Equation

We start from the enthalpy equation and neglect in the following the viscous dissipation term $-\tau : \text{grad } v$ and the radiative heat transfer term \dot{q}_R . Then, differentiating Eq. (2.4) as

$$dh = c_p dT + \sum_{i=1}^k h_i dY_i, \quad (3.38)$$

where c_p is the heat capacity at constant pressure of the mixture, we can write the heat flux as

$$\mathbf{j}_q = -\frac{\lambda}{c_p} \mathbf{grad} h + \sum_{i=1}^k h_i \left(\mathbf{j}_i + \frac{\lambda}{c_p} \mathbf{grad} Y_i \right). \quad (3.39)$$

For the special case that the diffusion flux can be approximated by Eq. (3.34) with an effective diffusion coefficient D_i we introduce the Lewis number

$$\text{Le}_i = \frac{\lambda}{\rho c_p D_i} \quad (3.40)$$

and write the last term in Eq. (3.39) as

$$\sum_{i=1}^k h_i \left(1 - \frac{1}{\text{Le}_i} \right) \frac{\lambda}{c_p} \mathbf{grad} Y_i. \quad (3.41)$$

This term vanishes if the Lewis numbers of all species can be assumed equal to unity. This is an interesting approximation because it leads to the following form of the enthalpy equation

$$\rho \frac{Dh}{Dt} = \frac{Dp}{Dt} + \text{div} \left(\frac{\lambda}{c_p} \mathbf{grad} h \right). \quad (3.42)$$

If furthermore the pressure is constant as it is approximately the case in all applications except in reciprocating engines, the enthalpy equation would be very much simplified. The assumption of unity Lewis numbers for all species is not justified in many combustion applications. In fact, deviations from that assumption lead to a number of interesting phenomena that have been studied recently in the context of flame stability and the response of flames to external disturbances. We will address these questions in some of the lectures below.

Another important form of the energy equation is that in terms of the temperature. With Eqs.

(3.38) and (3.17) the total derivative of the enthalpy can be written as

$$\rho \frac{Dh}{Dt} = \rho c_p \frac{DT}{Dt} + \sum_{i=1}^k (-\mathbf{div} \mathbf{j}_i + \dot{m}_i) h_i. \quad (3.43)$$

Then with Eq. (3.37), the enthalpy equation Eq. (3.31) without the second last term yields the temperature equation

$$\rho c_p \frac{DT}{Dt} + \mathbf{div} (\lambda \mathbf{grad} T) - \sum_{i=1}^k c_{pi} \mathbf{j}_i \cdot \mathbf{grad} T + \sigma_T + \dot{q}_R. \quad (3.44)$$

Here the last term describes the temperature change due to energy transfer by radiation and the penultimate term the temperature change due to chemical reactions which may be written as

$$\sigma_T = - \sum_{i=1}^k \dot{m}_i h_i = - \sum_{l=1}^r \sum_{i=1}^k \nu_{il} W_i h_i \omega_l = \sum_{l=1}^r Q_l \omega_l \quad (3.45)$$

where the definition Eq. (3.18) has been used for each reaction. The second term on the right hand side may be neglected, if one assumes that all specific heats c_{pi} are equal. This assumption is very often justified since this term does not contribute as much to the change of temperature as the other terms in the equation, in particular the chemical source term. If one also assumes that spatial gradients of c_p may be neglected for the same reason, the temperature equation takes the form

$$\rho \frac{DT}{Dt} = \frac{1}{c_p} \frac{Dp}{Dt} + \mathbf{div} \left(\frac{\lambda}{c_p} \mathbf{grad} T \right) + \sum_{l=1}^r \frac{Q_l}{c_p} \omega_l + \frac{\dot{q}_R}{c_p}. \quad (3.46)$$

For a constant pressure it is very similar to Eq. (3.17) with an effective equal diffusion coefficient $D = \lambda / \rho / c_p$ for all reactive species and a spatially constant Lewis number Le_i may be written as

$$\rho \frac{DY_i}{Dt} = \frac{1}{\text{Le}_i} \mathbf{div} \left(\frac{\lambda}{c_p} \mathbf{grad} Y_i \right) + W_i \sum_{l=1}^r \nu_{il} \omega_l. \quad (3.47)$$

For unity Lewis numbers this and the temperature equation are easily combined to obtain the enthalpy equation Eq. (3.42). Since the use of Eq. (3.46) and Eq. (3.47) does not require the unity Lewis number assumption, this formulation is often used when non-unity Lewis number effects are to be analyzed. For flame calculations a sufficiently accurate approximation for the transport

CH_4	O_2	H_2O	CO_2	H	O	OH	HO_2
0.97	1.11	0.83	1.39	0.18	0.70	0.73	1.10

H_2	CO	H_2O_2	HCO	CH_2O	CH_3	CH_3O
0.3	1.10	1.12	1.27	1.28	1.00	1.30

Table 3.1: Lewis numbers of some reacting species occurring in methane-air flames.

properties is [2]

$$\frac{\lambda}{c_p} = 2.58 \cdot 10^{-4} \frac{\text{g}}{\text{cm sec}} \left(\frac{T}{298 \text{ K}} \right)^{0.7}, \quad (3.48)$$

a constant Prandtl number

$$\text{Pr} = \frac{\mu c_p}{\lambda} = 0.75, \quad (3.49)$$

and constant Lewis numbers. For a number of species occurring in methane-air flames approximate values from [2] are listed in Tab. 3.1. A first approximation for other hydrocarbon species can be based on the assumption that the binary diffusion coefficients of species i with respect to nitrogen is approximately proportional to

$$D_i \sim \left(\frac{W_i + W_{\text{N}_2}}{2W_i W_{\text{N}_2}} \right)^{1/2}. \quad (3.50)$$

Then the ratio of its Lewis number to that of methane is

$$\frac{\text{Le}_i}{\text{Le}_{\text{CH}_4}} = \left(\frac{W_i}{W_{\text{CH}_4}} \frac{W_{\text{CH}_4} + W_{\text{N}_2}}{W_i + W_{\text{N}_2}} \right)^{1/2}. \quad (3.51)$$

3.9 Balance Equations for Element Mass Fractions

Summation of the balance equations for the mass fractions Eq. (3.17) according to Eq. (1.10) leads to the balance equations for Z_j

$$\rho \frac{DZ_j}{Dt} = -\text{div} \sum_{i=1}^k \frac{a_{ij} W_j}{W_i} \mathbf{j}_i. \quad (3.52)$$

Here the summation over the chemical source terms vanishes

$$W_j \sum_{i=1}^k \sum_{l=1}^r a_{ij} \nu_{il} w_l = W_j \sum_{l=1}^r w_l \sum_{i=1}^k a_{ij} \nu_{il} = 0, \quad (3.53)$$

since the last sum vanishes for each reaction. The diffusion term simplifies if one assumes that the diffusion coefficients of all species are equal. If one further more assumes a unity Lewis number this leads to

$$\rho \frac{DZ_j}{Dt} = \operatorname{div} \left(\frac{\lambda}{c_p} \operatorname{grad} Z_j \right). \quad (3.54)$$

A similar equation may be derived for the mixture fraction Z . Since Z is defined according to Eq. (1.35) as the mass fraction of the fuel stream, it represents the sum of element mass fractions contained in the fuel stream. The mass fraction of the fuel is the sum of the element mass fractions

$$Y_{F,u} = \sum_{j=1}^{k_e} Z_{j,F}, \quad (3.55)$$

where

$$Z_{j,F} = a_{F,j} \frac{W_j}{W_F} Y_{F,u}. \quad (3.56)$$

With Eq. (1.36) the mixture fraction may therefore be expressed as a sum of element mass fractions

$$Z = \frac{\sum_{j=1}^{k_e} Z_{j,F}}{Y_{F,1}}. \quad (3.57)$$

Then, with the assumption of unit Lewis numbers such that $\lambda/c_p = \rho D$, a summation over Eq. (3.54) leads to a balance equation for the mixture fraction

$$\rho \frac{DZ}{Dt} = \operatorname{div} \left(\rho D \operatorname{grad} Z \right). \quad (3.58)$$

For a one-step reaction with the reaction rate ω this equation can also be derived using Eqs. (1.38) and (3.47) for Y_F and Y_{O_2} with $L_{F,O_2} = L_{O_2,F} = 1$ as

$$\rho \frac{DY_F}{Dt} = \operatorname{div} \left(\frac{\lambda}{c_p} \operatorname{grad} Y_F \right) - \nu'_F W_F \omega \quad (3.59)$$

$$\rho \frac{DY_{O_2}}{Dt} = \operatorname{div} \left(\frac{\lambda}{c_p} \operatorname{grad} Y_{O_2} \right) - \nu'_{O_2} W_{O_2} \omega. \quad (3.60)$$

Dividing the first of these by $\nu'_{O_2} W_{O_2}$ and subtracting yields a source-free balance equation for the combination

$$\frac{Y_F}{\nu'_F W_F} = \frac{Y_{O_2}}{\nu'_{O_2} W_{O_2}} \quad (3.61)$$

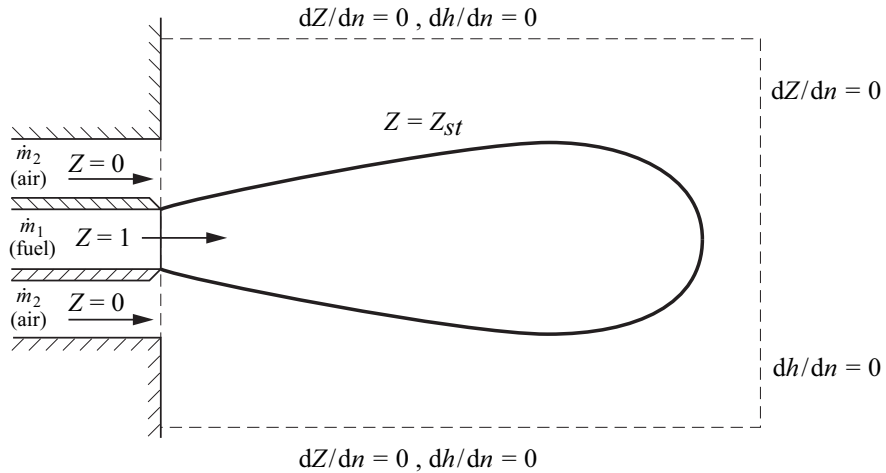


Figure 3.2: Coflow diffusion flame

which is a linear function of Z according to Eq. (1.35). This leads again to Eq. (3.58). For constant pressure the enthalpy equation Eq. (3.42) has the same form as v(3.58) and a coupling relation between the enthalpy and the mixture fraction may be derived

$$h = h_2 + Z(h_1 - h_2) \quad (3.62)$$

where h_1 is the enthalpy of the fuel stream and h_2 that of the oxidizer stream. Similarly, using Eqs. (3.54) and (3.58) the element mass fractions may be expressed in terms of the mixture fraction

$$Z_j = Z_{j,2} + Z(Z_{j,1} - Z_{j,2}), \quad (3.63)$$

where $Z_{j,1}$ and $Z_{j,2}$ are the element mass fractions in the fuel and oxidizer stream, respectively. It should be noted that the coupling relations Eqs. (3.62) and (3.63) required a two feed system with equivalent boundary conditions for the enthalpy and the mass fractions. A practical example is a single jet as fuel stream with co-flowing air as oxidizer stream into an open atmosphere, such that zero gradient boundary conditions apply everywhere except at the input streams as shown in Fig. 3.2. Once the mixture fraction field has been obtained by numerical solution of Eq. (3.58) the adiabatic flame temperature may be calculated using the methods of Lecture 2 as a local function of Z .

Bibliography

- [1] J.O. Hirschfelder, C. F. Curtiss, and R. B. Bird. Molecular theory of gases and liquids. *Wiley New York*, 1954.
- [2] M. D. Smooke and V. Giovangigli. Reduced kinetic mechanisms and asymptotic approximation for methane-air flames. *Lecture Notes in Physics, Springer-Verlag Berlin*, 384:29, 1992.

Lecture 4

Laminar Premixed Flame Configuration

4.1 The Laminar Burning Velocity

The classical device to generate a laminar premixed flame is the Bunsen burner shown in Fig. 4.1. Gaseous fuel from the fuel supply enters through an orifice into the mixing chamber, into which air is entrained through adjustable openings from the outside. The cross sectional area of the fuel orifice may be adjusted by moving the needle through an adjustment screw into the orifice. Thereby the velocity of the jet entering into the mixing chamber may be varied and the entrainment of the air and the mixing can be optimized. The mixing chamber must be long enough to generate a premixed gas issuing from the Bunsen tube into the surroundings. If the velocity of the issuing flow is larger than the laminar burning velocity to be defined below, a Bunsen flame cone establishes itself at the top of the tube. It represents a steady premixed flame propagating normal to itself with the burning velocity s_L into the unburnt mixture.

The kinematic balance of this process is illustrated for a steady oblique flame in Fig. 4.2. The oncoming flow velocity vector v_u of the unburnt mixture (subscript u) is split into a component $v_{t,u}$ which is tangential to the flame and into a component $v_{n,u}$ normal to the flame front. Due to thermal expansion within the flame front the normal velocity component is increased, since the mass flow density ρv_n through the flame must be the same in the unburnt mixture and in the burnt

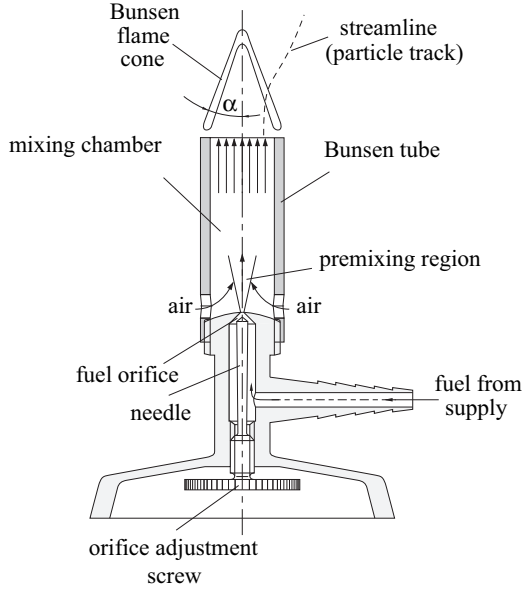


Figure 4.1: The Bunsen burner

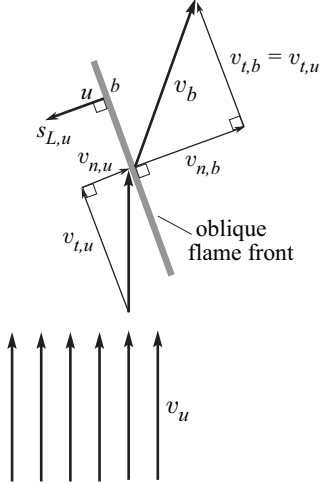


Figure 4.2: Kinematic balance for a steady oblique flame.

gas (subscript b)

$$(\rho v_n)_u = (\rho v_n)_b, \quad (4.1)$$

therefore

$$v_{n,b} = v_{n,u} \frac{\rho_u}{\rho_b}. \quad (4.2)$$

The tangential velocity component v_t is not affected by the gas expansion and remains the same

$$v_{t,b} = v_{t,u}. \quad (4.3)$$

Vector addition of the velocity components in the burnt gas in Fig. 4.2 then leads to v_b which points into a direction which is deflected from the flow direction of the unburnt mixture. Finally, since the flame front is stationary in this experiment, the burning velocity $s_{L,u}$ with respect to the unburnt mixture must be equal to the flow velocity of the unburnt mixture normal to the front.

$$s_{L,u} = v_{n,u} \quad (4.4)$$

With the Bunsen flame cone angle in Fig. 4.1 denoted by α the normal velocity is $v_{n,u} = v_u \sin \alpha$

and it follows

$$s_{L,u} = v_u \sin \alpha. \quad (4.5)$$

This allows to experimentally determine the burning velocity by measuring the cone angle α under the condition that the flow velocity v_u is uniform across the tube exit. If this is not the case the flame angle also varies with radial distance, since the burning velocity $s_{L,u}$ is essentially constant.

A particular phenomenon occurs at the flame tip. If the tip is closed, which is in general the case for hydrocarbon flames (but not necessarily for lean hydrogen flames) the burning velocity at the tip, being normal and therefore equal to the flow velocity, is by a factor $1/\sin\alpha$ larger than the burning velocity through the oblique part of the cone.

$$s_{L,u}|_{\text{flame tip}} = v_u. \quad (4.6)$$

This will be explained below by the strong curvature of the flame front at the tip leading to a preheating by the lateral parts of the flame front and thereby to an increase in burning velocity. This analysis also includes the effect of non-unity Lewis numbers by which, for instance, the difference between lean hydrogen and lean hydrocarbon flames can be explained. Finally, it is shown in (Fig. 4.1) that the flame is detached from the rim of the burner. This is due to conductive heat loss to the burner which leads in regions very close to the rim to temperatures, at which combustion cannot be sustained. Another example for an experimental device to measure laminar burning velocities is the combustion bomb (Fig. 4.3) within which a flame is initiated by a central spark. Spherical propagation of a flame then takes place which may optically be detected through quartz windows and the flame propagation velocity dr_f/dt may be recorded. Now the flame front is not stationary. If the radial flow velocities are defined positive in inward direction, the velocity of the front must be subtracted from these in the mass flow balance through the flame front

$$\rho u \left(v_u - \frac{dr_f}{dt} \right) = \rho_b \left(v_b - \frac{dr_f}{dt} \right). \quad (4.7)$$

At the flame front the kinematic balance between propagation velocity, flow velocity and burning velocity with respect to the unburnt mixture is

$$\frac{dr_f}{dt} = v_u + s_{L,u}. \quad (4.8)$$

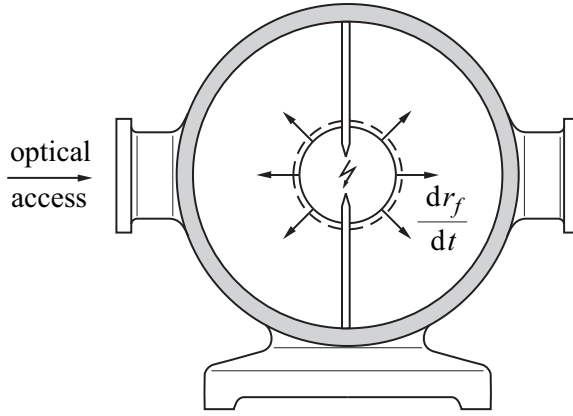


Figure 4.3: Laminar spherical flame propagation in a combustion bomb.

Similarly, the kinematic balance with respect to the burnt gas is

$$\frac{dr_f}{dt} = v_b + s_{L,b}. \quad (4.9)$$

In the present example the flow velocity v_b in the burnt gas behind the flame is zero due to symmetry. This leads with Eqs. (4.7) and (4.8) to

$$\frac{dr_f}{dt} = \frac{\rho_u}{\rho_u - \rho_b} v_u = v_u + s_{L,u} \quad (4.10)$$

from which the velocity in the unburnt mixture is calculated as

$$v_u = \frac{\rho_u}{\rho_u - \rho_b} s_{L,u}. \quad (4.11)$$

This velocity is induced by the expansion of the gas behind the flame front. Furthermore it follows that the flame propagation velocity is related to the burning velocity $s_{L,u}$ by

$$\frac{dr_f}{dt} = \frac{\rho_u}{\rho_b} s_{L,u}. \quad (4.12)$$

Measuring the flame propagation velocity dr_f/dt then allows to determine $s_{L,u}$. Furthermore, from Eq. (4.9) it follows with $v_b = 0$ that

$$\frac{dr_f}{dt} = s_{L,b}. \quad (4.13)$$

The comparison of Eqs. (4.12) and (4.13) shows that the burning velocity with respect to the

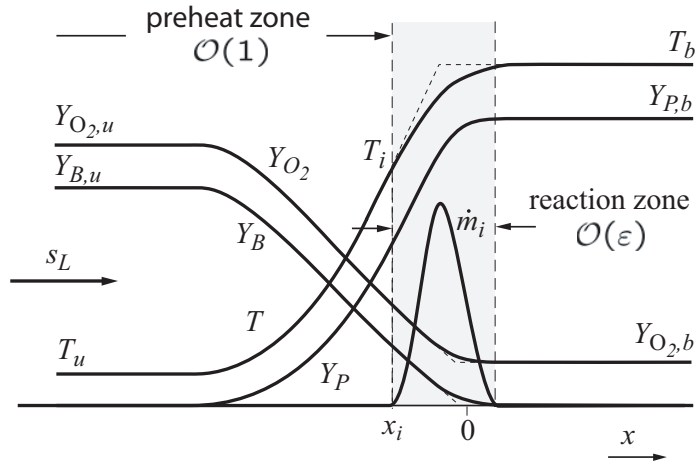


Figure 4.4: Flame structure of a laminar lean flame.

burnt gas is by a factor ρ_u/ρ_b larger than that with respect to the unburnt gas. This is equivalent to Eq. (4.2). For convenience we will denote in the following the burning velocity with respect to the unburnt gas by s_L

$$s_L \equiv s_{L,u}, \quad (4.14)$$

while we keep the notation $s_{L,b}$ for the burning velocity with respect to the burnt gas.

4.2 Governing Equations for Steady Premixed Flames, Numerical Calculations and Experimental Data

Let us consider a planar steady state flame configuration normal to the x -direction with the unburnt mixture at $x \rightarrow -\infty$ and the burnt gas at $x \rightarrow +\infty$. The flame structure is schematically shown in Fig. 4.4 for the case of a lean flame with a one-step reaction



The fuel and oxidizer are convected from upstream with the burning velocity s_L having the mass fractions $Y_{F,u}$ and $Y_{O_2,u}$ at $x \rightarrow -\infty$ and diffuse into the reaction zone. Here the fuel is entirely depleted while the remaining oxygen is convected downstream where it has the mass fraction $Y_{O_2,b}$. The chemical reaction forms the product P and releases heat which leads to a temperature

rise. The mass fraction Y_P increases therefore in a similar way from zero to $Y_{P,b}$ as the temperature from T_u to T_b . The products (not shown) diffuses upstream, and mix with the fuel and the oxidizer. Heat conduction from the reaction zone is also directed upstream leading to a preheating of the fuel/air mixture. Therefore the region upstream of the reaction zone is called the preheat zone.

We will now consider the general case with multi-step chemical kinetics. The fundamental property of a premixed flame, the burning velocity s_L may be calculated by solving the governing conservation equations for the overall mass, species and temperature.

Continuity

$$\frac{d(\rho u)}{dx} = 0, \quad (4.16)$$

Species

$$\rho u \frac{dY_i}{dx} = -\frac{dj_i}{dx} + \dot{m}_i, \quad (4.17)$$

Energy

$$\rho u c_p \frac{dT}{dx} = \frac{d}{dx} (\lambda \frac{dT}{dx}) - \sum_{i=1}^k h_i \dot{m}_i - \sum_{i=1}^k c_p j_i \frac{dT}{dx} + \frac{\partial p}{\partial t}. \quad (4.18)$$

For flame propagation with burning velocities much smaller than the velocity of sound, the pressure is spatially constant and is determined from the thermal equation of state. Therefore spatial pressure gradients are neglected in Eq. (4.18) while temporal pressure gradients have been retained.

The continuity equation may be integrated once to yield

$$\rho u = \rho_u s_L, \quad (4.19)$$

where the subscript u denotes conditions in the fresh, unburnt mixture, and where s_L denotes the burning velocity. The latter is an eigenvalue, which must be determined as part of the solution. The system of Eqs. (4.17)-(4.19) may be solved numerically with the appropriate upstream boundary conditions for the mass fractions and the temperature and zero gradient boundary conditions downstream.

As an example taken from [3] calculations of the burning velocity of premixed methane-air flames using a mechanism that contains only C₁-hydrocarbons and a mechanism that includes the C₂-species are shown in Fig. 4.5 as a function of the equivalence ratio ϕ . The two curves are compared with compilations of various data from the literature. It is seen that the calculations with the C₂-mechanism shows a better agreement than the C₁-mechanism. As another example

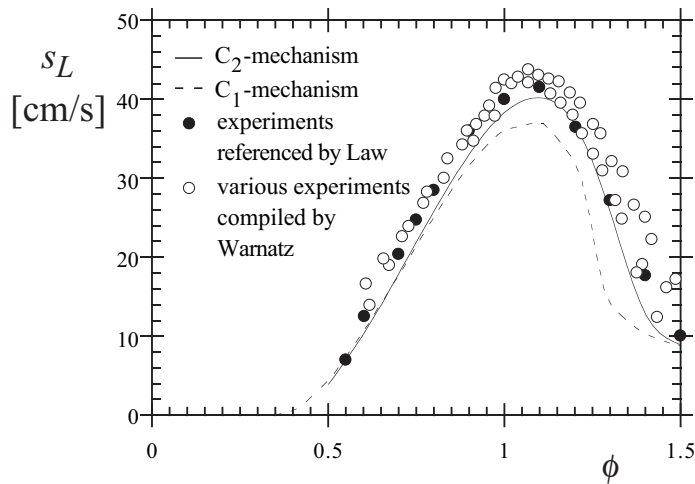


Figure 4.5: Burning velocities calculated with a starting C_1 -mechanism and a starting C_2 -mechanism, several data compiled by Warnatz [1], and recent data referenced by Law [2] for atmospheric methane-air-flames.

burning velocities of propane flames taken from [8] are shown in Fig. 4.6. Calculated values of burning velocities for lean flames based on Eqs. (4.17)-(4.19) are compared with approximations given in Lecture 6 in Figs. 6.6 and 6.7 for different pressures. Fig. 6.7 shows how s_L decreases with increasing pressure but increases with increasing preheat temperature.

The fundamental property of a premixed flame is its ability to propagate normal to itself with a burning velocity that, to first approximation, depends on thermo-chemical parameters of the premixed gas ahead of the flame only. In a steady flow of premixed gas a premixed flame will propagate against the flow until it stabilizes itself such that locally the flow velocity normal to the flame is equal to burning velocity. We have already discussed that for a Bunsen flame the condition of a constant burning velocity is violated at the top of the flame and that additional influences such as flame curvature must be taken into account. In this chapter we want to calculate flame shapes. We then will consider external influences that locally change the burning velocity and discuss the response of the flame to these disturbances.

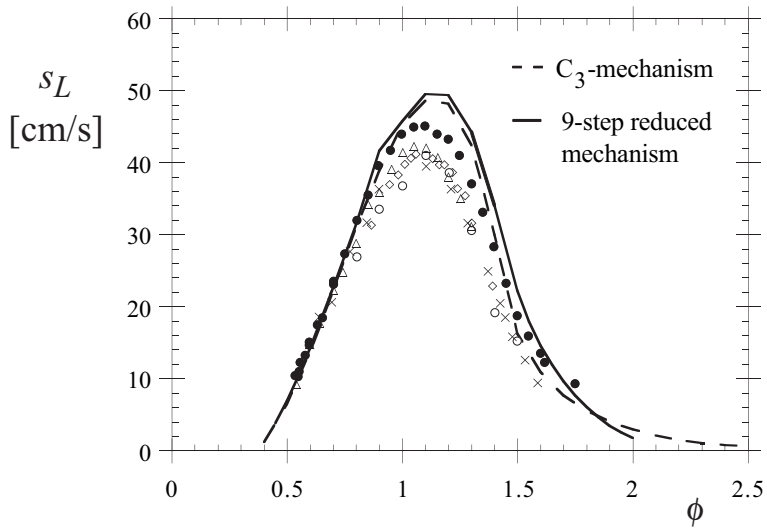


Figure 4.6: Burning velocity of propane-air flames vs. equivalence ratio ϕ obtained with an elementary mechanism containing only species up to C_3 hydrocarbons and a reduced 9-step mechanism [3] and from experimental results (\circ : Metghalchi et al [4], \times : Smith et al. [5], \diamond : Scholte et al. [6], \triangle : Yamaoka et al. [7], \bullet : C.K. Law, [2]).

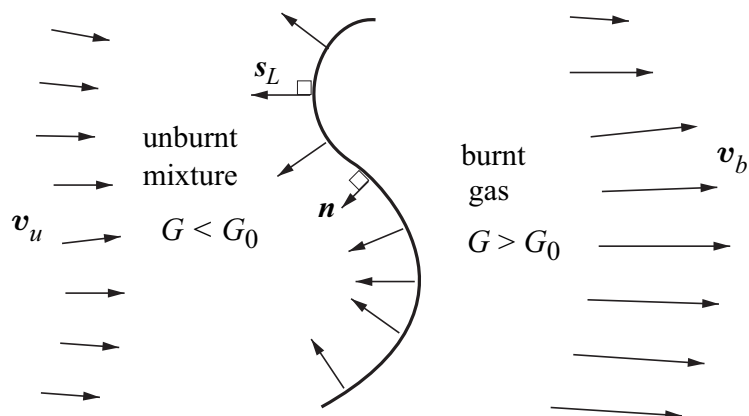


Figure 4.7: Schematic illustration of a propagating flame with arbitrary shape.

4.3 A Field Equation Describing the Flame Position

The kinematic relation Eq. (4.8) between the propagation velocity, the flow velocity, and the burning velocity that was derived for spherical flame propagation may be generalized by introducing the vector \mathbf{n} normal to the flame and writing

$$\frac{dx_f}{dt} = \mathbf{v} + s_L \mathbf{n}, \quad (4.20)$$

where x_f is the vector describing the flame position, dx_f/dt the flame propagation velocity, and \mathbf{v} the velocity vector. The normal vector points towards the unburnt mixture and is given by

$$\mathbf{n} = -\frac{\nabla G}{|\nabla G|}, \quad (4.21)$$

where $G(\mathbf{x}, t)$ can be identified as a scalar field whose level surfaces

$$G(\mathbf{x}, t) = G_0, \quad (4.22)$$

where G_0 is arbitrary, represent the flame surface (conf. Fig. 4.7). The flame contour $G(\mathbf{x}, t) = G_0$ divides the physical field into two regions, where $G > G_0$ is the region of burnt gas and $G < G_0$ that of the unburnt mixture. If one differentiates Eq. (4.22) with respect to t at $G = G_0$, such as

$$\frac{\partial G}{\partial t} + \nabla G \cdot \frac{d\mathbf{x}}{dt} \Big|_{G=G_0} = 0. \quad (4.23)$$

Introducing Eq. (4.20) and Eq. (4.21) into Eq. (4.23) one obtains the field equation

$$\frac{\partial G}{\partial t} + \mathbf{v} \cdot \nabla G = s_L |\nabla G|. \quad (4.24)$$

It will be called G -equation in the following. If the burning velocity s_L is defined with respect to the unburnt mixture, the flow velocity \mathbf{v} in Eq. (4.24) is defined as the conditioned velocity field in the unburnt mixture ahead of the flame. For a constant value of s_L the solution of Eq. (4.24) is non unique, and cusps will be formed where different parts of the flame intersect. Even an originally smooth undulated front in a quiescent flow will form cusps and eventually become flatter with time as illustrated in Fig. 4.8. This is called Huygens' principle.

As an example of a closed form solution of the G -equation let us consider the case of a slot burner with a constant exit velocity u for premixed combustion, Fig. 4.9. This is the two-dimensional

planar version of the axisymmetric Bunsen burner. The G -equation takes the form

$$u \frac{\partial G}{\partial x} = s_L \sqrt{\left(\frac{\partial G}{\partial x}\right)^2 + \left(\frac{\partial G}{\partial y}\right)^2} \quad (4.25)$$

With the ansatz

$$G = x + F(y) \quad (4.26)$$

and $G_0 = 0$ one obtains

$$u = s_L \sqrt{1 + \left(\frac{dF}{dy}\right)^2} \quad (4.27)$$

leading to

$$F = \sqrt{\frac{u^2 - s_L^2}{s_L^2}} |y| + const. \quad (4.28)$$

As the flame is attached at $x = 0, y = \pm b/2$, where $G = 0$, this leads to the solution

$$G = \sqrt{\frac{u^2 - s_L^2}{s_L^2}} \left(|y| - \frac{b}{2}\right) + x. \quad (4.29)$$

The flame tip lies with $y = 0, G = 0$ at

$$x_{F,0} = \frac{b}{2} \sqrt{\frac{u^2 - s_L^2}{s_L^2}} \quad (4.30)$$

and the flame angle α is given by

$$\tan \alpha = \frac{b}{2x_{F,0}} = \sqrt{\frac{u^2 - s_L^2}{s_L^2}}. \quad (4.31)$$

With $\tan^2 \alpha = \sin^2 \alpha / (1 - \sin^2 \alpha)$ it follows that

$$\sin \alpha = \frac{s_L}{u} \quad (4.32)$$

which is equivalent to Eq. (4.5). This solution shows a cusp at the flame tip $x = x_{F,0}, y = 0$. In order to obtain a rounded flame tip, one has to take modifications of the burning velocity due to flame curvature into account. This leads to the concept of flame stretch.

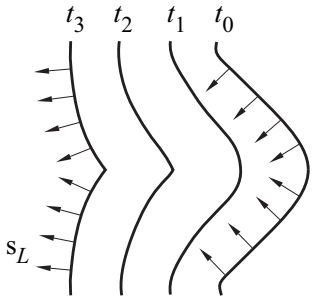


Figure 4.8: Illustration of Huygens' principle in flame propagation with constant s_L .

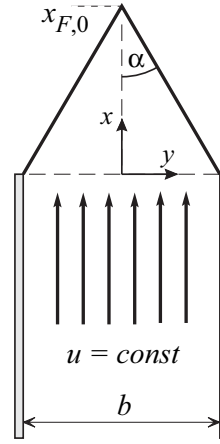


Figure 4.9: A premixed laminar flame on a slot burner.

4.4 Flame Stretch

Flame stretch consists of two contributions: One due to flame curvature and another due to flow divergence. It may be shown (cf. [9]) that for a one-step large activation energy reaction and with the assumption of constant properties the burning velocity s_L is modified by these two effects as

$$s_L = s_L^0 - s_L^0 \mathcal{L} \kappa + \mathcal{L} \mathbf{n} \cdot \nabla \mathbf{v} \cdot \mathbf{n}. \quad (4.33)$$

Here s_L^0 is the burning velocity for an unstretched flame and \mathcal{L} is the Markstein length to be presented below. The flame curvature κ is defined as

$$\kappa = \nabla \cdot \mathbf{n} = -\nabla \cdot \left(\frac{\nabla G}{|\nabla G|} \right), \quad (4.34)$$

which may be transformed as

$$\kappa = -\frac{\nabla^2 G + \mathbf{n} \cdot \nabla(\mathbf{n} \cdot \nabla G)}{|\nabla G|}. \quad (4.35)$$

The Markstein length \mathcal{L} appearing in Eq. (4.33) is of the same order of magnitude and proportional to the laminar flame thickness ℓ_F , their ratio \mathcal{L}/ℓ_F is called the Markstein number. For the case of a one-step reaction with a large activation energy, constant transport properties and a constant heat capacity c_p , the Markstein length with respect to the unburnt mixture reads, for example

$$\frac{\mathcal{L}_u}{\ell_F} = \frac{1}{\gamma} \ln \frac{1}{1-\gamma} + \frac{Ze(\text{Le}-1)}{2} \frac{(1-\gamma)}{\gamma} \int_0^{\gamma/(1-\gamma)} \frac{\ln(1+x)}{x} dx. \quad (4.36)$$

This expression was derived by Clavin and Williams (1982) [10] and Matalon and Matkowsky (1982) [9]. Here $Ze = E(T_b - T_u)/(\mathcal{R}T_b^2)$ is the Zeldovich number, where E is the activation energy and \mathcal{R} the universal gas constant, and Le is the Lewis number of the deficient reactant. Eq. (4.36) is valid if s_L is defined with respect to the unburnt mixture. A different expression can be derived, if both, s_L and \mathcal{L} are defined with respect to the burnt gas (cf. Clavin, 1985).[11]

We want to explore the influence of curvature on the burning velocity for the case of a spherical propagating flame. Since the flow velocity is zero in the burnt gas, it is advantageous to formulate the G -equation with respect to the burnt gas as in Eq. (4.13)

$$\frac{dr_f}{dt} = s_{L,b}, \quad (4.37)$$

where $r_f(t)$ is the radial flame position. The burning velocity is then $s_{L,b}^0$ and the Markstein length is that with respect to the burnt gas, \mathcal{L}_b , which differs from that given by Eq. (4.36) (cf. Clavin, 1985).[11] Here we assume $\mathcal{L}_b > 0$ to avoid complications associated with thermo-diffusive instabilities. In a spherical coordinate system Eq. (4.24) becomes

$$\frac{\partial G}{\partial t} = s_{L,b}^0 \left(\left| \frac{\partial G}{\partial r} \right| + \frac{2\mathcal{L}_b}{r} \frac{\partial G}{\partial r} \right), \quad (4.38)$$

where the entire term in round brackets represents the curvature in spherical coordinates. We introduce the ansatz

$$G = r_f(t) - r, \quad (4.39)$$

to obtain at the flame front $r = r_f$

$$\frac{\partial r_f}{\partial t} = s_{L,b}^0 \left(1 - \frac{2\mathcal{L}_b}{r_f} \right). \quad (4.40)$$

This equation may also be found in Clavin (1985) [11]. It reduces to Eq. (4.13) if \mathcal{L}_b is set equal to

zero. It may be integrated to obtain

$$s_{L,b}^0 t = r_f - r_{f,0} + 2\mathcal{L}_b \ln \left(\frac{r_f - 2\mathcal{L}_b}{r_{f,0} - 2\mathcal{L}_b} \right), \quad (4.41)$$

where the initial radius at $t = 0$ is denoted by $r_{f,0}$. This expression has no meaningful solutions for $r_{f,0} < 2\mathcal{L}_b$, indicating that there needs to be a minimum initial flame kernel for flame propagation to take off. It should be recalled that Eq. (4.33) is only valid if the product $\mathcal{L}\kappa$ is small compared to unity. For $r_{f,0} > 2\mathcal{L}_b$ curvature corrections are important at early times only.

4.5 Flame Front Instability

As it was discussed gas expansion in the flame front will lead to a deflection of a stream line that enters the front with an angle. This is shown in Fig. 4.10, where a slightly undulated flame front in the x, y -coordinate system is assumed. A stream tube with cross-sectional area A_0 and upstream flow velocity $u_{-\infty}$ widens due to flow divergence ahead of the flame. This divergence effect is generated by the expansion at the front that induces a flow component normal to the flame contour. As the stream lines cross the front they are deflected. At large distances from the front the stream lines are parallel again, but the downstream velocity is $u_\infty = (\rho_u / \rho_b) u_{-\infty}$. At a cross section A_1 , where the density is still equal to ρ_u the flow velocity due to continuity and the widening of the stream tube is

$$u_1 = \frac{A}{A_1} u_{-\infty} \leq u_{-\infty}. \quad (4.42)$$

Since the unperturbed flame propagates with $u_{-\infty} = s_{L,u}$ normal to itself the burning velocity is larger than u_1 and the flame will propagate upstream and thereby enhances the initial perturbation. In the following we will neglect viscous and gravity effects as well as compressibility in the burnt and unburnt gas, nevertheless density is discontinuous at the flame front. While the influence of the flame curvature on the burning velocity is retained, flame stretch due to flow divergence is neglected (see [12]). The burning velocity is then given by

$$s_L = s_L^0 (1 - \kappa \mathcal{L}). \quad (4.43)$$

The velocity components u and v will be normalized with the burning velocity $s_{L,u}$ (defined with respect to the unburnt mixture), the coordinates x and y with the flame thickness ℓ_F and the time with $\ell_F / s_{L,u}$. As a reference value for the density we take ρ_u , introduce the density rate

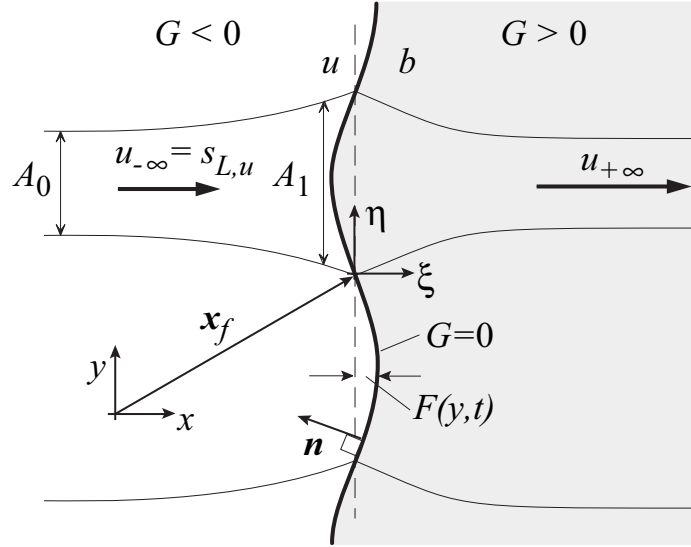


Figure 4.10: Illustration of the hydro-dynamic instability.

$r = \rho_b/\rho_u < 1$ and normalize the pressure with $\rho_u s_{L,u}^2$.

$$\begin{aligned} u^* &= u/s_{L,u}, & v^* &= v/s_{L,u}, & p^* &= \frac{p}{\rho_u s_{L,u}^2}, \\ x^* &= x/\ell_F, & y^* &= y/\ell_F, & t^* &= \frac{t}{\ell_F/s_{L,u}}. \end{aligned} \tag{4.44}$$

The non-dimensional governing equations are then (with the asterisks removed)

$$\begin{aligned} \frac{\partial u}{\partial x} + \frac{\partial v}{\partial y} &= 0 \\ \frac{\partial u}{\partial t} + u \frac{\partial u}{\partial x} + v \frac{\partial u}{\partial y} &= -\frac{1}{\rho} \frac{\partial p}{\partial x} \\ \frac{\partial v}{\partial t} + u \frac{\partial v}{\partial x} + v \frac{\partial v}{\partial y} &= -\frac{1}{\rho} \frac{\partial p}{\partial y}, \end{aligned} \tag{4.45}$$

where $\rho = 1$ and $\rho = r$ in the unburnt and burnt mixture respectively. If G is a measure of the distance to the flame front, the G -field is described by

$$G = x - F(y, t). \tag{4.46}$$

With Eqs. (4.21) and (4.23) the normal vector \mathbf{n} and the normal propagation velocity then are

$$\mathbf{n} = \left(-1, \frac{\partial F}{\partial y} \right) / \sqrt{1 + \left(\frac{\partial F}{\partial y} \right)^2}, \quad \mathbf{n} \cdot \frac{d\mathbf{x}}{dt} \Big|_{G=G_0} = \frac{\partial F}{\partial t} / \sqrt{1 + \left(\frac{\partial F}{\partial y} \right)^2}. \quad (4.47)$$

Due to the discontinuity in density at the flame front, the Euler equations Eqs. (4.45) are only valid on either side of the front, but do not hold across it. Therefore jump conditions for mass and momentum conservation across the discontinuity are introduced (conf. [13], p. 16):

$$\begin{aligned} (r-1) \mathbf{n} \cdot \frac{d\mathbf{x}}{dt} \Big|_{G=G_0} &= \mathbf{n} \cdot (r\mathbf{v}_+ - \mathbf{v}_-) \\ (r\mathbf{v}_+ - \mathbf{v}_-) \mathbf{n} \cdot \frac{d\mathbf{x}}{dt} \Big|_{G=G_0} &= \mathbf{n} \cdot \left(r\mathbf{v}_+ \mathbf{v}_+ - \mathbf{v}_- \mathbf{v}_- - (p_+ - p_-) \mathbf{I} \right) \end{aligned} \quad (4.48)$$

Here the subscripts $+$ and $-$ refer to the burnt and the unburnt gas respectively and denote the properties immediately downstream and upstream of the flame front. In terms of the u and v components the jump conditions are written

$$\begin{aligned} (r-1) \frac{\partial F}{\partial t} &= ru_+ - u_- - \frac{\partial F}{\partial y} (rv_+ - v_-) \\ (ru_+ - u_-) \frac{\partial F}{\partial t} &= ru_+ (u_+ - \frac{\partial F}{\partial y} v_+) - u_- (u_- - \frac{\partial F}{\partial y} v_-) + p_+ - p_- \\ (rv_+ - v_-) \frac{\partial F}{\partial t} &= rv_+ (u_+ - \frac{\partial F}{\partial y} v_+) - v_- (u_- - \frac{\partial F}{\partial y} v_-) - \frac{\partial F}{\partial y} (p_+ - p_-). \end{aligned} \quad (4.49)$$

With the coordinate transformation:

$$x = \xi + F(\eta, \tau), \quad y = \eta, \quad t = \tau \quad (4.50)$$

we fix the discontinuity at $\xi = 0$. Under the assumption of small perturbations of the front, the unknowns are expanded as

$$\begin{aligned} u &= U + \epsilon u, \quad v = \epsilon v \\ p &= P + \epsilon p, \quad F = \epsilon f, \end{aligned} \quad (4.51)$$

where ϵ is an asymptotically small parameter. Inserting Eqs. (4.50) and (4.51) into the jump conditions one obtains to the leading order the steady-state solution

$$\begin{aligned} U_- &= 1, \quad P_- = 0 \\ U_+ &= \frac{1}{r}, \quad P_+ = \frac{r-1}{r}, \end{aligned} \tag{4.52}$$

and to first order

$$\begin{aligned} (r-1) \frac{\partial f}{\partial \tau} &= ru_+ - u_- \\ 0 &= 2(u_+ - u_-) + p_+ - p_- \\ 0 &= v_+ - v_- + \frac{1-r}{r} \frac{\partial f}{\partial \eta}, \end{aligned} \tag{4.53}$$

where the leading order mass flux $\dot{m} = rU_+ = U_-$ has been set equal to 1. To first order the equations for the perturbed quantities on both sides of the flame front now read

$$\begin{aligned} \frac{\partial u}{\partial \xi} + \frac{\partial v}{\partial \eta} &= 0 \\ \frac{\partial u}{\partial \tau} + U \frac{\partial u}{\partial \xi} + \frac{1}{\rho} \frac{\partial p}{\partial \xi} &= 0 \\ \frac{\partial v}{\partial \tau} + U \frac{\partial u}{\partial \xi} + \frac{1}{\rho} \frac{\partial p}{\partial \eta} &= 0, \end{aligned} \tag{4.54}$$

where $\rho = 1$ for $\xi < 0$ (unburnt gas) and $\rho = r$ for $\xi > 0$ (burnt gas) is to be used. In case of instability perturbations which are initially periodic in the η -direction and vanish for $\xi \rightarrow \pm\infty$ would increase with time. Since the system is linear, the solution may be written as

$$\mathbf{w} = \begin{pmatrix} u \\ v \\ p \end{pmatrix} = \mathbf{w}_0 \exp(\alpha\xi) \exp(\sigma\tau - ik\eta), \tag{4.55}$$

where σ is the non-dimensional growth rate, k the non-dimensional wave number and i the imaginary unit. Introducing this into Eq. (4.54) the linear system may be written as

$$\mathbf{A} \cdot \mathbf{w} = \mathbf{0}, \tag{4.56}$$

where the matrix \mathbf{A} is given by

$$\mathbf{A} = \begin{pmatrix} \alpha & -ik & 0 \\ \sigma + \alpha U & 0 & \alpha/\rho \\ 0 & \sigma + \alpha U & -ik/\rho \end{pmatrix}. \quad (4.57)$$

The eigenvalues of \mathbf{A} are obtained by setting $\det(\mathbf{A}) = 0$. This leads to the characteristic equation

$$\det(\mathbf{A}) = \frac{1}{\rho} (k^2 - \alpha^2) (\sigma + \alpha U) = 0. \quad (4.58)$$

Here again $U = 1/r$, $\rho = r$ for $\xi > 0$ and $U = 1$, $\rho = 1$ for $\xi < 0$ should be considered. There are three solutions of Eq. (4.58) for the eigenvalues $\alpha_j, j = 1, 2, 3$, where positive values of α_j satisfy the upstream ($\xi < 0$) and negative values the downstream ($\xi > 0$) boundary conditions of Eq. (4.54). Therefore

$$\begin{aligned} \xi > 0 : \quad & \alpha_1 = -r\sigma, \quad \alpha_2 = -k \\ \xi < 0 : \quad & \alpha_2 = +k. \end{aligned} \quad (4.59)$$

The corresponding eigenvectors $\mathbf{w}_{0,j}, j = 1, 2, 3$ are determined by introducing the eigenvalues $\alpha_j, j = 1, 2, 3$ into \mathbf{A} and solving again

$$\mathbf{A}(\alpha_j) \cdot \mathbf{w}_j = \mathbf{0}, \quad j = 1, 2, 3. \quad (4.60)$$

This leads to

$$\begin{aligned} j = 1 : \quad & \mathbf{w}_{0,1} = \begin{pmatrix} 1 \\ i \frac{r\sigma}{k} \\ 0 \end{pmatrix} \\ j = 2 : \quad & \mathbf{w}_{0,2} = \begin{pmatrix} 1 \\ i \\ -1 + \frac{r\sigma}{k} \end{pmatrix} \\ j = 3 : \quad & \mathbf{w}_{0,3} = \begin{pmatrix} 1 \\ -i \\ -1 - \frac{\sigma}{k} \end{pmatrix} \end{aligned} \quad (4.61)$$

In terms of the original unknowns u , v and p the solution is now

$$\begin{aligned} \xi > 0 : \quad \begin{pmatrix} u \\ v \\ p \end{pmatrix} &= \left\{ a \begin{pmatrix} 1 \\ i \frac{r\sigma}{k} \\ 0 \end{pmatrix} \exp(-r\sigma\xi) + b \begin{pmatrix} 1 \\ i \\ -1 + \frac{r\sigma}{k} \end{pmatrix} \exp(-k\xi) \right\} \exp(\sigma\tau - ik\eta) \\ \xi < 0 : \quad \begin{pmatrix} u \\ v \\ p \end{pmatrix} &= c \begin{pmatrix} 1 \\ -i \\ -1 - \frac{\sigma}{k} \end{pmatrix} \exp(k\xi + \sigma\tau - ik\eta). \end{aligned} \tag{4.62}$$

For the perturbation $f(\eta, \tau)$ the form

$$f = \tilde{f} \exp(\sigma\tau - ik\eta) \tag{4.63}$$

will be introduced. Inserting Eqs. (4.35), (4.46) and (4.51) into the non-dimensional G -equation

$$\left(\frac{\partial G}{\partial t} + u \frac{\partial G}{\partial x} + v \frac{\partial G}{\partial y} \right) = \sqrt{\left(\frac{\partial G}{\partial x} \right)^2 + \left(\frac{\partial G}{\partial y} \right)^2} (1 + \kappa \mathcal{L}) \tag{4.64}$$

satisfies to leading order Eq. (4.52) and $x = 0_-$, $x = 0_+$ respectively and leads to first order to

$$\begin{aligned} u_- &= \frac{\partial f}{\partial \tau} - \frac{\partial^2 f}{\partial \eta^2} \mathcal{L} \\ u_+ &= \frac{\partial f}{\partial \tau} - \frac{\partial^2 f}{\partial \eta^2} \frac{\mathcal{L}}{r}. \end{aligned} \tag{4.65}$$

With Eq. (4.63) the jump conditions Eq. (4.53) can be written as

$$\begin{aligned} (r-1)\sigma\tilde{f} &= r(a+b)-c \\ 0 &= 2a+b(1+r\frac{\sigma}{k})+c(\frac{\sigma}{k}-1) \\ \frac{1-r}{r}k\tilde{f} &= a\frac{r\sigma}{k}+b+c \end{aligned} \tag{4.66}$$

and Eq. (4.65) then reads

$$\begin{aligned} c &= \tilde{f}(\sigma+k^2\mathcal{L}) \\ a+b &= \tilde{f}(\sigma+\frac{k^2\mathcal{L}}{r}). \end{aligned} \tag{4.67}$$

Since equation Eq. (4.66₁) is linearly dependent of Eqs. (4.67_{1,2}) it is dropped and the Eqs. (4.66_{2,3}) and (4.67_{1,2}) remain for the determination of a, b, c and $\sigma(k)$. Dividing all equations by $k\tilde{f}$ one obtains four equations for $\hat{a} = a/k\tilde{f}$, $\hat{b} = b/k\tilde{f}$, $\hat{c} = c/k\tilde{f}$ and $\varphi = \sigma/k$. The elimination of the first three unknown yields the equation

$$\varphi^2(1+r) + 2\varphi(1+k\mathcal{L}) + \frac{2k\mathcal{L}}{r} + \frac{r-1}{r} = 0. \quad (4.68)$$

The solution may be written in terms of dimensional quantities as

$$\sigma = \frac{s_{L0}^- k}{1+r} \left\{ \sqrt{1+k^2\mathcal{L}^2 - \frac{2k\mathcal{L}}{r} + \frac{1-r^2}{r}} - (1+k\mathcal{L}) \right\}. \quad (4.69)$$

Here only the positive root of Eq. (4.68) has been taken, since it refers to possible solutions with exponential growing amplitudes. Eq. (4.69) is the dispersion relation which shows that the perturbation f grows exponentially in time only for a certain wave number range $0 < k < k^*$ with $k^* = (r-1)/(2\mathcal{L})$.

For perturbations at wave numbers $k > k^*$ a plane flame of infinitively small thickness, described as a discontinuity in density, velocity and pressure is unconditionally stable. This is due to the influence of the front curvature on the burning velocity. As one would expect on the basis of simple thermal theories of flame propagation, the burning velocity increases when the flame front is concave and decreases when it is convex towards the unburnt gas, so that initial perturbations are smoothed. However, hydrodynamic and curvature effects are not the only influencing factors for flame front stability. Flame stretch due to flow divergence, gravity (in a downward propagating flame) and the thermo-diffusive effect with a Lewis number larger unity are stabilizing effects. A more detailed discussion of these phenomena may be found in [11] and [13].

Exercise 4.1

Under the assumption of a constant burning velocity $s_L = s_{L0}$ the linear stability analysis leads to the following dispersion relation

$$\sigma = \frac{s_{L0}^- k}{1+r} \left\{ \sqrt{1 + \frac{1-r^2}{r}} - 1 \right\}. \quad (4.70)$$

Validate this expression by inserting $\mathcal{L} = 0$ in Eq. (4.69).

What is the physical meaning of this result?

What effect has the front curvature on the flame front stability?

Solution

The dispersion relation for constant burning velocity $s_L = s_{L0}$, Eq. (4.70), shows that the perturbation F grows exponentially in time for all wave numbers. The growth rate σ is proportional to the wave number k and always positive since the density rate r is less than unity. This means that a plane flame front with constant burning velocity is unstable to any perturbation. The front curvature has a stabilizing effect on the flame front stability. As it is shown in Section 4.5, the linear stability analysis for a burning velocity with the curvature effect retained leads to instability of the front only for the wave number range $0 < k < k^* = (r - 1)/(2\mathcal{L})$, whereas the front is stable to all perturbations with $k > k^*$.

Bibliography

- [1] J. Warnatz. *Comb. Inst.*, 384:369, 1981.
- [2] C. K. Law. Compilation of recent experimental data of premixed laminar flames. *Lecture Notes in Physics, Springer-Verlag Berlin*, 30:19, 1993.
- [3] F. Mauss and N. Peters. Reduced kinetic mechanisms for premixed methane-air flames, in Reduced kinetic mechanisms for applications in combustion systems. *Lecture Notes in Physics, Springer-Verlag Berlin*, 75:58, 1993.
- [4] M. Metghalchi and J. C. Keck. *Comb. Flame*, 38:143, 1982.
- [5] D. B. Smith, S. C. Taylor, and A. Williams. Burning velocities in stretched flames. *Poster P220 presented at the Twenty-Second Symposium (International) on Combustion*, 1988.
- [6] T. G. Scholte and P. B. Vaags. *Comb. Flame*, 3:495, 1959.
- [7] I. Yamaoka and H. Tsuji. *Twentieth Symposium (International) on Combustion, The Combustion Institute. Pittsburgh*, page 1883, 1985.
- [8] C. Kennel, F. Mauss, and N. Peters. Reduced kinetic mechanisms for premixed propane-air flames, in Reduced kinetic mechanisms for applications in combustion systems. *Lecture Notes in Physics, Springer-Verlag Berlin*, 140:121, 1993.
- [9] M. Matalon and B. J. Matkowsky. Flames as gasdynamics discontinuities. *J. Fluid Mech.*, 124:239–259, 1982.
- [10] P. Clavin and F. A. Williams. Effects of molecular diffusion and thermal expansion on the structure and dynamics of premixed flames in turbulent flows of large scale and low intensity. *J. Fluid Mech.*, 116:251–282, 1982.

- [11] P. Clavin. Dynamic behaviour of premixed flame fronts in laminar and turbulent flows. *Progr. Energy Combust. Sci.*, 11:1–59, 1985.
- [12] G. H. Markstein. Experimental and theoretical studies of flame front stability. *J. Aeronautical Sciences*, pages 199–209, 1951.
- [13] F. A. Williams. *Combustion Theory, Second Edition*. The Benjamin Cummings Publishing Co. Menlo Park, 1985.

Lecture 5

The Thermal Flame Theory

5.1 Premixed Flames Based on One-step Asymptotics

A classical example of an asymptotic description of the structure of a premixed flame is due to Zeldovich and Frank-Kamenetzki in 1938. It is known as the thermal flame theory and considers the single one-step reaction Eq. (4.15). We will assume that the reaction rate is first order with respect to fuel and to oxygen

$$\omega = B \frac{\rho Y_F}{W_F} \frac{\rho Y_{O_2}}{W_{O_2}} \exp\left(\frac{-E}{RT}\right). \quad (5.1)$$

Alternative forms, in particular a rate which is first order with respect to the fuel only, may also be considered. We will show that this case will be contained as a limit for extremely lean flames in the expression above. In Eq. (5.1) the most important feature is the Arrhenius type temperature dependence, where the activation energy E is assumed to be large. Both the activation energy and the frequency factor B are adjustable parameters and cannot be deduced from elementary kinetic data. The one-step model has widely been used in descriptions of flame stability, where it essentially serves as model that produces a thin flame with a strong temperature sensitivity. In this lecture we will derive an explicit expression for the burning velocity. This is to be compared in lecture 7 to results derived from a four-step reduced mechanism for methane-air flames. The flame structure shown schematically in Fig. 5.1. Since the reaction is assumed to be irreversible, the reaction rate must vanish in the burnt gas. Therefore one of the reactants must be entirely depleted: the fuel in the case of lean flames, the oxidizer for rich flames and both for stoichiometric

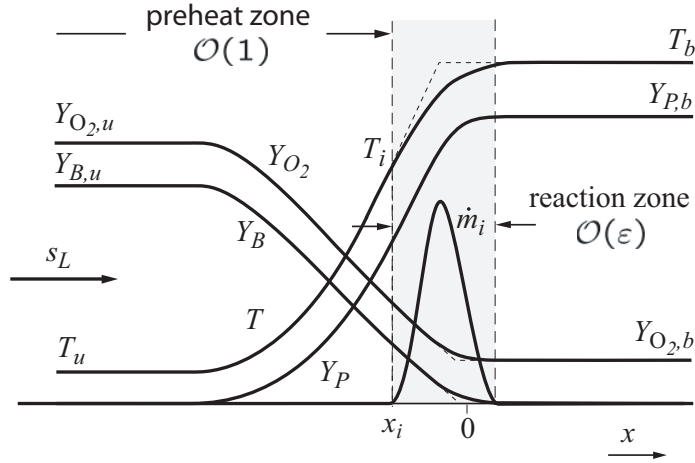


Figure 5.1: The structure of a premixed laminar flame as calculated from one-step asymptotics.

flames. This leads to the condition in the burnt gas

$$Y_{F,b} \cdot Y_{O_2,b} = 0. \quad (5.2)$$

The combustion of the reactants in the reaction zone leads to an increase in temperature and therefore an increase of the reaction rate. In the analysis to be developed, the large temperature dependence of the reaction rate, expressed by the large activation energy will play a crucial role. Let us assume at first that Eq. (3.35) for the diffusion flux can be employed and that the Lewis number is unity. The species balance equations Eq. (3.47) for the mass fractions of fuel and oxygen read

$$\begin{aligned} \rho_u s_L \frac{dY_F}{dx} &= \frac{d}{dx} \left(\frac{\lambda}{c_p} \frac{dY_F}{dx} \right) - \nu'_F W_F \omega \\ \rho_u s_L \frac{dY_{O_2}}{dx} &= \frac{d}{dx} \left(\frac{\lambda}{c_p} \frac{dY_{O_2}}{dx} \right) - \nu'_{O_2} W_{O_2} \omega. \end{aligned} \quad (5.3)$$

Then, using $\rho u = \rho_u s_L$ these can be combined with the temperature equation Eq. (3.46) in the form

$$\rho_u s_L \frac{dT}{dx} = \frac{d}{dx} \left(\frac{\lambda}{c_p} \frac{dT}{dx} \right) - \frac{Q}{c_p} \omega. \quad (5.4)$$

This leads to algebraic coupling relations between the mass fractions and the temperature which may be integrated from the burnt state to any state within the flame as

$$\begin{aligned} Y_F &= -\frac{\nu'_F W_F c_p}{Q} (T - T_b) + Y_{F,b} \\ Y_{O_2} &= -\frac{\nu'_{O_2} W_{O_2} c_p}{Q} (T - T_b) + Y_{O_2,b} \end{aligned} \quad (5.5)$$

Here Q and c_p have been assumed constant for simplicity. With Eq. (5.5) the reaction rate is a function of temperature and only Eq. (5.4) needs to be considered in the following.

In the small Mach number limit from the momentum equation one obtains the solution

$$p = \text{const.} \quad (5.6)$$

With the aid of the thermal equation of state and Eq. (5.5) the density, the thermal conductivity as well as the reaction rate can be expressed as a function of temperature. Again one obtains for the solution of the continuity equation Eq. (4.16) the expression Eq. (4.19). The only differential equation remaining describes the temperature profiles in x -direction.

$$\rho_u s_L \frac{dT}{dx} = \frac{d}{dx} \left(\frac{\lambda}{c_p} \frac{dT}{dx} \right) - \frac{Q}{c_p} \omega. \quad (5.7)$$

Zeldovich and Frank-Kamenetzki introduce the following assumptions introducing the ignition temperature T_i :

1. in the preheat zone ($T \leq T_i$) no reactions take place, therefore $\omega = 0$ is assumed.
2. in the reaction zone ($T \geq T_i$) the convective term at the left side of Eq. (5.7) can be neglected compared to the diffusion term and the reaction term.

In particular the admissibility of the second assumption is at first glance hard to accept. However it will become apparent when on the basis of the asymptotic theory the character of the reaction zone as a very thin boundary layer will be introduced. A mathematical justification can be given by a singular asymptotic expansion.

Using the first assumption Eq. (5.7) can be integrated in the pre heat zone. Considering the boundary conditions $dT/dx|_{x \rightarrow -\infty} = 0$ and $T|_{x \rightarrow +\infty} = T_u$ for the first derivative we have

$$\frac{dT}{dx} = \frac{c_p \rho_u s_L}{\lambda} (T - T_u). \quad (5.8)$$

With the second assumption Eq. (5.7) can be integrated once, if the temperature T is introduced as an independent variable. One substitutes the heat conduction term with

$$\frac{d}{dx} \left(\frac{\lambda}{c_p} \frac{dT}{dx} \right) = \frac{dT}{dx} \frac{d}{dT} \left(\frac{\lambda}{c_p} \frac{dT}{dx} \right) = \frac{c_p}{\lambda} \frac{1}{2} \frac{d}{dT} \left(\frac{\lambda}{c_p} \frac{dT}{dx} \right)^2. \quad (5.9)$$

After multiplication with λ/c_p from Eq. (5.7) it follows

$$\frac{1}{2} \frac{d}{dT} \left(\frac{\lambda}{c_p} \frac{dT}{dx} \right)^2 = - \frac{(-\Delta H)\lambda}{c_p^2} \omega(T). \quad (5.10)$$

With the boundary conditions $dT/dx|_{x \rightarrow \infty} = 0$ and $T|_{x \rightarrow \infty} = T_b$ this equation can be integrated for a first time

$$\frac{dT}{dx} = \sqrt{2 \frac{(-\Delta H)}{\lambda^2} \int_T^{T_b} \lambda \omega(T) dT}. \quad (5.11)$$

Now at the position x_i for $T = T_i$ Zeldovich and Frank-Kamenetzki set the derivatives of the preheat zone, Eq. (5.8), and the reaction zone, Eq. (5.11) equal to each other. This yields an equation for the burning velocity

$$\frac{c_p \rho_u s_L}{\lambda_i} (T_i - T_u) = \sqrt{2 \frac{(-\Delta H)}{\lambda_i^2} \int_{T_i}^{T_b} \lambda \omega(T) dT}. \quad (5.12)$$

This corresponds to a matching process to adjust the solutions from the preheat zone and the reaction zone. An analysis of the integral in closed form is only possible, if further simplifying assumptions are introduced. Expanding the term in the exponent of Eq. (5.1) in a series around T_b and neglecting higher order terms, one obtains

$$-\frac{E}{\mathcal{R}T} = -\frac{E}{\mathcal{R}T_b} + \frac{E(T - T_b)}{\mathcal{R}T_b^2}. \quad (5.13)$$

Since in the reaction zone T and T_b are only slightly different, it is useful to introduce the dimensionless temperature

$$\Theta = \frac{E(T - T_b)}{\mathcal{R}T_b^2}, \quad (5.14)$$

which stays of the order $\mathcal{O}(1)$ for large $E/(\mathcal{R}T_b^2)$. In the reaction zone for $T \approx T_b$ in first approximation and the properties can also assumed to be constant ($\rho = \rho_b$, $\lambda = \lambda_b$). Considering Eqs.

(5.2) and (5.3) the reaction rate can be written as

$$\begin{aligned}\omega &= B\rho_b^2 \frac{c_p \mathcal{R} T_b^2}{(-\Delta H)E} \exp\left(-\frac{E}{\mathcal{R} T_b}\right) \\ &\quad \left[-\left(\frac{\nu'_F Y_{O_2,b}}{M_{O_2}} + \frac{\nu'_{O_2} Y_{F,b}}{M_F}\right) \Theta + \frac{\nu'_{O_2} \nu'_F c_p \mathcal{R} T_b^2}{(-\Delta H)E} \Theta^2 \right] \exp \Theta.\end{aligned}\tag{5.15}$$

Integration yields

$$\begin{aligned}\int_{T_i}^{T_b} \lambda \omega dT &= \lambda_b \frac{\mathcal{R} T_b^2}{E} \int_{\Theta_i}^0 w(\Theta) d\Theta \\ &= \frac{\lambda_b B \rho_b^2 c_p \mathcal{R}^2 T_b^4}{(-\Delta H)E} \exp\left(-\frac{E}{\mathcal{R} T_b}\right) \left[\left(\frac{\nu'_F Y_{O_2,b}}{M_{O_2}} + \frac{\nu'_{O_2} Y_{F,b}}{M_F} \right) (1 + (\Theta_i - 1) \exp \Theta_i) \right. \\ &\quad \left. + 2 \frac{\nu'_{O_2} \nu'_F c_p \mathcal{R} T_b^2}{(-\Delta H)E} \left(1 - \left(1 - \Theta_i + \frac{\Theta_i^2}{2} \right) \exp \Theta_i \right) \right].\end{aligned}\tag{5.16}$$

Now a consideration is introduced which is obvious only for an asymptotic expansion for a large activation energy. In the integral Eq. (5.16) Θ_i is substituted by Θ_u , which may be interpreted as the assumption that the solution is valid far into the preheat zone. That is equivalent with the physical conception that underneath the temperature T_i the integral in Eq. (5.16) is negligible because of the strong dependence of the reaction rate on temperature. Then it makes no difference whether integration is performed between T_i and T_b or T_u and T_b . Since Θ_u takes large negative values for large activation energies, all terms containing $\exp \Theta_u$ will finally be replaced by $-\infty$, so that they disappear.

On the other hand on the left side of Eq. (5.12) T_i is replaced by T_b and λ_i by λ_b . This implies the concept that the reaction zone is so thin, that the temperature in the preheat zone extends to T_b and that T_i is hardly distinguishable from T_b . Eq. (5.12) then reads

$$\begin{aligned}\rho_u s_L &= \sqrt{2 \frac{B \rho_b^2 \lambda_b \mathcal{R}^2 T_b^4}{c_p (T_b - T_u)^2 E^2} \exp\left(-\frac{E}{\mathcal{R} T_b}\right) S} \\ S &= \frac{\nu'_F Y_{O_2,b}}{M_{O_2}} + \frac{\nu'_{O_2} Y_{F,b}}{M_F} + \frac{2 \nu'_{O_2} \nu'_F c_p \mathcal{R} T_b^2}{(-\Delta H)E}.\end{aligned}\tag{5.17}$$

The contribution of the individual terms in S depends strongly on the equivalence ratio $\phi = 1/\lambda$: in very lean or very fat mixtures respectively $Y_{O_2,b}$ or $Y_{F,b}$ are large, while both vanish for stoichio-

metric mixtures. Therefore in stoichiometric mixtures the last term is predominant. It holds

$$S = \begin{cases} \frac{\nu'_F Y_{O_2,b}}{M_{O_2}} & \text{for } \phi \ll 1, \\ \frac{2 \nu'_{O_2} \nu'_F c_p \mathcal{R} T_b^2}{(-\Delta H) E} & \text{for } \phi = 1, \\ \frac{\nu'_{O_2} Y_{F,b}}{M_F} & \text{for } \phi \gg 1. \end{cases} \quad (5.18)$$

Finally the assumptions introduced should be summarized:

1. In the preheat zone the reaction rate is neglected.
2. In the reaction zone the convective term is neglected
3. The reaction rate is approximated by an expansion around T_b , where only the exponential term is expanded. Properties are set constant and are evaluated at T_b
4. The integration over the reaction zone leads to an expression that correspond to an integral between the limits $T = -\infty$ and $T = T_b$.
5. In the solution of the preheat zone the ignition temperature T_i is equalized to T_b .

Originally the thermal flame theory of Zeldovich and Frank-Kamenetzki was not derived for reaction rates in the form of Eq. (5.1) being of first order both for the fuel and the oxidizer. Rather several solutions were derived for the reaction rate of zeroth, first and second order. The comparison with the result presented here, Eqs. (5.17) and (5.18) shows that a reaction of first order is conform with a very rich or very lean mixture, for which the component in-deficit determines the reaction rate. In contrast the stoichiometric mixture relates to a reaction of second order, since here both components are rate determining.

5.2 Flame Thickness and Flame Time

In Section 5.1 we have identified the burning velocity s_L as an eigenvalue of the problem, which results from the solution of the one-dimensional balance equations. Under the assumption of a one-step reaction, in which only a chemical time scale has been introduced, and with the assumption of $\text{Le} = 1$, by which the thermal diffusivity $a = \lambda/(\rho c_p)$ and mass diffusivity D are equal, with

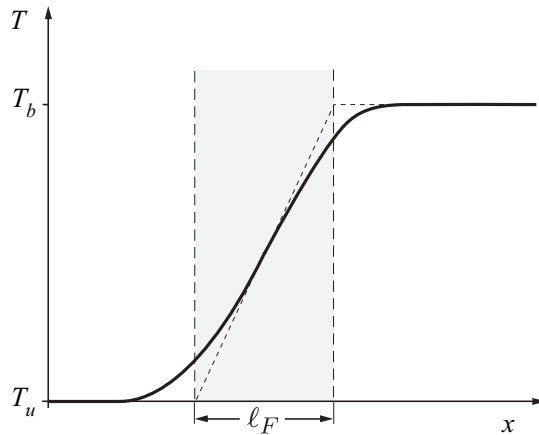


Figure 5.2: Graphical determination of the flame thickness.

Eq. (5.17) one obtains a relation for s_L , which combines the parameters diffusivity and chemical time as

$$s_L = \sqrt{D/t_c}. \quad (5.19)$$

Here the mass diffusivity D is related to the thermal diffusivity using $\rho = \rho_u$ and $\lambda = \lambda_b$ as

$$D = \frac{\lambda_b}{\rho_u c_p}, \quad (5.20)$$

while the chemical time is given by

$$t_c = \frac{\rho_u Z_e^2}{2B\rho_b^2 S} \exp\left(\frac{E}{RT_b}\right) \quad (5.21)$$

Here the Zeldovich number, defined by

$$Z_e = \frac{E(T_b - T_u)}{RT_b^2} \quad (5.22)$$

appears squared. Since Z_e is of the order of magnitude $\mathcal{O}(10)$, the chemical time t_c is by two orders of magnitude larger than a chemical time, which, irrespective of the density ratio ρ_u/ρ_b , would be calculated from the reaction rate for example for very lean flames $\phi \ll 1$ as the reciprocal of

$$B \frac{\rho Y_{O_2}}{M_{O_2}} \exp\left(\frac{-E}{RT}\right) \quad \text{at} \quad T = T_b, \rho = \rho_b, Y_{O_2} = Y_{O_2,b}$$

Obviously t_c is not a time, which is solely determined by chemistry, but t_c incorporates the structure of the flame as well. This will become apparent, if from dimensional arguments one defines the flame thickness as

$$\ell_F = \frac{D}{s_L} = \frac{\lambda_b}{c_p \rho_u s_L} \quad (5.23)$$

Then one can further introduce the flame time

$$t_F = \frac{\ell_F}{s_L} \quad (5.24)$$

This is the time, which the flame front requires, to propagate the distance of the thickness of the flame. The comparison between Eqs. (5.19) and (5.23) up to Eq. (5.24) show, that t_c mit

$$t_c = \frac{D}{s_L^2} = \frac{\ell_F}{s_L} = t_F \quad (5.25)$$

is equal to the flame time.

The flame thickness can be descriptively constructed from the temperature profile, Fig. 5.2. If one attaches a tangent to the turning point of the temperature profile and determines the intersection with the horizontal line at T_u and T_b , the length ℓ_F can be taken at the abscissa. If one substitutes in Eq. (5.8) the left side by $(T_b - T_u)/\ell_F$ and evaluates the right side at $T = T_b$, one obtains

$$\ell_F = \frac{\lambda_b}{c_p \rho_u s_L} \quad (5.26)$$

in accordance with Eq. (5.23).

In Eq. (6.17) in Lecture 6 we will introduce a normalized coordinate which eliminates all properties from the temperature equation, as will be shown in Eq. (7.5). This suggests

$$\rho_u s_L \int_0^{\ell_F} \frac{\lambda}{c_p} dx = 1. \quad (5.27)$$

Assuming $\lambda/c_p = (\lambda/c_p)_{T^0}$, where T^0 is the inner layer temperature to be defined in Lecture 6, one obtains a more suitable definition for ℓ_F :

$$\ell_F = \frac{(\lambda/c_p)_{T^0}}{(\rho s_L)_u}. \quad (5.28)$$

Since the reaction zone was assumed to be thin, the flame thickness hence describes the thickness of the preheat zone of the flame structure.

The flame thickness also is a measure for the quenching distance d . This is the distance, for whom a flame extinguishes, if it encounters a cold wall. Typically one has

$$d = c \ell_F, \quad c = 5\dots6.$$

Therefore a flame cannot pass through a metal grid, if the distance between the wires is smaller than d . In former times this observation was used at pit lamps. These lamps consist of an open flame encapsulated by a metal grid. If mine gas, normally methane, unexpectedly accumulated in a gallery, it diffused through the metal grid with the result that the flame of the pit lamp burned more lucidly. On the other hand there was no danger, that the mine gas got ignited by the pit lamp, if the quenching distance was respected in choosing the proper grid spacing. In case of a brighter pit lamp the miner knew that he has to seek shelter as fast as possible.

Lecture 6

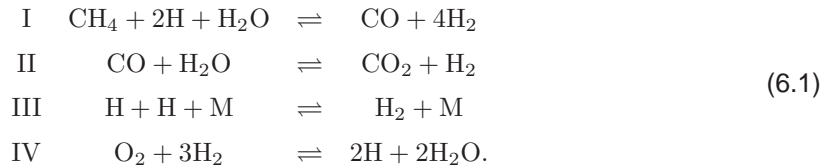
Asymptotic Structure of Four-Step Premixed Stoichiometric Methane Flames

In the previous lecture we have derived a description of premixed flames based on an assumed one-step reaction. This has provided a basic understanding of the flame structure when a large sensitivity to temperature was built into the model. There is no chemical basis for such a one-step assumption and the results must be regarded with caution when conclusions are drawn about the dependence of the burning velocity on pressure and reactant concentrations, as well as flammability and extinction limits. While numerical calculations based on full and reduced mechanisms are able to predict these properties, they contribute little to the understanding of the fundamental parameters that influence flame behavior. Therefore there is a need to fill the gap between the numerical calculations based on mechanisms with elementary kinetics and asymptotic analysis based on assumed chemistry models. The asymptotic description of stoichiometric methane-air flames from [1], based on a four-step reduced mechanism, shall be presented in this lecture. Since the basic chemical parameters were retained, this mechanism has been quite successful in describing the dependence of the burning velocity on pressure and preheat temperature. A similar asymptotic analysis as in [1] was also carried out for lean methane flames [2]. This description may, with some modifications, also serve as a model for other hydrocarbon flames. This will be shown by using analytical approximation formulas [3] that are based on the asymptotic description

of methane flames for flames of C₂H₆, C₂H₄, C₂H₂ and C₃H₈ in air.

6.1 The Four-Step Model for Methane-Air Flames

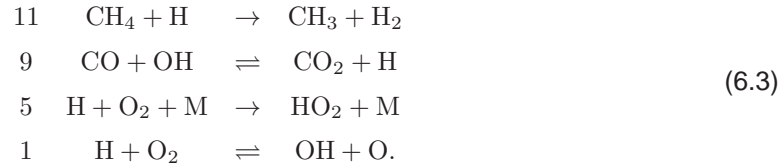
The four-step model for methane flames is



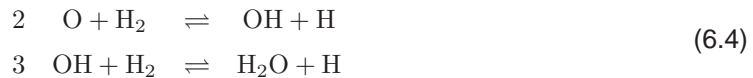
The principle rates governing these global reactions are

$$\begin{aligned} \omega_{\text{I}} &= \omega_{11}, & \omega_{\text{II}} &= \omega_9 \\ \omega_{\text{III}} &= \omega_5, & \omega_{\text{IV}} &= \omega_1 \end{aligned} \quad (6.2)$$

which correspond to the elementary reactions



We neglect the influence of the other reactions here in order to make the algebraic description more tractable. Since OH and O appear in this formulation as reactants we need to express them in terms of the species in the four-step mechanism by using the partial equilibrium assumption for the reaction:



such that

$$\begin{aligned} [\text{O}] &= \frac{[\text{H}][\text{OH}]}{K_2[\text{H}_2]} \\ [\text{OH}] &= \frac{[\text{H}_2\text{O}][\text{H}]}{K_3[\text{H}_2]}. \end{aligned} \quad (6.5)$$

where K_2 and K_3 are the equilibrium constants of reactions 2 and 3, respectively. This leads to the following reaction rates of the global steps I-IV:

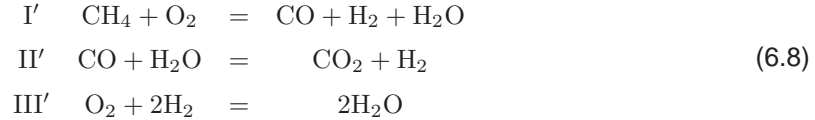
$$\begin{aligned}\omega_I &= k_{11}[\text{CH}_4][\text{H}] \\ \omega_{\text{II}} &= \frac{k_{9f}}{K_3} \frac{[\text{H}]}{[\text{H}_2]} \left([\text{CO}][\text{H}_2\text{O}] - \frac{1}{K_{\text{II}}} [\text{CO}_2][\text{H}_2] \right) \\ \omega_{\text{III}} &= k_5[\text{H}][\text{O}_2][\text{M}] \\ \omega_{\text{IV}} &= k_1 \frac{[\text{H}]}{[\text{H}_2]^3} \left([\text{O}_2][\text{H}_2]^3 - \frac{1}{K_{\text{IV}}} [\text{H}]^2 [\text{H}_2\text{O}]^2 \right)\end{aligned}\quad (6.6)$$

which is explicit in terms of the concentrations of species appearing in the four-step mechanism.

The equilibrium constants in these rates are given by

$$\begin{aligned}K_3 &= 0.216 \exp(7658/T) \\ K_{\text{II}} &= 0.035 \exp(3652/T) \\ K_{\text{IV}} &= 1.48 \exp(6133/T).\end{aligned}\quad (6.7)$$

We now want to go one step further and assume steady state of the radical H. Adding reaction IV to I and III leads to the three steps



with the first three rates of Eq. (6.6). The concentration of H must now be determined from the steady state equation for H

$$\omega_I + \omega_{\text{III}} = \omega_{\text{IV}}. \quad (6.9)$$

This may be written as

$$[\text{H}] = [\text{H}_{eq}] \left(1 - \frac{k_5[\text{M}]}{k_1} - \frac{k_{11}[\text{CH}_4]}{k_1[\text{O}_2]} \right)^{1/2}, \quad (6.10)$$

where $[\text{H}_{eq}]$ based on partial equilibrium of reaction IV

$$[\text{H}_{eq}] = K_{\text{IV}}^{1/2} \frac{[\text{O}_2]^{1/2} [\text{H}_2]^{3/2}}{\text{H}_2\text{O}}. \quad (6.11)$$

Eq. (6.10) shows an interesting structure: At temperatures of 1400 K and above the second term

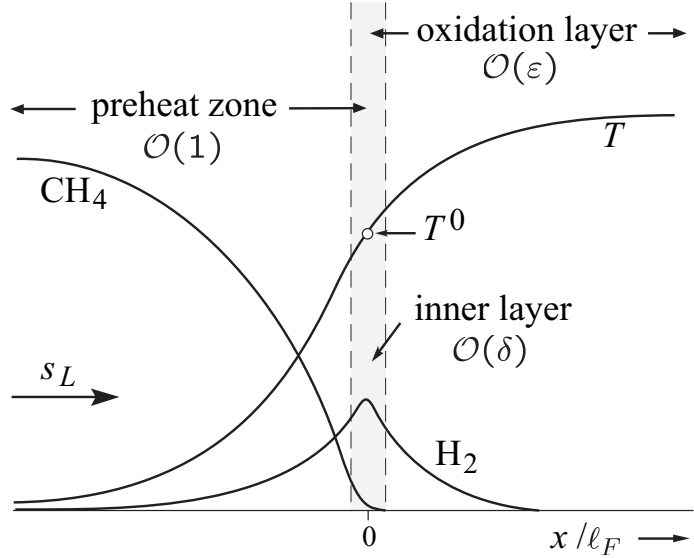


Figure 6.1: Schematic illustration of the structure of a premixed methane-air flame.

in the brackets is small while the ratio k_{11}/k_1 is much larger than unity. It follows that $[\text{CH}_4]/[\text{O}_2]$ must be much smaller than unity, if $[\text{H}]$ is to remain real. This will be used to develop an asymptotic description of the inner layer below but also shows that Eq. (6.10) cannot be valid in the preheat zone upstream of the inner layer where CH_4 is entirely consumed. The structure of the flame is schematically shown in Fig. 6.1. From Eq. (6.10) it follows that $[\text{H}]$ vanishes in the preheat zone which is therefore chemically inert. A further approximation that will reduce the three step mechanism Eq. (6.8) effectively to a two-step mechanism is the assumption of partial equilibrium of reaction II. Assuming the concentrations of H_2O and CO_2 to be known this leads to a coupling between the concentrations of CO and H_2 of the form

$$[\text{CO}] = \alpha' [\text{H}_2], \quad (6.12)$$

where

$$\alpha' = \frac{[\text{CO}_2]}{[\text{H}_2\text{O}]} K_{\text{II}}(T). \quad (6.13)$$

By introducing partial equilibrium of reaction II one assumes that the effective rate coefficient k_{9f}/K_3 in the second equation of Eq. (6.6) tends to infinity while the term in parenthesis tends to zero and ω_{II} remains finite. Since ω_{II} is undefined, the rate ω_{II} must be eliminated from the

balance equations. In order to show this the balance equations for the three-step mechanism are written in operator form

$$\begin{aligned} \text{Species } L_i(Y_i) &\equiv \rho_u s_L \frac{dY_i}{dx} - \frac{1}{Le_i} \frac{d}{dx} \left(\frac{\lambda}{c_p} \frac{dY_i}{dx} \right) = W_i \sum_{l=I'}^{III'} \nu_{il} \omega_l \\ \text{Temperature } L_T(T) &\equiv \rho_u s_L \frac{dT}{dx} - \frac{d}{dx} \left(\frac{\lambda}{c_p} \frac{dT}{dx} \right) = \frac{1}{c_p} \sum_{l=I'}^{III'} Q_l \omega_l. \end{aligned} \quad (6.14)$$

In terms of the variable $\Gamma_i = Y_i/W_i$ the balance equations for the concentrations are written

$$\begin{aligned} L_{CH_4}(\Gamma_{CH_4}) &= -\omega_I \\ L_{O_2}(\Gamma_{O_2}) &= \omega_I + \omega_{III} \\ L_{H_2}(\Gamma_{H_2}) &= \omega_I + \omega_{II} - 2\omega_{III} \\ L_{CO}(\Gamma_{CO}) &= \omega_I - \omega_{II} \\ L_{H_2O}(\Gamma_{H_2O}) &= \omega_I - \omega_{II} + 2\omega_{III}. \\ L_{CO_2}(\Gamma_{CO_2}) &= \omega_{II}. \end{aligned} \quad (6.15)$$

The rate ω_{II} may be eliminated from Eq. (6.15) by combining the balance equations of H_2 , H_2O , and CO_2 with that of CO

$$\begin{aligned} L_{H_2}(\Gamma_{H_2}) + L_{CO}(\Gamma_{CO}) &= 2\omega_I - 2\omega_{III} \\ L_{H_2O}(\Gamma_{H_2O}) - L_{CO}(\Gamma_{CO}) &= 2\omega_{III} \\ L_{CO_2}(\Gamma_{CO_2}) + L_{CO}(\Gamma_{CO}) &= \omega_I. \end{aligned} \quad (6.16)$$

We will anticipate that in the thin reaction layers to be considered below, the diffusive terms dominate for the same reason as in the thin reaction zone for the one-step model. Therefore we will neglect the convective terms in the operators Eq. (6.14) for the thin reaction zones and consider only the diffusive terms. This suggests that the concentrations should be scaled with the Lewis numbers. We introduce the non-dimensional variables

$$\begin{aligned} X_i &= \frac{Y_i W_{CH_4}}{Y_{CH_4 u} W_i}, \quad x_i = \frac{X_i}{Le_i}, \\ T^* &= \frac{T - T_u}{T_b - T_u}, \quad x^* = \rho_u s_L \int_0^x \frac{c_p}{\lambda} dx, \\ \omega_l^* &= \frac{\lambda W_{CH_4} \omega_l}{c_p Y_{CH_4 u} (\rho v)_u^2}, \quad Q_l^* = \frac{Q_l Y_{CH_4 u}}{c_p (T_b - T_u) W_{CH_4}} \end{aligned} \quad (6.17)$$

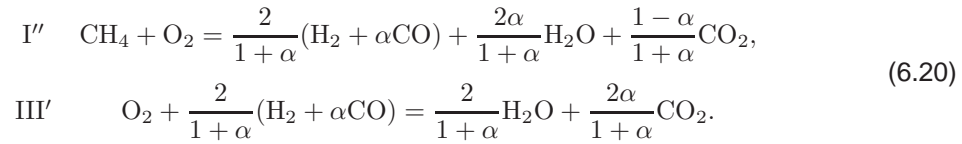
and redefine the parameter α'

$$\alpha = \alpha' \frac{Le_{H_2}}{Le_{CO}}. \quad (6.18)$$

With $x_{CO} = \alpha x_{H_2}$ one obtains the following balance equations of the two-step mechanism (the asterisks will be removed from here on)

$$\begin{aligned} -\frac{d^2 x_{CH_4}}{dx^2} &= -\omega_I, \\ -\frac{d^2 x_{O_2}}{dx^2} &= -\omega_I - \omega_{III}, \\ -\frac{d^2 x_{H_2}}{dx^2} &= \frac{2}{1+\alpha}(\omega_I - \omega_{III}), \\ -\frac{d^2 x_{CO}}{dx^2} &= \frac{2\alpha}{1+\alpha}(\omega_I - \omega_{III}), \\ -\frac{d^2 x_{H_2O}}{dx^2} &= \frac{2\alpha}{1+\alpha}\omega_I + \frac{2}{1+\alpha}\omega_{III}, \\ -\frac{d^2 x_{CO_2}}{dx^2} &= \frac{1-\alpha}{1+\alpha}\omega_I + \frac{2\alpha}{1+\alpha}\omega_{III}. \end{aligned} \quad (6.19)$$

The stoichiometric coefficients are those of the two global reactions



Here the combination $H_2 + \alpha CO$ appears as an intermediate which is formed in I'' and consumed in III'' . The rates of these reactions are still the same as of I and III in the four-step mechanism. If the balance equations Eqs. (6.19)₁ and (6.19)₃ are used to determine x_{CH_4} and x_{H_2} , all other concentrations and the temperature can be determined deriving the following coupling equations

from Eq. (6.19) and the corresponding temperature equation

$$\begin{aligned}\frac{d^2}{dx^2}[(1+\alpha)x_{H_2} + 4x_{CH_4} - 2x_{O_2}] &= 0, \\ \frac{d^2}{dx^2}[x_{H_2} + 2x_{CH_4} + x_{H_2O}] &= 0, \\ \frac{d^2}{dx^2}[x_{H_2} + x_{CH_4} + x_{CO_2}] &= 0, \\ \frac{d^2}{dx^2}[(q_{H_2} + \alpha q_{CO})x_{H_2} + x_{CH_4} + T] &= 0.\end{aligned}\tag{6.21}$$

Here the reduced heats of reaction are

$$\begin{aligned}q_{H_2} &= \frac{1}{2} \frac{Q_{III}}{Q} = 0.3116 \\ q_{CO} &= \frac{\left(\frac{1}{2}Q_{III} + Q_{II}\right)}{Q} = 0.3479,\end{aligned}\tag{6.22}$$

where Q is the heat of reaction of the global step



In the following we approximate both q_{H_2} and q_{CO} by $q = 0.33$ for simplicity.

6.2 The Asymptotic Structure

The flame structure of the two-step mechanism is shown in Fig. 6.1 and contains three layers

1. a chemically inert preheat zone of order $\mathcal{O}(1)$ upstream,
2. a thin inner layer of order $\mathcal{O}(\delta)$ in which the fuel is consumed and the intermediates H_2 and CO are formed according to the global step I'' ,
3. a thin oxidation layer of order $\mathcal{O}(\varepsilon)$ downstream where H_2 and CO are oxidized according to the global step III'' .

At first the inner layer shall be analyzed. We will denote quantities at the inner layer with a subscript 0 but the inner layer temperature as T^0 . In this layer all concentrations except that of the fuel, which is depleted may be assumed constant to leading order. Introducing Eq. (6.10) into the

Eq. (6.6)₁ and neglecting the second term in the parenthesis of Eq. (6.10) this leads to

$$\omega_I = Da_I x_{CH_4} \left(1 - \frac{x_{CH_4}}{\delta}\right)^{1/2} \quad (6.24)$$

where the Damköhler number of reaction I is

$$Da_I = \frac{\rho_0^2}{\rho_u^2 s_L^2} \frac{Y_{CH_4} u}{W_{CH_4}} \frac{\lambda_0}{c_{p0}} \frac{(K_{IV} X_{O_2} X_{H_2}^3)_0^{1/2}}{X_{H_2O}} Le_{CH_4} k_{11}(T^0). \quad (6.25)$$

The small parameter δ was defined as

$$\delta = \frac{k_1(T^0) X_{O_2,0}}{k_{11}(T^0) Le_{CH_4}} \quad (6.26)$$

It denotes the ratio of the rate coefficients of reaction I and II and thereby describes the competition of these two reactions in producing and consuming /HnR-radicals according to the global steps IV and I. Since it happens that the reaction rate k_1 is typically smaller than k_{11} , and since also X_{O_2} in the inner layer is smaller than unity, δ is around 0.1 and sufficiently small for an asymptotic expansion. If δ is small, since ω_I must be real it follows from the term in parenthesis in Eq. (6.24) that x_{CH_4} must not exceed the value of δ . Fig. 6.1 shows that the fuel is of order $\mathcal{O}(1)$ in the preheat zone but decreases rapidly towards the inner layer. In the inner layer x_{CH_4} is then of order $\mathcal{O}(\delta)$ and one may introduce the scaling

$$y = \frac{x_{CH_4}}{\delta} \quad (6.27)$$

and the stretched variable

$$\zeta = \frac{x}{\delta}. \quad (6.28)$$

Introducing these into the equation of Eq. (6.19)₁ leads to the differential equation that governs the structure of the inner layer

$$\frac{d^2 y}{d\zeta^2} = (\delta^2 Da_I) y (1 - y)^{1/2}. \quad (6.29)$$

The downstream boundary condition of this equation is

$$y = 0 \quad \text{as} \quad \zeta \rightarrow +\infty \quad (6.30)$$

since reaction I is irreversible. The matching with the preheat zone should, as for the one-step asymptotic problem, provide the second boundary condition. The solution for the fuel concentration in the preheat zone is

$$x_{\text{CH}_4} = 1 - \exp(\text{Le}_{\text{CH}_4} x), \quad (6.31)$$

which leads to the expansion $x_{\text{CH}_4} = -x$ around $x = 0$. It is shown in [1], however, that the inner layer and the preheat zone are separated by an additional thin layer, the radical consumption layer where the steady state approximation for the H-radical breaks down. This layer occurs at $y = 1, \zeta = -1$ in terms of the inner layer variables. Since the fuel is not consumed in this radical layer the slope of the fuel concentration is continuous and matching across this layer leads to

$$y = 1, \quad \frac{dy}{d\zeta} = -1 \quad \text{at} \quad \zeta = -1. \quad (6.32)$$

With the boundary conditions Eqs. (6.30) and (6.32) Eq. (6.29) can be integrated once to obtain the eigenvalue

$$\delta^2 \text{Da}_I = \frac{15}{8}. \quad (6.33)$$

With Eq. (6.33) one could now determine the burning velocity s_L if the temperature T^0 and all other properties at the inner layer were known. In order to determine these, the structure of the oxidation layer also must be resolved. In the oxidation layer $x_{\text{CH}_4} = 0$ and therefore $\omega_I = 0$. The temperature varies only slowly in this layer and since the activation energy of k_5 is small, temperature variations may be neglected. Since most of the chemical activity takes place in the vicinity of the inner layer, all properties shall be evaluated at $x = 0$. Choosing x_{H_2} as the dependent variable in the oxidation layer and scaling it in terms of a new variable z as

$$x_{\text{H}_2} = \frac{\varepsilon z}{(1 + \alpha)q} \quad (6.34)$$

one may use the coupling relations Eq. (6.21) to show that the downstream boundary conditions are satisfied by

$$x_{\text{O}_2} = \varepsilon z / 2q, \quad T = 1 - \varepsilon z. \quad (6.35)$$

In these expansions ε is the small parameter related to the thickness of the oxidation layer. Introducing Eqs. (6.34) and (6.35) into the third of Eqs. (6.6) leads to

$$\omega_{\text{III}} = 2q \text{Da}_{\text{III}} \varepsilon^3 z^3 \quad (6.36)$$

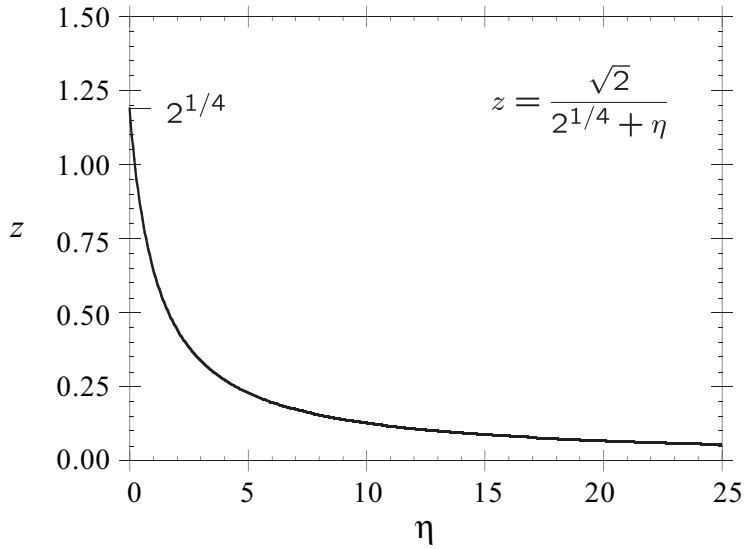


Figure 6.2: Normalized H_2 -profile in the oxidation layer.

where the Damköhler number of reaction III is defined

$$\text{Da}_{\text{III}} = \frac{\rho_0^2}{\rho_u^2 s_L^2} \frac{Y_{\text{CH}_4} u}{W_{\text{CH}_4}} \frac{\lambda_0}{c_{p0}} \left(\frac{K_{\text{IV}} \text{Le}_{\text{O}_2}^3 \text{Le}_{\text{H}_2}^3}{2^5 (1+\alpha)^3} \right)_0^{1/2} \frac{k_5 [\text{M}]}{q^4 X_{\text{H}_2\text{O}}}. \quad (6.37)$$

The concentration of the third body in reaction 5 may be determined approximately by using the third body efficiencies evaluated at the burnt gas conditions. This leads to

$$[\text{M}] = \frac{1.6p}{\mathcal{R}T} \quad (6.38)$$

which introduces a pressure dependence of Da_{III} and will finally determine the pressure dependence of the burning velocity. Introduction of a stretched coordinate

$$\eta = \frac{2qx}{\varepsilon} \quad (6.39)$$

then leads from the third equation of Eq. (6.19) with $\omega_I = 0$ to the governing equation of the oxidation layer

$$\frac{d^2z}{d\eta^2} = (\varepsilon^4 \text{Da}_{\text{III}}) z^3. \quad (6.40)$$

This suggests the definition

$$\varepsilon = \text{Da}_{\text{III}}^{-1/4}. \quad (6.41)$$

It turns out that for $p \geq 1 \text{ atm}$ ε is smaller than unity but typically larger than δ . Even though δ is not very small, we will consider it as small enough to justify an asymptotic description of the oxidation layer. The downstream boundary condition of Eq. (6.40) is

$$z = 0 \quad \text{for} \quad \eta \rightarrow \infty \quad (6.42)$$

since reaction III is irreversible. The upstream boundary condition must be determined from jump conditions across the inner layer. Since the fuel is depleted and H_2 is formed in the inner layer following reaction I'', the stoichiometry of this reaction also determines the change of slopes of the H_2 in comparison of those of the fuel. This is written as

$$\frac{dx_{\text{CH}_4}}{dx} \Big|_{0-} - \frac{dx_{\text{CH}_4}}{dx} \Big|_{0+} = \frac{1+\alpha}{2} \left(\frac{dx_{\text{H}_2}}{dx} \Big|_{0-} - \frac{dx_{\text{H}_2}}{dx} \Big|_{0+} \right) \quad (6.43)$$

Since the thickness of the preheat zone is of order $\mathcal{O}(1)$ and that of the oxidation layer of order $\mathcal{O}(\varepsilon)$ the upstream slope of the H_2 concentration $dx_{\text{H}_2}/dx|_{0+}$ can be neglected compared to the downstream slope $dx_{\text{H}_2}/dx|_{0-}$. It then follows with Eqs. (6.34) and (6.39) that the upstream boundary condition of Eq. (6.40) is

$$\frac{dz}{d\eta} = -1 \quad \text{at} \quad \eta = 0. \quad (6.44)$$

Then the solution of Eq. (6.40) with Eq. (6.41) is

$$z = \frac{2^{1/2}}{2^{1/4} + \eta} \quad (6.45)$$

with

$$z_0 = 2^{1/4} \quad \text{at} \quad \eta = 0. \quad (6.46)$$

The form of the solution is plotted in Fig. 6.2 showing a very slow decrease of z towards $\eta \rightarrow \infty$. This may explain why in numerically and experimentally obtained concentration and temperature profiles the downstream conditions are approached only very far behind the flame.

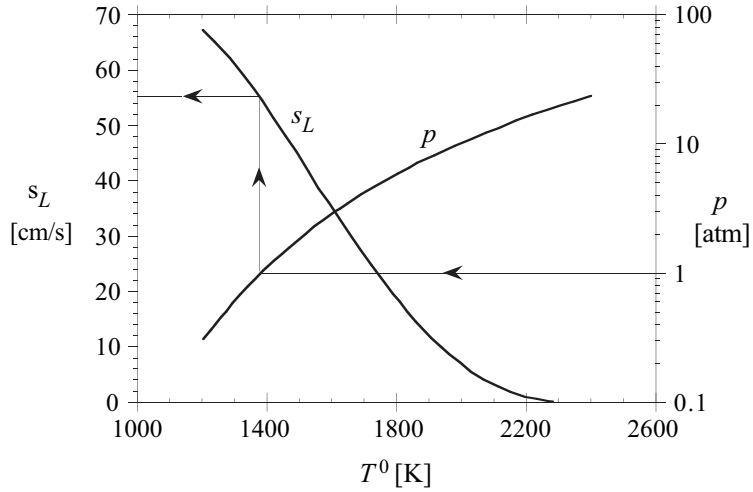


Figure 6.3: The burning velocity for an undiluted stoichiometric methane-air flame at $T_u = 300$ K.

6.3 An Analytic Expression for the Burning Velocity

The result Eq. (6.46) may now be used in Eqs. (6.34) and (6.36) to determine the quantities required in Eq. (6.25) and thereby the burning velocity s_L . Also by dividing Eq. (6.25) by Eq. (6.39) one can eliminate s_L and obtain a relation of the form

$$\frac{k_1^2(T^0)}{k_{11}(T^0)k_5(T^0)/(\mathcal{R}T^0)} = 1.5p \frac{\text{Le}_{\text{CH}_4}}{\text{Le}_{\text{O}_2}} \quad (6.47)$$

Here the universal gas constant \mathcal{R} must be used as $R = 82.05 \text{ atmcm}^3/\text{mol/K}$ in order to be consistent with the units of the reaction rates and the pressure. Eq. (6.47) shows that with the rate coefficients fixed, the inner layer temperature is function of the pressure only. It does not depend on the preheat temperature, the dilution of the fuel concentration in the unburnt mixture and thereby the adiabatic flame temperature. After some algebraic manipulations the expression for the burning velocity reads

$$s_L^2 = \frac{8}{15} \frac{k_1^2}{k_{11} q^4 X_{\text{H}_2\text{O}}} \frac{1}{W_{\text{CH}_4}} \frac{Y_{\text{CH}_4,u}}{c_{p_0}} \frac{\lambda_0}{\text{Le}_{\text{CH}_4}} \left(\frac{\text{Le}_{\text{O}_2}^5 \text{Le}_{\text{H}_2}^3 K_{\text{IV}}(T^0)}{2^5 (1 + \alpha_0)^3} \right)^{1/2} \left(\frac{T_u^2}{T^0} \right)^2 \left(\frac{T_b - T^0}{T_b - T_u} \right)^4 \quad (6.48)$$

where Eqs. (6.46) and (6.36) were used to relate ε to the difference between T_b and T^0

$$\varepsilon z_0 = \frac{T_b - T^0}{T_b - T_u}. \quad (6.49)$$

The burning velocity calculated from Eq. (6.48) and the pressure from Eq. (6.47) are plotted in Fig. 6.3 for an undiluted flame with $T_u = 300$ K as a function of T^0 choosing $p = 1$ atm one obtains a laminar burning velocity of 54 cm/s for stoichiometric methane flames. This value is satisfactory in view of the many approximations that were made and the few kinetic rates that were retained. In fact, it is seen from Eqs. (6.47) and (6.48) that only the rates of reactions 1, 5, and 11 influence the burning velocity in this approximation.

A further consequence of Eq. (6.48) is that the burning velocity vanishes as T^0 reaches T_b . This is seen in Fig. 6.3 with $T_b = 2320$ K the pressure is larger than approximately 20 atm. Different values of T_b would have been obtained for a diluted or preheated flame. The fact that at a fixed pressure T^0 is fixed by the rate of rate coefficients in Eq. (6.47) points towards the possibility to explain flammability limits at least in terms of dilution for stoichiometric flames: if the amount of fuel is so low that in the unburnt mixture the corresponding adiabatic flame temperature is lower than T^0 , a premixed flame cannot be established.

6.4 Relation to the Activation Energy of the One-step Model

Using the burning velocity expression Eq. (6.48) from the preceding section

$$\begin{aligned} \rho_u s_L &= \sqrt{2 \frac{B \rho_b^2 \lambda_b \mathcal{R}^2 T_b^4}{c_p (T_b - T_u)^2 E^2}} \exp\left(-\frac{E}{\mathcal{R} T_b}\right) S \\ S &= \frac{\nu'_{\text{CH}_4} Y_{\text{O}_2,b}}{M_{\text{O}_2}} + \frac{\nu'_{\text{O}_2} Y_{\text{CH}_4,b}}{M_{\text{CH}_4}} + \frac{2 \nu'_{\text{O}_2} \nu'_{\text{CH}_4} c_p \mathcal{R} T_b^2}{(-\Delta H) E}, \end{aligned}$$

one may plot the burning velocity in an Arrhenius diagram over $1/T_b$. Then in the limit of a large activation energy all pre-exponential dependencies on T_b are small and the slope in this diagram is given by

$$\frac{d \ln s_L^2}{d(1/T_b)} = -\frac{E}{\mathcal{R}} \quad (6.50)$$

or

$$\frac{d \ln s_L^2}{d \ln T_b} = \frac{E}{\mathcal{R} T_b} \quad (6.51)$$

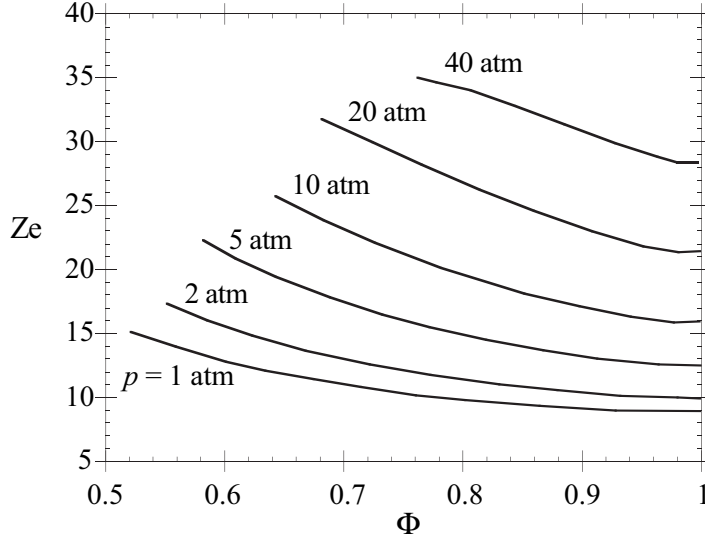


Figure 6.4: Variation in the value of the effective Zeldovich number with Φ for various values of p at $T_u = 300$ K.

Applying this form to Eq. (6.48) with T^0 fixed leads to

$$\frac{d \ln s_L^2}{d \ln T_b} = \frac{4T_b}{T_b - T^0} - \frac{4T_b}{T_b - T_u} \quad (6.52)$$

Since the second of the terms is much smaller than the first, one obtains with Eq. (6.49), when T^0 approaches T_b and ε is small,

$$\frac{E}{RT_b} = \frac{4T_b}{T_b - T_u} \frac{1}{\varepsilon z_0}. \quad (6.53)$$

Therefore the Zeldovich number

$$Ze = \frac{E(T_b - T_u)}{\mathcal{R}T_b^2}$$

introduced in Eq. (5.22) may be expressed as

$$Ze = \frac{E(T_b - T_u)}{RT_b^2} = \frac{4}{\varepsilon z_0} \quad (6.54)$$

In the one-step model the thickness of the reaction zone was of the order of the inverse of the Zeldovich number. This corresponds for the two-step model for methane flames to the thickness

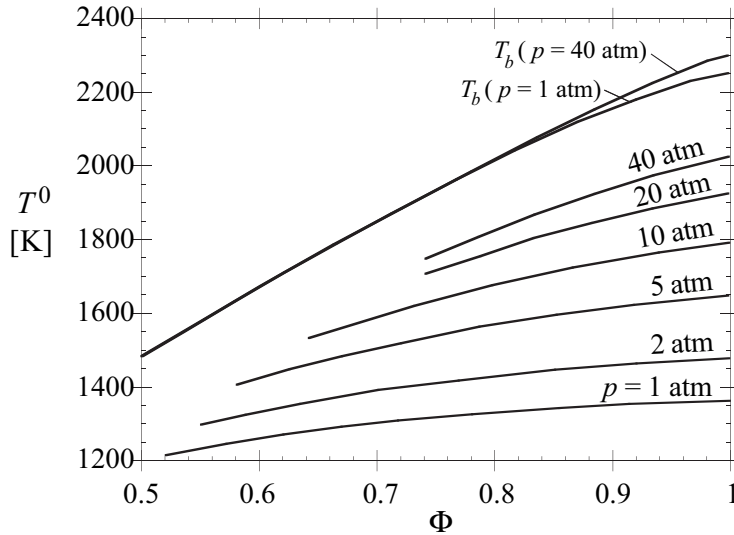


Figure 6.5: Variation of the adiabatic flame temperature T_b and the temperature at the inner layer T^0 with equivalence ratio Φ for various values of the pressure p and for $T_u = 300$ K.

of the oxidation layer. Therefore the oxidation layer seems to play a similar role in hydrocarbon flames as the reaction zone in one-step asymptotics. Values of the Zeldovich number for lean to stoichiometric methane flames, obtained by asymptotic analysis in [2] are shown in Fig. 6.4. The Zeldovich number measures the sensitivity of the burning velocity to perturbations of the maximum temperature. Fig. 6.4 shows that this sensitivity increases as the mixture becomes leaner and when the pressure increases. The flame will then become very sensitive to heat loss and flame stretch effects.

6.5 Analytic Approximations of Burning Velocities for Lean CH₄, C₂H₆, C₂H₄, C₂H₂, and C₃H₈ Flames

The burning velocity expression presented in Eqs. (6.47) and (6.48) may be generalized by writing an approximation formula for burning velocities as

$$s_L = Y_{F,u}^m A(T^0) \frac{T_u}{T^0} \left(\frac{T_b - T^0}{T_b - T_u} \right)^n \quad (6.55)$$

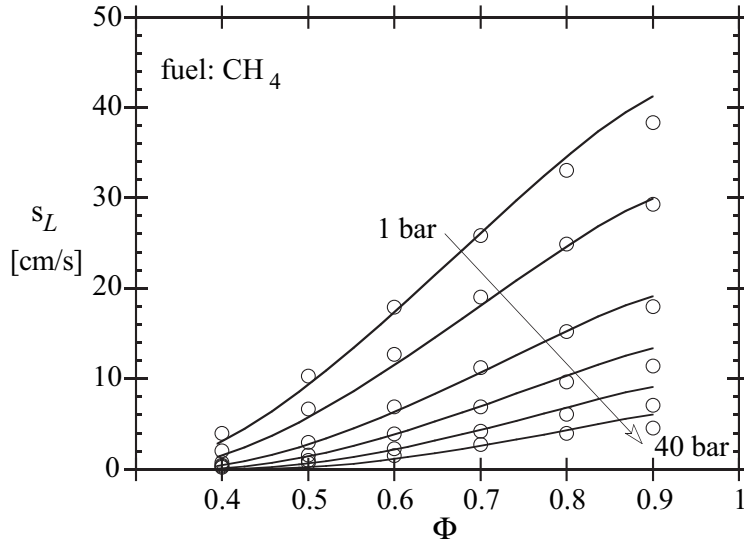


Figure 6.6: Burning velocity s_L of methane vs. fuel-air-equivalence ratio Φ for various pressures with a fixed unburnt temperature T_u of 298 K (solid lines). The markers denote the values of detailed numerical calculations.

and

$$p = P(T^0) \quad (6.56)$$

where the functions $A(T^0)$ and $P(T^0)$ are determined by fitting numerical or experimental data and the values $m = 1/2$ and $n = 2$ would correspond to the previous expressions for premixed methane flames. Eq. (6.56) assumes that the inner layer temperature is a function of pressure only, and it does not depend, for instance, on the equivalence ratio. This is a fairly crude approximation as may be seen from Fig. 6.5 where inner layer temperatures obtained from asymptotic analysis [2] are plotted together with the adiabatic temperatures as a function of the equivalence ratio. If one would replace the curves for the inner layer temperature by a horizontal line, its intersection with the curve for T_b would yield a lower theoretical limit for the lean flammability limit. This will be discussed in the next section. If the structure of any other hydrocarbon fuel is similar to that of methane, these exponents should not differ very much from these numbers. Since $A(T^0)$ and $B(T^0)$ contain essentially the temperature dependence due to rate coefficients, we express them in Arrhenius form

$$A(T^0) = F \exp(-G/T^0) \quad (6.57)$$

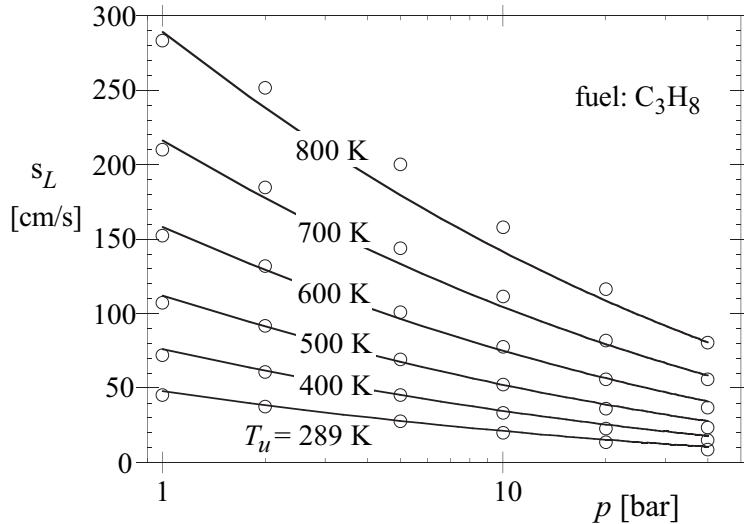


Figure 6.7: Burning velocity s_L of propane vs. pressure p for various unburnt gas temperatures T_u at stoichiometric mixture (solid lines). The markers denote the values of detailed numerical calculations.

$$P(T^0) = B \exp(-E/T^0). \quad (6.58)$$

This concept was tested in [3]. The basis of the approximation was a data set of 197, 223, 252, 248, and 215 premixed flames for CH₄, C₂H₆, C₂H₄, C₂H₂ and C₃H₈, respectively in the range between $p = 1$ atm and 40 atm, T_u between 298 K and 800 K, and the fuel-air equivalence ratio between $\Phi = 0.4$ and $\Phi = 1.0$. A nonlinear approximation procedure was employed, yielding the following values for the coefficients: The approximation was surprisingly the best for C₂H₂, yielding

fuel	B [bar]	E [K]	F [cm/s]	G [K]	m	n
CH ₄	3.1557e8	23873.0	22.176	-6444.27	0.565175	2.5158
C ₂ H ₂	56834.0	11344.4	37746.6	1032.36	0.907619	2.5874
C ₂ H ₄	3.7036e5	14368.7	9978.9	263.23	0.771333	2.3998
C ₂ H ₆	4.3203e6	18859.0	1900.41	-506.973	0.431345	2.1804
C ₃ H ₈	2.2502e6	17223.5	1274.89	-1324.78	0.582214	2.3970

Table 6.1: Approximation coefficients for the burning velocity.

a standard deviation for s_L of 2.3%, followed by C₂H₄ with 3.2%, C₂H₆ and C₃H₈ with 6.2%, and CH₄ with 7.4%. These deviations may be considered extremely small in view of the fact that such a large range of equivalence ratios, pressures and preheat temperatures has been covered with

an approximation formula containing only six coefficients which for some hydrocarbons are given in Tab. 6.1. A closer look at the exponents m and n shows that m is close to $1/2$ for CH_4 and C_3H_8 , but close to unity for C_2H_2 and C_2H_4 , suggesting that the asymptotic model for these flames should differ from the one for CH_4 in some important details. The exponent m lies around 2.5 and thereby sufficiently close to 2 for all fuels.

Burning velocities for methane calculated from Eqs. (6.55) and (6.56) are shown as a function of equivalence ratio for different pressures at $T_u = 298 \text{ K}$ in Fig. 6.6 and compared with the values obtained from the numerical computations. Generally the largest derivations from the numerical computations occur around $\Phi = 1$. The pressure and unburnt temperature variation of s_L at stoichiometric mixture is shown in Fig. 6.7 for propane.

Example 6.1

From the approximation Eq. (6.55) calculate in comparison with Eq. (5.17) those activation energy, which describes the change of the reaction rate as function of the change in T_b . Thereby T_u and T^0 should be considered constant.

Solution

If one writes Eq. (5.17) approximately as

$$(\rho_u s_L)^2 = \text{const} \exp(-E/\mathcal{R}T_b)$$

and logarithmizes this expression

$$2 \ln(\rho_u s_L) = \ln(\text{const}) - \frac{E}{\mathcal{R}T_b},$$

one can determine the activation energy by differentiation with respect to $1/T_b$ from

$$\frac{E}{\mathcal{R}} = -2 \frac{d \ln(\rho_u s_L)}{d(1/T_b)} = 2T_b^2 \frac{d}{dT_b} (\ln(\rho_u s_L)).$$

Using this in Eq. (6.55) for $\rho_u = \text{const}$, it follows

$$2T_b^2 \frac{d}{dT_b} (\ln(\rho_u s_L)) = \frac{2nT_b}{T_b - T^0} - \frac{2nT_b}{T_b - T_u}.$$

Therefore one obtains for the Zeldovich number Ze

$$\text{Ze} = n \left(\frac{T_b - T_u}{T_b - T^0} - 1 \right).$$

Here, following Eq. (6.56) T^0 is only dependent on pressure, while T_b following Eq. (2.24) depends both on T_u and on the fuel-air ratio $\phi = 1/\lambda$ via Eq. (1.55). If the difference $T_b - T^S S S 0$ is small compared with $T_b - T_u$, the second term in the parenthesis can be neglected.

Bibliography

- [1] N. Peters and F. A. Williams. Asymptotic structure of stoichiometric methane-air flames. *Comb. Flame*, 68:185–207, 1987.
- [2] K. Seshadri and J. Göttgens. Reduced kinetic mechanisms and asymptotic approximations for methane-air flames. *Lecture Notes in Physics*, 384:111–136, 1991.
- [3] J. Göttgens, F. Mauss, and N. Peters. Analytic approximations of burning velocities and flame thickness of lean hydrogen, methane, ethylene, ethane, acetylene and propane flames. *24 th Symposium (International) on Combustion*, 1992.

Lecture 7

Flame Extinction and Flammability Limits

Lean and rich flammability limits are a function of the temperature and the pressure of the original mixture. Fig. 7.1 shows the flammability limits of methane and hydrogen for increasing temperatures as a function of $1/\phi$ the air-fuel equivalence ratio. It is seen, that in particular for lean mixtures, which are on the r.h.s. of this diagram, the flammability limits of hydrogen extend to much larger values than for methane. This shows that hydrogen leakage may cause safety hazards more readily than, for instance, hydrocarbons which have flammability limits close to those of methane. Many data on flammability limits are given in [1].

The theory developed in the previous lecture shows that, differently from the one-step reaction, a flame cannot burn if the adiabatic flame temperature, which depends on the equivalence ratio and on dilation, is lower than the inner layer temperature T^0 , the latter being determined essentially by kinetics, as eq. (6.47) shows.

7.1 Lean Flammability Limits of Hydrocarbon Flames

Flammability is the ability of a mixture, once it has been ignited, to enable flame propagation without further heat addition. This requires that a sufficient amount of fuel is available to reach a temperature, that, in view of the flame structure as shown in Fig. 6.1 should exceed the inner layer temperature T^0 . Le Chatelier in 1891 was the first to point towards a criterion that relates

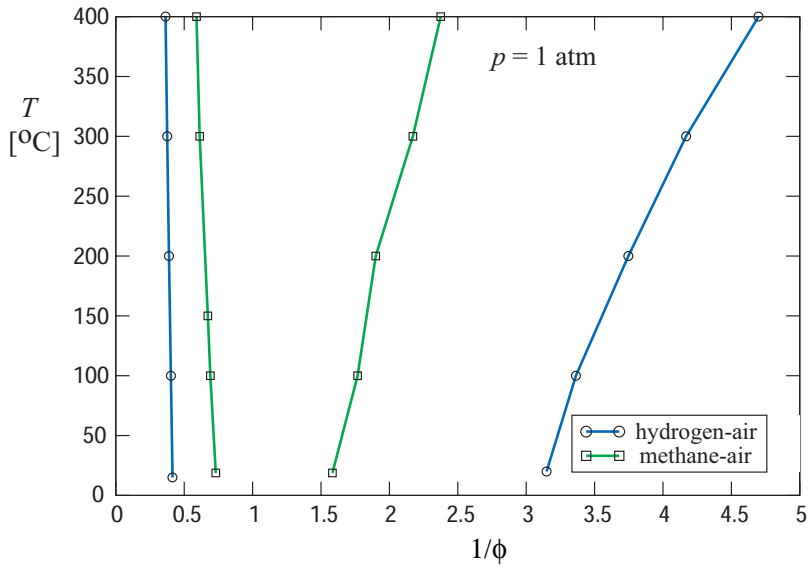


Figure 7.1: Flammability limits of hydrogen and methane as a function of the temperature.

the flammability limit to the thermodynamic properties of the fuel mixture. In 1898 Le Chatelier and Boudouard investigated experimental data and wrote that the flammability limit of most hydrocarbons corresponds to a heat of combustion close to 12.5 kcal. This is essentially Le Chatelier's famous mixing rule. It determines an adiabatic flame temperature and should be valid for mixtures of hydrocarbons with inerts, too. Eq. (6.55) now shows that the burning velocity vanishes if the adiabatic flame temperature is equal to the inner layer temperature. A lower theoretical limit for the lean flammability limit is therefore given by

$$T_b = T^0. \quad (7.1)$$

In view of this criterion the adiabatic flame temperature identified by Le Chatelier and Boudouard corresponds to the inner layer temperature and thus describes a chemical rather than a thermodynamic property.

As the lean flammability limit is approached, the burning velocity drops sharply, but shows a finite value at the limiting point. Egerton and Thabet [2] and Powling [3] report a value of 5 cm/s at atmospheric pressure using flat flame burners. Experimental data for the lean flammability limit are always influenced by external disturbances, such as radiative heat loss or flame stretch. Radiation heat loss will be discussed in Section 7.2. We note that flame extinction occurs at a finite value of

the burning velocity. Eq. (7.1) may be used to calculate the limiting fuel mass fraction $(Y_{F,u})_{l.l.}$ as a quantity that determines the flammability limit. At the flammability limit it is accurate enough to assume complete combustion and to use Eq. (2.20) to determine T_b as a function of $Y_{F,u}$ and T_u . Then, with $T_b = T^0$, one obtains

$$(Y_{F,u})_{l.l.} = \frac{(T^0 - T_u)c_p\nu'_F W_F}{Q_{\text{ref}}} \quad (7.2)$$

This indicates that the limiting fuel mass fraction decreases linearly with increasing T_u .

7.2 Extinction of a Plane Flame by Volumetric Heat Loss

An additional influence that affects the stability of flames is volumetric heat loss. In order to analyze this effect we will compare the one-step model with a large activation energy and unity Lewis number and the four-step model. We will assume that the volumetric heat loss q_R is proportional to the temperature difference $T - T_u$ and write

$$q_R = -\alpha(T - T_u), \quad (7.3)$$

where α is a heat loss coefficient. The one-dimensional temperature equation for a steady state premixed flame is then written as

$$\rho_u s_L \frac{dT}{dx} = \frac{d}{dx} \left(\frac{\lambda}{c_p} \frac{dT}{dx} \right) + \frac{Q}{c_p} \omega - \alpha(T - T_u). \quad (7.4)$$

In terms of the non-dimensional quantities defined in Eq. (6.17) this may be written (with the asterisks removed)

$$M \frac{dT}{dx} = \frac{d^2T}{dx^2} + \omega - \pi T. \quad (7.5)$$

Here M is the burning velocity of the plane flame with heat loss normalized by the reference burning velocity $s_{L,\text{ref}}$ of a plane flame without heat loss

$$M = \frac{s_L}{s_{L,\text{ref}}}. \quad (7.6)$$

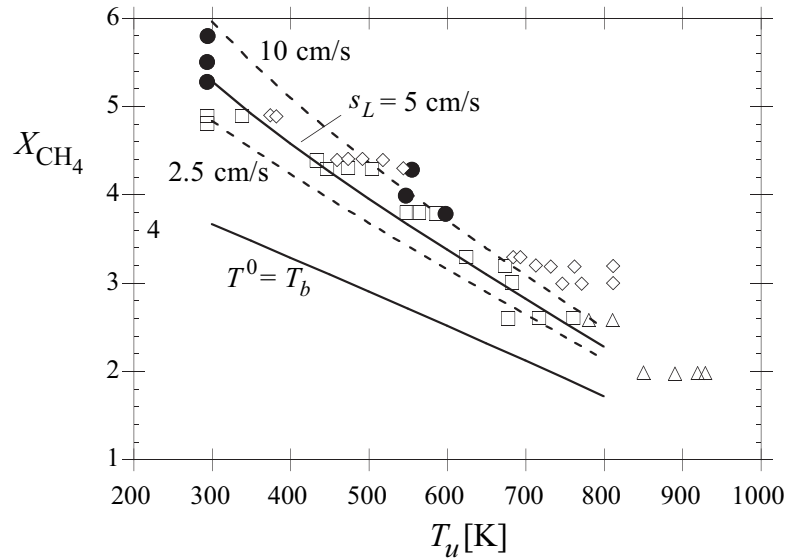


Figure 7.2: Comparison of experimental data for the lean limit CH_4 mole fraction from [4] for different preheat temperatures with the two criteria.

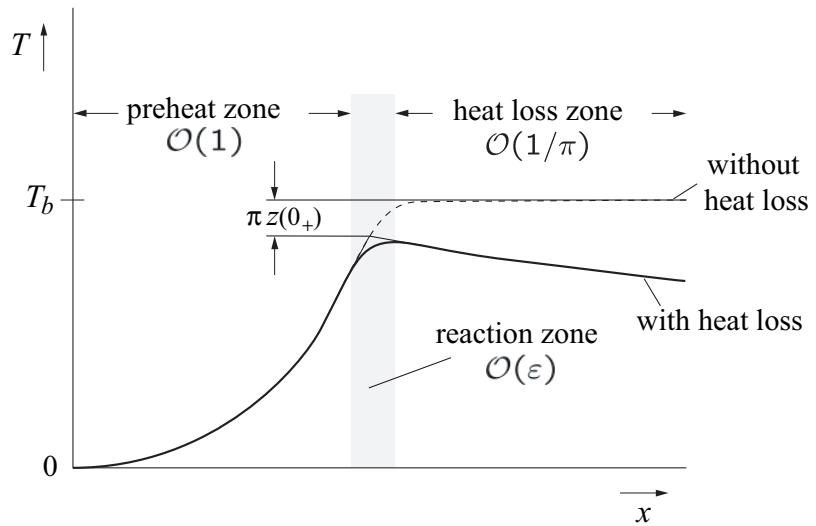


Figure 7.3: Structure of a premixed flame with heat loss.

The non-dimensional heat loss parameter is defined

$$\pi = \frac{\lambda\alpha}{\rho_u^2 s_{L,\text{ref}}^2 c_p^2}. \quad (7.7)$$

It will be assumed constant with λ evaluated at $T = T^0$. It should be noted here that π increases rapidly as $s_{L,\text{ref}}$ decreases. Therefore heat loss has a strong influence close to the flammability limit when $s_{L,\text{ref}}$ is small. The structure of a premixed flame with heat loss is shown in Fig. 7.3. We will treat π as a small expansion parameter and expand the temperature as

$$T = T^0(1 + \pi z) \quad (7.8)$$

where T^0 is the leading order temperature for $\pi \rightarrow 0$. The reaction term ω in Eq. (7.4) can be eliminated by coupling it with the Eq. (5.3) for the fuel mass fraction. In non-dimensional form one then obtains the enthalpy

$$h = T + Y - 1 \quad (7.9)$$

governed by the equation

$$M \frac{dh}{dx} = \frac{d^2 h}{dx^2} - \pi T. \quad (7.10)$$

This equation may be integrated across the thin reaction zone from $x = -\infty$ to $x = 0_+$. This leads to

$$Mh(0_+) = \left. \frac{dh}{dx} \right|_{0_+} - \pi \int_{-\infty}^{0_+} T^0 dx \quad (7.11)$$

since at $x \rightarrow -\infty$ the enthalpy and its gradient vanishes. Introducing Eq. (7.8) into Eq. (7.9) at $x = 0_+$, where $T^0 = 1$ and $Y = 0$ one obtains

$$h(0_+) = \pi z(0_+). \quad (7.12)$$

The integral over the preheat zone in Eq. (7.11) may be evaluated by integrating the temperature equation Eq. (7.5) to leading order

$$M \frac{dT^0}{dx} = \frac{d^2 T^0}{dx^2} \quad (7.13)$$

leading to

$$T^0 = \exp(Mx) \quad \text{for } x < 0. \quad (7.14)$$

The downstream enthalpy gradient at the flame front is equal to the downstream temperature gradient since $Y = 0$ for $x \geq 0$. It can be evaluated by realizing that the heat loss region behind the flame is broad of order $O(\pi^{-1})$. This suggest the introduction of a contracted coordinate

$$\tilde{x} = \pi x \quad (7.15)$$

into the downstream temperature equation

$$M \frac{dT}{d\tilde{x}} = \pi \frac{d^2T}{d\tilde{x}^2} - T \quad x > 0. \quad (7.16)$$

In the limit $\pi \rightarrow 0$ the heat conduction term can now be neglected and with $T^0(0_+) = 1$ one obtains to leading order

$$\left. \frac{dh}{dx} \right|_{0_+} = \left. \frac{dT}{dx} \right|_{0_+} = -\frac{\pi}{M}. \quad (7.17)$$

With Eqs. (7.12), (7.14) and (7.17) inserted into Eq. (7.11) the flame temperature perturbation is

$$z(0_+) = -\frac{2}{M^2}. \quad (7.18)$$

Since for a one step flame with a large activation energy the burning velocity depends according to Eq. (5.17) on the flame temperature as

$$s_L^2 \sim \exp\left(-\frac{E}{RT_b}\right), \quad (7.19)$$

a perturbation of the temperature at $x = 0_+$ behind the reaction zone will lead in terms of the dimensional temperature to

$$M = \exp\left\{-\frac{E}{2R}\left(\frac{1}{T(0_+)} - \frac{1}{T^0}\right)\right\} \quad (7.20)$$

Using the expansion Eq. (7.8) in terms of the non-dimensional temperature one obtains with Eq. (5.22)

$$M^2 = \exp(\pi Ze z(0_+)) \quad (7.21)$$

When this is combined with Eq. (7.18) one obtains

$$M^2 \ln M^2 = -2\pi Ze. \quad (7.22)$$

A similar analysis may be performed for the four-step asymptotic analysis of methane flames. Then, since with Eq. (6.48)

$$s_L^2 \sim (T_b - T^0)^4 \quad (7.23)$$

one obtains with Eqs. (6.49) and (6.54)

$$M^2 = \frac{(T_b - T^0 + T_b \pi z(0_+))^4}{(T_b - T^0)^4} = \left(1 + \frac{\pi Z e z(0_+)}{4}\right)^4, \quad (7.24)$$

since $T_b = (T_b - T^0) = 1/(\varepsilon z_0) = Z e / 4$ to leading order. If this is now combined with Eq. (7.18) one obtains

$$M^2 \left(1 - M^{1/2}\right) = \pi Z e \quad (7.25)$$

instead of Eq. (7.22). Both Eqs. (7.22) and (7.25) are plotted in Fig. 7.4 showing a qualitatively and even quantitatively very similar behavior. Only the upper branch of these curves represents a stable solution. It shows a decrease of the burning velocity as the heat loss parameter π increases. There is a maximum value for the product $\pi Z e$ for each of these curves beyond which no solution exists. At these values heat loss extinguishes the flame. The non-dimensional burning rates at which this happens are very close to each other: $M_{ex} = 0.61$ for the one step kinetics and $M_{ex} = 0.64$ for the four-step kinetics. This is surprising because the kinetics for both cases are fundamentally different. This supports the previous conclusion that the one-step large activation energy model is a good approximation for the temperature sensitivity of hydrocarbon flames.

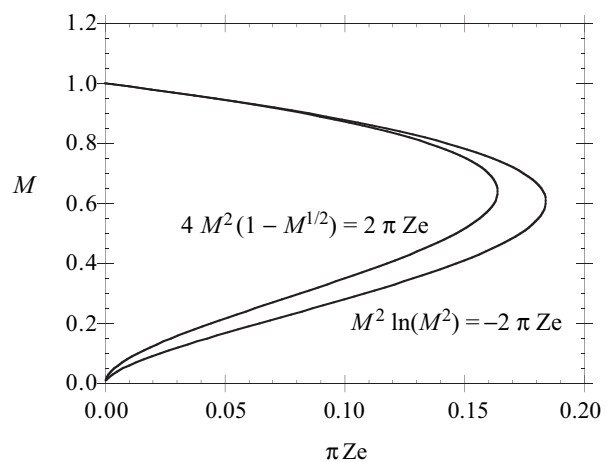


Figure 7.4: The change of burning velocity and flame extinction due to heat loss for one-step and four-step asymptotics.

Bibliography

- [1] H. F. Coward and G. W. Jones. Limits of flammability of gases and vapors. *U.S Bur. Min.*, 503, 1952.
- [2] A. Egerton and S. K. Thabet. *Proc. R. Soc. (London)*, 211:455, 1952.
- [3] J. Powling. Experimental methods in combustion research. *Pergamon Press London*, 1961.
- [4] J. E. Hustad and O. K. Sonju. *Comb. Flame*, 71:283–294, 1988.

Lecture 8

Laminar Diffusion Flames: Basic Theory

In this lecture we will consider systems, where fuel and oxidizer enter separately into the combustion chamber. Mixing then takes place by convection and diffusion. Only where fuel and oxidizer are mixed on the molecular level, chemical reactions can occur. Since the time scale of reaction is much shorter than the time scale for diffusion, the latter processes is rate determining. This is why flames in non-premixed combustion are called diffusion flames. A classical example of a diffusion flame is a candle flame shown in Fig. 8.1.

Its structure is similar to that shown in the introduction, except that the flow entraining the air into the flame is driven by buoyancy rather than by forced convection as in a jet flame. The paraffin of the candle first melts due to radiative heat from the flame to the candle, mounts by capillary forces into the wick where it then evaporates to become paraffin vapor, a gaseous fuel. In this lecture we will focus on the structure of the combustion zones in a diffusion flame. These are best described by an asymptotic expansion for very fast chemistry starting from the limit of complete combustion. To leading order one obtains the adiabatic flame temperature which is a function of mixture fraction only as already shown in Lecture 2. The asymptotic expansion around this limit will then describe the influence of finite rate chemistry. If the expansion takes the temperature sensitivity of the chemistry into account diffusion flame quenching can also be described. It will be shown that by introducing the mixture fraction as an independent coordinate for all reacting scalars, a universal coordinate transformation leads in the limit of sufficiently fast chemistry to a

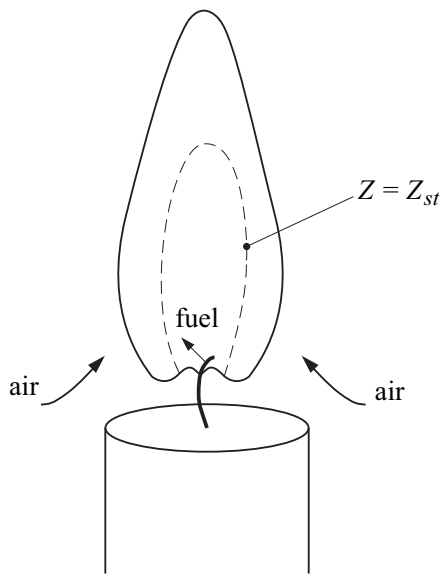


Figure 8.1: The candle flame as the classical example of a laminar diffusion flame.

one-dimensional problem for the reaction zone. This is the basis of the flamelet formulation for non-premixed combustion.

8.1 Flamelet Structure of a Diffusion Flame

Under the condition that equal diffusivities of chemical species and temperature can be assumed (an assumption that is good for hydrocarbon flames but much less realistic for hydrogen flames), all Lewis numbers

$$\text{Le}_i = \lambda / (c_p \rho D_i) = 1, \quad i = 1, 2, \dots, k \quad (8.1)$$

are unity, and a common diffusion coefficient $D = \lambda / (\rho c_p)$ can be introduced. In Cartesian coordinates the balance equation for mixture fraction Z Eq. (3.58), temperature T Eq. (3.46) and species

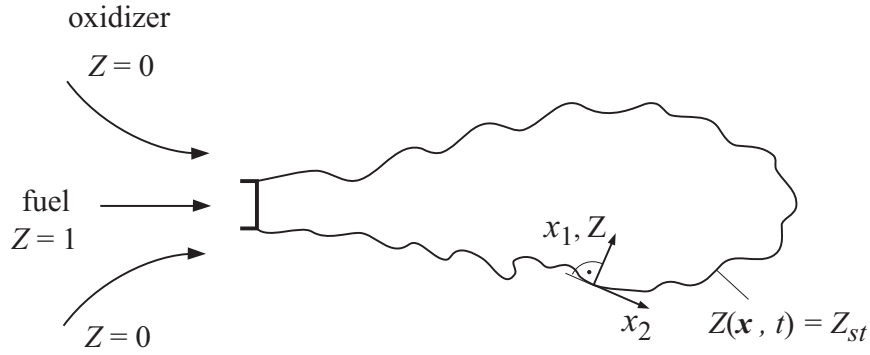


Figure 8.2: Schematic picture of a diffusion flame illustrating the flamelet transformation.

Y_i Eq. (3.47) read

$$\begin{aligned}
 \rho \frac{\partial Z}{\partial t} + \rho v_\alpha \frac{\partial Z}{\partial x_\alpha} - \frac{\partial}{\partial x_\alpha} \left(\rho D \frac{\partial Z}{\partial x_\alpha} \right) &= 0, \\
 \rho \frac{\partial T}{\partial t} + \rho v_\alpha \frac{\partial T}{\partial x_\alpha} - \frac{\partial}{\partial x_\alpha} \left(\rho D \frac{\partial T}{\partial x_\alpha} \right) &= \sum_{i=1}^k \dot{m}_i \frac{h_i}{c_p} + \frac{\dot{q}_R}{c_p} + \frac{1}{c_p} \frac{\partial p}{\partial t}, \\
 \rho \frac{\partial Y_i}{\partial t} + \rho v_\alpha \frac{\partial Y_i}{\partial x_\alpha} - \frac{\partial}{\partial x_\alpha} \left(\rho D \frac{\partial Y_i}{\partial x_\alpha} \right) &= \dot{m}_i \quad i = 1, 2, \dots, k.
 \end{aligned} \tag{8.2}$$

Here the low Mach number limit that leads to zero spatial pressure gradients has been employed, but the temporal pressure change $\partial p / \partial t$ has been retained. The heat capacity c_p is assumed constant for simplicity. The Eqs. (3.47) for the mass fractions of the species could also have been written down and can be analyzed in a similar way as the temperature equation. They are omitted here for brevity. Eq. (8.2)₁ does not contain a chemical source term, since the mixture fraction Z represents the chemical elements originally contained in the fuel, and elements are conserved during combustion. We assume the mixture fraction Z to be given in the flow field as a function of space and time by solution of Eq. (8.2)₁ as shown schematically in Fig. 3.2. Then the surface of the stoichiometric mixture can be determined from

$$Z(x_\alpha, t) = Z_{st}. \tag{8.3}$$

Combustion occurs in a thin layer in the vicinity of this surface if the local mixture fraction gradient is sufficiently high ([1]). Let us locally introduce an orthogonal coordinate system x_1, x_2, x_3, t

attached to the surface of stoichiometric mixture as shown in Fig. 8.1, where x_1 points normal to the surface $Z(x_\alpha, t) = Z_{st}$ and x_2 and x_3 lie within the surface. We replace the coordinate x_1 by the mixture fraction Z and x_2 , x_3 and t by $Z_2 = x_2$, $Z_3 = x_3$ and $t = \tau$. This is a coordinate transformation of the Crocco type. (Crocco expressed the temperature in a flat-plate boundary layer as functions of another dependent variable, the velocity.) Here the temperature T , and similarly the mass fractions Y_i , will be expressed as a function of the mixture fraction Z . By definition, the new coordinate Z is locally normal to the surface of the stoichiometric mixture. With the transformation rules

$$\begin{aligned}\frac{\partial}{\partial t} &= \frac{\partial}{\partial \tau} + \frac{\partial Z}{\partial t} \frac{\partial}{\partial Z}, \\ \frac{\partial}{\partial x_\alpha} &= \frac{\partial}{\partial Z_\alpha} + \frac{\partial Z}{\partial x_\alpha} \frac{\partial}{\partial Z} \quad (\alpha = 2, 3), \\ \frac{\partial}{\partial x_1} &= \frac{\partial Z}{\partial x_1} + \frac{\partial}{\partial Z}\end{aligned}\tag{8.4}$$

we obtain the temperature equation in the form

$$\begin{aligned}&\rho \left(\frac{\partial T}{\partial \tau} + v_2 \frac{\partial T}{\partial Z_2} + v_3 \frac{\partial T}{\partial Z_3} \right) - \frac{\partial(\rho D)}{\partial x_2} \frac{\partial T}{\partial Z_2} - \frac{\partial(\rho D)}{\partial x_3} \frac{\partial T}{\partial Z_3} \\ &- \rho D \left[\left(\frac{\partial Z}{\partial x_\alpha} \right)^2 \frac{\partial^2 T}{\partial Z^2} + 2 \frac{\partial Z}{\partial x_2} \frac{\partial^2 T}{\partial Z \partial Z_2} + 2 \frac{\partial Z}{\partial x_3} \frac{\partial^2 T}{\partial Z \partial Z_3} + \frac{\partial^2 T}{\partial Z_2^2} + \frac{\partial^2 T}{\partial Z_3^2} \right] \\ &= \sum_{i=1}^k \dot{m}_i \frac{h_i}{c_p} + \frac{\dot{q}_R}{c_p} + \frac{1}{c_p} \frac{\partial p}{\partial t}.\end{aligned}\tag{8.5}$$

The transformation of the equation for the mass fraction is similar. If the flamelet is thin in the Z direction, an order-of-magnitude analysis similar to that for a boundary layer shows that the second derivative with respect to Z is the dominating term on the left-hand side of Eq. (8.5). This term must balance the terms on the right-hand side. All other terms containing spatial derivatives in x_2 and x_3 directions can be neglected to leading order. This is equivalent to the assumption that the temperature derivatives normal to the flame surface are much larger than those in tangential direction. The term containing the time derivative in Eq. (8.5) is important only if very rapid changes, such as extinction, occur. Formally, this can be shown by introducing the stretched coordinate ξ and the fast time scale σ

$$\xi = (Z - Z_{st})/\varepsilon, \quad \sigma = \tau/\varepsilon^2\tag{8.6}$$

where ε is a small parameter, the inverse of a large Damköhler number or a large activation energy, for example, representing the width of the reaction zone. If the time derivative term is retained, the flamelet structure is to leading order described by the one-dimensional time-dependent equations

$$\begin{aligned}\rho \frac{\partial T}{\partial t} - \rho \frac{\chi_{st}}{2} \frac{\partial^2 T}{\partial Z^2} &= \sum_{l=1}^r \frac{Q_l}{c_p} \omega_l + \frac{\dot{q}_R}{c_p} + \frac{1}{c_p} \frac{\partial p}{\partial t} \\ \rho \frac{\partial Y_i}{\partial t} - \rho \frac{\chi_{st}}{2} \frac{\partial Y_i}{\partial Z^2} &= \dot{m}_i \quad i = 1, 2, \dots, k.\end{aligned}\tag{8.7}$$

Here

$$\chi_{st} = 2D \left(\frac{\partial Z}{\partial x_\alpha} \right)_{st}^2\tag{8.8}$$

is the instantaneous scalar dissipation rate at stoichiometric conditions. It has the dimension 1/s and may be interpreted as the inverse of a characteristic diffusion time. It may depend on t and Z and acts as a prescribed parameter in Eq. (8.7)₁, representing the flow and the mixture field. As a result of the transformation, it implicitly incorporates the influence of convection and diffusion normal to the surface of the stoichiometric mixture. In the limit $\chi_{st} \rightarrow 0$, equations for the homogeneous reactor, are obtained. The neglect of all spatial derivatives tangential to the flame front is formally only valid in the thin reaction zone around $Z = Z_{st}$. This is shown in [9.1]. There are, however, a number of typical flow configurations where Eq. (8.7)₁ is valid in the entire Z -space. As example, we will analyze here the planar counterflow diffusion flame.

8.2 The Planar Counterflow Diffusion Flame

Counterflow diffusion flames are very often used experimentally because they represent an essentially one-dimension diffusion flame structures. Fig. 8.3 shows two typical cases where counterflow flames have been established between an oxidizer stream from above and a fuel stream from below. The latter may either be a gaseous fuel or an evaporating liquid fuel. If one assumes that the flow velocities of both streams are sufficiently large and sufficiently removed from the stagnation plane, the flame is embedded between two potential flows, one coming from the oxidizer and one from the fuel side. Prescribing the potential flow velocity gradient in the oxidizer stream by $a = -\partial v_\infty / \partial y$, the velocities and the mixture fraction are there

$$y \rightarrow \infty : \quad v_\infty = -ay, \quad u_\infty = ax, \quad Z = 0.\tag{8.9}$$

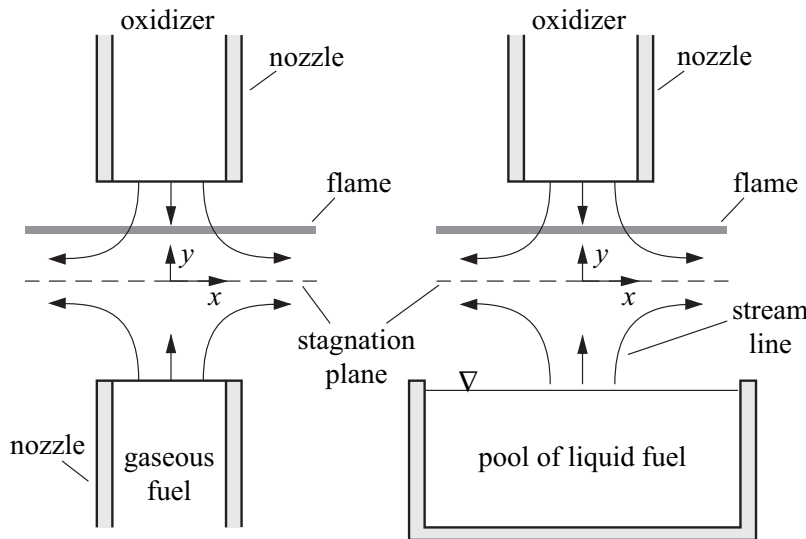


Figure 8.3: A schematic illustration of the experimental configuration for counterflow flames for gaseous and liquid fuels.

Equal stagnation point pressure for both streams requires that the velocities in the fuel stream are

$$y \rightarrow -\infty : \quad v_{-\infty} = -\sqrt{\frac{\rho_\infty}{\rho_{-\infty}}} ay, \quad u_{-\infty} = \sqrt{\frac{\rho_\infty}{\rho_{-\infty}}} ax, \quad Z = 1. \quad (8.10)$$

The equations for continuity, momentum and mixture fraction are given by

$$\begin{aligned} \frac{\partial(\rho u)}{\partial x} + \frac{\partial(\rho v)}{\partial y} &= 0, \\ \rho u \frac{\partial u}{\partial x} + \rho v \frac{\partial u}{\partial y} &= -\frac{\partial p}{\partial x} + \frac{\partial}{\partial y} \left(\mu \frac{\partial u}{\partial y} \right), \\ \rho u \frac{\partial Z}{\partial x} + \rho v \frac{\partial Z}{\partial y} &= \frac{\partial}{\partial y} \left(\rho D \frac{\partial Z}{\partial y} \right). \end{aligned} \quad (8.11)$$

Introducing the similarity transformation

$$\eta = \left(\frac{a}{(\rho \mu)_\infty} \right)^{1/2} \int_0^y \rho dy, \quad \xi = x \quad (8.12)$$

one obtains the system of ordinary differential equations

$$f = \int_0^\eta f' d\eta \quad (8.13)$$

$$\frac{\partial}{\partial \eta} \left(C \frac{\partial f'}{\partial \eta} \right) + f \frac{\partial f'}{\partial \eta} + \frac{\rho_\infty}{\rho} - f'^2 = 0 \quad (8.14)$$

$$\frac{\partial}{\partial \eta} \left(\text{Sc} \frac{\partial Z}{\partial \eta} \right) + f \frac{\partial Z}{\partial \eta} = 0 \quad (8.15)$$

in terms of the non-dimensional stream function

$$f = \frac{\rho v}{\sqrt{(\rho \mu)_\infty a}} \quad (8.16)$$

and the normalized tangential velocity

$$f' = \frac{u}{ax}. \quad (8.17)$$

Furthermore the Chapman-Rubesin parameter C and the Schmidt number Sc are defined

$$C = \frac{\rho \mu}{(\rho \mu)_\infty}, \quad \text{Sc} = \frac{\mu}{\rho D}. \quad (8.18)$$

The boundary equations are

$$\begin{aligned} \eta = +\infty : \quad & f' = 1, \quad Z = 0 \\ \eta = -\infty : \quad & f' = \sqrt{\rho_\infty / \rho_{-\infty}}, \quad Z = 1. \end{aligned} \quad (8.19)$$

An integral of the Z -equation is obtained as

$$Z = \frac{1}{2} \frac{I(\infty) - I(\eta)}{I(\infty)} \quad (8.20)$$

where the integral $I(\eta)$ is defined as

$$I(\eta) = \int_0^\eta \frac{\text{Sc}}{C} \exp \left\{ - \int_0^\eta f \text{ Sc} / C d\eta \right\} d\eta. \quad (8.21)$$

For constant properties ($\rho = \rho_\infty, C = 1$) $f = \eta$ satisfies Eq. (8.14) and

$$Z = \frac{1}{2} \operatorname{erfc}\left(\eta/\sqrt{2}\right). \quad (8.22)$$

The instantaneous scalar dissipation rate is here

$$\chi = 2D \left(\frac{\partial Z}{\partial y} \right)^2 = 2 \left(\frac{C}{Sc} \right) a \left(\frac{\partial Z}{\partial \eta} \right)^2 \quad (8.23)$$

where Eqs. (8.12) and (8.18) have been used. When the scalar dissipation rate is evaluated with the assumptions that led to Eq. (8.22) one obtains

$$\chi = \frac{a}{\pi} \exp[-\eta^2(Z)] = \frac{a}{\pi} \exp(-2[\operatorname{erfc}^{-1}(2Z)]^2) \quad (8.24)$$

where $\eta(Z)$ is obtained as inverse of Eq. (8.22). For small Z one obtains with l'Hospital's rule

$$\frac{dZ}{d\eta} = -\frac{1}{2} \frac{dI}{d\eta} \frac{1}{I(\infty)} = -\frac{dI}{d\eta} \frac{Z}{I(\infty) - I(\eta)} = -\frac{Sc}{C} f Z. \quad (8.25)$$

Therefore, in terms of the velocity gradient a the scalar dissipation rate becomes

$$\chi = 2af^2Z^2(Sc/C) \quad (8.26)$$

showing that χ increases as Z^2 for small Z .

8.3 Steady State Combustion and Quenching of Diffusion Flames with One-Step Chemistry

If the unsteady term is neglected, Eq. (8.7) is an ordinary differential equation that describes the structure of a steady state flamelet normal to the surface of stoichiometric mixture. It can be solved for general reaction rates either numerically or by asymptotic analysis. In the following we will express the chemistry by a one-step reaction with a large activation energy, assume constant pressure and the radiative heat \dot{q}_R to be negligible. We will analyze the upper branch of the S-shaped curve shown in Fig. 8.4. We will introduce an asymptotic analysis for large Damköhler numbers and large activation energies. In the limit of large Damköhler numbers which corresponds to complete combustion the chemical reaction is confined to an infinitely thin sheet around $Z = Z_{st}$.

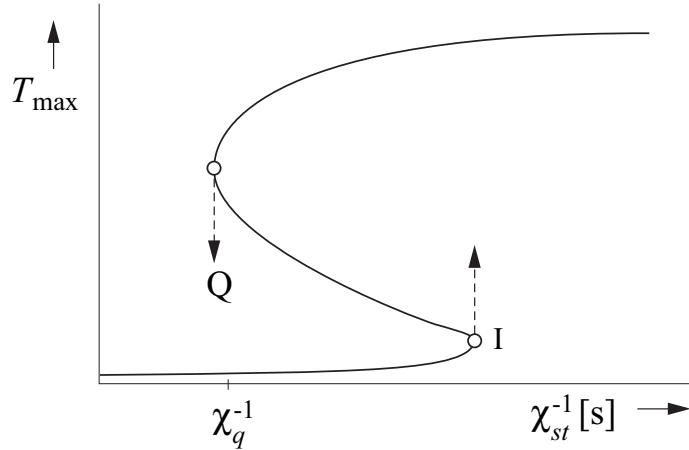


Figure 8.4: The S-shaped curve showing the maximum temperature in a diffusion flame as a function of the inverse of the scalar dissipation rate at stoichiometric mixture.

Assuming constant c_p the temperature and the fuel, oxidizer, and product mass fraction profiles are piecewise linear functions of Z . These are shown in Figs. 1.1 and 2.1. The temperature profile is given by Eq. (2.24) with Eq. (2.23). This is called the Burke-Schumann solution. The coupling relations Eq. (5.5) yield the corresponding profiles for Y_F and Y_{O_2} :

lean mixture, $Z \leq Z_{st}$:

$$T(Z) = T_u(Z) + \frac{Q Y_{F,1}}{c_p \nu'_F W_F} Z, \quad Y_F = 0, Y_{O_2} = Y_{O_2,2} \left(1 - \frac{Z}{Z_{st}} \right), \quad (8.27)$$

rich mixture, $Z \geq Z_{st}$:

$$T(Z) = T_u(Z) + \frac{Q Y_{O_2,2}}{c_p \nu'_{O_2} W_{O_2}} (1 - Z), \quad Y_{O_2} = 0, Y_F = Y_{F,1} \left(\frac{Z - Z_{st}}{1 - Z_{st}} \right), \quad (8.28)$$

where

$$T_u(Z) = T_2 + Z (T_1 - T_2). \quad (8.29)$$

The mass fractions of product species may be written similarly. We define the reaction rate as in Eq. (5.1) to show that Eq. (8.7) is able to describe diffusion flame quenching. For simplicity we will

assume $T_1 = T_2 = T_u$. Then, for one reaction with

$$\frac{Q}{c_p} = \frac{(T_{st} - T_u)\nu'_F W_F}{Y_{F,1} Z_{st}} \quad (8.30)$$

Eq. (8.7) is written as

$$\frac{d^2T}{dZ^2} = -\frac{2B\nu'_F\rho(T_{st} - T_u)}{\chi Y_{F,1} Z_{st} W_{O_2}} Y_F Y_{O_2} \exp\left(\frac{-E}{RT}\right). \quad (8.31)$$

The temperature and the fuel and oxygen mass fraction are expanded around Z_{st} as

$$\begin{aligned} T &= T_{st} - \varepsilon(T_{st} - T_u)y \\ Y_F &= Y_{F,1}\varepsilon(Z_{st}y + \xi) \\ Y_{O_2} &= Y_{O_2,2}\varepsilon((1 - Z_{st})y - \xi), \end{aligned} \quad (8.32)$$

where ε is a small parameter to be defined during the analyses. The exponential term in the reaction rate may be expanded as

$$\exp\left(\frac{-E}{RT}\right) = \exp\left(\frac{-E}{RT_{st}}\right) = \exp(-Ze\varepsilon y), \quad (8.33)$$

where the Zeldovich number is defined as

$$Ze = \frac{E(T_{st} - T_u)}{RT_{st}^2} \quad (8.34)$$

If all other quantities in Eq. (8.31) are expanded around their value at the stoichiometric flame temperature one obtains

$$\frac{d^2y}{d\xi^2} = 2Da\varepsilon^3 (Z_{st}y + \xi)((1 - Z_{st})y - \xi) \exp(-Ze\varepsilon y), \quad (8.35)$$

where

$$Da = \frac{B\rho_{st}\nu'_{O_2}Y_{F,1}}{\chi_{st}W_F(1 - Z_{st})} \exp\left(\frac{-E}{RT}\right) \quad (8.36)$$

is the Damköhler number. The differential equation Eq. (8.35) is cast into the same form as the one that governs Linn's diffusion flame regime [2] by using the further transformation

$$\begin{aligned} z &= 2y(1 - Z_{st})Z_{st} - \gamma\xi \\ \gamma &= 2Z_{st} - 1 \\ \beta &= Ze/[2Z_{st}(1 - Z_{st})] \end{aligned} \quad (8.37)$$

to yield

$$\frac{d^2z}{d\xi^2} = Da\varepsilon^3(z^2 - \xi^2) \exp[-\beta\varepsilon(z + \gamma\xi)]. \quad (8.38)$$

There are evidently two ways to define the expansion parameter ε , either by setting $\beta\varepsilon = 1$ or by setting $Da\varepsilon^3 = 1$. The first one would be called a large activation energy expansion and the second one a large Damköhler number expansion. Both formulations are interrelated if we introduce the distinguished limit where the rescaled Damköhler number

$$\delta = Da/\beta^3 \quad (8.39)$$

is assumed to be of order one. Thus a definite relation between the Damköhler number and the activation energy is assumed as ε goes to zero. We set

$$\varepsilon = Da^{-1/3} = \delta^{-1/3}/\beta \quad (8.40)$$

to obtain Liñán's equation for the diffusion flame regime

$$\frac{d^2z}{d\xi^2} = (z^2 - \xi^2) \exp[-\delta^{-1/3}(z + \gamma\xi)]. \quad (8.41)$$

The boundary conditions are obtained by matching to the outer flow solution

$$\begin{aligned} \frac{dz}{d\xi} &= 1 && \text{for } \xi \rightarrow \infty, \\ \frac{dz}{d\xi} &= -1 && \text{for } \xi \rightarrow -\infty. \end{aligned} \quad (8.42)$$

The essential property of this equation, as compared to the large Damköhler number limit ($\delta \rightarrow \infty$) is that the exponential term remains, since δ was assumed to be finite. This allows extinction to occur if the parameter δ decreases below a critical value δ_q . Liñán gives an approximation of δ_q

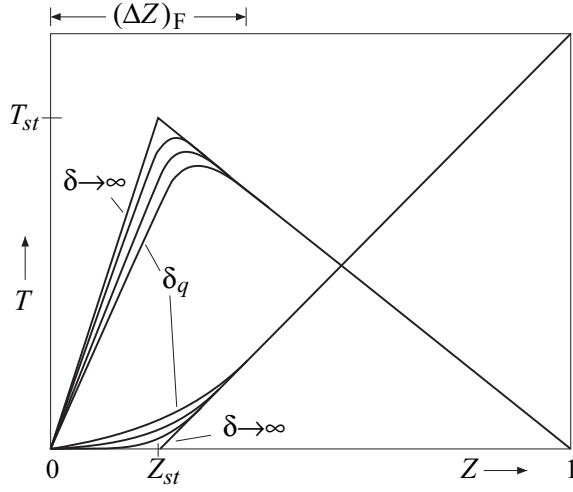


Figure 8.5: Temperature and fuel mass fraction profiles over mixture fraction for diffusion flamelet at increasing Damköhler numbers.

in terms of $|\gamma|$. For small values of Z_{st} extinction occurs at the transition to the premixed-flame regime [2]. He obtains

$$\delta_q = e(1 - |\gamma|). \quad (8.43)$$

Characteristic profiles for the temperature over Z are schematically shown in Fig. 8.5 with δ as a parameter. There is a limiting profile $T_q(Z)$ corresponding to δ_q . Any solution below this profile is unstable, and the flamelet would be extinguished. The extinction condition $\delta = \delta_q$ defines with Eqs. (8.39) and (8.36) a maximum dissipation rate χ_q at the surface of stoichiometric mixture for a flamelet to be burning, namely

$$\chi_q = \frac{8B\rho_{st}\nu'_{O_2}Y_{F,1}Z_{st}^3(1-Z_{st})^2}{W_F\delta_q Ze^3} \exp\left(\frac{-E}{RT_{st}}\right). \quad (8.44)$$

We may interpret χ_{st} as the inverse of a characteristic diffusion time. If χ_{st} is large, heat will be conducted to both sides of the flamelet at a rate that is not balanced by the heat production due to chemical reaction. Thus the maximum temperature will decrease until the flamelet is quenched at a value of $\chi_{st} = \chi_q$. This is shown in Fig. 8.4. Burning of the flamelet corresponds to the upper branch of the S-shaped curve. If χ_{st} is increased, the curve is traversed to the left until χ_q is reached, beyond which value only the lower, nonreacting branch exists. Thus at $\chi_{st} = \chi_q$ the quenching of the diffusion flamelet occurs. The transition from the point Q to the lower state

corresponds to the unsteady transition. Auto-ignition, which would correspond to an unsteady transition from the point I to the upper curve, is unlikely to occur in open diffusion flames, since the required very large residence times (very small values of χ_{st}) are not reached. An example for auto-ignition in non-premixed systems is the combustion in a Diesel engine. Here interdiffusion of the fuel from the Diesel spray with the surrounding hot air leads to continuously decreasing mixture fraction gradients and therefore to decreasing scalar dissipation rates. This corresponds to a shift on the lower branch of the S-shaped curve up to the point I where ignition occurs.

8.4 Time and Length Scales in Diffusion Flames

We will define the chemical time scale at extinction as

$$t_c = Z_{st}^2 (1 - Z_{st})^2 / \chi_q. \quad (8.45)$$

This definition is motivated by expression Eq. (8.44) for χ_q . By comparing this with the time scale of a premixed flame with the same chemical source term one obtains

$$t_c = \frac{\delta_q (\rho \lambda / c_p)_{st}}{2(\rho_u s_L)_{st}^2}, \quad (8.46)$$

where $\rho_u s_L$ has been calculated using Eqs. (5.17) and (5.18) for a stoichiometric premixed flame. This indicates that there is a fundamental relation between a premixed flame and a diffusion flame at extinction: In a diffusion flame at extinction the heat conduction out of the reaction zone towards the lean and the rich side just balances the heat generation by the reaction. In a premixed flame the heat conduction towards the unburnt mixture is such that it balances the heat generation by the reaction for a particular burning velocity. These two processes are equivalent. A diffusion flame, however, can exist at lower scalar dissipation rates and therefore at lower characteristic flow times. The flow time in a premixed flow is fixed by the burning velocity, which is an eigenvalue of the problem. Therefore combustion in diffusion flame offers an additional degree of freedom: that of choosing the ratio of the convective to the reactive time, represented by the Damköhler number defined in Eq. (8.36) as long as χ_{st} is smaller than χ_q . This makes non-premixed combustion to be better controllable and diffusion flames more stable. It is also one of the reasons why combustion in Diesel engines which operate in the non-premixed regime is more robust and less fuel quality dependent than that in spark ignition engines where fuel and air are premixed before ignition.

Eqs. (8.45) and (8.24) may now be used to calculate chemical time scales for diffusion flames. The inverse complementary error function $\text{erfc}^{-1}(2Z_{st})$ is 1.13 for methane-air flames with $Z_{st} = 0.055$ and 1.34 for H₂-air flames with $Z_{st} = 0.0284$. Extinction of the H₂-air diffusion flame occurs at a strain rate $a_q = 14260/\text{s}$ and that of the CH₄-air flame at 420/s. This leads to $t_c = 0.64 \cdot 10^{-5}\text{s}$ for hydrogen-air/diffusion flames and to $t_c = 0.29 \cdot 10^{-3}\text{s}$ for methane-air/diffusion flames. The latter estimate is of the same order of magnitude as t_c for stoichiometric premixed methane flames.

In diffusion flames, in contrast to premixed flames, there is no velocity scale, such as the burning velocity, by which a characteristic length scale such as the premixed flame thickness ℓ_F could be defined. There is, however, the velocity gradient a , the inverse of which may be interpreted as a flow time.

Based on this flow time one may define an appropriate diffusive length scale. Dimensional analysis leads to a diffusive flame thickness

$$\ell_F = \sqrt{\frac{D_{\text{ref}}}{a}}. \quad (8.47)$$

Here the diffusion coefficient D should be evaluated at a suitable reference condition, conveniently chosen at stoichiometric mixture. Assuming a one-dimensional mixture fraction profile in y -direction as for the insteady mixing layer the flame thickness in mixture fraction space may be defined

$$(\Delta Z)_F = \left(\frac{\partial Z}{\partial y} \right)_F \ell_F. \quad (8.48)$$

Here $(\partial Z / \partial y)_F$ is the mixture fraction gradient normal to the flamelet. This flamelet thickness contains the reaction zone and the surrounding diffusive layers. Eq. (8.48) leads with Eqs. (8.47) and (8.8) to

$$(\Delta Z)_F = \sqrt{\frac{\chi_{\text{ref}}}{2a}}, \quad (8.49)$$

where χ_{ref} represents the scalar dissipation rate at the reference condition. If χ_{ref} is evaluated at Z_{st} and Eq. (8.26) is used, it is seen that $(\Delta Z)_F$ is of the order of Z_{st} , if Z_{st} is small. With an estimate $(\Delta Z)_F = 2Z_{st}$ the flame thickness would cover the reaction zone and the surrounding diffusive layers in a plot of the flamelet structure in mixture fraction space.

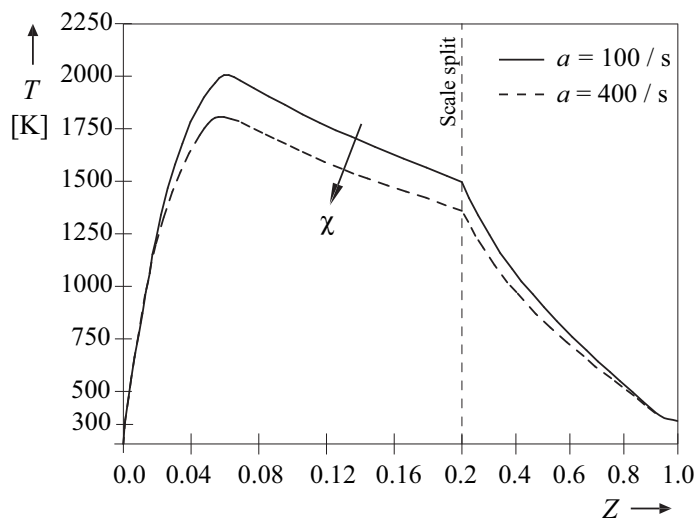


Figure 8.6: Temperature profiles of methane-air diffusion flames for $a = 100/\text{s}$ and $a = 400/\text{s}$ as a function of mixture fraction.

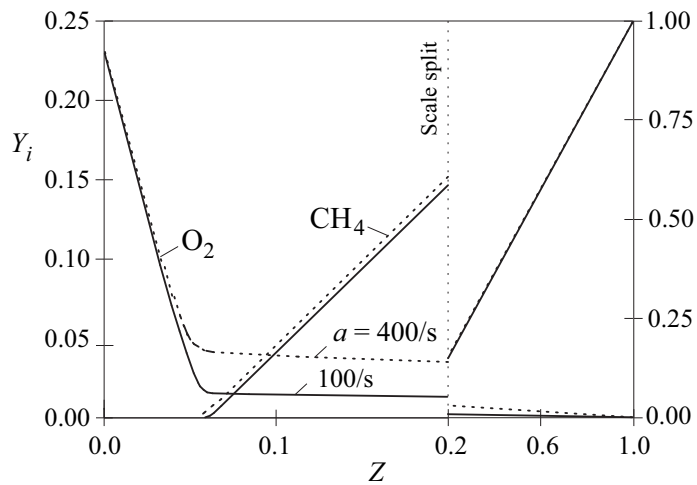
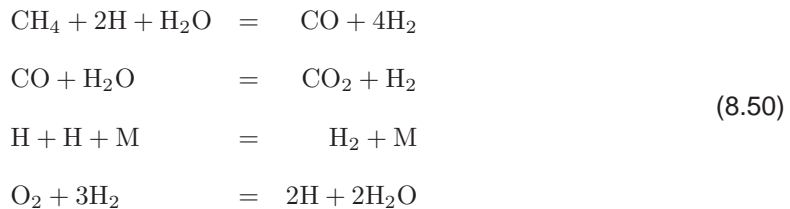


Figure 8.7: Fuel and oxygen mass fractions for $a = 100/\text{s}$ and $a = 400/\text{s}$ as a function of mixture fraction.

8.5 Diffusion Flame Structure of Methane-Air Flames

The one-step model with a large activation energy is able to predict important features such as extinction, but for small values of Z_{st} it predicts the leakage of fuel through the reaction zone. This was schematically shown in Fig. 8.5. Experiments of methane flames, on the contrary, show leakage of oxygen rather than of fuel through the reaction zone. A numerical calculation with the four-step reduced mechanism



has been performed [3] for the counter-flow diffusion flame in the stagnation region of a porous cylinder. This flow configuration, initially used by Tsuji and Yamaoka [4], will be presented in the next lecture 9 in Fig. 9.1.

Temperature and fuel and oxygen mass fractions profiles are plotted in Figs. 8.6 and 8.7 for the strain rates of $a = 100/\text{s}$ and $a = 400/\text{s}$ as a function of mixture fraction. The second value of the strain rate corresponds to a condition close to extinction. It is seen that the temperature in the reaction zone decreases and the oxygen leakage increases as extinction is approached. An asymptotic analysis [5] based on the four-step model shows a close correspondence between the different layers identified in the premixed methane flame in Lecture 6 and those in the diffusion flame. The structure obtained from the asymptotic analysis is schematically shown in Fig. 8.8. The outer structure of the diffusion flame is the classical Burke-Schumann structure governed by the overall one-step reaction $\text{CH}_4 + 2\text{O}_2 \rightarrow \text{CO}_2 + 2\text{H}_2\text{O}$, with the flame sheet positioned at $Z = Z_{st}$. The inner structure consists of a thin $\text{H}_2 - \text{CO}$ oxidation layer of thickness $\mathcal{O}(\varepsilon)$ toward the lean side and a thin inner layer of thickness $\mathcal{O}(\delta)$ slightly toward the rich side of $Z = Z_{st}$. Beyond this layer the rich side is chemically inert because all radicals are consumed by the fuel. The comparison of the diffusion flame structure with that of a premixed flame shows that the rich part of the diffusion flame corresponds to the upstream preheat zone of the premixed flame while its lean part corresponds to the downstream oxidation layer. The maximum temperature which corresponds to the inner layer temperature of the asymptotic structure, is shown in Fig. 8.9 as a function of the inverse of the scalar dissipation rate. This plot corresponds to the upper branch

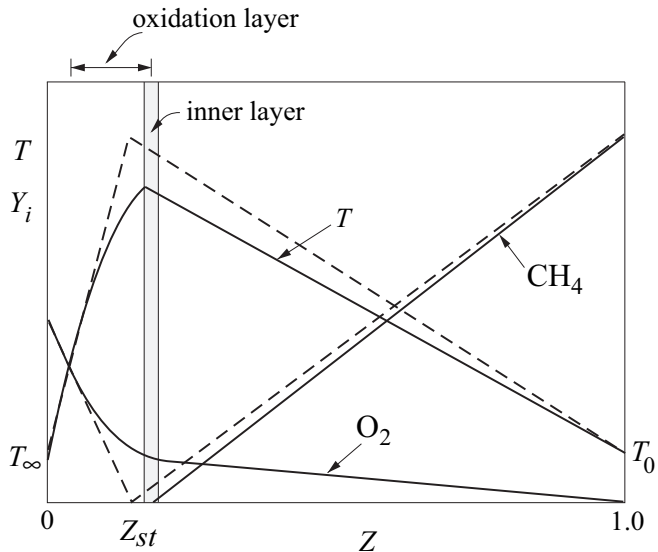


Figure 8.8: Illustration of the asymptotic structure of the methane-air diffusion flame based on the reduced four-step mechanism [5]. The dotted line is the Burke-Schumann solution.

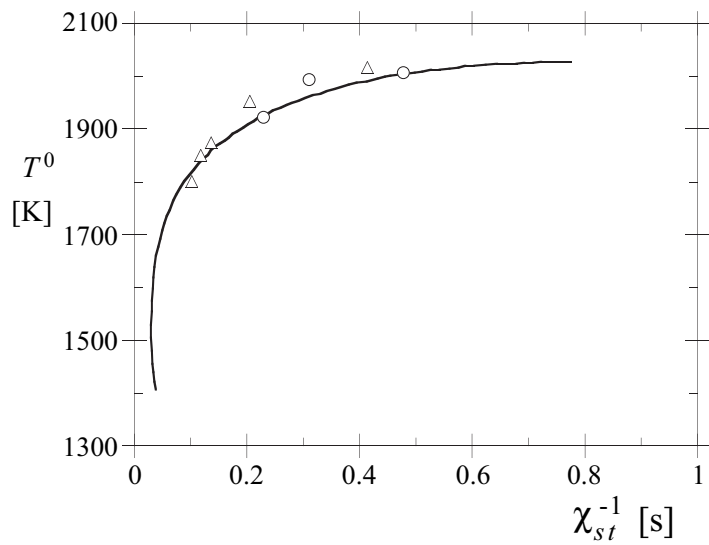


Figure 8.9: Inner flame temperature T^0 plotted as a function of χ_{st}^{-1} : \triangle numerical calculations using the four-step mechanism [3]; \circ experimental data quoted in [5].

of the S-shaped curve shown in Fig. 8.4. The calculations agree well with numerical [3] and experimental [6] data and also show the vertical slope of T^0 versus χ_{st}^{-1} which corresponds to extinction.

Bibliography

- [1] N. Peters. *Progress in Energy and Combustion Science*, 10:319–339, 1984.
- [2] A. Liñán. *Acta Astronautica*, 1:1007, 1974.
- [3] N. Peters and R. J. Kee. *Combustion and Flame*, 68:17–29, 1987.
- [4] H. Tsuji and I. Yamaoka. *13th Symposium (International) on Combustion, The Combustion Institute, Pittsburgh*, page 723, 1971.
- [5] K. Seshadri and N. Peters. *Combustion and Flame*, 73:23–44, 1988.
- [6] M. D. Smooke, I. K. Puri, and K. Seshadri. *21th Symposium (International) on Combustion, The Combustion Institute, Pittsburgh*, pages 1783–1792, 1986.

Lecture 9

Laminar Diffusion Flame Configurations:

Different Flame Geometries and Single Droplet Burning

In this lecture we want to present solutions for the velocities and the mixture fraction fields for some typical laminar flame configurations. Based on the assumption of fast chemistry we will then be able to calculate the flame contour defined by the condition $Z(x, t) = Z_{st}$. We will for simplicity always assume the Lewis number to be equal to unity and the heat capacity to be constant. The first case to be considered is the flame stagnation point boundary layer, which is similar to the counterflow flow of the previous lecture but with different boundary conditions. We then will investigate a laminar plane jet diffusion flame and determine its flame length. The third example will include the effect of buoyancy in a vertical plane diffusion flame. Finally we will also calculate the combustion of a single droplet surrounded by a diffusion flame.

9.1 Diffusion Flames in a Stagnation Point Boundary Layer: The Tsuji Flame

Let us consider the flame configuration shown in Fig. 9.1. Gaseous fuel from a sinter metal tube is injected into the surrounding air which flows vertically upwards. Below the tube a stagnation point is formed. This burner is known as the Tsuji burner [1]. If the Reynolds number based on the cylinder radius and the free stream velocity is large, the flow field may be split into an inviscid outer

flow and a boundary layer close to the surface. The potential flow solution for the flow around a cylinder then yields the velocity gradient at the stagnation point

$$a = \frac{2v_\infty}{R}, \quad (9.1)$$

where v_∞ is the velocity very far from the cylinder. The free-stream velocities at the edge of the boundary layer are

$$u_e = ax, \quad v_e = -ay. \quad (9.2)$$

If the kinematic viscosity is small, the boundary layer thickness δ is proportional to the viscous length

$$l_\nu = \sqrt{\frac{\nu_e}{a}}, \quad (9.3)$$

where ν_e is the kinematic viscosity at the edge of the boundary layer. In case the boundary layer thickness is thin compared to the cylinder radius the curvature of the cylinder surface may be neglected and the boundary may be treated as two-dimensional allowing the usage of a Cartesian coordinate system. The equations describing the boundary layer flow are the

continuity

$$\frac{\partial(\rho u)}{\partial x} + \frac{\partial(\rho u)}{\partial y} = 0, \quad (9.4)$$

momentum

$$\rho u \frac{\partial u}{\partial x} + \rho v \frac{\partial u}{\partial y} = -\frac{dp}{dx} \Big|_e + \frac{\partial}{\partial y} \left(\rho \nu \frac{\partial u}{\partial y} \right), \quad (9.5)$$

mixture fraction

$$\rho u \frac{\partial Z}{\partial x} + \rho v \frac{\partial Z}{\partial y} = \frac{\partial}{\partial y} \left(\rho D \frac{\partial Z}{\partial y} \right). \quad (9.6)$$

The pressure gradient at the boundary layer edge is obtained from Bernoulli's equation

$$\rho_e u_e \frac{du_e}{dx} = -\frac{dp}{dx} \Big|_e = \rho_e a^2 x. \quad (9.7)$$

The boundary conditions are

$$u = 0, \quad \dot{m}_w = (\rho v)_w, \quad (\rho D)_w \frac{\partial Z}{\partial y} \Big|_w = m_w(Z_w - 1) \quad \text{at} \quad y = 0, \quad (9.8)$$

and

$$u = ax, \quad Z = 0 \quad \text{at} \quad y \rightarrow \infty. \quad (9.9)$$

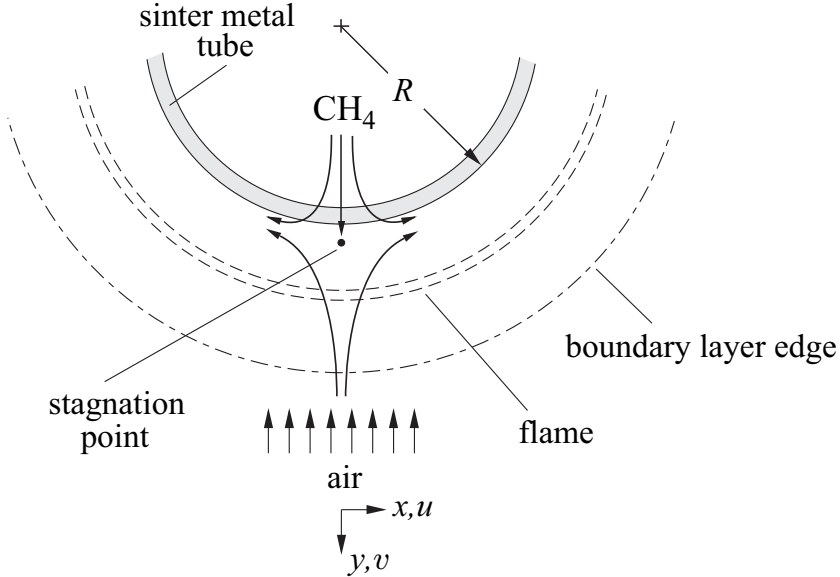


Figure 9.1: Schematic diagram of a stagnation point diffusion flame in front of a porous cylinder.

Here $u = 0$ is the symmetry condition at the surface. The mass flow rate \dot{m}_w of fuel issuing through the porous metal into the boundary layer is imposed. The boundary condition for the mixture fraction equation represents the integrated mixture fraction balance at the surface of the porous metal by assuming that the mixture fraction gradient within the metal is zero. The continuity equation is satisfied by introducing the stream function ψ such that

$$\rho u = \frac{\partial \psi}{\partial y}, \quad \rho v = -\frac{\partial \psi}{\partial x}. \quad (9.10)$$

Introducing the similarity variable

$$\eta = \left(\frac{a}{\nu_e}\right)^{1/2} \int_0^y \frac{\rho}{\rho_e} dy \quad (9.11)$$

a non-dimensional stream function $f(\eta)$, that depends on the similarity variable η only, is then defined as

$$f(\eta) = \frac{\psi}{\rho_e x \sqrt{a \nu_e}}, \quad (9.12)$$

such that the velocities are

$$u = ax \frac{\partial f}{\partial \eta}, \quad v = -\frac{\rho_e}{\rho} (a \nu_e)^{1/2} f(\eta). \quad (9.13)$$

One obtains the similarity equations

$$\begin{aligned}-f \frac{d^2 f}{d\eta^2} &= \left[\frac{\rho_e}{\rho} - \left(\frac{df}{d\eta} \right)^2 \right] \frac{d}{d\eta} \left(C \frac{d^2 f}{d\eta^2} \right) \\ -f \frac{dZ}{d\eta} &= \frac{d}{d\eta} \left(\frac{C}{Sc} \frac{dZ}{d\eta} \right).\end{aligned}\quad (9.14)$$

Here $Sc = \nu/D$ is the Schmidt number and C is the Chapman-Rubesin parameter

$$C = \frac{\rho^2 \nu}{\rho_e^2 \nu_e}. \quad (9.15)$$

Since ν changes with temperature as $T^{1.7}$ and ρ as T^1 , this quantity changes less than the viscosity itself in a flow with strong heat release. The boundary conditions for the similar solution are

$$f_w = -\frac{(\rho\nu)_w}{(\rho_e^2 a \nu_e)^{1/2}}, \quad f' = 0, \quad \left. \frac{C}{Sc} \frac{dZ}{d\eta} \right|_w = f_w(1-Z) \quad \text{at} \quad \eta = 0 \quad (9.16)$$

$$f'(\infty) = 1 \quad \text{for} \quad \eta \rightarrow \infty. \quad (9.17)$$

The mixture fraction equation may be transformed into

$$\frac{d}{d\eta} \left[\ln \left(\frac{C}{Sc} \frac{dZ}{d\eta} \right) \right] = -\frac{f Sc}{C} \quad (9.18)$$

which can formally be solved as

$$Z = f_w \frac{I(\eta) - I(\infty)}{1 - f_w I(\infty)}, \quad (9.19)$$

where

$$I(\eta) = \int_0^\eta \frac{Sc}{C} \exp \left(- \int_0^\eta \frac{f Sc}{C} d\eta \right) d\eta. \quad (9.20)$$

The mixture fraction at the surface is given by

$$Z_w = \frac{-f_w I(\infty)}{1 - f_w I(\infty)}. \quad (9.21)$$

This indicates that the mixture fraction varies between $Z = 0$ and $Z = Z_w$ rather than between 0 and 1. The boundary condition for the fuel and oxidizer fractions satisfy the Burke-Schumann solution at Z_w , as may easily be shown. The boundary condition for the temperature at the surface is to be imposed at $Z = Z_w$.

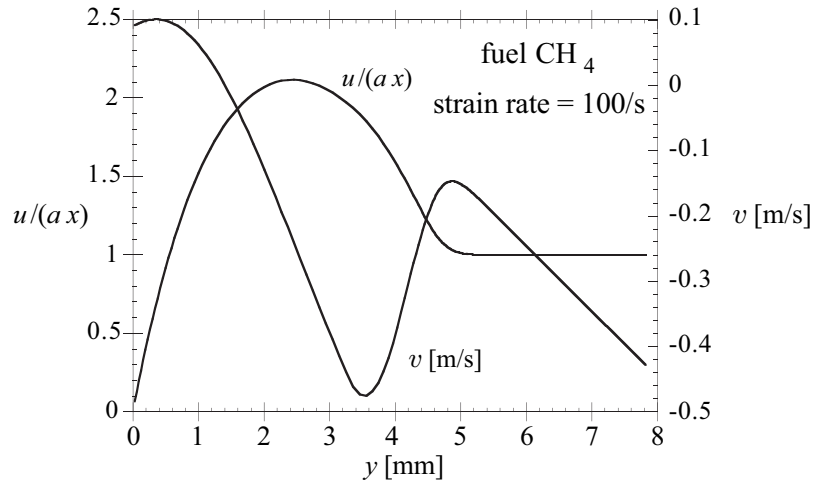


Figure 9.2: Velocity profiles for the Tsuji geometry.

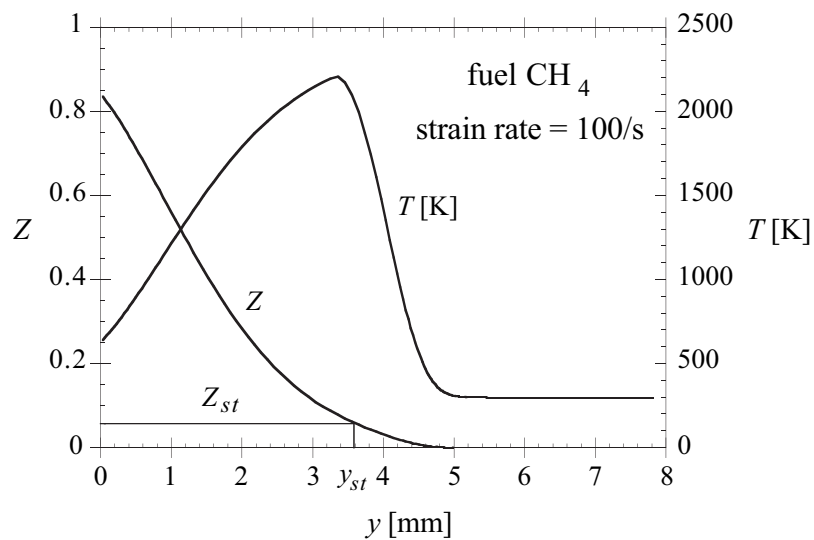


Figure 9.3: Mixture fraction and temperature profiles for the Tsuji geometry.

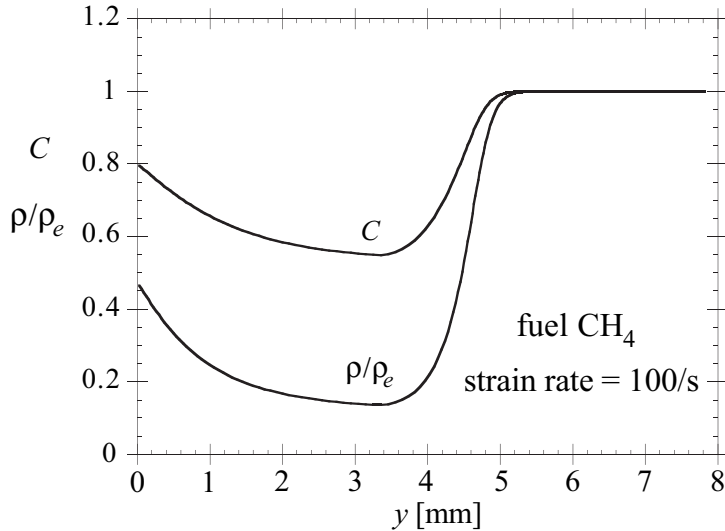


Figure 9.4: Chapman-Rubesin parameter and temperature profiles for the Tsuji geometry.

If the mass flow rate at the surface is increased and f_w takes large negative values, the mixture fraction at the surface tends towards unity. This is the limit of a counter-flow diffusion flame detached from the surface. Eqs. (9.14) have been solved numerically using the Burke-Schumann solution for combustion of methane in air Eqs. (2.24), (2.25) with $Z_{st} = 0.055$, $T_u = 300\text{ K}$, and $T_{st} = 2263\text{ K}$. The profiles of $u = ax$, v , T , Z , $\rho = \rho_e$, and C are shown in Figs. 9.2, 9.3 and 9.4.

9.2 The Round Laminar Diffusion Flame

In many applications fuel enters into the combustion chamber as a round jet, either laminar or turbulent. To provide an understanding of the basic properties of jet diffusion flames, we will consider here the easiest case, the laminar axisymmetric jet flame without buoyancy, for which we can obtain approximate analytical solutions. This will enable us to determine, for instance, the flame length. The flame length is defined as the distance from the nozzle to the point on the centerline of the flame where the mixture fraction is equal to Z_{st} . The flow configuration and the flame contour of a vertical jet diffusion flame are shown schematically in Fig. 9.5.

We consider a fuel jet issuing from a nozzle with diameter d and exit velocity u_0 into quiescent air. The indices 0 and ∞ denote conditions at the nozzle and in the ambient air, respectively. Using

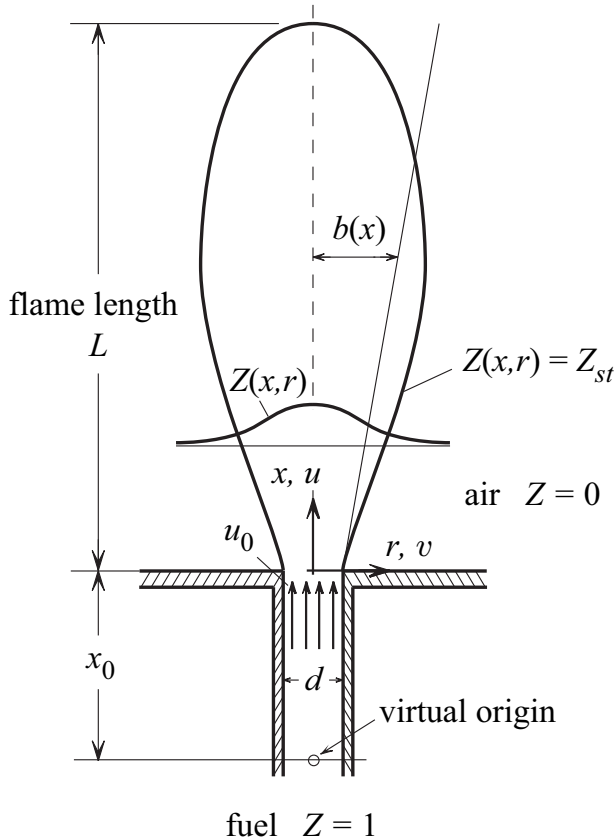


Figure 9.5: Schematic representation of a vertical laminar jet flame into quiescent air.

the boundary layer assumption with constant pressure we obtain a system of two-dimensional axisymmetric equations, in terms of the axial coordinate x and the radial coordinate r :

continuity

$$\frac{\partial(\rho ur)}{\partial x} + \frac{\partial(\rho vr)}{\partial r} = 0, \quad (9.22)$$

momentum in x direction

$$\rho ur \frac{\partial u}{\partial x} + \rho vr \frac{\partial u}{\partial r} = \frac{\partial}{\partial r} \left(\mu r \frac{\partial u}{\partial r} \right), \quad (9.23)$$

mixture fraction

$$\rho u r \frac{\partial Z}{\partial x} + \rho v r \frac{\partial Z}{\partial r} = \frac{\partial}{\partial r} \left(\frac{\mu}{Sc} r \frac{\partial Z}{\partial r} \right) \quad (9.24)$$

scalar flux we have replaced D by introducing the Schmidt number $Sc = \nu/D$. The dimensionality of the problem may be reduced by introducing the similarity transformation

$$\eta = \frac{\bar{r}}{\xi}, \quad \bar{r}^2 = 2 \int_0^r \frac{\rho}{\rho_\infty} r dr, \quad \xi = x + x_0, \quad (9.25)$$

which contains a density transformation defining the density weighted radial coordinate \bar{r} . The new axial coordinate ξ starts from the virtual origin of the jet located at $x = -x_0$. Introducing a stream function ψ by

$$\rho u r = \frac{\partial \psi}{\partial r}, \quad \rho v r = -\frac{\partial \psi}{\partial x} \quad (9.26)$$

we can satisfy the continuity equation. The convective terms in the momentum equation and in the equation for the mixture fraction may be expressed using the transformation rules

$$\frac{\partial}{\partial x} = \frac{\partial}{\partial \xi} + \frac{\partial \eta}{\partial x} \frac{\partial}{\partial \eta}, \quad \frac{\partial}{\partial r} = \frac{\partial \eta}{\partial r} \frac{\partial}{\partial \eta} \quad (9.27)$$

which leads to

$$\rho u r \frac{\partial}{\partial x} + \rho v r \frac{\partial}{\partial r} = \frac{\partial \eta}{\partial r} \left(\frac{\partial \psi}{\partial \eta} \frac{\partial}{\partial \xi} - \frac{\partial \psi}{\partial \xi} \frac{\partial}{\partial \eta} \right). \quad (9.28)$$

For the diffusive terms one obtains

$$\frac{\partial}{\partial r} \left(\mu r \frac{\partial}{\partial r} \right) = \mu_\infty \frac{\partial \eta}{\partial r} \frac{\partial}{\partial \eta} \left(C \eta \frac{\partial}{\partial \eta} \right). \quad (9.29)$$

Here the Chapman-Rubesin-parameter

$$C = \frac{\rho \mu r^2}{2 \mu_\infty \int_0^r \rho r dr} \quad (9.30)$$

was introduced. For constant density with $\mu = \mu_\infty$ one obtains $C = 1$. The axial and radial velocity components may now be expressed in terms of the nondimensional stream function $F(\xi, \eta)$ defined by

$$\psi = \mu_\infty \xi F(\xi, \eta) \quad (9.31)$$

as

$$u = \frac{\partial F}{\partial \eta} \frac{\mu_\infty}{\rho_\infty \xi}, \quad \rho v r = -\mu_\infty (\xi \frac{\partial F}{\partial \xi} + F - \frac{\partial F}{\partial \eta} \eta). \quad (9.32)$$

For the mixture fraction the ansatz

$$Z = Z_{CL}(\xi) \omega(\eta) \quad (9.33)$$

is introduced, where Z_{CL} stands for the mixture fraction on the centerline.

For a jet into still air a similarity solution exists if the nondimensional stream function F and Chapman Rubesin parameter C are no function of ξ . Introducing Eqs. (9.25)-(9.33) into Eqs. (9.22)-(9.24) one obtains the ordinary differential equations, valid in the similarity region of the jet:

$$\begin{aligned} -\frac{d}{d\eta} \left(\frac{F}{\eta} \frac{dF}{d\eta} \right) &= \frac{d}{d\eta} \left(C \eta \frac{d}{d\eta} \left(\frac{1}{\eta} \frac{dF}{d\eta} \right) \right) \\ -\frac{d}{d\eta} (F \omega) &= \frac{d}{d\eta} \left(\frac{C}{Sc} \eta \frac{d\omega}{d\eta} \right). \end{aligned} \quad (9.34)$$

To derive an analytical solution we must assume that C is a constant in the entire jet. With a constant value of C one obtains from Eq. (9.34) the solutions

$$F(\eta) = \frac{C(\gamma\eta)^2}{1 + (\gamma\eta/2)^2}, \quad \omega(\eta) = \left(\frac{1}{1 + (\gamma\eta/2)^2} \right)^{2Sc}. \quad (9.35)$$

The axial velocity profile then is obtained from Eq. (9.32) as

$$u = \frac{2C\gamma^2\nu}{\xi} \left(\frac{1}{1 + (\gamma\eta/2)^2} \right)^2, \quad (9.36)$$

where the jet spreading parameter

$$\gamma^2 = \frac{3 \cdot Re^2}{64} \frac{\rho_0}{\rho_\infty C^2} \quad (9.37)$$

is obtained from the requirement of integral momentum conservation along the axial direction:

$$\int_0^\infty \rho u^2 r dr = \rho_0 u_0^2 d^2 / 8 \quad (9.38)$$

Here ρ_0 is the density of the fuel and $Re = \rho_\infty u_0 d / \mu_\infty$ is the Reynolds number. Similarly, conservation of the mixture fraction integral across the jet yields the mixture fraction on the centerline

$$Z_{CL} = \frac{Re(1 + 2Sc)}{32} \frac{\rho_0}{\rho_\infty C} \frac{d}{\xi} \quad (9.39)$$

such that the mixture fraction profile is given by

$$Z = \frac{(1 + 2Sc)d}{\xi} \frac{\text{Re}}{32} \frac{\rho_0}{\rho_\infty C} \left(\frac{1}{1 + (\gamma\eta/2)^2} \right)^{2Sc}. \quad (9.40)$$

From this equation the flame length L can be calculated by setting $Z = Z_{st}$ at $x = L, r = 0$:

$$\frac{L + x_0}{d} = \frac{(1 + 2Sc)}{32 \cdot Z_{st}} \frac{\rho_0}{\rho_\infty C} \frac{u_0 d}{\nu} \quad (9.41)$$

This shows that the flame length of a laminar round jet increases linearly with increasing exit velocity u_0 .

9.3 Single Droplet Combustion

In many practical applications liquid fuel is injected into the combustion chamber resulting in a fuel spray. By the combined action of aerodynamical shear, strain, and surface tension the liquid spray will decompose into a large number of single droplets of different diameters. The fuel will then evaporate and a non-homogeneous fuel air mixture will be formed in the flow field surrounding the droplets. When the spray is ignited, the droplets will burn either as a cloud surrounded by a enveloping flame or as single droplets, each being surrounded by its own diffusion flame. The former will be the case if the fuel air mixture between different droplets is fuel rich such that the surface of stoichiometric mixture will surround the droplet cloud. We will consider here the latter case, where the surface of stoichiometric mixture surrounds the single droplet. We will furthermore consider very small droplets which follow the flow very closely and assume that the velocity difference between the droplet and the surrounding fuel is zero. Therefore we may consider the case of a spherically symmetric droplet in a quiescent surrounding. We assume the evaporation and combustion process as quasi-steady and can therefore use the steady state equations (cf. [2])

continuity

$$\frac{d}{dr}(r^2 \rho v) = 0 \quad (9.42)$$

mixture fraction

$$\rho v \frac{dZ}{dr} = \frac{1}{r^2} \frac{d}{dr} \left(r^2 \rho D \frac{dZ}{dr} \right) \quad (9.43)$$

temperature

$$\rho v \frac{dT}{dr} = \frac{1}{r^2} \frac{d}{dr} \left(r^2 \frac{\lambda}{c_p} \frac{dT}{dr} \right) + \frac{Q}{c_p} \omega \quad (9.44)$$

In these equations r is the radial coordinate, and v is the flow velocity in radial direction. Here again a unity Lewis number leading to $\lambda = \rho c_p D$ and a one step reaction with fast chemistry will be assumed. The reaction rate ω is then a δ -function at the flame surface located at $Z = Z_{st}$. The expected temperature and mixture fraction profiles are schematically shown in Fig. 9.6. The boundary conditions for Eqs. (9.42)and (9.44) at the droplet surface $r = R$ are obtained by integrating the balance equations once in radial direction. Since temperature and concentration gradients within the droplet are assumed negligible, the convective flux through the surface equals the diffusive flux in the gas phase at the droplet surface. The convective heat flux through the boundary involves a change of enthalpy, namely the enthalpy of evaporation h_L . Therefore

$$r = R : \quad \lambda \frac{dT}{dr} \Big|_R = (\rho v)_R h_L. \quad (9.45)$$

Here $(\rho v)_R$ is the convective mass flux through the surface. The mixture fraction of the convective flux involves the difference between the mixture fraction within the droplet, which is unity by definition, and that in the gas phase at the droplet surface, where $Z = Z_R$. This leads to

$$r = R : \quad \rho D \frac{dZ}{dr} \Big|_R = (\rho v)_R (Z_R - 1). \quad (9.46)$$

The changes of temperature and mixture fraction at the surface are also shown in Fig. 9.6. The boundary conditions in the surrounding air are

$$r \rightarrow \infty : \quad T = T_2, \quad Z = 0. \quad (9.47)$$

In addition, we assume that the temperature at the droplet surface is equal to the boiling temperature of the liquid

$$T = T_L. \quad (9.48)$$

Then the temperature equation must satisfy three boundary conditions. This leads to an eigenvalue problem for the mass burning rate

$$\dot{m} = 4\pi R^2 (\rho v)_R \quad (9.49)$$

of the droplet which thereby can be determined. Integration of the continuity equation leads to

$$\rho v r^2 = R^2 (\rho v)_R \quad (9.50)$$

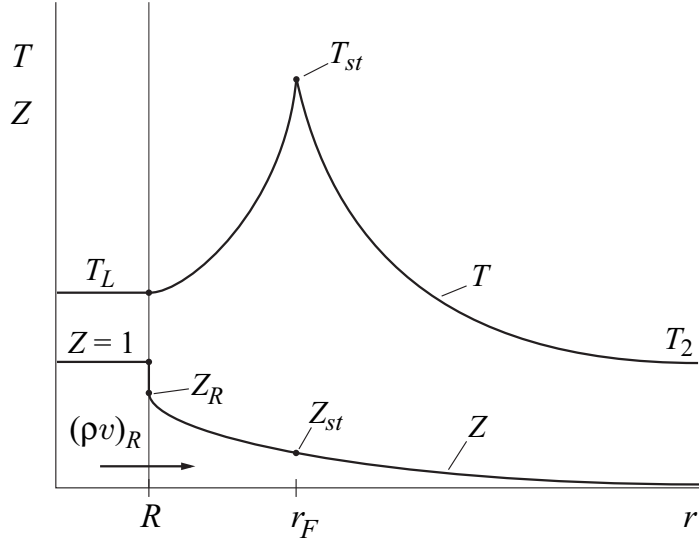


Figure 9.6: Temperature and mixture fraction profiles at the surface and in the surroundings of a burning spherical droplet.

We will now introduce the nondimensional coordinate

$$\eta = \int_r^\infty \frac{v}{D} \exp(-\zeta) dr, \quad (9.51)$$

where

$$\zeta = \int_r^\infty \frac{v}{D} dr = \frac{\dot{m}}{4\pi} \int_r^\infty (\rho D r^2)^{-1} dr. \quad (9.52)$$

Between η and ζ there is the relation

$$\frac{d\eta}{d\zeta} = \frac{d\eta/dr}{d\zeta/dr} = \exp(-\zeta). \quad (9.53)$$

This may be integrated with the boundary conditions at $r \rightarrow \infty : \zeta = 0, \eta = 0$ to yield

$$\eta = 1 - \exp(-\zeta) \quad (9.54)$$

and at $r = R$

$$\eta_R = 1 - \exp(-\zeta_R). \quad (9.55)$$

Transformation of Eqs. (9.43)and (9.44) with their boundary conditions leads to

$$\frac{d^2Z}{d\eta^2} = 0 \quad (9.56)$$

$$\eta = \eta_R : \quad (\eta_R - 1) \frac{dZ}{d\eta} = Z_R - 1 \quad (9.57)$$

$$\eta \rightarrow \infty : \quad Z = 0, \quad \rho D \left(\frac{d\eta}{dr} \right)^2 \frac{d^2T}{d\eta^2} = - \frac{Q}{c_p} \omega \quad (9.58)$$

$$\eta = \eta_R : \quad (\eta - 1) \frac{dT}{d\eta} = \frac{h_L}{c_p}, \quad T_R = T_L \quad (9.59)$$

$$\eta \rightarrow 0 : \quad T = T_2 \quad (9.60)$$

The solution of the mixture fraction equation with its boundary condition is readily seen to be

$$Z = \eta \quad (9.61)$$

If this is introduced into the temperature equation and the scalar dissipation rate for the present problem is defined as

$$\chi = 2D \left(\frac{dZ}{dr} \right)^2 = 2D \left(\frac{d\eta}{dr} \right)^2 \quad (9.62)$$

one obtains

$$\rho \frac{\chi}{2} \frac{d^2T}{dZ^2} = - \frac{Q}{c_p} \omega \quad (9.63)$$

which reducescompares to Eq. (8.7) if the steady state, negligible heat loss, and one-step chemistry was assumed. We therefore find that the one-dimensional droplet combustion problem satisfies the laminar flamelet assumptions exactly. Here we want to consider the Burke-Schumann solution Eq. (2.24). Then, in the fuel rich region between $r = R$ and $r = r_F$ (conf. Fig. 9.6) we have

$$T(Z) = T_2 + Z(T_1 - T_2) + \frac{Y_{O_2,2} Q}{c_p \nu'_{O_2} W_{O_2}} (1 - Z). \quad (9.64)$$

Here T_1 is by definition the temperature at $Z = 1$, which does not exist in the present problem. We know, however, from the boundary conditions Eq. (9.59) the slope and the value at $Z = Z_R$ where

$$T_L = T_2 + Z_R(T_1 - T_2) + \frac{Y_{\text{O}_2,2}Q}{c_p\nu'_{\text{O}_2}W_{\text{O}_2}}(1 - Z_R). \quad (9.65)$$

Introducing Eqs. (9.64) and (9.65) into Eq. (9.59) one obtains

$$T_1 = T_L - \frac{h_L}{c_p}. \quad (9.66)$$

This is a hypothetical temperature corresponding to the fuel if one considers the droplet as a point source of gaseous fuel. The heat of vaporization then decreases the temperature of the liquid fuel by the amount h_L/c_p . It should be used in flamelet calculations if one wishes to calculate flamelet profiles in the range $0 < Z < 1$ rather than $0 < Z < Z_R$. The boundary condition Eq. (9.59) may also be used with Eqs. (9.64) and (9.55) to calculate the non-dimensional mass burning rate

$$\zeta_R = \ln \left(1 + \frac{c_p(T_2 - T_L) + Y_{\text{O}_2,2}Q/\nu'_{\text{O}_2}W_{\text{O}_2}}{h_L} \right). \quad (9.67)$$

From this, the mass burning rate may be determined using Eq. (9.52). We will introduce radially averaged properties $\overline{\rho D}$ defined by

$$(\overline{\rho D})^{-1} = R \int_R^\infty \frac{dr}{\rho Dr^2} \quad (9.68)$$

to obtain

$$\dot{m} = 4\pi \overline{\rho D} R \zeta_R. \quad (9.69)$$

Now it is possible to determine the time needed to burn a droplet with initial radius R_0 at time $t = 0$. The droplet mass is $m = 4\pi\rho_L R^3/3$, where ρ_L is the density of the liquid. Its negative time rate of change equals the mass loss due to the mass burning rate

$$\frac{dm}{dt} = 4\pi\rho_L R^2 \frac{dR}{dt} = -\dot{m}. \quad (9.70)$$

Introducing Eq. (9.69) and assuming $\overline{\rho D}$ independent of time one obtains by separation of variables

$$dt = -\frac{\rho_L}{\zeta_R \overline{\rho D}} R dR, \quad t \cong R_0^2 - R^2. \quad (9.71)$$

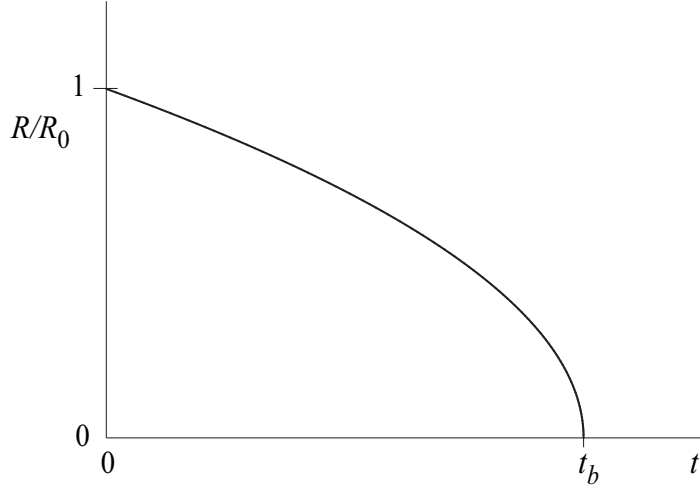


Figure 9.7: Droplet radius versus time (d^2 -Law) for single droplet combustion Eq. (9.72).

Integrating from $R = R_0$ to $R = 0$ one obtains the burnout time

$$t_b = \frac{\rho_L}{8\zeta_R \overline{\rho D}} d^2 \quad (9.72)$$

where $d = 2R_0$ is the initial droplet diameter. This is called the d^2 -law of droplet combustion and shown in Fig. 9.7. It represents a very good first approximation for the droplet combustion time and has often been confirmed by experiments.

Finally, we want to calculate the radial position of the surrounding flame. Evaluating Eq. (9.54) for $Z = Z_{st} = \eta_{st}$ one obtains

$$1 - Z_{st} = \exp(-\zeta_{st}), \quad (9.73)$$

where with Eqs. (9.50) and (9.52)

$$\zeta_{st} = \frac{\dot{m}}{4\pi \overline{\rho D} r_{st}}. \quad (9.74)$$

Here $\overline{\rho D}$ is defined as in Eq. (9.68) but averaging by an integration from r_{st} to ∞ rather than from R to ∞ . If both are assumed equal one may use Eq. (9.69) to determine the flame radius as

$$\frac{r_{st}}{R} = \frac{\zeta_R}{-\ln(1 - Z_{st})}. \quad (9.75)$$

For sufficiently small values of Z_{st} the denominator of Eq. (9.75) may be approximated by Z_{st} itself showing that ratio r_{st}/R may take quite large values.

Exercise 9.1

Determine the non-dimensional mass burning rate and r_{st}/R for a Diesel fuel where $h_L/c_p = 160 \text{ K}$, $T_L = 560 \text{ K}$, $T_2 = 800 \text{ K}$ and $T_{st} - T_u(Z_{st}) = 2000 \text{ K}$, $Z_{st} = 0.036$.

Solution

Using the Burke-Schumann solution the non-dimensional mass burning rate may be written as

$$\zeta_R = \ln \left[1 + \frac{T_2 - T_L + (T_{st} - T_u(Z_{st}))/c_p}{h_L/c_p} \right] = 2.74. \quad (9.76)$$

The ratio of the flame radius to the droplet radius is then

$$\frac{r_{st}}{R} \approx 75. \quad (9.77)$$

Exercise 9.2

Compare the evaporation rate for the same droplet as in problem Fig. 9.1 to that of the mass burning rate.

Solution

The non-dimensional evaporation rate of a droplet may be obtained in a similar way as Eq. (9.67). It follows from Eq. (9.67) in the limit $Q = 0$, therefore

$$\zeta_R = \ln \left(1 + \frac{T_2 - T_L}{h_L/c_p} \right) = 0.916 \quad (9.78)$$

The combustion rate is approximately three times faster than the evaporation rate.

Bibliography

- [1] H. Tsuji and I. Yamaoka. *13th Symposium (International) on Combustion, The Combustion Institute, Pittsburgh*, page 723, 1971.
- [2] F. A. Williams. *Combustion Theory, Second Edition*. The Benjamin Cummings Publishing Co. Menlo Park, 1985.

Lecture 10

Turbulent Combustion: The State of the Art

10.1 What is Specific about Turbulence with Combustion?

Since the flow is turbulent in nearly all engineering applications, the urgent need for resolving engineering problems has led to preliminary solutions called turbulence models. These models use systematic mathematical derivations based on the Navier-Stokes equations up to a certain point, but then they introduce closure hypotheses that rely on dimensional arguments and require empirical input. This semi-empirical nature of turbulence models puts them into the category of an art rather than a science.

The apparent success of turbulence models in solving engineering problems for non-reactive flows has encouraged similar approaches for turbulent combustion which consequently led to the formulation of turbulent combustion models. This is, however, where problems arise. Combustion requires that fuel and oxidizer are mixed at the molecular level. How this takes place in turbulent combustion depends on the turbulent mixing process. The general view is that once a range of different size eddies has developed, strain and shear at the interface between the eddies enhance the mixing. During the eddy break-up process and the formation of smaller eddies, strain and shear will increase and thereby steepen the concentration gradients at the interface between reactants, which in turn enhances their molecular interdiffusion. Molecular mixing of fuel and oxidizer, as a prerequisite of combustion, therefore takes place at the interface between small eddies.

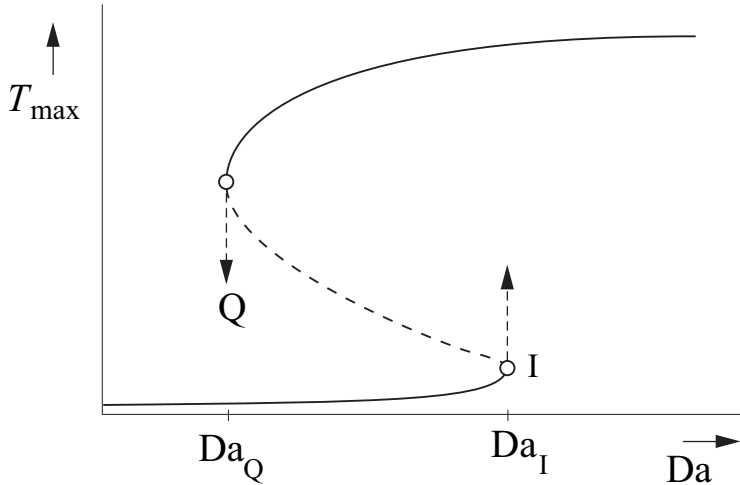


Figure 10.1: The S-shaped curve showing the maximum temperature in a well-stirred reactor as a function of the Damköhler number.

There remains, however, the question to what extend we can expect an interaction between chemical and turbulent scales. Here, we must realize that combustion differs from isothermal mixing in chemically reacting flows by two specific features:

- heat release by combustion induces an increase of temperature which in turn
- accelerates combustion chemistry. Due to the competition between chain branching and chain breaking reactions this process is very sensitive to temperature changes.

Heat release combined with temperature sensitive chemistry leads to typical combustion phenomena like ignition and extinction. This is illustrated in Fig. 10.1 where the maximum temperature in a homogeneous flow combustor is plotted as a function of the Damköhler number, which here represents the ratio of the residence time to the chemical time. This is called the S-shaped curve in the combustion literature. The lower branch of this curve corresponds to a slowly reacting state of the combustor prior to ignition, where the short residence times prevent a thermal runaway. If the residence time is increased by lowering the flow velocity, for example, the Damköhler number increases until the ignition point I is reached. For values larger than Da_I thermal runaway leads to a rapid unsteady transition to the upper close-to-equilibrium branch. If one starts on that branch and decreases the Damköhler number, thereby moving to the left in Fig. 10.1, one reaches the point Q where extinction occurs. This is equivalent to a rapid transition to the lower branch. The

middle branch between the point I and Q is unstable. In the range of Damköhler numbers between Da_Q and Da_I , where two stable branches exist, any initial state with a temperature in the range between the lower and the upper branch is rapidly driven to either one of them. Due to the temperature sensitivity of combustion reactions the two stable branches represent strong attractors. Therefore, only regions close to chemical equilibrium or close to the non-reacting state are frequently accessed.

10.2 Statistical Description of Turbulent Flows

The aim of stochastic methods in turbulence is the description of the fluctuating velocity and scalar fields in terms of their statistical distributions. A convenient starting point for this description is the distribution function of a single variable of the velocity component u , for instance. The distribution function $F_u(U)$ of u is defined by the probability p of finding a value of $u < U$

$$F_u(U) = p(u < U) \quad (10.1)$$

where U is the so-called sample space variable associated with the random stochastic variable u . The sample space of the random stochastic variable u consists of all possible realizations of u . The probability of finding a value of u in a certain interval $U_- < u < U_+$ is given by

$$p(U_- < u < U_+) = F_u(U_+) - F_u(U_-). \quad (10.2)$$

The probability density function (pdf) of u is now defined as

$$P_u(U) = \frac{dF_u(U)}{dU}. \quad (10.3)$$

It follows that $P_u(U)dU$ is the probability of finding u in the range $U \leq u < U + dU$. If the possible realizations of u range from $-\infty$ to $+\infty$, it follows that

$$\int_{-\infty}^{+\infty} P_u(U)dU = 1 \quad (10.4)$$

which states that the probability of finding the value u between $-\infty$ and $+\infty$ is certain, i.e. it has the probability unity. It also serves as a normalizing condition for P_u .

In turbulent flows the pdf of any stochastic variable depends, in principle, on the position x and

on time t . These functional dependencies are expressed by the following notation

$$P_u(U; \mathbf{x}, t). \quad (10.5)$$

The semicolon used here indicates that P_u is a probability density in U -space and a function of \mathbf{x} and t . In stationary turbulent flows it does not depend on t and in homogeneous turbulent fields not on \mathbf{x} . In the following we will, for simplicity of notation, not distinguish between the random stochastic variable u and the sample space variable U , drop the index and write the pdf as

$$P(u; \mathbf{x}, t). \quad (10.6)$$

Once the pdf of a variable is known one may define its moments by

$$\overline{u(\mathbf{x}, t)^n} = \int_{-\infty}^{+\infty} u^n P(u; \mathbf{x}, t) du. \quad (10.7)$$

Here the overbar denotes the average or mean value, sometimes also called expectation, of u^n . The first moment ($n = 1$) is called the mean of u

$$\overline{u}(\mathbf{x}, t) = \int_{-\infty}^{+\infty} u P(u; \mathbf{x}, t) du. \quad (10.8)$$

Similarly, the mean value of a function $g(u)$ can be calculated from

$$\overline{g}(\mathbf{x}, t) = \int_{-\infty}^{+\infty} g(u) P(u; \mathbf{x}, t) du. \quad (10.9)$$

For flows with large density changes as they occur in combustion, it is often convenient to introduce a density-weighted average \tilde{u} , called the Favre average, by splitting $u(\mathbf{x}, t)$ into $\tilde{u}(\mathbf{x}, t)$ and $u''(\mathbf{x}, t)$ as

$$u(\mathbf{x}, t) = \tilde{u}(\mathbf{x}, t) + u''(\mathbf{x}, t). \quad (10.10)$$

This averaging procedure is defined by requiring that the average of the product of u'' with the density ρ (rather than u'' itself) vanishes

$$\overline{\rho u''} = 0. \quad (10.11)$$

The definition for \tilde{u} may then be derived by multiplying Eq. (10.10) by the density ρ and averaging

$$\overline{\rho u} = \overline{\rho \tilde{u}} + \overline{\rho u''} = \bar{\rho} \tilde{u}. \quad (10.12)$$

Here the average of the product $\rho \tilde{u}$ is equal to the product of the averages $\bar{\rho}$ and \tilde{u} , since \tilde{u} is already an average defined by

$$\tilde{u} = \overline{\rho u} / \bar{\rho}. \quad (10.13)$$

This density-weighted average can be calculated, if simultaneous measurements of ρ and u are available. Then, by taking the average of the product ρu and dividing it by the average of ρ one obtains \tilde{u} . While such measurements are often difficult to obtain, Favre averaging has considerable advantages in simplifying the formulation of the averaged Navier-Stokes equations in variable density flows. In the momentum equations, but also in the balance equations for the temperature and the chemical species, the convective terms are dominant in high Reynolds number flows. Since these contain products of the dependent variables and the density, Favre averaging is the method of choice. For instance, the average of the product of the density ρ with the velocity components u and v would lead with conventional averages to four terms

$$\overline{\rho u v} = \bar{\rho} \overline{u} \overline{v} + \overline{\rho u' v'} + \overline{\rho' u' \overline{v}} + \overline{\rho' v' \overline{u}} + \overline{\rho' u' v'}. \quad (10.14)$$

Using Favre averages one writes

$$\begin{aligned} \rho u v &= \rho(\tilde{u} + \tilde{u}'')(\tilde{v} + \tilde{v}'') \\ &= \rho \tilde{u} \tilde{v} + \rho u'' \tilde{v} + \rho v'' \tilde{u} + \rho u'' v''. \end{aligned} \quad (10.15)$$

Here fluctuations of the density do not appear. Taking the average leads to two terms only

$$\overline{\rho u v} = \bar{\rho} \tilde{u} \tilde{v} + \widetilde{\rho u'' v''}. \quad (10.16)$$

This expression is much simpler than Eq. (10.14) and has formally the same structure as the conventional average of uv for constant density flows

$$\overline{u v} = \overline{u} \overline{v} + \overline{u' v'}. \quad (10.17)$$

Difficulties arising with Favre averaging in the viscous and diffusive transport terms are of less

importance since these terms are usually neglected in high Reynolds number turbulence.

The introduction of density weighted averages requires the knowledge of the correlation between the density and the other variable of interest. A Favre pdf of u can be derived from the joint pdf $P(\rho, u)$ as

$$\bar{\rho}\tilde{P}(u) = \int_{\rho_{\min}}^{\rho_{\max}} \rho P(\rho, u) d\rho = \int_{\rho_{\min}}^{\rho_{\max}} \rho P(\rho|u)P(u) d\rho = \langle \rho | u \rangle P(u). \quad (10.18)$$

Multiplying both sides with u and integrating yields

$$\bar{\rho} \int_{-\infty}^{+\infty} u \tilde{P}(u) du = \int_{-\infty}^{+\infty} \langle \rho | u \rangle u P(u) du \quad (10.19)$$

which is equivalent to $\bar{\rho}\tilde{u} = \overline{\rho u}$. The Favre mean value of u therefore is defined as

$$\tilde{u} = \int_{-\infty}^{+\infty} \tilde{P}(u) du. \quad (10.20)$$

10.3 Navier-Stokes Equations and Turbulence Models

In the following we will first describe the classical approach to model turbulent flows. It is based on single point averages of the Navier-Stokes equations. These are commonly called Reynolds Averaged Navier-Stokes Equations (RANS). We will formally extend this formulation to non-constant density by introducing Favre averages. In addition we will present the most simple model for turbulent flows, the k - ε model. Even though it certainly is the best compromise for engineering design using RANS, the predictive power of the k - ε model is, except for simple shear flows, often found to be disappointing. We will present it here, mainly to be able to define turbulent length and time scales.

For non-constant density flows the Navier-Stokes equations are written in conservative form (cf. Lecture 3)

Continuity

$$\frac{\partial \rho}{\partial t} + \nabla \cdot (\rho \mathbf{v}) = 0 \quad (10.21)$$

Momentum

$$\frac{\partial(\rho \mathbf{v})}{\partial t} + \nabla \cdot (\rho \mathbf{v} \mathbf{v}) = -\nabla p - \nabla \cdot \boldsymbol{\tau} + \rho \mathbf{g}. \quad (10.22)$$

In Eq. (10.22) the two terms on the left hand side (l.h.s.) represent the local rate of change

and convection of momentum, respectively, while the first term on the right hand side (r.h.s.) is the pressure gradient and the second term on the r.h.s. represents molecular transport due to viscosity. Here τ is the viscous stress tensor (cf. Lecture 3, Eq. (3.32))

$$\tau = -\mu \left[2S - \frac{2}{3} \nabla \cdot v \right] \quad (10.23)$$

and

$$S = \frac{1}{2} (\nabla v + \nabla v^T) \quad (10.24)$$

is the rate of strain tensor, where ∇v^T is the transpose of the velocity gradient and μ is the dynamic viscosity. It is related to the kinematic viscosity ν as $\mu = \rho\nu$. The last term in Eq. (10.22) represents forces due to buoyancy.

Using Favre averaging on Eqs. (10.21) and (10.22) one obtains

$$\frac{\partial \bar{\rho}}{\partial t} + \nabla \cdot (\bar{\rho} \tilde{v}) = 0 \quad (10.25)$$

$$\frac{\partial(\bar{\rho}\tilde{v})}{\partial t} + \nabla \cdot (\bar{\rho}\tilde{v}\tilde{v}) = -\nabla \bar{p} - \nabla \cdot \bar{\tau} - \nabla \cdot (\bar{\rho} \widetilde{v''v''}) + \bar{\rho}g. \quad (10.26)$$

Eq. (10.26) is similar to Eq. (10.22) except for the third term on the l.h.s. containing the correlation $-\bar{\rho} \widetilde{v''v''}$, which is called the Reynolds stress tensor.

An important simplification is obtained by introducing the kinematic eddy viscosity ν_t which leads to the following expression for the Reynolds stress tensor

$$-\bar{\rho} \widetilde{v''v''} = \bar{\rho} \nu_t \left[2\tilde{S} - \frac{2}{3} \nabla \cdot \tilde{v} I \right] + \frac{2}{3} \bar{\rho} \tilde{k}. \quad (10.27)$$

Here I is the unit tensor. The kinematic eddy viscosity ν_t is related to the Favre average turbulent kinetic energy

$$\tilde{k} = \frac{1}{2} \widetilde{v'' \cdot v''} \quad (10.28)$$

and its dissipation $\tilde{\varepsilon}$ by

$$\nu_t = c_\mu \frac{\tilde{k}^2}{\tilde{\varepsilon}}, \quad c_\mu = 0.09. \quad (10.29)$$

The introduction of the Favre averaged variables \tilde{k} and $\tilde{\varepsilon}$ requires that modeled equations are available for these quantities. These equations are given here in their most simple form

Turbulent kinetic energy

$$\bar{\rho} \frac{\partial \tilde{k}}{\partial t} + \bar{\rho} \tilde{v} \cdot \nabla \tilde{k} = \nabla \cdot \left(\frac{\bar{\rho} \nu_t}{\sigma_k} \nabla \tilde{k} \right) - \bar{\rho} \widetilde{\mathbf{v}'' \mathbf{v}''} : \nabla \tilde{v} - \bar{\rho} \tilde{\varepsilon}, \quad (10.30)$$

Turbulent dissipation

$$\bar{\rho} \frac{\partial \tilde{\varepsilon}}{\partial t} + \bar{\rho} \tilde{v} \cdot \nabla \tilde{\varepsilon} = \nabla \cdot \left(\bar{\rho} \frac{\nu_t}{\sigma_\varepsilon} \nabla \tilde{\varepsilon} \right) - c_{\varepsilon 1} \bar{\rho} \frac{\tilde{\varepsilon}}{\tilde{k}} \widetilde{\mathbf{v}'' \mathbf{v}''} : \nabla \tilde{v} - c_{\varepsilon 2} \bar{\rho} \frac{\tilde{\varepsilon}^2}{\tilde{k}}. \quad (10.31)$$

In these equations the two terms on the l.h.s. represent the local rate of change and convection, respectively. The first term on the r.h.s. represents the turbulent transport, the second one turbulent production and the third one turbulent dissipation. As in the standard $k-\varepsilon$ model, the constants $\sigma_k = 1.0$, $\sigma_\varepsilon = 1.3$, $c_{\varepsilon 1} = 1.44$ and $c_{\varepsilon 2} = 1.92$ are generally used. A more detailed discussion concerning additional terms in the Favre averaged turbulent kinetic energy equation may be found in Libby and Williams (1994) [1].

10.4 Two-Point Velocity Correlations and Turbulent Scales

A characteristic feature of turbulent flows is the occurrence of eddies of different length scales. If a turbulent jet shown in Fig. 10.2 enters with a high velocity into initially quiescent surroundings, the large velocity difference between the jet and the surroundings generate a shear layer instability which after a transition, becomes turbulent further downstream from the nozzle exit. The two shear layers merge into a fully developed turbulent jet. In order to characterize the distribution of eddy length scales at any position within the jet, one measures at point x and time t the axial velocity $u(x, t)$, and simultaneously at a second point $(x + r, t)$ with distance r apart from the first one, the velocity $u(x + r, t)$. Then the correlation between these two velocities is defined by the average

$$R(x, r, t) = \overline{u'(x, t) u'(x + r, t)}. \quad (10.32)$$

For homogeneous isotropic turbulence the location x is arbitrary and r may be replaced by its absolute value $r = |r|$. For this case the normalized correlation

$$f(r, t) = R(r, t) / \overline{u'^2(t)} \quad (10.33)$$

is plotted schematically in Fig. 10.3.

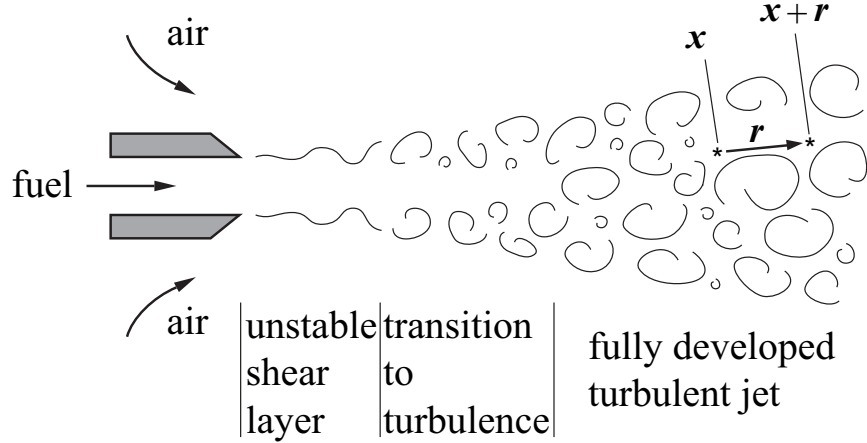


Figure 10.2: Schematic representation of two-point correlation measurements in a turbulent jet.

Kolmogorov's 1941 theory for homogeneous isotropic turbulence assumes that there is a steady transfer of kinetic energy from the large scales to the small scales and that this energy is being consumed at the small scales by viscous dissipation. This is the eddy cascade hypothesis. By equating the energy transfer rate (kinetic energy per eddy turnover time) with the dissipation ε it follows that this quantity is independent of the size of the eddies within the inertial range. For the inertial subrange, extending from the integral scale ℓ to the Kolmogorov scale η , ε is the only dimensional quantity apart from the correlation co-ordinate r that is available for the scaling of $f(r, t)$. Since ε has the dimension [m^2/s^3], the second order structure function defined by

$$F_2(r, t) = \overline{(u'(x, t) - u'(x + r, t))^2} = 2 \overline{u'^2(t)}(1 - f(r, t)) \quad (10.34)$$

with the dimension [m^2/s^2] must therefore scale as

$$F_2(r, t) = C(\varepsilon r)^{2/3} \quad (10.35)$$

where C is a universal constant called the Kolmogorov constant.

There are eddies of a characteristic size which contain most of the kinetic energy. At these eddies there still is a relatively large correlation $f(r, t)$ before it decays to zero. The length scale of

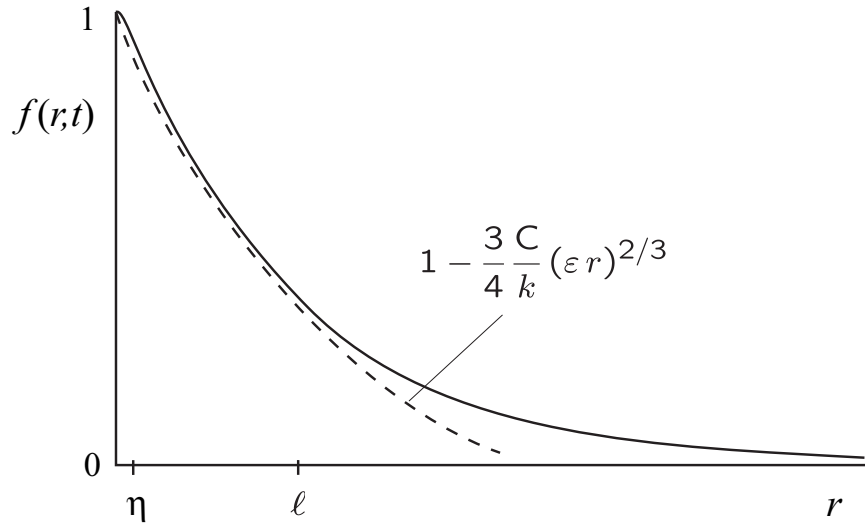


Figure 10.3: The normalized two-point velocity correlation for homogeneous isotropic turbulence as a function of the distance r between the two points.

these eddies is called the integral length scale ℓ and is defined by

$$\ell(t) = \int_0^\infty f(r, t) dr. \quad (10.36)$$

The integral length scale is also shown in Fig. 10.3.

We denote the root-mean-square (r.m.s.) velocity fluctuation by

$$v' = \sqrt{2k/3} \quad (10.37)$$

which represents the turnover velocity of integral scale eddies. The turnover time ℓ/v' of these eddies is then proportional to the integral time scale

$$\tau = \frac{k}{\varepsilon}. \quad (10.38)$$

For very small values of r only very small eddies fit into the distance between x and $x + r$. The motion of these small eddies is influenced by viscosity which provides an additional dimensional

quantity for scaling. Dimensional analysis then yields the Kolmogorov length scale

$$\eta = \left(\frac{\nu^3}{\varepsilon} \right)^{1/4} \quad (10.39)$$

which is also shown in Fig. 10.3.

The range of length scales between the integral scale and the Kolmogorov scale is called the inertial range. In addition to η a Kolmogorov time and a velocity scale may be defined as

$$t_\eta = \left(\frac{\nu}{\varepsilon} \right)^{1/2}, \quad v_\eta = (\nu \varepsilon)^{1/4}. \quad (10.40)$$

According to Kolmogorov's 1941 theory the energy transfer from the large eddies of size ℓ is equal to the dissipation of energy at the Kolmogorov scale η . Therefore we will relate ε directly to the turnover velocity and the length scale of the integral scale eddies

$$\varepsilon \sim \frac{v'^3}{\ell}. \quad (10.41)$$

We now define a discrete sequence of eddies within the inertial subrange by

$$\ell_n = \frac{\ell}{2^n} \geq \eta, \quad n = 1, 2, \dots. \quad (10.42)$$

Since ε is constant within the inertial subrange, dimensional analysis relates the turnover time t_n and the velocity difference v_n across the eddy ℓ_n to ε in that range as

$$\varepsilon \sim \frac{v_n^2}{t_n} \sim \frac{v_n^3}{\ell_n} \sim \frac{\ell_n^2}{t_n^3}. \quad (10.43)$$

This relation includes the integral scales and also holds for the Kolmogorov scales as

$$\varepsilon = \frac{v_\eta^2}{t_\eta} = \frac{v_\eta^3}{\eta}. \quad (10.44)$$

A Fourier transform of the isotropic two-point correlation function leads to a definition of the kinetic energy spectrum $E(k)$, which is the density of kinetic energy per unit wave number k . Here, rather than to present a formal derivation, we relate the wave number k to the inverse of the eddy size ℓ_n as

$$k = \ell_n^{-1}. \quad (10.45)$$

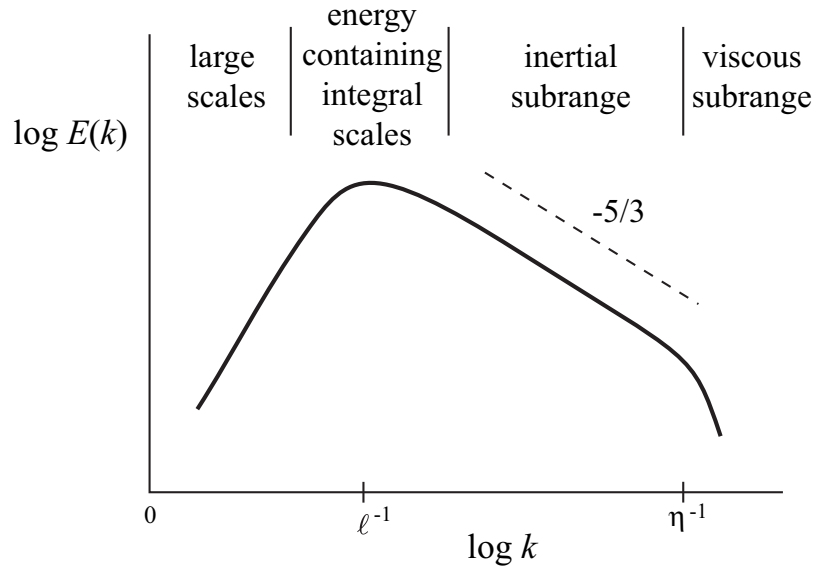


Figure 10.4: Schematic representation of the turbulent kinetic energy spectrum as a function of the wave number k .

The kinetic energy v_n^2 at scale ℓ_n is then

$$v_n^2 \sim (\varepsilon \ell_n)^{2/3} = \varepsilon^{2/3} k^{-2/3} \quad (10.46)$$

and its density in wave number space is proportional to

$$E(k) = \frac{dv_n^2}{dk} \sim \varepsilon^{2/3} k^{-5/3}. \quad (10.47)$$

This is the well-known $k^{-5/3}$ law for the kinetic energy spectrum in the inertial subrange.

If the energy spectrum is measured in the entire wave number range one obtains a behavior that is shown schematically in a log-log plot in Fig. 10.4. For small wave numbers corresponding to large scale eddies the energy per unit wave number increases with a power law between k^2 and k^4 . This range is not universal and is determined by large scale instabilities which depend on the boundary conditions of the flow. The spectrum attains a maximum at a wave number that corresponds to the integral scale, since eddies of that scale contain most of the kinetic energy. For larger wave numbers corresponding to the inertial subrange the energy spectrum decreases following the $k^{-5/3}$ law. There is a cut-off due to viscous effects at the Kolmogorov scale η . Beyond

this cut-off, in the range called the viscous subrange, the energy per unit wave number decreases exponentially due to viscous effects.

In one-point averages the energy containing eddies at the integral length scale contribute the most to the kinetic energy. Therefore RANS averaged mean quantities essentially represent averages over regions in physical space that are of the order of the integral scale. In Large Eddy Simulations (LES) the filtering over smaller regions than the integral length scale leads to different mean values and, in particular, to smaller variances.

10.5 Balance Equations for Reactive Scalars

For simplicity, we will assume that the specific heat capacities $c_{p,i}$ are all equal and constant, the pressure is constant and the heat transfer due to radiation is neglected. Then the temperature equation becomes (cf. Lecture 3, Eq. (3.46))

$$\rho \frac{\partial T}{\partial t} + \rho \mathbf{v} \cdot \nabla T = \nabla \cdot (\rho D \nabla T) + \omega. \quad (10.48)$$

Here Eq. (3.44) with unity Lewis number was used and the heat release (cf. Lecture 3, Eq. (3.44)) due to chemical reactions is written as

$$\omega_T = -\frac{1}{c_p} \sum_{i=1}^k h_i \dot{m}_i. \quad (10.49)$$

This form of the temperature equation is similar to that for the mass fractions of species i (cf. Lecture 3, Eq. (3.17)), which becomes with the binary diffusion approximation

$$\rho \frac{\partial Y_i}{\partial t} + \rho \mathbf{v} \cdot \nabla Y_i = \nabla \cdot (\rho D_i \nabla Y_i) + \dot{m}_i. \quad (10.50)$$

If, in addition, a one-step reaction and equal diffusivities ($D_i = D$) were assumed, coupling relations between the temperature and the species mass fractions can be derived (cf. Williams, (1985)a [2]). These assumptions are often used in mathematical analyzes of combustion problems.

In the following we will use the term “reactive scalars” for the mass fraction of all chemical species and temperature and introduce the vector

$$\psi = (Y_1, Y_2, \dots, Y_k, T). \quad (10.51)$$

Here k is the number of reactive species. For simplicity of notation, the balance equation for the reactive scalar ψ_i will be written

$$\rho \frac{\partial \psi_i}{\partial t} + \rho \mathbf{v} \cdot \nabla \psi_i = \nabla \cdot (\rho D_i \nabla \psi_i) + \sigma_i, \quad i = 1, 2, \dots, k+1, \quad (10.52)$$

where $i = 1, 2, \dots, k+1$. The diffusivities D_i ($i = 1, 2, \dots, k$) are the mass diffusivities for the species and $D_{k+1} = D$ denotes the thermal diffusivity. Similarly, σ_i ($i = 1, 2, \dots, k$) are the species source terms \dot{m}_i , $i = 1, 2, \dots, k$ (cf. Lecture 3, Eq. (3.12)) and σ_{k+1} is defined as ω_T Eq. (10.49) (cf. Lecture 3, Eq. (3.46)). The chemical source term will also be written as

$$\sigma_i = \rho S_i. \quad (10.53)$$

10.6 Moment Methods for Reactive Scalars

Favre averaged equations for the mean and the variance of the reactive scalars can be derived by splitting $\psi_i(\mathbf{x}, t)$ into a Favre mean and a fluctuation

$$\psi_i(\mathbf{x}, t) = \tilde{\psi}_i(\mathbf{x}, t) + \psi_i''(\mathbf{x}, t). \quad (10.54)$$

When this is introduced into Eq. (10.52) one obtains in a similar way as for the momentum equation after averaging

$$\bar{\rho} \frac{\partial \tilde{\psi}_i}{\partial t} + \bar{\rho} \tilde{\mathbf{v}} \cdot \nabla \tilde{\psi}_i = \nabla \cdot (\overline{\rho D_i \nabla \psi_i}) - \nabla \cdot (\bar{\rho} \tilde{\mathbf{v}}'' \tilde{\psi}_i'') + \bar{\rho} \tilde{S}_i. \quad (10.55)$$

In this equation the terms on the l.h.s. are closed, while those on the r.h.s. must be modeled. In high Reynolds number flows the molecular transport term containing the molecular diffusivities D_i are small and can be neglected. Closure is required for the second term on the r.h.s., the turbulent transport term, and for the last term, the mean chemical source term.

The modeling of the mean chemical source term has often been considered as the main problem of moment methods in turbulent combustion. In order to discuss the difficulties associated with the closure of this term, we assume that coupling relations exist between the chemical species and the temperature. As noted before, such coupling relations can easily be derived for the case of a one step reaction and equal diffusivities. With this assumption we consider the following form of the heat release rate

$$\omega_T(T) = \rho S_T(T) = \rho B(T_b - T) \exp\left(-\frac{E}{RT}\right). \quad (10.56)$$

Here B contains the frequency factor and the heat of reaction, T_b is the adiabatic flame temperature, E the activation energy and \mathcal{R} the universal gas constant. Introducing $T = \tilde{T} + T''$ into Eq. (10.56) the argument of the exponential term may be expanded around \tilde{T} for small T'' as

$$\frac{E}{\mathcal{R}T} = \frac{E}{\mathcal{R}\tilde{T}} - \frac{ET''}{\mathcal{R}\tilde{T}^2}. \quad (10.57)$$

If the expansion is also introduced into the preexponential term, the quantity S_T becomes

$$S_T(T) = S_T(\tilde{T}) \left(1 - \frac{T''}{T_b - \tilde{T}}\right) \exp\left(\frac{ET''}{\mathcal{R}\tilde{T}^2}\right). \quad (10.58)$$

Typically, the grouping $E/\mathcal{R}\tilde{T}$ is of the order of 10 in the reaction zone of a flame and the absolute value of T''/\tilde{T} varies between 0.1 ∕ 0.3. Therefore the exponential term in Eq. (10.58) causes enhanced fluctuations of the chemical source term around its mean value evaluated with the mean temperature \tilde{T} . It may be concluded that moment methods for reactive scalars will fail due to the strong nonlinearity of the chemical source term.

10.7 Dissipation and Scalar Transport of Non-Reacting Scalars

As an example for a nonreactive scalar we will use the mixture fraction Z Eq. (3.58). It is general practice in turbulent combustion to employ the gradient transport assumption for non-reacting scalars. The scalar flux then takes the form

$$-\widetilde{\mathbf{v}'' Z''} = D_t \nabla \tilde{Z}. \quad (10.59)$$

Here D_t is a turbulent diffusivity which is modeled by analogy to the eddy viscosity as

$$D_t = \frac{\nu_t}{Sc_t}, \quad (10.60)$$

where Sc_t is a turbulent Schmidt number. The equation for the mean mixture fraction then reads

$$\rho \frac{\partial \tilde{Z}}{\partial t} + \rho \tilde{\mathbf{v}} \cdot \nabla \tilde{Z} = \nabla \cdot (\bar{\rho} D_t \nabla \tilde{Z}), \quad (10.61)$$

where the molecular term has been neglected. In order to derive an equation for $\widetilde{Z''^2}$ we first must derive an equation for Z'' . By subtracting Eqs. (10.55) and (10.52), when the source terms have

been removed and D_i is set to D , and after both have been divided by ρ and $\bar{\rho}$, respectively, an equation for the fluctuation Z'' is obtained:

$$\begin{aligned} \frac{\partial Z''}{\partial t} + (\tilde{\mathbf{v}} + \mathbf{v}'') \cdot \nabla Z'' + \mathbf{v}'' \cdot \nabla \tilde{Z} &= \frac{1}{\rho} \nabla \cdot (\rho D \nabla Z) \\ &\quad - \frac{1}{\bar{\rho}} \nabla \cdot (\bar{\rho} D \nabla \tilde{Z}) + \nabla \cdot (\bar{\rho} \widetilde{\mathbf{v}'' Z''}). \end{aligned} \quad (10.62)$$

Also the continuity equation was used. If derivatives of ρ and D and their mean values are neglected for simplicity, the first two terms on the r.h.s. of Eq. (10.62) can be combined to obtain a term proportional to $D_i \nabla^2 Z''$. Introducing this and multiplying Eq. (10.62) by $2\rho Z''$ one obtains an equation for Z''^2 . With the use of the continuity equation and averaging one obtains

$$\begin{aligned} \bar{\rho} \frac{\partial \widetilde{Z''^2}}{\partial t} + \bar{\rho} \tilde{\mathbf{v}} \cdot \nabla \widetilde{Z''^2} &= -\nabla \cdot (\bar{\rho} \widetilde{\mathbf{v}'' Z''^2}) \\ &\quad + 2\bar{\rho} (-\widetilde{\mathbf{v}'' Z''}) \cdot \nabla \tilde{Z} - \bar{\rho} \widetilde{\chi}. \end{aligned} \quad (10.63)$$

As before, the terms on the r.h.s. describe the local change and convection. The first term on the r.h.s. is the turbulent transport term. The second term on the r.h.s. accounts for the production of scalars fluctuations. The mean molecular transport term has been neglected for simplicity but the molecular diffusivity still appears in the dissipation term. The Favre scalar dissipation rate is defined as

$$\widetilde{\chi} = 2D(\widetilde{\nabla Z''})^2. \quad (10.64)$$

An integral scalar time scale can be defined by

$$\tau_Z = \frac{\widetilde{Z''^2}}{\widetilde{\chi}}. \quad (10.65)$$

It is often set proportional to the flow time $\tau = \tilde{k}/\tilde{\varepsilon}$

$$\tau = c_\chi \tau_Z, \quad (10.66)$$

where the constant of proportionality c_χ is of order unity but its value varies between 1.5 and 3.0. A value $c_\chi = 2.0$ is often used. Combining Eqs. (10.65) and (10.66) leads to the model

$$\tilde{\chi} = c_\chi \frac{\tilde{\varepsilon}}{\tilde{k}} \widetilde{Z''^2}. \quad (10.67)$$

10.8 The Eddy Break Up and the Eddy Dissipation Model

An early attempt to provide a closure for the chemical source term is due to Spalding (1971) [3] who argued that since turbulent mixing may be viewed as a cascade process from the integral down to the molecular scales, the cascade process also controls the chemical reactions as long as mixing rather than reaction is the rate determining process. This model was called the Eddy-Break-Up model (EBU). The turbulent mean reaction rate of products was expressed as

$$\bar{\omega}_P = \rho C_{EBU} \frac{\varepsilon}{k} \left(\overline{Y_P''^2} \right)^{1/2} \quad (10.68)$$

where $\overline{Y_P''^2}$ is the variance of the product mass fraction and C_{EBU} is the Eddy-Break-Up constant.

This model has been modified by Magnussen and Hjertager (1977) [4] who replaced $(\overline{Y_P''^2})^{1/2}$ simply by the mean mass fraction of the deficient species (fuel for lean or oxygen for rich mixtures) calling it the Eddy Dissipation Model (EDM). The model takes the minimum of three rates, those defined with the mean fuel mass fraction

$$\bar{\omega}_F = \bar{\rho} A \overline{Y_F} \frac{\varepsilon}{k}, \quad (10.69)$$

with the mean oxidizer mass fraction

$$\bar{\omega}_{O_2} = \bar{\rho} \frac{A \overline{Y_{O_2}}}{\nu} \frac{\varepsilon}{k}, \quad (10.70)$$

and with the product mass fraction

$$\bar{\omega}_P = \bar{\rho} \frac{A \cdot B}{(1 + \nu)} \overline{Y_P} \frac{\varepsilon}{k}, \quad (10.71)$$

in order to calculate the mean chemical source term. In Eqs. (10.69)-(10.71) A and B are modeling constants and ν is the stoichiometric oxygen to fuel mass ratio defined in Eq. (1.32).

The Eddy Break-Up model and its modifications are based on intuitive arguments. The main

idea is to replace the chemical time scale of an assumed one-step reaction by the turbulent time scale $\tau = k/\varepsilon$. Thereby the model eliminates the influence of chemical kinetics, representing the fast chemistry limit only. When these models are used in CFD calculations, it turns out that the constants C_{EBU} or A and B must be “tuned” within a wide range in order to obtain reasonable results for a particular problem.

10.9 The Pdf Transport Equation Model

Similar to moment methods, models based on a pdf transport equation for the velocity and the reactive scalars are usually formulated for one-point statistics. Within that framework, however, they represent a general statistical description of turbulent reacting flows, applicable to premixed, nonpremixed and partially premixed combustion. A joint pdf transport equation for the velocity and the reactive scalars can be derived, which is equivalent to an infinite hierarchy of one-point moment equations for these quantities, Pope (1990) [5].

For simplicity, we will consider here the transport equation for the joint pdf of velocity and reactive scalars only. Denoting the set of reactive scalars, such as the temperature and the mass fraction of reacting species by the vector ψ , $P(\mathbf{v}, \psi; \mathbf{x}, t)d\mathbf{v}d\psi$ is the probability of finding at point \mathbf{x} and time t the velocity components and the reactive scalars within the intervals $\mathbf{v} - d\mathbf{v}/2 < \mathbf{v} < \mathbf{v} + d\mathbf{v}/2$ and $\psi - d\psi/2 < \psi < \psi + d\psi/2$.

There are several ways to derive a transport equation for the probability density $P(\mathbf{v}, \psi; \mathbf{x}, t)$ (cf. O’Brien (1980) [6]). We refer here to the presentation in Pope (1985) [7] cf. also Pope (2000) [8], but write the convective terms in conservative form

$$\begin{aligned} \frac{\partial(\rho P)}{\partial t} + \nabla \cdot (\rho \mathbf{v} P) + (\rho \mathbf{g} - \nabla \bar{p}) \cdot \nabla_{\mathbf{v}} P + \sum_{i=1}^n \frac{\partial}{\partial \psi_i} [\omega_i P] = \\ \nabla_{\mathbf{v}} \cdot [\langle -\nabla \cdot \boldsymbol{\tau} + \nabla \langle p' | \mathbf{v}, \psi \rangle P \rangle] - \sum_{i=1}^n \frac{\partial}{\partial \psi_i} [\langle \nabla \cdot (\rho D \nabla \psi_i) | \mathbf{v}, \psi \rangle P]. \end{aligned} \quad (10.72)$$

In deriving this equation, the equations for all reactive scalars, including that for temperature have been cast into the form Eq. (10.52), for simplicity. The symbol $\nabla_{\mathbf{v}}$ denotes the divergence operator with respect to the three components of velocity. The angular brackets denote conditional averages, conditioned with respect to fixed values of \mathbf{v} and ψ . For simplicity of presentation we

do not use different symbols for the random variables describing the stochastic fields and the corresponding sample space variables which are the independent variables in the pdf equation.

The first two terms on the l.h.s. of Eq. (10.72) are the local change and convection of the probability density function in physical space. The third term represents transport in velocity space by gravity and the mean pressure gradient. The last term on the l.h.s. contains the chemical source terms. All these terms are in closed form, since they are local in physical space. Note that the mean pressure gradient does not present a closure problem, since the pressure is calculated independently of the pdf equation using the mean velocity field. For chemical reacting flows it is of particular interest that the chemical source terms can be treated exactly for arbitrarily complex chemical kinetics. It has often been argued that in this respect the transported pdf formulation has a considerable advantage compared to other formulations.

However, on the r.h.s. of the transport equation there are two terms that contain gradients of quantities conditioned on the values of velocity and composition. Therefore, if gradients are not included as sample space variables in the pdf equation, these terms occur in unclosed form and have to be modeled. The first unclosed term on the r.h.s. describes transport of the probability density function in velocity space induced by the viscous stresses and the fluctuating pressure gradient. The second term represents transport in reactive scalar space by molecular fluxes. This term represents molecular mixing.

When chemistry is fast, mixing and reaction take place in thin layers where molecular transport and the chemical source term balance each other. Therefore, the closed chemical source term and the unclosed molecular mixing term, being leading order terms in a asymptotic description of the flame structure, are closely linked to each other. Pope and Anand (1984) [9] have illustrated this for the case of premixed turbulent combustion by comparing a standard pdf closure for the molecular mixing term with a formulation, where the molecular diffusion term was combined with the chemical source term to define a modified reaction rate. They call the former distributed combustion and the latter flamelet combustion and find considerable differences in the Damköhler number dependence of the turbulent burning velocity normalized with the turbulent intensity.

From a numerical point of view, the most apparent property of the pdf transport equation is its high dimensionality. Finite-volume and finite-difference techniques are not very attractive for this type of problem, as memory requirements increase roughly exponentially with dimensionality. Therefore, virtually all numerical implementations of pdf methods for turbulent reactive flows employ Monte-Carlo simulation techniques (cf. Pope (1981), (1985) [10, 7]). The advantage of Monte-Carlo methods is that their memory requirements depend only linearly on the dimensional-

ity of the problem. Monte-Carlo methods employ a large number, N , of particles. In the Lagrangian algorithm (Pope (1985) [7]) the particles are not bound to grid nodes. Instead, each particle has its own position and moves through the computational domain with its own instantaneous velocity. The particles should be considered as different realizations of the turbulent reactive flow problem under investigation. The state of the particle is described by its position and velocity, and by the values of the reactive scalar that it represents as a function of time. These particles should not be confused with real fluid elements, which behave similarly in a number of respects.

10.10 The Laminar Flamelet Concept

The view of a turbulent diffusion flame as an ensemble of stretched laminar flamelets is due to Williams (1975) [11]. Flamelet equations based on the mixture fraction as independent variable, using the scalar dissipation rate for the mixing process, were independently derived by Peters (1980) [12] and Kuznetsov (1982) [13]. A first review of diffusion flamelet models was given by Peters (1984) [14]. For premixed and diffusion flames the flamelet concept was reviewed by Peters (1986) [15] and Bray and Peters (1994) [16].

Flamelets are thin reactive-diffusive layers embedded within an otherwise non-reacting turbulent flow field. Once ignition has taken place, chemistry accelerates as the temperature increases due to heat release. When the temperature reaches values that are of the order of magnitude of those of the close-to-equilibrium branch in Fig. 10.1, the reactions that determine fuel consumption become very fast. For methane combustion, for example, the rate determining reaction in the fuel consumption layer is the reaction of CH_4 with the $\text{H}^{\circ 0}$ -radical. Since the chemical time scale of this reaction is short, chemistry is active only within a thin layer, namely the fuel consumption or inner layer. If this layer is thin compared to the size of a Kolmogorov eddy, it is embedded within the quasi-laminar flow field of such an eddy and the assumption of a laminar flamelet structure is justified. If, on the contrary, turbulence is so intense, that Kolmogorov eddies become smaller than the inner layer and can penetrate into it, they are able to destroy its structure. Under these conditions the entire flame is likely to extinguish.

The location of the inner layer defines the flame surface. Differently from moment methods or methods based on a pdf transport equation, statistical considerations in the flamelet concept focus on the location of the flame surface and not on the reactive scalars themselves. That location is defined as an iso-surface of a non-reacting scalar quantity, for which a suitable field equation is derived. For nonpremixed combustion the mixture fraction Z is that scalar quantity, for premixed

combustion the scalar G will be introduced. Once equations that describe the statistical distributions of Z and G are solved, the profiles of the reactive scalars normal to the surface are calculated using flamelet equations. These profiles are assumed to be attached to the flame surface and are convected with it in the turbulent flow field. Therefore the statistical moments of the reactive scalars can be obtained from the statistical distribution of the scalar quantities Z and G . Details of this procedure will be discussed in Lecture 12.

10.11 The BML-Model and the Coherent Flamelet Model

For premixed combustion, flamelet models are typically based on the progress variable c . The progress variable c is defined as a normalized temperature or normalized product mass fraction

$$c = \frac{T - T_u}{T_b - T_u} \quad \text{or} \quad c = \frac{Y_P}{Y_{P,b}} \quad (10.73)$$

which implies a one-step reaction $A \rightarrow P$ and a corresponding heat release raising the temperature from T_u to T_b . In flamelet models based on the progress variable the flame structure is assumed to be infinitely thin and no intermediate values of temperature between T_u and T_b are resolved. This corresponds to the fast chemistry limit. The progress variable therefore is a step function that separates unburnt mixture and burnt gas in a given flow field.

The classical model for premixed turbulent combustion, the Bray-Moss-Libby (BML) model was initiated by Bray and Moss (1977) [17] by assuming the pdf of the progress variable c to be a two delta function distribution. This assumption only allows for entries at $c = 0$ and $c = 1$ in a turbulent premixed flame, but it illustrates important features, like counter-gradient diffusion of the progress variable. This appears in the equation for the Favre mean progress variable \tilde{c}

$$\bar{\rho} \frac{\partial \tilde{c}}{\partial t} + \bar{\rho} \mathbf{v} \cdot \nabla \tilde{c} + \nabla \cdot (\widetilde{\bar{\rho} \mathbf{v}'' c''}) = \overline{w_c} \quad (10.74)$$

where the molecular diffusion term has been neglected. This equation requires the modeling of the turbulent transport term $\widetilde{\bar{\rho} \mathbf{v}'' c''}$ and the mean reaction term $\overline{w_c}$. Libby and Bray (1981) [18] and Bray et al. (1981) [19] have shown that the gradient transport assumption Eq. (10.59) is not applicable to $\widetilde{\bar{\rho} \mathbf{v}'' c''}$. This is due to gas expansion effects at the flame surface and is called counter-gradient diffusion. Counter-gradient diffusion has been found in many experiments and in many one-dimensional numerical analyzes. However, there is no model available that could be used in

three-dimensional calculations solving Eq. (10.74) with counter-gradient diffusion included.

Models for the mean reaction rate by Bray et al. (1984a) [20] and Bray and Libby (1986) [21] focus on a time series of step function events of the progress variable. This makes the mean source term proportional to the flamelet crossing frequency. Further modeling, discussed in more detail in Bray and Libby (1994) [22], then leads to the expression

$$\bar{\omega}_c = \rho_u s_L I_0 \Sigma \quad (10.75)$$

where s_L is the laminar burning velocity, I_0 is a stretch factor and Σ is the flame surface density (flame surface per unit volume).

A model for Σ has been proposed by Candel et al. (1990) [23]. This is called the Coherent Flame Model (CFM). A comparison of the performance of different formulations of the model for one-dimensional turbulent flames was made by Duclos et al. (1993) [24]. Modeling based on DNS data has led Trouv   and Poinsot (1994) [25] to the following equation for the flame surface density Σ :

$$\frac{\partial \Sigma}{\partial t} + \nabla \cdot (\tilde{v} \Sigma) = \nabla \cdot (D_t \nabla \Sigma) + C_1 \frac{\varepsilon}{k} \Sigma - C_2 s_L \frac{\Sigma^2}{1 - \bar{c}}. \quad (10.76)$$

The terms on the l.h.s. represent the local change and convection, the first term on the r.h.s. represents turbulent diffusion, the second term production by flame stretch and the last term flame surface annihilation. The stretch term is proportional to the inverse of the integral time scale $\tau = k/\varepsilon$ which is to be evaluated in the unburnt gas.

10.12 Combustion Models used in Large Eddy Simulation

Turbulence models based on Reynolds Averaged Navier-Stokes Equations (RANS) employ turbulent transport approximations with an effective turbulent viscosity that is by orders of magnitude larger than the molecular viscosity. In particular if steady state versions of these equations are used, this tends to suppress large scale instabilities which occur in flows with combustion even more frequently than in non-reacting flows. If those instabilities are to be resolved in numerical simulations, it is necessary to recur to more advanced, but computationally more expensive methods such as Large Eddy Simulation (LES).

Large Eddy Simulation does not intend to numerically resolve all turbulent length scales, but only a fraction of the larger energy containing scales within the inertial subrange. Modeling is then applied to represent the smaller unresolved scales which contain only a small fraction of

the turbulent kinetic energy. Therefore the computed flows are usually less sensitive to modeling assumptions. The distinction between the resolved large scales and the modeled small scales is made by the grid resolution that can be afforded. The model for the smaller scales is called the subgrid model. In deriving the basic LES equations, the Navier-Stokes equations are spatially filtered with a filter of size Δ , which is of the size of the grid cell (or a multiple thereof) in order to remove the direct effect of the small scale fluctuations (cf. Ghosal and Moin (1995) [26]). These show up indirectly through nonlinear terms in the subgrid-scale stress tensor as subgrid-scale Reynolds stresses, Leonard stresses, and subgrid-scale cross stresses. The latter two contributions result from the fact that, unlike with the traditional Reynolds averages, a second filtering changes an already filtered field. In a similar way, after filtering the equations for non-reacting scalars like the mixture fraction, one has to model the filtered scalar flux vectors which contain subgrid scalar fluxes, Leonard fluxes, and subgrid-scale cross fluxes.

The reason why LES still provides substantial advantages for modeling turbulent combustion is that the scalar mixing process is of paramount importance in chemical conversion. Nonreactive and reactive system studies show that LES predicts the scalar mixing process and dissipation rates with considerably improved accuracy compared to RANS, especially in complex flows. For example, to study the importance of turbulent scalar dissipation rate fluctuations on the combustion process and to highlight the differences between RANS and LES, [27] compared the results of two different LES simulations using unsteady flamelet models in which the scalar dissipation rate appears as a parameter. The only difference between the simulations was that only the Reynolds-averaged dissipation rate was used in one simulation [28], whereas the other considered the resolved fluctuations of the filtered scalar dissipation rate predicted by LES. The results show substantially improved predictions, especially for minor species, when fluctuations are considered. Another such example is the simulation of a bluff-body stabilized flame [29], where a simple steady-state diffusion flamelet model [14] in the context of an LES with a recursive filter refinement method led to excellent results. Such accuracy has not been achieved with RANS simulations of the same configuration [30], [31]. Both studies are discussed in more detail below. Similar arguments can be made for premixed turbulent combustion LES.

In RANS modeling it has long been realized that the direct closure of the mean chemical source term in the averaged species transport equations can hardly be accomplished, and conserved scalar methods have been used in many applications. Using so-called coupling functions, the rate of mixing of fuel and oxidizer can be described by a nonreactive scalar, the mixture fraction. Different definitions have been used for the mixture fraction [32], [33], but essentially the mixture fraction

is a measure of the local equivalence ratio. Hence, the mixture fraction is a conserved scalar, independent of the chemistry. This leads to the so-called conserved scalar method, which forms the basis for most of the combustion models for nonpremixed turbulent combustion. Considering the simplest case of infinitely fast chemistry, all species mass fractions and the temperature are a function of mixture fraction only. If the subfilter probability distribution of the mixture fraction is known, the Favre-filtered mass fractions \tilde{Y}_i , for instance, can then be obtained as

$$\tilde{Y}_i = \int_0^1 Y_i(Z) f(Z) dZ, \quad (10.77)$$

where Z is the mixture fraction and $f(Z)$ is the marginal density-weighted filter probability density function (FPDF) of the mixture fraction. Applications of simple conserved scalar models in LES have been based on infinitely fast irreversible chemistry [34] and equilibrium chemistry [35]. The flamelet model is a conserved scalar model that can account for finite-rate chemistry effects. Many models that have been formulated for LES are variants of these and some are discussed below. These models essentially provide state relationships for the reactive scalars as functions of mixture fraction and other possible parameters, such as the scalar dissipation rate. Filtered quantities are then obtained by a relation similar to Eq. (10.77), but using a presumed joint FPDF of the mixture fraction and, for example, the scalar dissipation rate.

Because the probability density function (PDF) plays a central role in most models for non-premixed combustion, it is necessary to emphasize the special meaning of the FPDF in LES. Here, the example of the marginal FPDF of the mixture fraction is discussed, but similar arguments can be made for the joint composition FPDF. In Reynolds-averaged methods, a one-point PDF can be determined by repeating an experiment many times and recording the mixture fraction at a given time and position in space. For a sufficiently large number of samples, the PDF of the ensemble can be determined with good accuracy. In LES, assuming a simple box filter, the data of interest is a one-time, one-point probability distribution in a volume corresponding to the filter size surrounding the point of interest. If an experimentally observed spatial mixture fraction distribution is considered at a given time, the FPDF cannot simply be evaluated from these data, because the observed distribution is characteristic of this particular realization and it is not a statistical property. As a statistical property, the FPDF must be defined by an ensemble that can potentially have an arbitrary large number of samples. In the context of transported PDF model formulations for LES, which are discussed below, [5] introduced the notion of the filtered density function (FDF), which describes the local subfilter state of the considered experiment. The FDF is not an FPDF,

because it describes a single realization. The FPDF is defined only as the average of the FDF of many realizations given the same resolved field [36]. It is important to distinguish between the FDF and the FPDF, especially in using direct numerical simulation (DNS) data to evaluate models, and in the transported FDF models discussed below. Only the FDF can be evaluated from typical DNS data, whereas the FPDF is required for subfilter modeling. For conserved scalar models, a presumed shape of the FPDF has to be provided. Similar to RANS models, a beta-function distribution is usually assumed for the marginal FPDF of the mixture fraction, and parameterized by the first two moments of the mixture fraction. The filtered mixture fraction is determined by the solution of a transport equation, whereas algebraic models are mostly used for the subfilter scalar variance. The beta-function is expected to be a better model for the FPDF in LES than for the PDF in RANS, because the FPDF is generally more narrow, and hence the exact shape is less important. It can also be expected that intermittency, which is a main source of error when using the beta-function in RANS, will mostly occur on the resolved scales. The validity of the beta-function representation of the FPDF of the mixture fraction has been investigated by several authors using DNS data of nonpremixed reacting flows of both constant and variable density [35], [37], [38]. The main conclusion of these studies is that the beta-function distribution provides a good estimate for the FPDF of the mixture fraction and that this estimate is even better in LES than in RANS models. Furthermore, the model is particularly good when evaluated using the mixture fraction variance taken from DNS data, suggesting that the beta-function as a model for the statistical distribution of the mixture fraction performs much better than the commonly used subgrid-scale models for the mixture fraction variance. However, recent studies by [39] and [40] show that the FPDF often substantially deviates from the beta-function. This is discussed in more detail below.

In the following, different variants of the flamelet model are discussed. Because all such models require the scalar dissipation rate, modeling of this quantity is discussed first. We follow the presentation in [41].

10.13 Modeling the Scalar Dissipation Rate

Although different conceptual ideas and assumptions are used in the combustion models discussed here, most of them need a model for the scalar dissipation rate. The dissipation rate of the mixture fraction is a fundamental parameter in nonpremixed combustion, which determines the filtered reaction rates, if combustion is mixing controlled. High rates of dissipation can also lead to local or global flame extinction. Models based on presumed FPDFs also require a model

for the subfilter scalar variance. Here, the most commonly used model formulations for LES are reviewed briefly, differences with the typical RANS models are pointed out, and potential areas of improvement are discussed.

An illustration of the importance of the scalar variance and dissipation rate in LES of non-premixed combustion modeling is given by the following example. [43] pointed out that LES is an incomplete model if the filter size can be arbitrarily specified. This is an important issue, especially for combustion LES, because of the importance of the subfilter models. To fix the arbitrariness of the filter, [29] proposed a recursive filter refinement method, where the local filter width is determined such that the ratio of subfilter scalar variance to the maximum possible variance is smaller than a specified value. The maximum possible variance can be expressed in terms of the resolved mixture fraction as $\tilde{Z}(1 - \tilde{Z})$. It was demonstrated in the simulation of a bluff-body stabilized flame that this method better resolves high scalar variance and dissipation regions, which leads to significant improvement in results. Some of these results are shown in Fig. 10.5.

In RANS models, typically a transport equation is solved for the scalar variance (Z'^2), in which the Reynolds-averaged scalar dissipation rate χ appears as an unclosed sink term that requires modeling. The additional assumption of a constant ratio of the integral timescale of the velocity τ_t and the scalar fields leads to the expression

$$\langle \chi \rangle = c_\phi \frac{1}{\tau_t} \langle Z'^2 \rangle, \quad (10.78)$$

where c_ϕ is the so-called timescale ratio.

In the models most commonly used in LES [45, 34], the scalar variance transport equation and the timescale ratio assumption are actually used in the opposite sense. Instead of solving the subfilter variance equation, the assumption that the scalar variance production appearing in that equation equals the dissipation term leads to an algebraic model for the dissipation rate of the form

$$\tilde{\chi} = 2D_t(\nabla \tilde{Z})^2, \quad (10.79)$$

where an eddy diffusivity model was used for the subfilter scalar flux in the production term. $D_t = (c_Z \nabla)^2 \tilde{S}$ is the eddy diffusivity, where c_Z can be determined using a dynamic procedure and $\tilde{S} = |2\tilde{S}_{ij}\tilde{S}_{ij}|^{1/2}$ is the characteristic Favre-filtered rate of strain. Writing Eq. (10.78) for the subfilter scales and combining it with Eq. (10.79) then leads to the model for the scalar variance

$$\tilde{Z}'^2 = c_V \Delta^2 (\nabla \tilde{Z})^2, \quad (10.80)$$

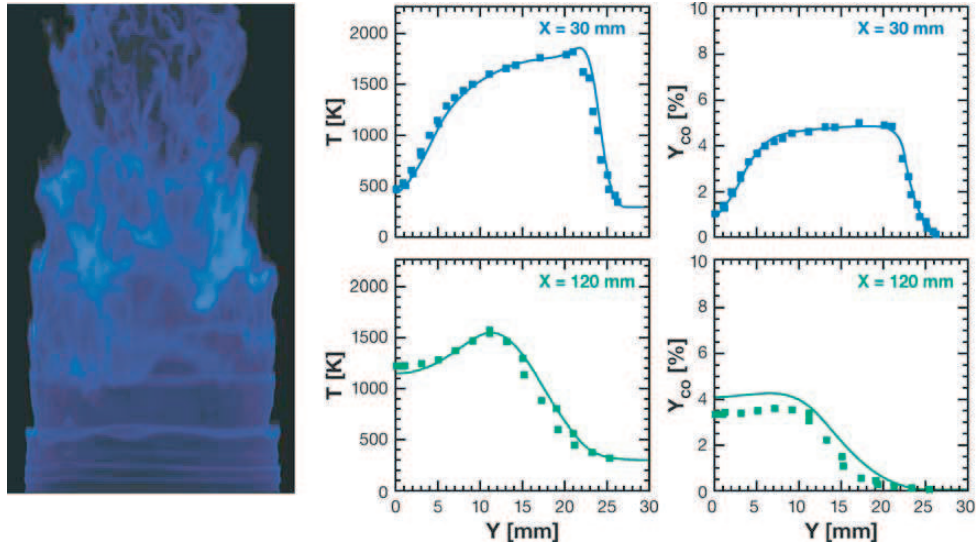


Figure 10.5: Results from large-eddy simulation of the Sydney bluff-body flame [29]. Flame representation from simulation results (left) and time-averaged radial profiles of temperature and CO mass fraction at $x = 30$ mm and $x = 120$ mm, which are in and downstream of the recirculation region, respectively. The left figure shows computed chemiluminescence emissions of CH° collected in an observation plane with a ray tracing technique (M. Herrmann, private communication). Experimental data are taken from [42]. Courtesy of [41].

where $\tau_{t,\Delta} \sim 1/\tilde{S}$ is assumed, and a new coefficient c_V is introduced, which can be determined dynamically following [34]. From Eqs. (10.78) and (10.79), and the dynamically determined coefficients of the eddy diffusivity and the scalar variance, the timescale ratio c_ϕ can be determined as $c_\phi = 2c_Z^2/c_V$.

Pitsch and Steiner (2000) [28, 46] used the Lagrangian flamelet model (LFM) [33] as a subfilter combustion model for LES in an application to a piloted methane/air diffusion flame [44] using a 20-step reduced chemical scheme based on the GRI 2.11 mechanism [47]. The unsteady flamelet equations are solved coupled with the LES solution to provide the filtered density and other filtered scalar quantities using a presumed FPDF of the mixture fraction. The scalar dissipation rate χ required to solve the flamelet equation Eq. (8.7)₂

$$\rho \frac{\partial Y_i}{\partial t} - \rho \frac{\chi}{2} \frac{\partial^2 Y_i}{\partial Z^2} = \dot{m}_i, \quad i = 1, 2, \dots, k \quad (10.81)$$

is determined from the LES fields as a cross-sectional conditionally averaged value using a model

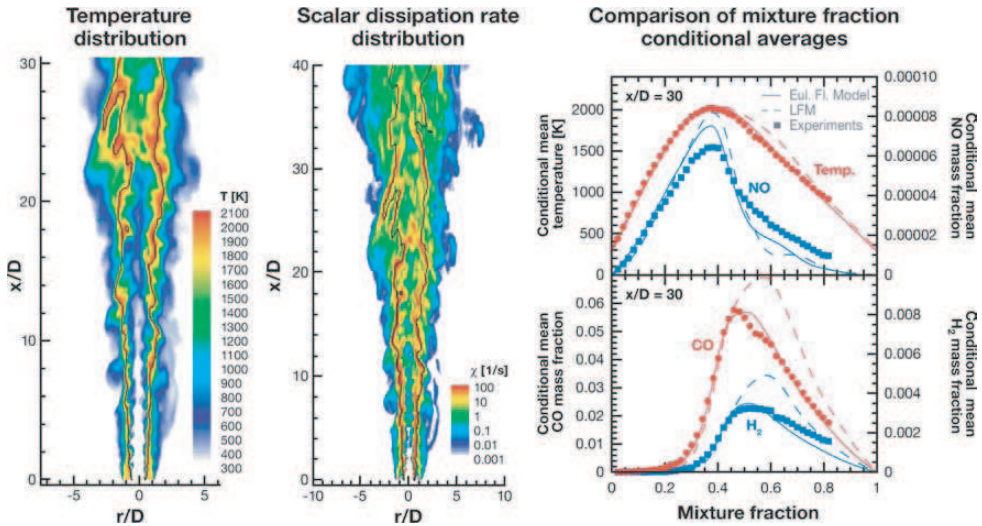


Figure 10.6: Results from large-eddy simulation of Sandia flame D ([27], [28]) using the Eulerian flamelet model (solid lines) and the Lagrangian flamelet model (dashed lines) compared with experimental data of [44]. Temperature distribution (left), scalar dissipation rate distribution (center), and comparison of mixture fractionconditional averages of temperature and mass fractions of NO, CO, and H_2 at $x/D = 30$. Courtesy of [41].

similar to the conditional source term estimation method by [48], which is described below. The unconditional scalar dissipation rate was determined from a dynamic model [34]. This study is the first demonstration of combustion LES of a realistic configuration using a detailed description of the chemistry. The results are promising, especially for NO, but because of the cross sectional averaging of the scalar dissipation rate, local fluctuations of this quantity are not considered and the potential of LES is not fully realized. Also, this model cannot be easily applied in simulations of more complex flow fields. In a more recent formulation, the Eulerian flamelet model [27], the flamelet equations are rewritten in an Eulerian form, which leads to a full coupling with the LES solver, and thereby enables the consideration of the resolved fluctuations of the scalar dissipation rate in the combustion model. Examples of the results are shown in Fig. 10.6. The resolved scalar dissipation rate field is dominated by features occurring on the large scale of the turbulence. Layers of high dissipation rate alternate with low dissipation rate regions. In the LFM results, as well as in several earlier RANS-type modeling studies [51], where these fluctuations are not considered, some heat release occurs on the rich partially premixed side of the flame, which leads to strong CO formation in these regions. Accounting for the richness of the predicted spatial distribution of

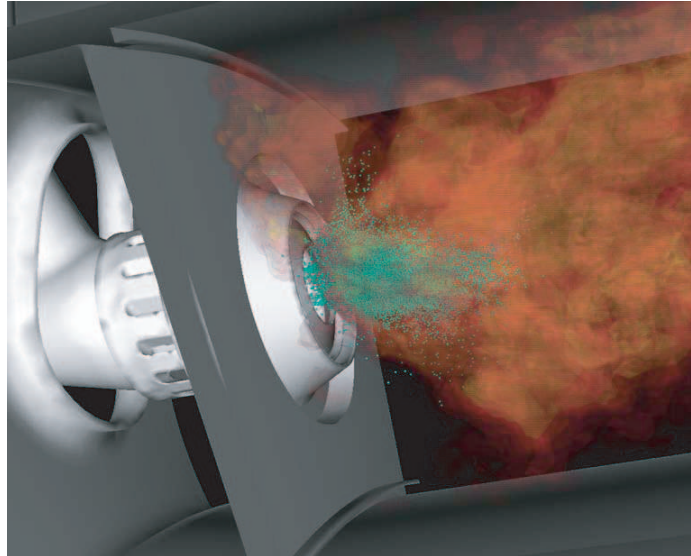


Figure 10.7: Large-eddy simulation of a modern Pratt & Whitney gas turbine combustor ([49, 50]). The combustor bulkhead is to the left of the flame. Fuel and air enter the combustor through the injector/swirler assembly, which has three different air passages. Fuel droplets are shown in green. The remaining color representation shows iso-surfaces of the temperature. Dilution by secondary air occurs to the right of the figure and is not shown. Courtesy of [41].

the scalar dissipation rate substantially improves the comparison with the experimental data by suppressing the heat release in the rich regions, and hence the formation of CO.

10.14 LES of Real Combustion Devices

Several investigators have reported simulations of real combustion devices with LES. Most of these use either structured or block-structured curvi-linear meshes, which cannot deal with very complex geometries. Simulations of gas turbines, for instance, typically require unstructured meshing strategies, for which the formulation of energy conserving and accurate numerical algorithms, of particular importance for combustion LES, proves to be even more difficult. Among the few fully unstructured multiphysics LES codes are the AVBP code of CERFACS, which has been applied in many studies on combustion instabilities and flashback in premixed gas turbines [52, 53], and the Stanford CDP code1 CDP solves both low-Ma number variable-density and fully compressible LES equations using the unstructured collocated finite volume discretization of [54] and its subsequent

improvements by [55]. It applies Lagrangian particle tracking with adequate models for breakup, particle drag, and evaporation for liquid fuel sprays. Closure for subfilter transport terms and other turbulence statistics is accomplished using dynamic models. The FPV combustion model is applied to model turbulence/chemistry interactions. The code is parallelized with advanced load balancing procedures for both gas and particle phases. Computations have been conducted with over two billion cells using several thousand processors. A state-of-the-art simulation of a section of a modern Pratt & Whitney gas turbine combustor that uses all these capabilities has been performed [49, 50] and is shown in Fig. 10.7. The figure shows the spray and temperature distribution and demonstrates the complexity of the geometry and the associated flow physics.

Bibliography

- [1] P. A. Libby and F. A. Williams. *Fundamental aspects and a review*. Academic Press, 1994.
- [2] F. A. Williams. *Combustion Theory, Second Edition*. The Benjamin Cummings Publishing Co. Menlo Park, 1985.
- [3] D. B. Spalding. Mixing and chemical reaction in steady confined turbulent flames. *Thirteenth Symposium (International) on Combustion, The Combustion Institute, Pittsburgh*, pages 649–657, 1971.
- [4] B. F. Magnussen and B. H. Hjertager. On mathematical models of turbulent combustion with special emphasis on soot formation and combustion, journal = Sixteenth Symposium (International) on Combustion, The Combustion Institute, Pittsburgh, volume = 19, pages = 719–729., 1977.
- [5] S. B. Pope. Computations of turbulent combustion: Progress and challenges. *Twenty-Third Symposium (International) on Combustion, The Combustion Institute, Pittsburgh*, 23:591–612, 1990.
- [6] E. E. O'Brien. The probability density function (pdf) approach to reacting turbulent flows. In P. A. Libby and F. A. Williams, editors, *Turbulent Reacting Flows*, pages 67–75. Springer-Verlag, Berlin, 1980.
- [7] S.B. Pope. Pdf methods for turbulent reactive flows. *Prog. Energy Combust. Sci.*, 11:119–192, 1985.
- [8] S.B. Pope. *Turbulent Flows*. Cambridge University Press, Cambridge, U.K., 2000.

- [9] S. B. Pope and M. S. Anand. Flamelet and distributed combustion in premixed turbulent flames. *Twentieth Symposium (International) on Combustion, The Combustion Institute, Pittsburgh*, 25:403–410, 1984.
- [10] S. B. Pope. A Monte Carlo method for the pdf equations of turbulent reactive flow. *Combust. Sci. and Tech.*, 25:159–174, 1981.
- [11] F. A. Williams. Recent advances in theoretical descriptions of turbulent diffusion flames. In S. N. B. Murthy, editor, *Turbulent mixing in nonreactive and reactive flows*, pages 189–208. Plenum Press, New York, 1975.
- [12] N. Peters. Local quenching of diffusion flamelets and non-premixed turbulent combustion. *Western States Section of the Combustion Institute, paper WSS 80-4, Spring Meeting, Irvine*, 1980.
- [13] V. R. Kuznetsov. Effect of turbulence on the formation of large superequilibrium concentration of atoms and free radicals in diffusion flames. *Mehan. Zhidkosti Gasa*, 6:3–9, 1982.
- [14] N. Peters. *Progress in Energy and Combustion Science*, 10:319–339, 1984.
- [15] N. Peters. Laminar flamelet concepts in turbulent combustion. *Twenty-First Symposium (International) on Combustion, The Combustion Institute, Pittsburgh*, pages 1231–1250, 1986.
- [16] K. N. C. Bray and N. Peters. Laminar flamelets in turbulent flames. In P. A. Libby and F. A. Williams, editors, *Turbulent Reacting Flows*, pages 63–113. Academic Press, 1994.
- [17] K. N. C. Bray and J. B. Moss. A unified statistical model of the premixed turbulent flame. *Acta Astronautica*, 4:291–319, 1977.
- [18] P. A. Libby and K. N. C. Bray. Countergradient diffusion in premixed turbulent flames. *AIAA J.*, 19:205–213, 1981.
- [19] Libby P. A. Masuya G. Bray, K. N. C. and J. B. Moss. Turbulence production in premixed turbulent flames. *Combust. Sci. and Tech.*, 25:127–140, 1981.
- [20] Libby P. A. Bray, K. N. C. and J. B. Moss. Flamelet crossing frequencies and mean reaction rates in premixed turbulent combustion. *Combust. Sci. and Tech.*, 41:143–172, 1984.
- [21] K. N. C. Bray and P. Libby. Passage time and flamelet crossing frequencies in premixed turbulent combustion. *Combust. Sci. and Tech.*, 47:253–274, 1986.

- [22] K. N. C. Bray and P. Libby. Recent developments in the BML model of premixed turbulent combustion. In P. A. Libby and F. A. Williams, editors, *Turbulent Reacting Flows*, pages 115–151. Academic Press, 1994.
- [23] Veynante D. Lacas F. Maistret E. Darabiha N. Candel, S. M. and T. J. Poinsot. Coherent flamelet model: Applications and recent extensions. In B. Larrouturou, editor, *Recent Advances in Combustion Modelling, Series on Advances in Mathematics for Applied Sciences*, volume 6, pages 19–64. World Scientific, Singapore, 1990.
- [24] Veynante D. Duclos, J. M. and T. J. Poinsot. A comparison of flamelet models for premixed turbulent combustion. *Combust. Flame*, 95:101–117, 1993.
- [25] A. Trouv  and T. J. Poinsot. The evolution equation for the flame surface density in turbulent premixed combustion. *J. Fluid Mech.*, 278:1–31, 1994.
- [26] S. Ghosal and P. Moin. The basic equations for the large eddy simulation of turbulent flows in complex geometry. *J. Comput. Phys.*, 118:24–37, 1995.
- [27] H. Pitsch. Improved pollutant predictions in large-eddy simulations of turbulent non-premixed combustion by considering scalar dissipation rate fluctuations. *Proc. Combust. Inst.*, 29:1971–78, 2002.
- [28] H. Pitsch and H. Steiner. Large-eddy simulation of a turbulent piloted methane-air diffusion flame (sandia flame d). *Phys. Fluid*, 12:2541–2554, 2000.
- [29] H. Pitsch and V. Raman. Large-eddy simulation of a bluff-body stabilized non-premixed flame using a recursive-refinement procedure. *Combust. Flame*, 142:329–47, 2005.
- [30] S. H. Kim and K. Y. Huh. Use of conditional moment closure model to predict no formation in a turbulent CH₄/H₂ flame over a bluff-body. *Combust. Flame*, 130(1-2):94–111, 2002.
- [31] M. Muradoglu, K. Liu, and S. B. Pope. Pdf modeling of a bluff-body stabilized turbulent flame. *Combust. Flame*, 132(1-2):115–37, 2003.
- [32] R. w. Bilger. The structure of diffusion flames. *Combust. Sci. Technol.*, 13:155, 1976.
- [33] H. Pitsch and N. Peters. A consistent flamelet formulation for non-premixed combustion considering differential diffusion effects. *Combust. Flame*, 114:26–40, 1998.

- [34] C. D. Pierce and P. Moin. A dynamic model for subgrid-scale variance and dissipation rate of a conserved scalar. *Phys. Fluids*, 10:3041–44, 1998.
- [35] A. W. Cook and J. J. Riley. A subgrid model for equilibrium chemistry in turbulent flows. *Phys. Fluids*, 6:2868–70, 1994.
- [36] R. O. Fox. Computational models for turbulent reacting flows. *Cambridge Univ. Press*, 2003.
- [37] J. Jimenez, A. Liñán, M. M. Rogers, and F. J. Higuera. A priori testing of subgrid models for chemically reacting non-premixed turbulent shear flows. *J. Fluid Mech.*, 349:149–71, 1997.
- [38] C. Wall, B. Boersma, and P. Moin. An evaluation of the assumed beta pdf subgrid-scale model for les of non-premixed, turbulent combustion with heat release. *Phys. Fluids*, 12(10):2522–29, 2000.
- [39] C. Tong. Measurements of conserved scalar filtered density function in a turbulent jet. *Phys. Fluids*, 13(10):2923–37, 2001.
- [40] C. Tong, D. Wang, R. S. Barlow, and A. N. Karpetis. Investigation of scalar filtered mass density function in turbulent partially premixed flames. *Jt. Meet. U.S. Sect. Combust. Inst., Philadelphia, PA*, E23, 2005.
- [41] H. Pitsch. Large-eddy simulation of turbulent combustion. *Ann. Rev. Fluid Mech.*, 38:453–482, 2006.
- [42] B.B. Dally, A.R. Masri, R. S. Barlow, and G. J. Fietchner. Instantaneous and mean compositional structure of bluff-body stabilized nonpremixed flames. *Combust. Flame*, 114:119–148, 1998.
- [43] S. Pope. Ten questions concerning the large-eddy simulation of turbulent flows. *N. J. Phys.*, 6:35, 2004.
- [44] R. S. Barlow and J. H. Frank. Effect of turbulence on species mass fractions in methane/air jet flames. *Proc. Combust. Inst.*, 27:1087–95, 1998.
- [45] S. S. Girimaji. Analysis and modeling of subgrid scalar mixing using numerical data. *Phys. Fluids*, 8:1224–36, 1996.
- [46] H. Pitsch and H. Steiner. Scalar mixing and dissipation rate in large-eddy simulations of non-premixed turbulent combustion. *Phys. Fluid*, 28:41–49, 2000.

- [47] C. T. Bowman, R. K. Hanson, D. F. Davidson, W. C. Gardiner Jr., and et al V. Lissianski. *Gri-mech 2.11*, http://www.me.berkeley.edu/gri_mech/, 1995.
- [48] W. K. Bushe and H. Steiner. Conditional moment closure for large eddy simulation of non-premixed turbulent reacting flows. *Phys. Fluids*, 11:1896–906, 1999.
- [49] K. Mahesh, G. Constantinescu, S. Apte, G. Iaccarino, f. Ham, and P. Moin. Large eddy simulation of reacting turbulent flows in complex geometries. *ASME J Appl. Mech.*, 2005.
- [50] S. Apte. Large-eddy simulation of realistic gas turbine combustors. *AIAA J.*, 2005.
- [51] R. S. Barlow. *Proc. Fifth Int. Workshop Meas. Comput. Turbulent Nonpremixed Flames*, 2000.
- [52] Poinsot T Koch R Schildmacher K Selle L, Lartigue G. Compressible large eddy simulation of turbulent combustion in complex geometry on unstructured meshes. *Combust. Flame*, 137(4):489–505, 2004.
- [53] Poinsot T Ducruix S Lacas F Veynante D. Sommerer Y, Galley D. Large eddy simulation and experimental study of flashback and blow-off in a lean partially premixed swirled burner. *J. Turb.*, 5:037, 2004.
- [54] K. Mahesh, G. Constantinescu, and P. Moin. A numerical method for large-eddy simulation in complex geometries. *J. Comp. Phys.*, 197:215–40, 2004.
- [55] F. Ham and G. Iaccarino. Energy conservation in collocated discretization schemes on unstructured meshes. In *CTR Annual Research Briefs*. Stanford, CA: Center for Turbulence Research, NASA Ames/Stanford Univ., 2004.

Lecture 11

Premixed Turbulent Combustion: The Regime Diagram

11.1 Regimes in Premixed Turbulent Combustion

Diagrams defining regimes of premixed turbulent combustion in terms of velocity and length scale ratios have been proposed by Borghi (1985) [1], Peters (1986) [2], Abdel-Gayed and Brandley (1989) [3], Poinsot et al. (1990) [4] and many others. For scaling purposes it is useful to assume equal diffusivities for all reactive scalars, a Schmidt number $\text{Sc} = \nu/D$ of unity and to define the flame thickness ℓ_F and the flame time t_F as

$$\ell_F = \frac{D}{s_L}, \quad t_F = \frac{D}{s_L^2}. \quad (11.1)$$

Then, using $\nu = D$ and the turbulent intensity v' and the turbulent length scale ℓ introduced in Lecture 10, we define the turbulent Reynolds number as

$$\text{Re} = \frac{v'\ell}{s_L \ell_F} \quad (11.2)$$

and the turbulent Damköhler number

$$\text{Da} = \frac{s_L \ell}{v' \ell_F}. \quad (11.3)$$

Furthermore, with the Kolmogorov time, length, and velocity scales defined in Lecture 10, we introduce two turbulent Karlovitz numbers, the first one defined as

$$Ka = \frac{t_F}{t_\eta} = \frac{\ell_F^2}{\eta^2} = \frac{v_\eta^2}{s_L^2} \quad (11.4)$$

measures the ratios of the flame scales in terms of the Kolmogorov scales. Using the definitions Eqs. (10.39)–(10.40) with $\nu = D$ and Eq. (10.43) taken as equality it is seen that Eqs. (11.2)–(11.4) can be combined to show that

$$Re = Da^2 Ka^2. \quad (11.5)$$

Referring to the discussion about the appropriate reaction zone thickness δ in premixed flames, a second Karlovitz number Ka_δ may be introduced as

$$Ka_\delta = \frac{\ell_\delta^2}{\eta^2} = \delta^2 K \quad (11.6)$$

where $\ell_\delta = \delta \ell_F$ has been used.

In the following we will discuss a regime diagram, Fig. 11.1, for premixed turbulent combustion, where the logarithm of v'/s_L is plotted versus the logarithm of ℓ/ℓ_F . Using Eqs. (11.1) and (11.2) and the definition of the Kolmogorov length scale Eq. (10.39) where, for scaling purposes, ε is set equal to v'^3/ℓ , the ratios v'/s_L and ℓ/ℓ_F may be expressed in terms of the two non-dimensional numbers Re and Ka as

$$\frac{v'}{s_L} = Re \left(\frac{\ell}{\ell_F} \right)^{-1} = Ka^{2/3} \left(\frac{\ell}{\ell_F} \right)^{1/3}. \quad (11.7)$$

Using these relations the lines $Re = 1$, $Ka = 1$ represent boundaries between different regimes of premixed turbulent combustion in Fig. 11.1. Other boundaries of interest are the line $v'/s_L = 1$, which separates the wrinkled flamelets from the corrugated flamelets, and the line denoted by $Ka_\delta = 1$, which separates thin reaction zones from broken reaction zones.

The line $Re = 1$ separates all turbulent flame regimes characterized by $Re > 1$ from the regime of laminar flames ($Re < 1$), which is situated in the lower-left corner of the diagram. As stated in the introduction, we will consider turbulent combustion in the limit of large Reynolds numbers, which corresponds to a region sufficiently removed from the line $Re = 1$ towards the upper right in Fig. 11.1. We will not consider the wrinkled flamelet regime, because it is not of much practical interest. In that regime, where $v' < s_L$, the turn-over velocity v' of even the large eddies is not large enough to compete with the advancement of the flame front with the laminar burning velocity s_L . Laminar

flame propagation therefore is dominating over flame front corrugations by turbulence. We will also not consider the broken reaction zones regime in any detail for reasons to be discussed at the end of this lecture.

Among the remaining two regimes, the corrugated flamelets regime is characterized by the inequalities $\text{Re} > 1$ and $\text{Ka} < 1$. In view of Eq. (11.4) the latter inequality indicates that $\ell_F < \eta$, which means that the entire reactive-diffusive flame structure is embedded within eddies of the size of the Kolmogorov scale, where the flow is quasi-laminar. Therefore the flame structure is not perturbed by turbulent fluctuations and remains quasi-steady.

The boundary of the corrugated flamelets regime to the thin reaction zones regime is given by $\text{Ka} = 1$, which, according to Eq. (11.4), is equivalent to the condition that the flame thickness is equal to the Kolmogorov length scale. This is called the Klimov-Williams criterion. From Eq. (11.4) also follows that for $\text{Ka} = 1$ the flame time is equal to the Kolmogorov time and the burning velocity is equal to the Kolmogorov velocity.

The thin reaction zones regime is characterized by $\text{Re} > 1$, $\text{Ka}_\delta < 1$, and $\text{Ka} > 1$, the last inequality indicating that the smallest eddies of size η can enter into the reactive-diffusive flame structure since $\eta < \ell_F$. These small eddies are still larger than the inner layer thickness ℓ_δ and can therefore not penetrate into that layer. The non-dimensional thickness δ of the inner layer in a premixed flame is typically one tenth, such that ℓ_δ is one tenth of the preheat zone thickness, which is of the same order of magnitude as the flame thickness ℓ_F . Using Eq. (11.6) we see that the line $\text{Ka}_\delta = 1$ corresponds with $\delta = 0.1$ to $\text{Ka} = 100$. This value is used in Fig. 11.1 for the upper limit of the thin reaction zones regime. It seems roughly to agree with the flamelet boundary obtained in numerical studies by Poinsot et al. (1991) [5], where two-dimensional interactions between a laminar premixed flame front and a vortex pair were analyzed. These simulations correspond to $\text{Ka} = 180$ for cases without heat loss and $\text{Ka} = 25$ with small heat loss. The authors argued that since quenching by vortices occurs only for larger Karlovitz numbers, the region below the limiting value of the Karlovitz number should correspond to the flamelet regime.

We will now enter into a more detailed discussion of the two flamelet regimes. In the regime of corrugated flamelets there is a *kinematic* interaction between turbulent eddies and the advancing laminar flame. Here we have with $\text{Ka} < 1$

$$v' \geq s_L \geq v_\eta. \quad (11.8)$$

To determine the size of the eddy that interacts locally with the flame front, we set the turn-over

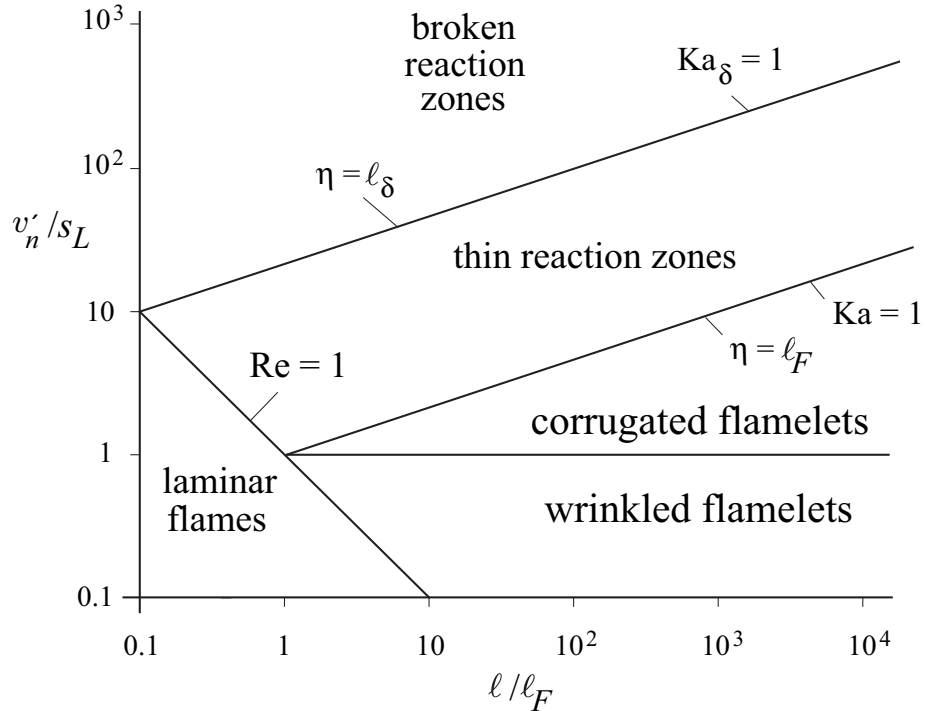


Figure 11.1: Kinematic interaction between a propagating flame front and an eddy of the size $\ell_n = \ell_G$. The dashed line marks the thickness of the preheat zone.

velocity v_n in Eq. (10.43) equal to the burning velocity s_L . This determines the corresponding length ℓ_n as the Gibson scale (cf. Peters (1986) [2])

$$\ell_G = \frac{s_L^3}{\varepsilon}. \quad (11.9)$$

Only eddies of size ℓ_G , which have a turnover velocity $v_n = s_L$ can interact with the flame front. This is illustrated in Fig. 11.2. Since the turn-over velocity of the large eddies is larger than the laminar burning velocity, these eddies will push the flame front around, causing a substantial corrugation. Smaller eddies of size $\ell_n < \ell_G$ having a turnover velocity smaller than s_L will not even be able to wrinkle the flame front. Replacing ε by v'^3/ℓ one may also write Eq. (11.9) in the form

$$\frac{\ell_G}{\ell} = \left(\frac{s_L}{v'} \right)^3. \quad (11.10)$$

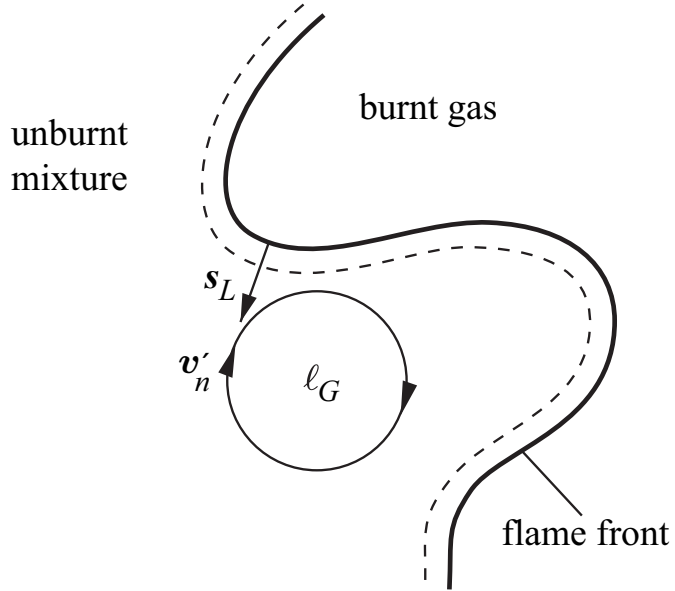


Figure 11.2: Kinematic interaction between a propagating flame front and an eddy of the size $\ell_n = \ell_G$. The dashed line marks the thickness of the preheat zone.

A graphical derivation of the Gibson scale ℓ_G within the inertial range is shown in Fig. 11.3. Here, following Kolmogorov scaling in the inertial range given by Eq. (10.43), the logarithm of the velocity v_n is plotted over the logarithm of the length scale ℓ_n . We assume v' and ℓ and thereby ε , and also ν and thereby v_η and η to be fixed. If one enters on the vertical axis with the burning velocity s_L equal to v_n into the diagram, one obtains ℓ_G as the corresponding length scale on the horizontal axis. The laminar flame thickness ℓ_F , which is smaller than η in the corrugated flamelets regime is also shown. This diagram illustrates the limiting values of ℓ_G : If the burning velocity is equal to v' , ℓ_G is equal to the integral length scale ℓ . This case corresponds to the borderline between corrugated and wrinkled flamelets in Fig. 11.1. Conversely, if s_L is equal to the Kolmogorov velocity v_η , ℓ_G is equal to η , which corresponds to the line $Ka = 1$ in Fig. 11.1.

It has been shown by Peters (1992) [6] that the Gibson scale ℓ_G is the lower cut-off scale of the scalar spectrum function in the corrugated flamelets regime. At that cut-off there is only a weak change of slope in the scalar spectrum function. This is the reason why the Gibson scale is difficult

to measure. The stronger diffusive cut-off occurs at the Obukhov-Corrsin scale defined by

$$\ell_C = \left(\frac{D^3}{\varepsilon} \right)^{1/4}. \quad (11.11)$$

Since we have assumed $D = \nu$ this scale is equal to the Kolmogorov scale η .

The next flamelet regime in Fig. 11.1 is the regime of thin reaction zones. As noted earlier, since $\eta < \ell_F$ in this regime, small eddies can enter into the preheat zone and increase scalar mixing, but they cannot penetrate into the inner layer since $\eta > \ell_\delta$. The burning velocity is smaller than the Kolmogorov velocity which would lead to a Gibson scale that is smaller than η . Therefore the Gibson scale has no meaning in this regime.

A time scale, however, can be used in the thin reaction zones regime to define a characteristic length scale using Kolmogorov scaling in the inertial range. That time scale should represent the response of the thin reaction zone and the surrounding diffusive layer to unsteady perturbations. The appropriate time is the as the flame time t_F . Combining t_F with the diffusivity D , the resulting diffusion thickness ℓ_D

$$\ell_D = \sqrt{D t_F} \quad (11.12)$$

is then of the order of the flame thickness ℓ_F . By setting $t_n = t_F$ in Eq. (10.45), one obtains the length scale

$$\ell_m = (\varepsilon t_F^3)^{1/2}. \quad (11.13)$$

An appropriate interpretation is that of a mixing length scale, which has been advocated based on the concept of thin reaction zones by Peters (1999) [7]. It is the size of an eddy within the inertial range which has a turnover time equal to the time needed to diffuse scalars over a distance equal to the diffusion thickness ℓ_D . During its turnover time an eddy of size ℓ_m will interact with the advancing reaction front and will be able to transport preheated fluid from a region of thickness ℓ_D in front of the reaction zone over a distance corresponding to its own size. This is schematically shown in Fig. 11.4. Much smaller eddies will also do this but since their size is smaller, their action will be masked by eddies of size ℓ_m . Larger eddies have a longer turn-over time and would therefore be able to transport thicker structures than those of thickness ℓ_D . They will therefore corrugate the broadened flame structure at scales larger than ℓ_m . The physical interpretation of ℓ_m is therefore that of the maximum distance that preheated fluid can be transported ahead of the flame. As a mixing length scale ℓ_m had already been identified by Zimont (1979) [8].

Differently from the Gibson length scale the mixing length scale can be observed experimen-

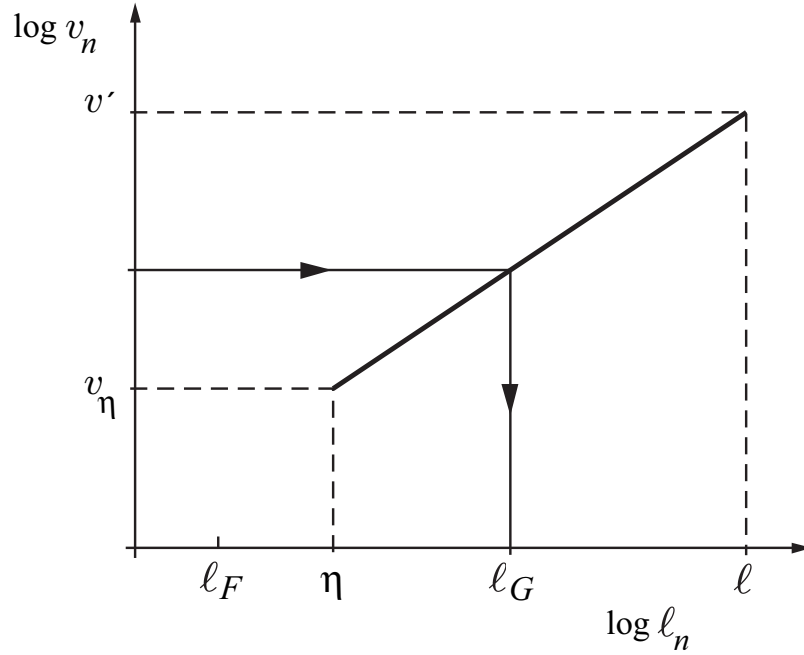


Figure 11.3: Graphical illustration of the Gibson scale ℓ_G within the inertial range for the corrugated flamelets regime.

tally. Changes of the instantaneous flame structure with increasing Karlovitz numbers have been measured by Buschmann et al. (1996) [9] who used 2D-Rayleigh thermometry combined with 2D laser-induced fluorescence on a turbulent premixed Bunsen flame. They varied the Karlovitz number between 0.03 and 13.6 and observed at $\text{Ka} > 5$ thermal thicknesses that largely exceed the size of the smallest eddies in the flow.

The derivation of ℓ_m also is illustrated in a diagram in Fig. 11.5, showing Eq. (10.45) in a log-log plot of t_n over ℓ_n . If one enters the time axis at $t_F = t_n$, the mixing length scale ℓ_m on the length scale axis is obtained. If t_F is equal to the Kolmogorov time t_η , Fig. 11.5 shows that ℓ_m is equal to the Kolmogorov scale η . In this case, one obtains $\ell_m = \ell_D \approx \ell_F$ at the border between the thin reaction zones regime and the corrugated flamelets regime. Similarly, from Fig. 11.5, if the flame time t_F is equal to the integral time $\tau = k/\varepsilon \approx \ell/v'$, ℓ_m is equal to the integral length scale. This corresponds to $\text{Da} = 1$, which Borghi (1985) [1] interpreted as the borderline between two regimes in turbulent combustion. However, it merely sets a limit for the mixing scale ℓ_m which cannot increase beyond the integral scale ℓ .

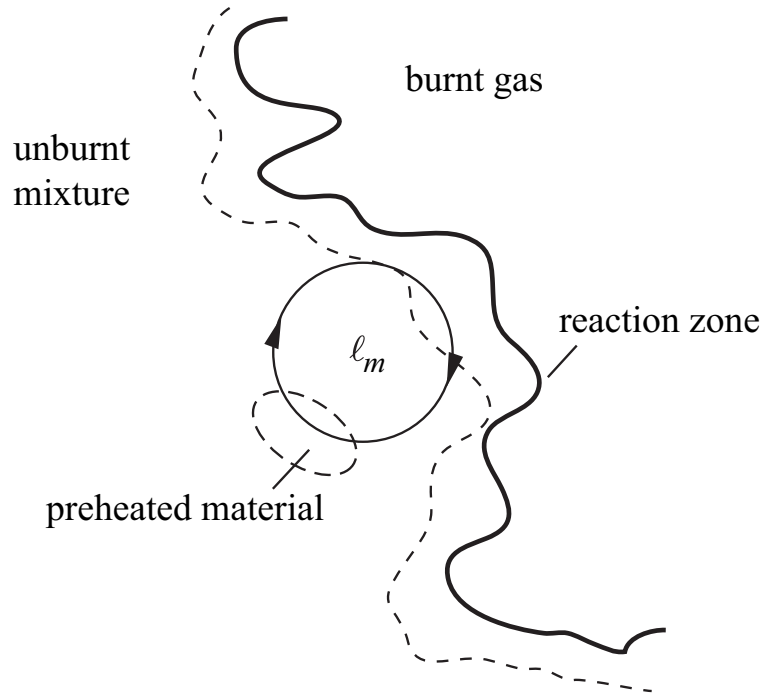


Figure 11.4: Transport of preheated gas from a region of thickness ℓ_D by an eddy of size $\ell_n = \ell_m$ during half a turnover time $t_n = t_q$.

The diffusion thickness ℓ_D , lying between η and ℓ_m , is also marked in Fig. 11.5. There also appears the Obukhov-Corrsin scale ℓ_C , which is the lower cut-off scale of the scalar spectrum in the thin reaction zones regime. Since we have assumed $\nu = D$, the Obukhov-Corrsin scale ℓ_C is equal to the Kolmogorov length scale η .

As a final remark related to the corrugated flamelets regime and the thin reaction zones regime, it is important to realize that turbulence in high Reynolds number turbulence is intermittent and the dissipation ε has a statistical distribution. This refinement of Kolmogorov's theory has led to the notion of intermittency or "spottiness" of the activity of turbulence in a flow field (cf. Monin and Yaglom (1975) [10]). This may have important consequences on the physical appearance of turbulent flames at sufficiently large Reynolds numbers. One may expect that the flame front shows manifestations of strong local mixing by small eddies as in the thin reaction zones regime as well as rather smooth regions where corrugated flamelets appear. The two regimes discussed

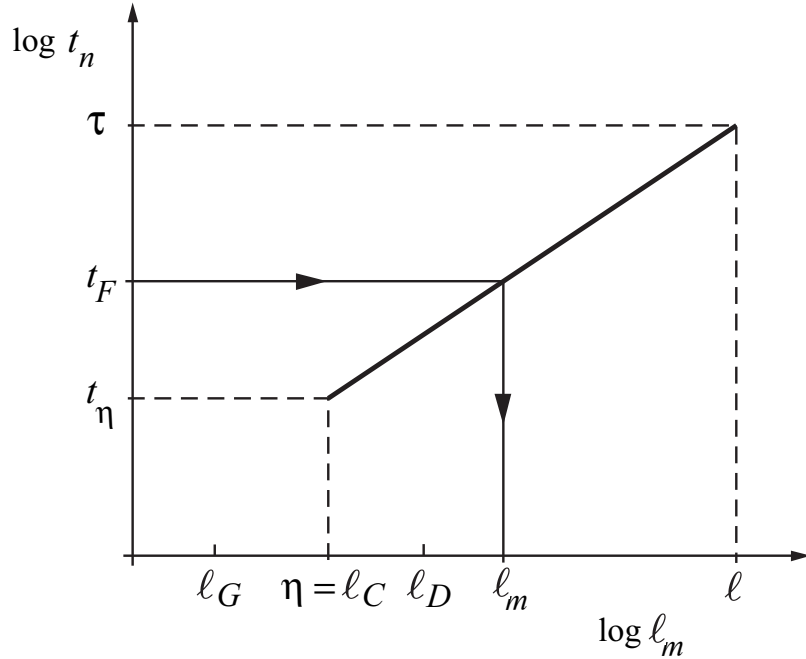


Figure 11.5: Graphical illustration of the mixing scale ℓ_m within the inertial range for the thin reaction zones regime.

above may therefore both be apparent in the same experimentally observed turbulent flame.

Beyond the line $Ka_\delta = 1$ there is a regime called the broken reaction zones regime where Kolmogorov eddies are smaller than the inner layer thickness ℓ_δ . They may therefore enter into the inner layer and perturb it with the consequence that chemistry breaks down locally due to enhanced heat loss to the preheat zone followed by temperature decrease and the loss of radicals. When this happens the flame will extinguish and fuel and oxidizer will interdiffuse and mix at lower temperatures where combustion reactions have ceased.

In a series of papers Mansour et al. (1992) [11], Chen et al. (1996) [12], Chen and Mansour (1997) [13] and Mansour et al. (1998) [14] have investigated highly stretched premixed flames on a Bunsen burner, which were surrounded by a large pilot. Among the flames F1, F2 and F3 that were investigated, the flame F1 with an exit velocity of 65 m/s was close to total flame extinction which occurred on this burner at 75 m/s. A photograph of the flame is shown in Chen et al. (1996) [12]. Mansour (1999) [15] has reviewed the recent results obtained from laser-diagnostics applied

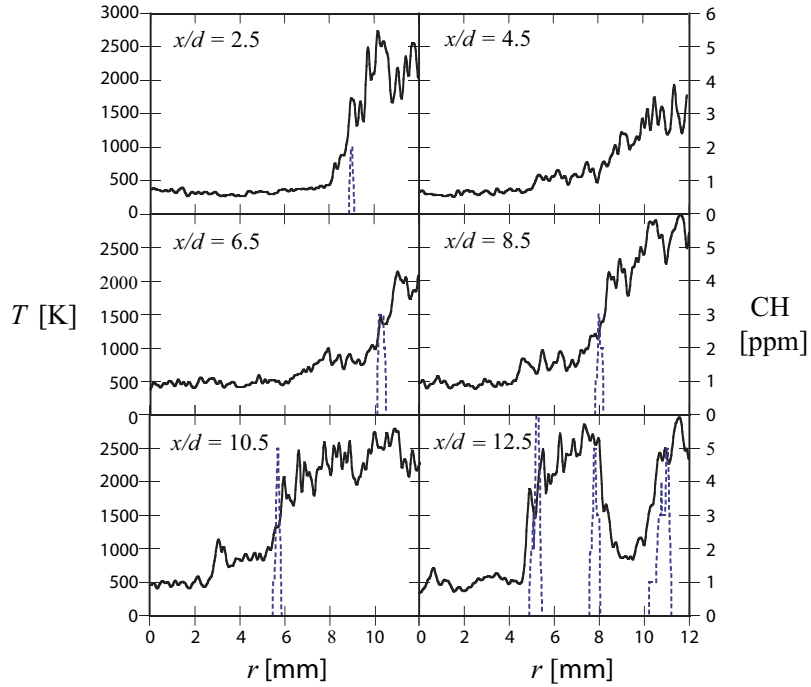


Figure 11.6: Line cuts of one-dimensional temperature and CH concentration profiles in the images presented in Mansour et al. (1998).

to turbulent premixed and partially premixed flames.

Mansour et al. (1998) [14] have shown that the flame F1 is on the borderline to the broken flamelets regime in Fig. 11.1 having a Karlovitz number of $Ka = 91$. In simultaneous temperature and CH measurements shown in Fig. 11.6 they found a thin reaction zone, as deduced from the CH profile and steep temperature gradients in the vicinity of that zone. There also was evidence of occasional extinction of the reaction zone. This corresponds to instantaneous shots where the CH profile was absent as in the picture on the upper r.h.s. in Fig. 11.6. Such extinction events do not occur in the flame F3 which has a Karlovitz number of 23 and is located in the middle of the thin reaction zones regime. It can be expected that local extinction events would appear more frequently, if the exit velocity is increased and the flame enters into the broken reaction zones regime. This will occur at an exit velocity close to 75 m/s so frequently that the entire flame extinguishes. Therefore one may conclude that in the broken reaction zones regime a premixed flame is unable to survive.

The pictures in Fig. 11.6 also show strong perturbations of the temperature profile on the

unburnt side of the reaction zone. This is most evident in the picture on the lower l.h.s., where the temperature reaches more than 1100 K but falls back to 800 K again. This seems to be due to small eddies that enter into the preheat zone and confirms the concept of the thin reaction zones regime.

11.2 Regimes in Premixed Combustion LES

A similar diagram as in Fig. 11.1 can be constructed for LES using the filter size Δ as the length scale and the subfilter velocity fluctuation v'_Δ as the velocity scale. Such a representation introduces both physical and modeling parameters into the diagram. A change in the filter size, however, also leads to a change in the subfilter velocity fluctuation. This implies that the effect of the filter size, which is a numerical or model parameter, cannot be studied independently. In response to this issue, an LES regime diagram for characterizing subfilter turbulence/flame interactions in premixed turbulent combustion was proposed by Pitsch & Duchamp de Lageneste (2002) [16], and recently extended by Pitsch (2005) [17]. This diagram is shown in Fig. 11.7. In contrast to the RANS regime diagrams, Δ/ℓ_F and the Karlovitz number Ka are used as the axes of the diagram. The Karlovitz number, defined as the ratio of the Kolmogorov timescale to the chemical timescale, describes the physical interaction of flow and combustion on the smallest turbulent scales. It is defined solely on the basis of physical quantities, and is hence independent of the filter size.

The subfilter Reynolds and Damköhler numbers and the Karlovitz number relevant in the diagram are defined as

$$Re_\Delta = \frac{v'_\Delta \Delta}{s_L \ell_F}, \quad Da_\Delta = \frac{s_L \Delta}{v'_\Delta \ell_F}, \quad \text{and} \quad Ka = \frac{\ell_F^2}{\eta^2} = \left(\frac{v'^3 \ell_F}{s_L^3 \Delta} \right)^{1/2} \quad (11.14)$$

where η is the Kolmogorov scale.

In LES, the Karlovitz number is a fluctuating quantity, but for a given flow field and chemistry it is fixed. The effect of changes in filter size can therefore easily be assessed at constant Ka number. An additional benefit of this regime diagram is that it can be used equally well for DNS if Δ is associated with the mesh size. In the following, the physical regimes are briefly reviewed and relevant issues for LES are discussed.

The three regimes with essentially different interactions of turbulence and chemistry are the corrugated flamelet regime, the thin reaction zones regime, and the broken reaction zones regime. In the corrugated flamelet regime, the laminar flame thickness is smaller than the Kolmogorov

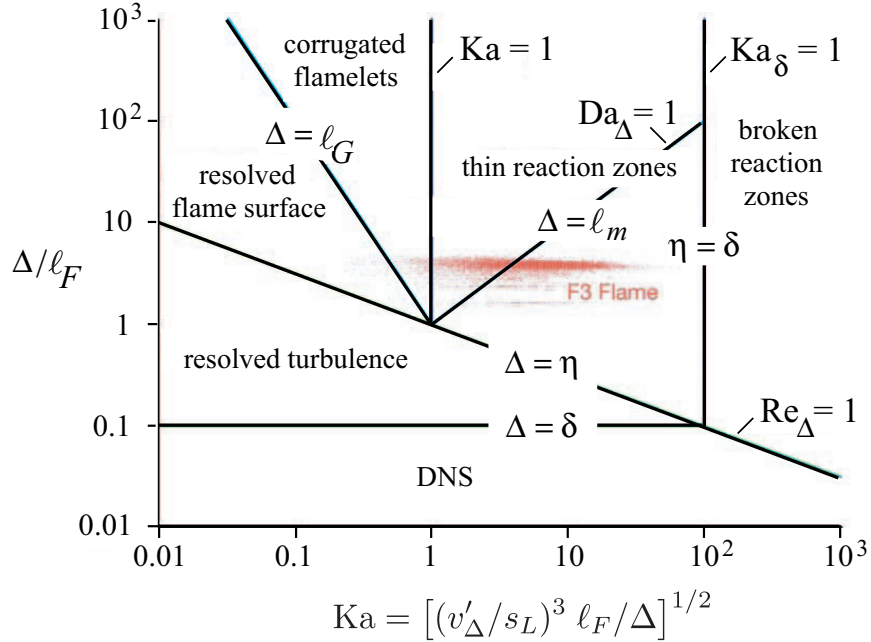


Figure 11.7: Regime diagram for large-eddy simulation (LES) and direct numerical simulation of premixed turbulent combustion (Pitsch (2006) [18]). Conditions for the simulation correspond to flame F3 of Chen et al. (1996). Courtesy of [18].

scale, and hence $Ka < 1$. Turbulence will therefore wrinkle the flame, but will not disturb the laminar flame structure. In the thin reaction zones regime, the Kolmogorov scale becomes smaller than the flame thickness, which implies $Ka > 1$. Turbulence then increases the transport within the chemically inert preheat region. In this regime, the reaction zone thickness ℓ_δ is still smaller than the Kolmogorov scale. Because the reaction zone, which appears as a thin layer within the flame, can be estimated to be an order of magnitude smaller than the flame thickness, the transition to the broken reaction zones regime occurs at approximately $Ka = 100$. The thin reaction zone retains a laminar structure in the thin reaction zones regime, whereas the preheat region is governed by turbulent mixing, which enhances the burning velocity. In the broken reaction zones regime, the Kolmogorov scale becomes smaller than the reaction zone thickness. This implies that the Karlovitz number based on the reaction zone thickness, Ka_δ , becomes larger than one.

Most technical combustion devices are operated in the thin reaction zones regime, because mixing is enhanced at higher Ka numbers, which leads to higher volumetric heat release and shorter combustion times. The broken reaction zones regime is usually avoided in fully premixed

systems. In this regime, mixing is faster than the chemistry, which leads to local extinction. This can cause noise, instabilities, and possibly global extinction. However, the broken reaction zones regime is significant, for instance, in partially premixed systems. In a lifted jet diffusion flame, the stabilization occurs by partially premixed flame fronts, which burn fastest at conditions close to stoichiometric mixture. Away from the stoichiometric surface toward the center of the jet, the mixture is typically very rich and the chemistry slow. Hence, the Ka number becomes large. This behavior has been found in the analysis of DNS results of a lifted hydrogen/air diffusion flame (Mizobuchi et al. (2002) [19]).

The effect of changing the LES filter width can be assessed by starting from any one of these regimes at large Δ/ℓ_F . As the filter width is decreased, the subfilter Reynolds number, Re_Δ , eventually becomes smaller than one. Then the filter size is smaller than the Kolmogorov scale, and no subfilter modeling for the turbulence is required. However, the entire flame including the reaction zone is only resolved if $\Delta < \delta$. In the corrugated flamelets regime, if the filter is decreased below the Gibson scale ℓ_G , which is the smallest scale of the subfilter flame-front wrinkling, the flame-front wrinkling is completely resolved. It is apparent that in the corrugated flamelet regime, where the flame structure is laminar, the entire flame remains on the subfilter scale, if Δ/ℓ_F is larger than one. This is always the case for LES. In the thin reaction zones regime, the preheat region is broadened by the turbulence. Peters (1999) [7] estimated the broadened flame thickness from the assumption that the timescale of the turbulent transport in the preheat zone has to be equal to the chemical timescale, which for laminar flames leads to the burning velocity scaling given in the beginning of this section. From this, the ratio of the broadened flame thickness ℓ_m and the filter size can be estimated as (Pitsch (2006) [18])

$$\frac{\ell_m}{\Delta} = \left(\frac{v'_\Delta \ell_F}{s_L \Delta} \right)^{3/2} = Ka \frac{\ell_F}{\Delta} = Da_\Delta^{-3/2}. \quad (11.15)$$

Hence, the flame is entirely on the subfilter scale as long as $Da_\Delta > 1$, and is partly resolved otherwise. It is important to realize that the turbulence quantities, especially v'_Δ , and hence most of the nondimensional numbers used to characterize the flame/turbulence interactions, are fluctuating quantities and can significantly change in space and time. To give an example, the variation of these quantities from a specific turbulent stoichiometric premixed methane/air flame simulation is shown in Fig. 11.7. This simulation was done for an experimental configuration with a nominal Ka number of $Ka = 11$, based on experimentally observed integral scales. The simulated conditions correspond to flame F3 of Chen et al. (1996) [12], and details of the simulation can be found in

Pitsch & Duchamp de Lageneste (2002) [20]. For a given point in time, the Ka number has been evaluated using appropriate subfilter models for all points on the flame surface. Because of the spatially varying filter size, but also because of heat losses to the burner, which locally lead to changes in ℓ_F , there is a small scatter in Δ/ℓ_F . Although the flame is mostly in the thin reaction zones regime, there is a strong variation in Ka number, ranging from the corrugated to the broken reaction zones regime.

Bibliography

- [1] R. W. Borghi. On the structure and morphology of turbulent premixed flames. *Recent Advances in the Aerospace Science*, pages 117–138, 1985.
- [2] N. Peters. Laminar flamelet concepts in turbulent combustion. *Twenty-First Symposium (International) on Combustion, The Combustion Institute, Pittsburgh*, pages 1231–1250, 1986.
- [3] R. G. Abdel-Gayed and D. Bradley. Combustion regimes and the straining of turbulent premixed flames. *Combust. Flame*, 76:213–218, 1989.
- [4] Veynante D. Poinsot, T. J. and S. Candel. Diagrams of premixed turbulent combustion based on direct simulation. *Twenty-Third Symposium (International) on Combustion, The Combustion Institute, Pittsburgh*, pages 613–619, 1990.
- [5] Veynante D. Poinsot, T. J. and S. Candel. Quenching process and premixed turbulent combustion diagrams. *J. Fluid Mech.*, 228:561–606, 1991.
- [6] N. Peters. A spectral closure for premixed turbulent combustion in the flamelet regime. *J. Fluid Mech.*, 242:611–629, 1992.
- [7] N. Peters. The turbulent burning velocity for large scale and small scale turbulence. *J. Fluid Mech.*, 384:107–132, 1999.
- [8] V. L. Zimont. Theory of turbulent combustion of a homogeneous fuel mixture at high reynolds numbers. *Combust. Expl. and Shock Waves*, 15:305–311, 1979.
- [9] Dinkelacker F. Schäfer T. Buschmann, A. and J. Wolfrum.
- [10] A. S. Monin and A. M. Yaglom. Statistical fluid mechanics. *Mechanics of Turbulence, Vol. 2, MIT Press*, 1975.

- [11] Chen Y.-C. Mansour, M. S. and N. Peters. The reaction zonestructure of turbulent premixed methane-helium-air flames near extinction. *Twenty-Fourth Symposium (International) on Combustion, The Combustion Institute, Pittsburgh*, pages 461–468, 1992.
- [12] J.-Y. Chen and W.-C. Chang. Flamelet and pdf modeling of co and no_x emissions from a turbulent, methane hydrogen jet nonpremixed flame. *Twenty-Sixth Symposium (International) on Combustion, The Combustion Institute, Pittsburgh*, pages 2207–2214, 1996.
- [13] Y.-C. Chen and M. Mansour. imultaneous rayleigh scattering and laser-induced ch fluorescence for reaction zone imaging in premixed hydrocarbon flames. *Appl. Phys.*, B64:599–609, 1997.
- [14] Peters N. Mansour, M. S. and Y.-C. Chen. Investigation of scalar mixing in the thin reaction zones regime using a simultaneous ch-lif/rayleigh laser technique. *Twenty-Seventh Symposium (International) on Combustion, the Combustion Institute, Pittsburgh*, pages 767–773, 1998.
- [15] M. S. Mansour. Turbulent premixed and partially premixed combustion diagnostics based on advanced laser techniques. *Mediterranean Combustion Symposium Antalya, Turkey*, pages 40–69, 1999.
- [16] H. Pitsch. Improved pollutant predictions in large-eddy simulations of turbulent non-premixed combustion by considering scalar dissipation rate fluctuations. *Proc. Combust. Inst.*, 29:1971–78, 2002.
- [17] H. Pitsch. A consistent level set formulation for large-eddy simulation of premixed turbulent combustion. *Combust. Flame*, 143:587–598, 2005.
- [18] H. Pitsch. Large-eddy simulation of turbulent combustion. *Ann. Rev. Fluid Mech.*, 38:453–482, 2006.
- [19] Y. Mizobuchi, S. Tachibana, J. Shinjo, S. Ogawa, and T. Takeno. A numerical analysis of the structure of a turbulent hydrogen jet lifted flame. *Proc. Combust. Inst.*, 29:2009–2015, 2002.
- [20] H. Pitsch and L. Duchamp de Lageneste. Large-eddy simulation of premixed turbulent combustion using a level-set approach. *Proc. Combust. Inst.*, 29:2001–8, 2002.

Lecture 12

The Level Set Approach for Turbulent Premixed Combustion

A model for premixed turbulent combustion, based on the non-reacting scalar G rather than on the progress variable, has been developed in recent years. It avoids complications associated with counter-gradient diffusion and, since G is non-reacting, there is no need for a source term closure. An equation for G can be derived by considering an iso-scalar surface

$$G(\mathbf{x}, t) = G_0. \quad (12.1)$$

As shown in Fig. 12.1 this surface divides the flow field into two regions where $G > G_0$ is the region of burnt gas and $G < G_0$ is that of the unburnt mixture. The choice of G_0 is arbitrary, but fixed for a particular combustion event. This is called the level set approach (cf. Sethian (1996) [1]).

We introduce the vector normal to the front in direction of the unburnt gas, as shown in Fig. 12.1, by

$$\mathbf{n} = -\frac{\nabla G}{|\nabla G|}. \quad (12.2)$$

In a general three-dimensional flow field the propagation velocity dx_f/dt of the front is equal to the sum of the flow velocity and the burning velocity in normal direction

$$\frac{dx_f}{dt} = \mathbf{v}_f + \mathbf{n} s_L. \quad (12.3)$$

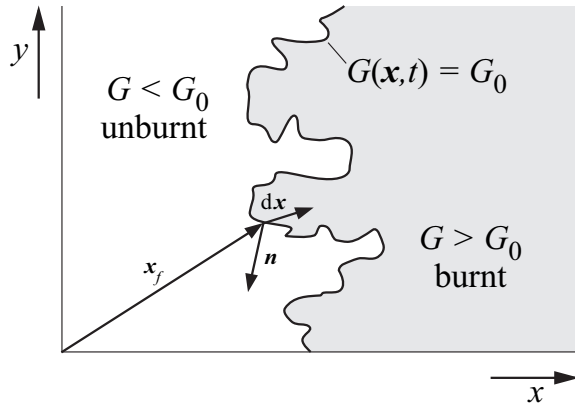


Figure 12.1: A schematic representation of the flame front as an iso-scalar surface $G(\mathbf{x}, t) = G_0$.

A field equation can now be derived by differentiating Eq. (12.1) with respect to t

$$\frac{\partial G}{\partial t} + \nabla G \cdot \frac{dx_f}{dt} = 0 \quad (12.4)$$

and by introducing Eq. (12.3) and $\nabla G = -n|\nabla G|$ to obtain the field equation

$$\frac{\partial G}{\partial t} + \mathbf{v}_f \cdot \nabla G = s_L |\nabla G|. \quad (12.5)$$

This equation was introduced by Williams (1985b) [2] and is known as the G -equation in the combustion literature. It is applicable to thin flame structures which propagate with a well-defined burning velocity. It therefore is well-suited for the description of premixed turbulent combustion in the corrugated flamelets regime, where it is assumed that the laminar flame thickness is smaller than the smallest turbulent length scale, the Kolmogorov scale. Therefore, the entire flame structure is embedded within a locally quasi-laminar flow field and the laminar burning velocity remains well-defined. Eq. (12.5) contains a local and a convective term on the l.h.s, a propagation term with the burning velocity s_L on the r.h.s but no diffusion term. G is a scalar quantity which is defined at the flame surface only, while the surrounding G -field is not uniquely defined. This originates simply from the fact that the kinematic balance Eq. (12.3) describes the dynamics of a two-dimensional surface while the G -equation Eq. (12.5) is an equation in three-dimensional space. In this respect $G(\mathbf{x}, t)$ differs fundamentally from the mixture fraction $Z(\mathbf{x}, t)$ used in nonpremixed combustion, which is a conserved scalar that is well defined in the entire flow field.

The distance x_n from the flame surface in normal direction, however, can be uniquely defined by introducing its differential increase towards the burnt gas side by

$$dx_n = -\mathbf{n} \cdot d\mathbf{x} = \frac{\nabla G}{|\nabla G|} \cdot d\mathbf{x}. \quad (12.6)$$

Here $d\mathbf{x}$ is a differential vector pointing from the front to its surroundings, as shown in Fig. 12.1. If we consider a frozen G -field, a differential increase of the G -level is given by

$$dG = \nabla G \cdot d\mathbf{x}. \quad (12.7)$$

Introducing this into Eq. (12.6) it is seen that the differential increase dx_n is related to dG by

$$dx_n = \frac{dG}{|\nabla G|}. \quad (12.8)$$

In the following the absolute value of the gradient of G at $G(\mathbf{x}, t) = G_0$ will be denoted by

$$\sigma = |\nabla G|. \quad (12.9)$$

Its value depends on the ansatz that is introduced in solving a particular problem using the G -equation.

For illustration purpose we choose as ansatz for the G -field

$$G(\mathbf{x}, t) - G_0 = x + F(y, z, t). \quad (12.10)$$

Thereby the flame front displacement $F(y, z, t)$ is assumed to be a single-valued function of y and z as shown for the two-dimensional case in Fig. 12.2. This assumption does not allow for multiple crossings of the flame surface. Note that x is the co-ordinate normal to the mean flame surface. In Fig. 12.2 G is measured in x -direction. It is also seen that the angle β between the flame normal direction $-\mathbf{n}$ and the x -axis is equal to the angle between the tangential direction t and the y -axis.

In the corrugated flamelets regime the reactive-diffusive flame structure is assumed to be thin compared to all length scales of the flow. Therefore it may be approximated by a jump of temperature, reactants and products. For such a very thin flame structure the iso-scalar surface $G(\mathbf{x}, t) = G_0$ is often defined to lie in the unburnt mixture immediately ahead of the flame structure.

Since Eq. (12.5) was derived from Eq. (12.3), the velocity v_f and the burning velocity s_L are values defined at the surface $G(\mathbf{x}, t) = G_0$. In numerical studies values for these quantities must

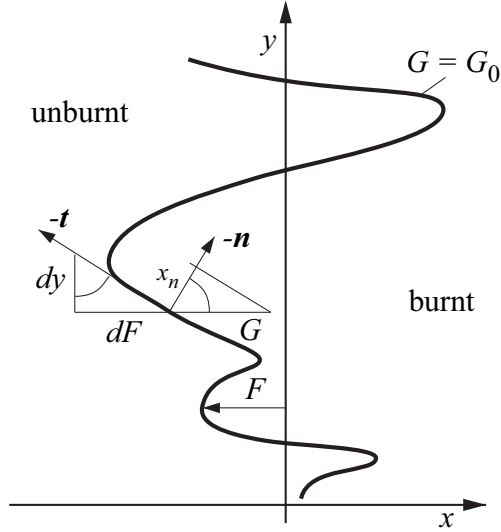


Figure 12.2: Graphical interpretation of the G -field. The movement of the instantaneous flame front position $G = G_0$ is related to spatial fluctuations F .

be assigned in the entire flow field. The flow velocity v_f can simply be replaced by the local flow velocity v , a notation which we will adopt in the following.

The burning velocity s_L appearing in Eqs. (12.3) and (12.5) may be modified to account for the effect of flame stretch as already has been discussed in Lecture 4, Section 4.4. Performing two-scale asymptotic analyses of corrugated premixed flames Pelce and Clavin (1982) [3] and Matalon and Matkowsky (1982) [4] derived first order correction terms for small curvature and strain. The expression for the modified burning velocity s_L becomes

$$s_L = s_L^0 - s_L^0 \mathcal{L} \kappa - \mathcal{L} S. \quad (12.11)$$

Here s_L^0 is the burning velocity of the unstretched flame, κ is the curvature and S is the strain rate.

The flame curvature κ is defined in terms of the G -field as

$$\kappa = \nabla \cdot \mathbf{n} = \nabla \cdot \left(-\frac{\nabla G}{|\nabla G|} \right) = -\frac{\nabla^2 G - \mathbf{n} \cdot \nabla(\mathbf{n} \cdot \nabla G)}{|\nabla G|}, \quad (12.12)$$

where $\nabla(|\nabla G|) = -\nabla(\mathbf{n} \cdot \nabla G)$ has been used. It is positive if the flame is convex with respect to

the unburnt mixture. The strain rate imposed on the flame by velocity gradients is defined as

$$S = -\mathbf{n} \cdot \nabla \mathbf{v} \cdot \mathbf{n}. \quad (12.13)$$

Strain due to flow divergence can be interpreted as stream line curvature. Since strain and curvature have similar effects on the burning velocity they may be summarized as flame stretch (cf. Matalon (1983) [5]). The concept of stretch was generalized to account for finite flame thickness (cf. de Goey and Ten Thije Boonkamp (1997) [6], de Goey et al. (1997) and Echekki (1997) [7]). In these papers a quasi-one-dimensional analysis of the governing equations was performed to identify different contributions to flame stretch. Experimental studies of stretched flames were performed by Egolfopoulos et al. (1990a) [8], (1990b) [9], Erard et al. (1996) [10], Deshaies and Cambray (1990) [11] and many others.

The Lewis number is approximately unity for methane flames and larger than unity for fuel-rich hydrogen and all fuel-lean hydrocarbon flames other than methane. Therefore, since the first term on the r.h.s. of Eq. (4.36)

$$\frac{\mathcal{L}_u}{\ell_F} = \frac{1}{\gamma} \ln \frac{1}{1-\gamma} + \frac{Ze(\text{Le}-1)}{2} \frac{(1-\gamma)}{\gamma} \int_0^{\gamma/(1-\gamma)} \frac{\ln(1+x)}{x} dx \quad (12.14)$$

is always positive, the Markstein length is positive for most practical applications of premixed hydrocarbon combustion, occurring typically under stoichiometric or fuel-lean conditions. Whenever the Markstein length is negative, as in lean hydrogen-air mixtures, diffusional-thermal instabilities tend to increase the flame surface area. This is believed to be an important factor in gas cloud explosions of hydrogen-air mixtures. Although turbulence tends to dominate such local effects the combustion of diffusional-thermal instabilities and instabilities induced by gas expansion could lead to strong flame accelerations.

If Eq. (12.11) is introduced into the G -equation Eq. (12.5) it may be written as

$$\frac{\partial G}{\partial t} + \mathbf{v} \cdot \nabla G = s_L^0 |\nabla G| - \mathcal{D}_{\mathcal{L}} \kappa |\nabla G| - \mathcal{L} S |\nabla G|. \quad (12.15)$$

Here

$$\mathcal{D}_{\mathcal{L}} = s_L^0 \mathcal{L} \quad (12.16)$$

is defined as the Markstein diffusivity. The curvature term adds a second order derivative to the G -equation. This avoids the formation of cusps that would result from Eq. (12.5) for a constant

value s_L^0 . If $\mathcal{L} > 0$, the mathematical nature of Eq. (12.15) is that of a Hamilton-Jacobi equation with a parabolic second order differential operator coming from the curvature term. While the solution of the G -equation Eq. (12.5) with a constant s_L^0 is solely determined by specifying the initial conditions, the parabolic character of Eq. (12.15) requires that the boundary conditions for each iso-surface G must be specified. For the iso-surface $G(\mathbf{x}, t) = G_0$ in particular, the flame front position at the boundaries is that where the flame is anchored.

As an illustration of the level set approach, in Lecture 4 Section 4.3 we already presented an examples of laminar flames to determine the flame front position by solving the G -equation.

12.1 The Level Set Approach for the Thin Reaction Zones Regime

Eq. (12.15) is suitable for thin flame structures in the corrugated flamelets regime, where the entire flame structure is quasi-steady and the laminar burning velocity is well defined, but not for the thin reaction zones regime. We now want to derive a level set formulation for the case, where the flame structure cannot be assumed quasi-steady because Kolmogorov eddies enter into the preheat zone and cause unsteady perturbations. The resulting equation will be valid in the thin reaction zones regime.

Since the inner layer shown in Fig. 6.1 is responsible for maintaining the reaction process alive, we define the thin reaction zone as the inner layer. Its location will be determined by the iso-scalar surface of the temperature setting $T(\mathbf{x}, t) = T^0$, where T^0 is the inner layer temperature. We now consider the temperature equation

$$\rho \frac{\partial T}{\partial t} + \rho \mathbf{v} \cdot \nabla T = \nabla \cdot (\rho D \nabla T) + \omega_T, \quad (12.17)$$

where D is the thermal diffusivity and ω_T the chemical source term. Similar to Eq. (12.4) for the scalar G the iso-temperature surface $T(\mathbf{x}, t) = T^0$ satisfies the condition

$$\frac{\partial T}{\partial t} + \nabla T \cdot \frac{d\mathbf{x}}{dt} \Big|_{T=T^0} = 0. \quad (12.18)$$

Gibson (1968) [12] has derived an expression for the displacement speed s_d for an iso-surface of non-reacting diffusive scalars. Extending this result to the reactive scalar T this leads to

$$\frac{d\mathbf{x}}{dt} \Big|_{T=T^0} = \mathbf{v}^0 + \mathbf{n} s_d, \quad (12.19)$$

where the displacement speed s_d is given by

$$s_d = \left[\frac{\nabla \cdot (\rho D \nabla T) + \omega_T}{\rho |\nabla T|} \right]_0. \quad (12.20)$$

Here the index 0 defines conditions immediately ahead of the thin reaction zone. The normal vector on the iso-temperature surface is defined as

$$\mathbf{n} = -\frac{\nabla T}{|\nabla T|} \Big|_{T=T^0}. \quad (12.21)$$

We want to formulate a G -equation that describes the location of the thin reaction zones such that the iso-surface $T(\mathbf{x}, t) = T^0$ coincides with the iso-surface defined by $G(\mathbf{x}, t) = G_0$. Then the normal vector defined by Eq. (12.21) is equal to that defined by Eq. (12.2) and also points towards the unburnt mixture. Using Eqs. (12.2) and (12.4) together with Eq. (12.20) leads to

$$\frac{\partial G}{\partial t} + \mathbf{v} \cdot \nabla G = \left[\frac{\nabla \cdot (\rho D \nabla T) + \omega_T}{\rho |\nabla T|} \right] |\nabla G|, \quad (12.22)$$

where the index 0 is omitted here and in the following for simplicity of notation.

Echekki and Chen (1999) [13] and Peters et al. (1998) [14] show that the diffusive term appearing in the brackets in this equation may be split into one term accounting for curvature and another for diffusion normal to the iso-surface

$$\nabla \cdot (\rho D \nabla T) = -\rho D |\nabla T| \nabla \cdot \mathbf{n} + \mathbf{n} \cdot \nabla (\rho D \mathbf{n} \cdot \nabla T). \quad (12.23)$$

This is consistent with the definition of the curvature in Eq. (12.12) if the iso-surface $G(\mathbf{x}, t) = G_0$ is replaced by the iso-surface $T(\mathbf{x}, t) = T^0$ and if ρD is assumed constant. Introducing Eq. (12.23) into Eq. (12.22) one obtains

$$\frac{\partial G}{\partial t} + \mathbf{v} \cdot \nabla G = (s_n + s_r) |\nabla G| - D \kappa |\nabla G|. \quad (12.24)$$

Here $\kappa = \nabla \cdot \mathbf{n}$ is to be expressed by Eq. (12.12) in terms of the G -field. The quantities s_n and s_r are contributions due to normal diffusion and reaction to the displacement speed of the thin

reaction zone and are defined as

$$s_n = \frac{\mathbf{n} \cdot \nabla (\rho D \mathbf{n} \cdot \nabla T)}{\rho |\nabla T|}, \quad (12.25)$$

$$s_r = \frac{\omega_T}{\rho |\nabla T|}. \quad (12.26)$$

In a steady unstretched planar laminar flame the sum of s_n and s_r would be equal to the burning velocity s_L^0 . In the thin reaction zones regime, however, the unsteady mixing and diffusion of chemical species and the temperature in the regions ahead of the thin reaction zone will influence the local displacement speed. Then the sum of s_n and s_r , denoted by $s_{L,s}$

$$s_{L,s} = s_n + s_r, \quad (12.27)$$

is not equal to s_L^0 , but is a fluctuating quantity that couples the G -equation to the solution of the balance equations of the reactive scalars. There is reason to expect, however, that $s_{L,s}$ is of the same order of magnitude as the laminar burning velocity. The evaluation of DNS-data by Peters et al. (1998) [14] confirms this estimate. In that paper it was also found that the mean values of s_n and s_r slightly depend on curvature. This leads to a modification of the diffusion coefficient which partly takes Markstein effects into account. We will ignore these modifications here and consider the following level set equation for flame structures of finite thickness

$$\frac{\partial G}{\partial t} + \mathbf{v} \cdot \nabla G = s_{L,s} |\nabla G| - D \kappa |\nabla G|. \quad (12.28)$$

This equation is defined at the thin reaction zone and \mathbf{v} , $s_{L,s}$, and D are values at that position. Eq. (12.28) is very similar to Eq. (12.15), which was derived for thin flame structures in the corrugated flamelets regime. An important difference, apart from the difference between s_L^0 and $s_{L,s}$, is the difference between D_C and D and the disappearance of the strain term. The latter is implicitly contained in the burning velocity $s_{L,s}$.

In an analytical study of the response of one-dimensional constant density flames to time-dependent strain and curvature, Joulin (1994) [15] has shown that in the limit of high frequency perturbations the effect of strain disappears entirely and Lewis-number effects also disappear in the curvature term such that D_C approaches D . This analysis was based on one-step large activation energy asymptotics with the assumption of a single thin reaction zone. It suggests that Eq. (12.28) could also have been derived from Eq. (12.15) for the limit of high frequency perturbations of the flame structure. This strongly supports it as level set equation for flame structures of finite

thickness and shows that unsteadiness of that structure is an important feature in the thin reaction zones regime.

Since the derivation of Eq. (12.28) was based on the balance equation Eq. (12.17) for the temperature, the diffusion coefficient is the thermal diffusivity. However, a similar derivation could have been based on any other reactive scalar defining the position of the inner layer. Then the diffusivity of that particular scalar would appear in Eq. (12.28). In order to obtain the same result we therefore must assume equal diffusivities for all reactive scalars. Since the temperature plays a particular role in combustion due to the strong temperature sensitivity of chemistry, the use of the thermal diffusivity D is the appropriate.

The important difference between the level set formulation Eq. (12.28) and the equation for the reactive scalar Eq. (12.17), from which it has been derived, is the appearance of a burning velocity which replaces normal diffusion and reaction at the flame surface. It should be noted that both level set equations, Eqs. (12.15) and (12.28), are only defined at the flame surface, while Eq. (12.17) is valid in the entire field.

12.2 A Common Level Set Equation for Both Regimes

It has been anticipated that the two different formulations Eqs. (12.15) and (12.28) of the G -equation apply to different regimes in premixed turbulent combustion, namely to the corrugated flamelets regime and the thin reaction zones regime of Fig. 11.1, respectively. In order to show this we will analyze the order of magnitude of the different terms in (12.28). This can be done by normalizing the independent variables and the curvature in this equation with respect to Kolmogorov length, time and velocity scales

$$\begin{aligned} t^* &= t/t_\eta, & x^* &= x/\eta, & v^* &= v/v_\eta, \\ \kappa^* &= \eta\kappa, & \nabla^* &= \eta\nabla. \end{aligned} \tag{12.29}$$

Using $\eta^2/t_\eta = \nu$ one obtains

$$\frac{\partial G}{\partial t^*} + v^* \cdot \nabla^* G = \frac{s_{L,s}}{v_\eta} |\nabla^* G| - \frac{D}{\nu} \kappa^* |\nabla^* G|, \tag{12.30}$$

where the density ρ has been canceled. Since Kolmogorov eddies can perturb the flow field as well as the G -field, all derivatives, the curvature and the velocity v^* are typically of order unity. In

flames D/ν is also of order unity. However, since $s_{L,s}$ is of the same order of magnitude as s_L , the definition Eq. (11.4) shows that the ratio $s_{L,s}/v_\eta$ is proportional to $\text{Ka}^{-1/2}$. Since $\text{Ka} > 1$ in the thin reaction zones regime it follows that

$$s_{L,s} < v_\eta \quad (12.31)$$

in that regime. The propagation term therefore is small and the curvature term will be dominant. Relative small mean values of $s_{L,s}$ may, for instance, result from instantaneously negative values of the burning velocity. Even though wrinkling of the reaction zone by small eddies leading to large local curvatures is an important feature, it is the enhanced mixing within the preheat zone that is responsible for the advancement of the front. On the contrary, as can be shown by a similar analysis of Eq. (12.15) in the corrugated flamelets regime where $\text{Ka} < 1$ and therefore

$$s_L^0 > v_\eta, \quad (12.32)$$

the propagation term $s_L^0 \sigma$ is dominant in Eq. (12.15) and the curvature and strain terms are of higher order.

We want to base the following analysis on an equation which contains only the leading order terms in both regimes. Therefore we take the propagation term with a constant laminar burning velocity s_L^0 from the corrugated flamelets regime and the curvature term multiplied with the diffusivity D from the thin reaction zones regime. The strain term $\mathcal{L} S$ in the G -equation Eq. (12.15) will be neglected in both regimes. Since the Markstein length \mathcal{L} is of the order of the flame thickness, this term is unimportant in the corrugated flamelets regime, where \mathcal{L} is smaller than the Kolmogorov scale. A term called scalar-strain co-variance resulting from this term is effective in the diffusive subrange of the scalar spectrum only (cf. Peters (1992) [16]). It therefore does not interact with the turbulent part of the spectrum and is unimportant for leading order scaling arguments required for turbulent closure. In the thin reaction zone regime there is no quasi-steady laminar flame structure and a Markstein length cannot be defined.

The leading order equation valid in both regimes then reads

$$\rho \frac{\partial G}{\partial t} + \rho \mathbf{v} \cdot \nabla G = (\rho s_L^0) \sigma - (\rho D) \kappa \sigma. \quad (12.33)$$

For consistency with other field equations that will be used as a starting point for turbulence modeling, we have multiplied all terms in this equation with ρ . This will allow to apply Favre averaging

to all equations. Furthermore, we have set (ρs_L^0) constant and denoted this by parenthesis. This takes into account that the mass flow rate (ρs_L^0) through a planar steady flame is constant as shown by Eq. (4.19). The parenthesis of (ρD) also denote that this product was assumed constant in deriving Eq. (12.23). There it was defined at T^0 , and since $\rho D = \lambda/c_p$, it is equal to $(\lambda/c_p)_0$ used in the definition of the flame thickness in Eq. (5.28). With that definition the last term in Eq. (12.33) can also be expressed as $(\rho s_L^0)\ell_F\kappa\sigma$. Again, Eq. (12.33) is defined at the flame surface $G(\mathbf{x}, t) = G_0$ only.

12.3 Modeling Premixed Turbulent Combustion Based on the Level Set Approach

If the G -equation is to be used as a basis for turbulence modeling, it is convenient to ignore at first its non-uniqueness outside the surface $G(\mathbf{x}, t) = G_0$. Then the G -equation would have similar properties as other field equations used in fluid dynamics and scalar mixing. This would allow to define, at point \mathbf{x} and time t in the flow field, a probability density function $P(G; \mathbf{x}, t)$ for the scalar G . From $P(G; \mathbf{x}, t)$ the first two moments of G , the mean and the variance, can be calculated as

$$\bar{G}(\mathbf{x}, t) = \int_{-\infty}^{+\infty} GP(G; \mathbf{x}, t) dG, \quad (12.34)$$

$$\bar{G'^2}(\mathbf{x}, t) = \int_{-\infty}^{+\infty} (G - \bar{G})^2 P(G; \mathbf{x}, t) dG. \quad (12.35)$$

If modeled equations for these two moments are formulated and solved, one could, for instance, use the presumed shape pdf approach to calculate $P(G; \mathbf{x}, t)$ by presuming a two-parameter shape function. However, since G is only defined at the flame front, $P(G; \mathbf{x}, t)$ and its moments carry the non-uniqueness of its definition outside $G(\mathbf{x}, t) = G_0$.

There is, nevertheless, a quantity that is well-defined and of physical relevance, which may be derived from $P(G; \mathbf{x}, t)$. This is the probability density of finding the flame surface $G(\mathbf{x}, t) = G_0$ at \mathbf{x} and t given by

$$P(G_0, \mathbf{x}, t) = \int_{-\infty}^{+\infty} \delta(G - G_0) P(G; \mathbf{x}, t) dG = P(\mathbf{x}, t). \quad (12.36)$$

This quantity can be measured, for instance, by counting the number of flame crossings in a small volume ΔV located at \mathbf{x} over a small time difference Δt .

In Figs. 12.3 and 12.4 two experimental examples of this pdf are shown. The pdf $P(G')$ in

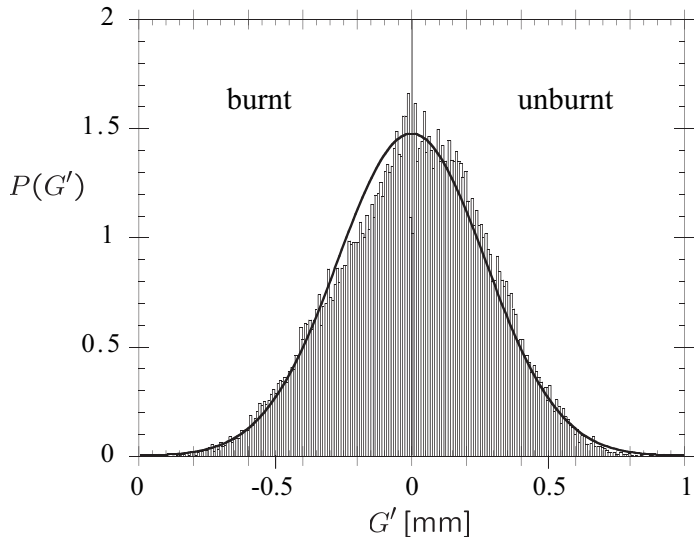


Figure 12.3: Probability density function of flame front fluctuations in an internal combustion engine. — Gaussian distribution. Measurements by Wirth et al. (1993) [17].

Fig. 12.3 was obtained by Wirth et al. (1993) [17] by evaluating photographs of the flame front in the transparent spark-ignition engine. Smoke particles, which burnt out immediately in the flame front, were added to the unburnt mixture. Thereby the front could be visualized by a laser sheet as the borderline of the region where Mie scattering of particles could be detected. Experimental details may be found in Wirth and Peters (1992) [19] and Wirth et al. (1993) [17]. The pdf $P(G')$ represents the pdf of fluctuations around the mean flame contour of several instantaneous images.

By comparing the measured pdf in Fig. 12.3 with a Gaussian distribution it is seen to be slightly skewed to the unburnt gas side. This is due to the non-symmetric influence of the laminar burning velocity on the shape of the flame front: there are rounded leading edges towards the unburnt mixture, but sharp and narrow troughs towards the burnt gas.

This non-symmetry is also found in the experimental pdfs shown in Fig. 12.4. Plessing et al. (1999) [18] have measured the probability density of finding the flame surface in steady turbulent premixed flames on a weak swirl burner. The flames were stabilized nearly horizontally on the burner thus representing one-dimensional steady turbulent flames. The pdfs were obtained by averaging over 300 temperature images obtained from Rayleigh scattering. The three profiles of $P(x)$, shown in Fig. 12.4, for three velocity ratios v'/s_L , nearly coincide and are slightly skewed towards the unburnt gas side.

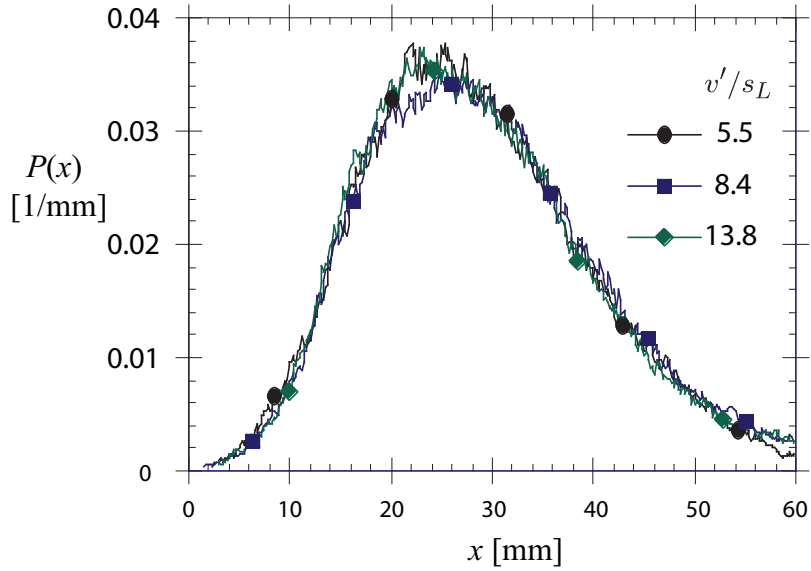


Figure 12.4: The probability density of finding the instantaneous flame front at the axial position x in a turbulent flame stabilized on a weak swirl burner (Measurements by Plessing et al. (1999) [18]).

Without loss of generality, we now want to consider, for illustration purpose, a one-dimensional steady turbulent flame propagating in x -direction. We will analyze its structure by introducing the flame-normal coordinate x , such that all turbulent quantities are a function of this coordinate only. Then the pdf of finding the flame surface at a particular location x within the flame brush simplifies to $P(G_0; x)$ which we write as $P(x)$. We normalize $P(x)$ by

$$\int_{-\infty}^{+\infty} P(x) dx = 1 \quad (12.37)$$

and define the mean flame position x_f as

$$x_f = \int_{-\infty}^{+\infty} x P(x) dx. \quad (12.38)$$

The turbulent flame brush thickness $\ell_{F,t}$ can also be defined using $P(x)$. With the definition of the variance

$$\overline{(x - x_f)^2} = \int_{-\infty}^{+\infty} (x - x_f)^2 P(x) dx \quad (12.39)$$

a plausible definition is

$$\ell_{F,t} = \left(\overline{(x - x_f)^2} \right)^{1/2}. \quad (12.40)$$

We note that from $P(x)$ two important properties of a premixed turbulent flame, namely the mean flame position and the flame brush thickness can be calculated.

The G -equation has been used in a number of papers to investigate quantities relevant to premixed turbulent combustion. An early review was given by Ashurst (1994) [20]. Kerstein et al. (1988) [21] have performed direct numerical simulations of Eq. (12.5) in a cubic box assigning a stationary turbulent flow field and constant density. The constant density assumption has the advantage that the flow field is not altered by gas expansion effects. The gradient $\partial \bar{G} / \partial x$ in direction of mean flame propagation was fixed equal to unity and cyclic boundary conditions in the two other directions were imposed. In this formulation all instantaneous G -levels can be interpreted as representing different flame fronts. Therefore G_0 was considered as a variable and averages over all G -levels were taken in order to show that for large times the mean gradient $\bar{\sigma}$ can be interpreted as the flame surface area ratio.

Peters (1992) [16] considered turbulent modeling of the G -equation in the corrugated flamelets regime and derived Reynolds-averaged equations for the mean and the variance of G . Constant density was assumed and G and the velocity v were split into a mean and a fluctuation. The main sink term in the variance equation resulted from the propagation term $s_L^0 |\nabla G| = s_L^0 \sigma$ in Eq. (12.15) and was defined as

$$\bar{\omega} = -2 s_L^0 \overline{G' \sigma'}. \quad (12.41)$$

The quantity $\bar{\omega}$ was called kinematic restoration in order to emphasize the effect of local laminar flame propagation in restoring the G -field and thereby the flame surface. Corrugations produced by turbulence, which would exponentially increase the flame surface area with time of a non-diffusive iso-scalar surface are restored by this kinematic effect. Closure of this term was achieved by deriving the scalar spectrum function of two-point correlations of G in the limit of large Reynolds numbers. From that analysis resulted a closure assumption which relates $\bar{\omega}$ to the variance $\overline{G'^2}$ and the integral time scale k/ε as

$$\bar{\omega} = c_\omega \frac{\varepsilon}{k} \overline{G'^2}, \quad (12.42)$$

where $c_\omega = 1.62$ is a constant of order unity. This expression shows that kinematic restoration plays a similar role in reducing fluctuations of the flame front as scalar dissipation does in reducing fluctuations of diffusive scalars.

It was also shown by Peters (1992) [16] that kinematic restoration is active at the Gibson scale

ℓ_G , since the cut-off of the inertial range in the scalar spectrum function occurs at that scale. A dissipation term involving a positive Markstein diffusivity $D_{\mathcal{L}}$ was shown to be effective at the Obukhov-Corrsin scale ℓ_C and a term called scalar-strain co-variance was shown to be most effective at the Markstein length \mathcal{L} . In the corrugated flamelets regime the Gibson scale ℓ_G is larger than ℓ_C and \mathcal{L} . Therefore these additional terms are higher order corrections, which, in view of the order of magnitude assumptions used in turbulence modeling, will be neglected.

A similar analysis was performed by Peters (1999) [16] for the thin reaction zones regime. In that regime the diffusion term in Eq. (12.28) is dominant as shown by the order of magnitude analysis of Eq. (12.30). This leads to a dissipation term replacing kinematic restoration as the leading order sink term in the variance equation. It is defined as

$$\overline{\chi} = 2D \overline{(\nabla G')^2}. \quad (12.43)$$

Closure of that term is obtained in a similar way as for non-reacting scalars and leads to

$$\overline{\chi} = c_\chi \frac{\varepsilon}{k} \overline{G'^2}. \quad (12.44)$$

Below we will use the two closure relations Eqs. (12.42) and (12.43) as the basis for the modeling of the turbulent burning velocity in the two different regimes.

12.4 Equations for the Mean and the Variance of G

In order to obtain a formulation that is consistent with the well-established use of Favre averages in turbulent combustion, we split G and the velocity vector v into Favre means and fluctuations

$$G = \tilde{G} + G'', \quad v = \tilde{v} + v''. \quad (12.45)$$

Here \tilde{G} and \tilde{v} are at first viewed as unconditional averages. At the end, however, only the respective conditional averages are of interest. Since in a turbulent flame G was interpreted as the scalar distance between the instantaneous and the mean flame front, evaluated at $G(x, t) = G_0$, the Favre mean $\tilde{G} = \overline{\rho G}/\bar{\rho}$ represents the Favre average of that distance. If $G(x, t) = G_0$ is defined to lie in the unburnt mixture immediately ahead of the thin flame structure, as often assumed for the corrugated flamelets regime, the density at $G(x, t) = G_0$ is constant equal to ρ_u . Similarly, if it is an iso-temperature surface, as assumed for the thin reaction zones regime, changes of the density

along that surface are expected to be small. In both cases the Favre average \tilde{G} is approximately equal to the conventional mean value \bar{G} . Using Favre averages rather than conventional averages, which might have appeared more appropriate for a non-conserved quantity like the scalar G , therefore has no practical consequences.

Using a number of closure assumptions described in Peters (2000) [22], one finally obtains the following equations for the Favre near and variance of G .

$$\bar{\rho} \frac{\partial \tilde{G}}{\partial t} + \bar{\rho} \tilde{v} \cdot \nabla \tilde{G} = (\bar{\rho} s_T^0) |\nabla \tilde{G}| - \bar{\rho} D_t \tilde{k} |\nabla \tilde{G}|, \quad (12.46)$$

$$\bar{\rho} \frac{\partial \widetilde{G''^2}}{\partial t} + \bar{\rho} \tilde{v} \cdot \nabla \widetilde{G''^2} = \nabla_{||} \cdot (\bar{\rho} D_t \nabla_{||} \widetilde{G''^2}) + 2\bar{\rho} D_t (\nabla \tilde{G})^2 - c_s \bar{\rho} \frac{\tilde{\varepsilon}}{\tilde{k}} \widetilde{G''^2}. \quad (12.47)$$

It is easily seen that Eq. (12.46) has the same form as Eq. (12.33) and therefore shares its mathematical properties. It also is valid at $\tilde{G}(x, t) = G_0$ only, while the solution outside of that surface depends on the ansatz for $\tilde{G}(x, t)$ that is introduced. The same argument holds for Eq. (12.47) since the variance is a property of the flame front. The solution of that equation will provide the conditional value $(\widetilde{G''^2})_0$ at the mean flame surface $\tilde{G}(x, t) = G_0$. Following Eq. (12.40), its square root is a measure of the flame brush thickness $\ell_{F,t}$, which for an arbitrary value of $|\nabla \tilde{G}|$ at the front, will be defined as

$$\ell_{F,t} = \left. \frac{(\widetilde{G''^2}(x, t))^{1/2}}{|\nabla \tilde{G}|} \right|_{\tilde{G}=G_0}. \quad (12.48)$$

In order to solve Eq. (12.46), a model for the turbulent burning velocity s_T^0 must be provided. A first step would be to use empirical correlations from the literature. Alternatively, a modeled balance equation for the mean gradient $\bar{\sigma}$ will be derived. According to [21] $\bar{\sigma}$ represents the flame surface area ratio, which is proportional to the turbulent burning velocity.

Example 12.1

An Example Solution for the Turbulent Flame Brush Thickness

For illustration purpose we want to solve the variance equation for a one-dimensional unsteady planar flame using $|\nabla \tilde{G}| = 1$. We pose the problem such that at time $t = 0$ a one-dimensional steady laminar flame with flame thickness ℓ_F is already present and that the laminar flow is suddenly replaced by a fully developed turbulent flow field. We assume that the turbulence quantities D_t , \tilde{k} and $\tilde{\varepsilon}$ are constant, independent of time. Since the flame is planar and, furthermore, since the variance must not depend on the coordinate normal to the mean flame, if it is supposed to

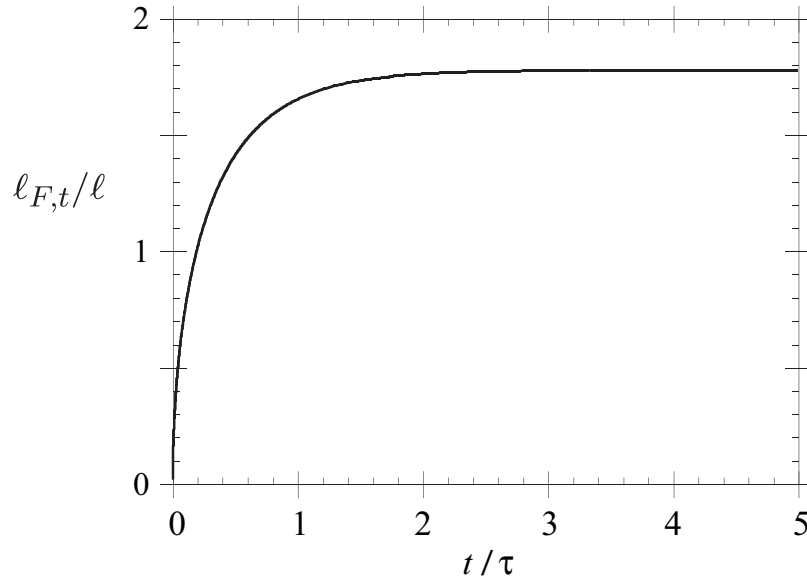


Figure 12.5: Time evolution of the turbulent flame brush thickness $\ell_{F,t}$ normalized by the integral length scale ℓ . the time t is normalized by the integral time scale $\tau = k/\varepsilon$.

represent the conditional variance, all gradients of $\widetilde{G''^2}$ must vanish. Therefore, the convective and diffusive terms in Eq. (12.47) disappear entirely.

For modeling purposes we will use a turbulent Schmidt number $Sc_t = \nu_t/D_t = 0.7$ and the empirical relations given in Tab. 13.1 of Lecture 13 below. They follow from Eqs. (10.29) and (10.38) and relate \tilde{k} , $\tilde{\varepsilon}$ and D_t to v' , ℓ and τ . Non-dimensionalizing the time in Eq. (12.47) by the integral time scale $\tau = \tilde{k}/\tilde{\varepsilon}$, the variance equation becomes an equation for the turbulent flame brush thickness

$$\frac{\partial \ell_{F,t}^2}{\partial(t/\tau)} = 2 a_3 a_4 \ell^2 - c_s \ell_{F,t}^2 \quad (12.49)$$

which has the solution

$$\ell_{F,t}^2 = b_2^2 \ell^2 [1 - \exp(-c_s t/\tau)] + \ell_F^2 \exp(-c_s t/\tau) \quad (12.50)$$

where $b_2 = (2a_3 a_4 / c_s)^{1/2} = 1.78$ for $c_s = 2.0$. Here ℓ_F was used as initial value. In the limit $\ell_F/\ell \rightarrow 0$ one obtains

$$\ell_{F,t} = b_2 \ell [1 - \exp(-c_s t/\tau)]^{1/2}. \quad (12.51)$$

The unsteady development of the flame brush thickness in this limit is shown in Fig. 12.5. For large times it becomes proportional to the integral length scale ℓ .

Bibliography

- [1] F. A. Sethian. *Level Set Methods*. Cambridge Monographs on Applied and Computational Mathematics, Cambridge University Press, 1996.
- [2] F. A. Williams. Turbulent combustion. In John Buckmaster, editor, *The Mathematics of Combustion*, pages 97–131. SIAM, 1985.
- [3] P. Pelce and P. Clavin. Influence of hydrodynamics and diffusion upon the stability limits of laminar premixed flames. *J. Fluid Mech.*, 124:219–237, 1982.
- [4] M. Matalon and B. J. Matkowsky. Flames as gasdynamics discontinuities. *J. Fluid Mech.*, 124:239–259, 1982.
- [5] M. Matalon. On flame stretch. *Combust. Sci. and Tech.*, 31:169–181, 1983.
- [6] Mallens R. M. M. de Goey, L. P. H. and J. H. M. Ten Thije Boonkkamp. An evaluation of different contributions to flame stretch for stationary premixed flames. *Combust. Flame*, 110:54–66, 1997.
- [7] T. Echekki. A quasi-one-dimensional premixed flame model with cross-stream effects. *Combust. Flame*, 110:335–350, 1997.
- [8] Zhu D. L. Egolfopoulos, F. N. and C. K. Law. Experimental and numerical determination of laminar flame speeds: Mixtures of c_2 -hydrocarbons with oxygen and nitrogen. *Twenty-Third Symposium (International) on Combustion, The Combustion Institute, Pittsburgh*, pages 471–478, 1990.
- [9] Egolfopoulos and C. K. Law. An experimental and computational determination of the burning rates of ultra-lean to moderately rich $h_2/o_2/n_2$ laminar flames with pressure variations journal

- = Twenty-Third Symposium (International) on Combustion, The Combustion Institute, Pittsburgh, volume = , pages = 330-340., 1990.
- [10] Boukhalfa A. Puechberty D. Erard, V. and M. Trinité. A statistical study on surface properties of freely propagating premixed turbulent flames. *Combust. Sci. Tech.*, 113–114:313–327, 1996.
 - [11] B. Deshaies and P. Cambray. The velocity of a premixed flame as a function of the flame stretch: An experimental study. *Combust. Flame*, 82:361–375, 1990.
 - [12] C. H. Gibson. Fine structure of scalar fields mixed by turbulence i. zero gradient points and minimal gradient surfaces. *Phys. Fluids*, 11:2305–2315, 1968.
 - [13] Echekki T. Chen, J. H. and W. Kollman. The mechanism of two-dimensional pocket formation in lean premixed methane-air flames with implications to turbulent combustion. *Combust. Flame*, 116:15–48, 1998.
 - [14] N. Peters and N. Rogg. Reduced kinetic mechanisms for applications in combustion systems. In N. Peters and N. Rogg, editors, *Lecture Notes in Physics*, volume m15, pages 27–40. Springer-Verlag, Heidelberg, 1993.
 - [15] G. Joulin. On the response of premixed flames to time-dependent stretch and curvature. *Combust. Sci. and Tech.*, 97:219–229, 1994.
 - [16] N. Peters. A spectral closure for premixed turbulent combustion in the flamelet regime. *J. Fluid Mech.*, 242:611–629, 1992.
 - [17] Keller P. Wirth, M. and N. Peters. A flamelet model for premixed turbulent combustion in si-engines. *SAE-paper 932646*, 1993.
 - [18] Mansour M. S. Peters N. Plessing, T. and R. K. Cheng. Ein neuartiger niedrigdrallbrenner zur untersuchung turbulenter vormischflammen. *VDI-Berichte*, 1492:457–462, 1999.
 - [19] M. Wirth and N. Peters. Turbulent premixed combustion: A flamelet formulation and spectral analysis in theory and ic-engine experiments. *Twenty-Fourth Symposium (International) on Combustion, The Combustion Institute, Pittsburgh*, pages 493–501, 1992.
 - [20] W. T. Ashurst. Modelling turbulent flame propagation. *Twenty-Fifth Symposium (International) on Combustion, The Combustion Institute, Pittsburgh*, pages 1075–1089, 1994.

- [21] A. R. Kerstein. Fractal dimension of turbulent premixed flames. *Combust. Sci. and Tech.*, 60:441–445, 1988.
- [22] N. Peters. *Turbulent Combustion*. Cambridge University Press, 2000.

Lecture 13

The Turbulent Burning Velocity

13.1 The Turbulent Burning Velocity

One of the most important unresolved problems in premixed turbulent combustion is that of the turbulent burning velocity. This statement implies that the turbulent burning velocity is a well-defined quantity that only depends on local mean quantities. The mean turbulent flame front is expected to propagate with that burning velocity relative to the flow field. Gas expansion effects induced at the mean front will change the surrounding flow field and may generate instabilities in a similar way as flame instabilities of the Darrieus-Landau type are generated by a laminar flame front (cf. Clavin (1985) [1]).

Damköhler (1940) [2] was the first to present theoretical expressions for the turbulent burning velocity. He identified two different regimes of premixed turbulent combustion which he called large scale and small scale turbulence. We will identify these two regimes with the corrugated flamelets regime and the thin reaction zones regime, respectively.

Damköhler equated the mass flux \dot{m} through the instantaneous turbulent flame surface area A_T with the mass flux through the cross sectional area A , using the laminar burning velocity s_L for the mass flux through the instantaneous surface and the turbulent burning velocity s_T for the mass flux through the cross-sectional area A as

$$\dot{m} = \rho_u s_L A_T = \bar{\rho}_u s_T A. \quad (13.1)$$

This is schematically shown in Fig. 13.1. In Eq. (13.1) the burning velocities s_L and s_T are defined

with respect to the conditions in the unburnt mixture and the density ρ_u is assumed constant. From that equation it follows that the burning velocity ratio s_T/s_L is equal to the flame surface area ratio A_T/A

$$\frac{s_T}{s_L} = \frac{A_T}{A}. \quad (13.2)$$

Since only continuity is involved, averaging of the flame surface area can be performed at any length scale Δ within the inertial range. If Δ is interpreted as a filter width one obtains a filtered flame surface area \hat{A}_T . Eq. (13.1) then implies that the product of the filtered burning velocity \hat{s}_T and a filtered area \hat{A} is also equal to $s_L A_T$ and to $s_T A$

$$s_L A_T = \hat{s}_T \hat{A}_T = s_T A. \quad (13.3)$$

This shows that the product $\hat{s}_T \hat{A}$ is inertial range invariant, similar to dissipation in the inertial range of turbulence. As a consequence, by analogy to the large Reynolds number limit used in turbulent modeling, the additional limit of the ratio of the turbulent to the laminar burning velocity for large values of v'/s_L is the backbone of premixed turbulent combustion modeling.

For large scale turbulence, Damköhler (1940) [2] assumed that the interaction between a wrinkled flame front and the turbulent flow field is purely kinematic. Using the geometrical analogy with a Bunsen flame, he related the area increase of the wrinkled flame surface area to the velocity fluctuation divided by the laminar burning velocity

$$\frac{A_T}{A} \sim \frac{v'}{s_L}. \quad (13.4)$$

Combining Eqs. (13.2) and (13.4) leads to

$$s_T \sim v' \quad (13.5)$$

in the limit of large v'/s_L , which is a kinematic scaling. We now want to show that this is consistent with the modeling assumption for the G -equation in the corrugated flamelets regime.

For small scale turbulence, which we will identify with the thin reaction zones regime, Damköhler (1940) [2] argued that turbulence only modifies the transport between the reaction zone and the unburnt gas. In analogy to the scaling relation for the laminar burning velocity

$$s_L \sim \left(\frac{D}{t_c} \right)^{1/2}, \quad (13.6)$$

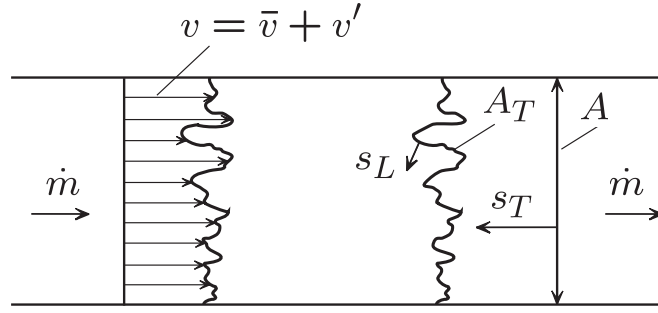


Figure 13.1: An idealized steady premixed flame in a duct.

where t_c is the chemical time scale and D the molecular diffusivity, he proposes that the turbulent burning velocity can simply be obtained by replacing the laminar diffusivity D by the turbulent diffusivity D_t

$$s_T \sim \left(\frac{D_t}{t_c} \right)^{1/2}, \quad (13.7)$$

while the chemical time scale remains the same. Thereby it is implicitly assumed that the chemical time scale is not affected by turbulence.¹ Combining Eqs. (13.6) and (13.7) the ratio of the turbulent to the laminar burning velocity becomes

$$\frac{s_T}{s_L} \sim \left(\frac{D_t}{D} \right)^{1/2}. \quad (13.8)$$

Since the turbulent diffusivity D_t is proportional to the product $v'\ell$, and the laminar diffusivity is proportional to the product of the laminar burning velocity and the flame thickness ℓ_F one may write Eq. (13.8) as

$$\frac{s_T}{s_L} \sim \left(\frac{v'}{s_L} \frac{\ell}{\ell_F} \right)^{1/2} \quad (13.9)$$

showing that for small scale turbulence the burning velocity ratio not only depends on the velocity ratio v'/s_L but also on the length scale ratio ℓ/ℓ_F .

There were many attempts to modify Damköhler's analysis and to derive expressions that would reproduce the large amount of experimental data on turbulent burning velocities. By introducing

¹This assumption breaks down when Kolmogorov eddies penetrate into the thin reaction zone. This implies that there is an upper limit for the thin reaction zones which was identified as the condition $Ka_\delta = 1$ in Fig. 11.1.

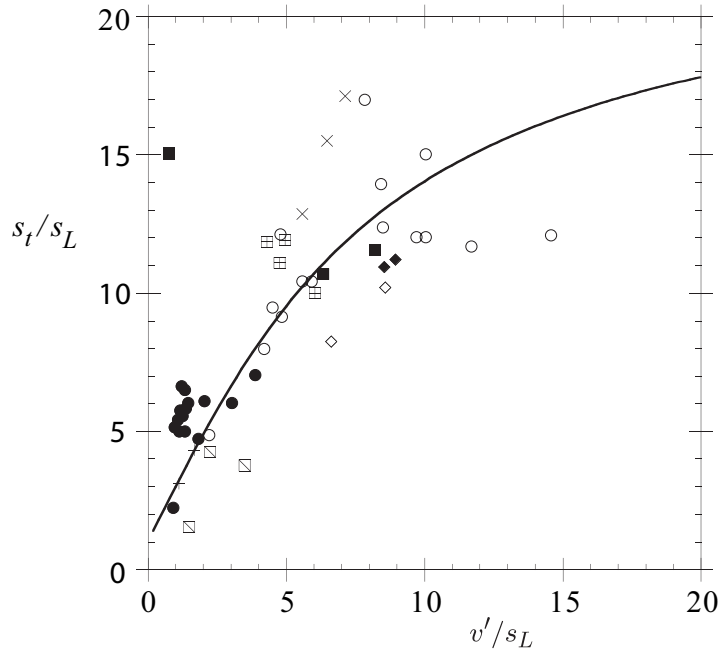


Figure 13.2: Comparison of the burning velocity ratio calculated from Eq. (13.31) (solid line), using $\text{Re} = 625$ with data from Abdel-Gayed and Bradley (1981) for Reynolds number ranging between 500 and 750. The origin of the individual data points may be found in that reference.

an adjustable exponent n , where $0.5 < n < 1.0$, Eqs. (13.5) and (13.9) may be combined to obtain expressions of the form

$$\frac{s_T}{s_L} = 1 + C \left(\frac{v'}{s_L} \right)^n. \quad (13.10)$$

This includes the limit $v' \rightarrow 0$ for laminar flame propagation where $s_T = s_L$. The constant C is expected to depend on the length scale ratio ℓ/ℓ_F . By comparison with experiments the exponent n is often found to be in the vicinity of 0.7 (cf. Williams (1985a) [3], p. 429ff). Attempts to justify a single exponent on the basis of dimensional analysis, however, fall short even of Damköhler's pioneering work who had recognized the existence of two different regimes in premixed turbulent combustion.

There is a large amount of data on turbulent burning velocities in the literature. Correlations of this material, mostly presented in terms of the burning velocity ratio s_T/s_L plotted as a function of v'/s_L , called the burning velocity diagram, date back to the fifties and sixties. An example taken from Peters (1999) [4] is shown in Fig. 13.2. When experimental data from different authors are

collected in such a diagram, they usually differ considerably. In the review articles by Bray (1990) [5] and Bradley (1992) [6] the many physical parameters that affect the turbulent burning velocity are discussed.

In a very careful review Abdel-Gayed and Bradley (1981) [7] collected and interpreted all the material that was available at that time. More recent correlations are due to Abdel-Gayed et al. (1987) [8], Gülder (1990b) [9], Bradley et al. (1992) [6] and Zimont and Lipatnikov (1995) [10].

The apparently fractal geometry of the flame surface and the fractal dimension that can be extracted from it, also has led to predictions of the turbulent burning velocity. Gouldin (1987) [11] has derived a relationship between the flame surface area ratio A_T/A and the ratio of the outer and inner cut-off of the fractal range

$$\frac{A_T}{A} = \left(\frac{\varepsilon_0}{\varepsilon_i} \right)^{D_f - 2}. \quad (13.11)$$

Here D_f is the fractal dimension. While there is general agreement that the outer cut-off scale ε_0 should be the integral length scale, there are different suggestions by different authors concerning the inner cut-off scale ε_i . While Peters (1986) [12] and Kerstein (1988a [13]) propose, based on theoretical grounds that ε_i should be the Gibson scale, most experimental studies reviewed by Gülder (1990a [14]) and Gülder et al. (1999) [15] favour the Kolmogorov scale η or a multiple thereof.

As far as the fractal dimension D_f is concerned, the reported values in the literature also vary considerably. Kerstein (1988a) [13] has suggested the value $D_f = 7/3$, which, in combination with the Gibson scale as the inner cut-off, is in agreement with Damköhler's result $s_T \sim v'$ in the corrugated flamelets regime. This is easily seen by inserting Eq. (13.11) into Eq. (13.2) using Eq. (11.10). On the other hand, if the Kolmogorov scale is used as inner cut-off, one obtains $s_T/s_L \sim Re^{1/4}$ as Gouldin (1987) [11] has pointed out. This power law dependence seems to have been observed by Kobayashi et al. (1998) [16] in high pressure flames. Gülder (1999) [15] shows in his recent review that most of the measured values for the fractal dimension are smaller than $D_f = 7/3$. He concludes that the available fractal parameters are not capable of correctly predicting the turbulent burning velocity.

13.2 A Model Equation for the Flame Surface Area Ratio

At the end of Section 12.4 it was stated that the mean gradient $\bar{\sigma}$ represents the flame surface area ratio. In the two-dimensional illustration in Fig. 13.3 the instantaneous flame surface area A_T is identified with the length of the line $G = G_0$. The blow-up Fig. 13.3 shows that a differential section dS of that line and the corresponding differential section dy of the cross sectional area A are related to each other by

$$\frac{dS}{dy} = \frac{1}{|\cos \beta|}. \quad (13.12)$$

On the other hand, in two dimensions the gradient σ is given by

$$\sigma = \left(1 + \left(\frac{\partial F}{\partial y} \right)^2 \right)^{1/2}. \quad (13.13)$$

It can be seen from Fig. 12.2 that $\partial F / \partial y = \tan \beta$ which relates σ to the angle β as

$$\sigma = \frac{1}{|\cos \beta|} \quad (13.14)$$

and therefore, combining this with Eq. (13.12), the differential flame surface area ratio is equal to the gradient σ

$$\frac{dS}{dy} = \sigma. \quad (13.15)$$

We therefore expect to be able to calculate the mean flame surface area ratio from a model equation for the mean gradient $\bar{\sigma}$. There remains, however, the question whether this is also valid for multiple crossings of the flame surface with respect to the x -axis. To resolve this conceptual difficulty one may define a filtered flame surface by eliminating large wave-number contributions in a Fourier representation of the original surface, so that in a projection of the original surface on the filtered surface no multiple crossings occur. This is also shown in Fig. 13.3. The normal co-ordinate x_n on the filtered surface then corresponds to x in Fig. 12.2, showing that the ansatz assuming a single valued function of x is again applicable. A successive filtering procedure can then be applied, so that the flame surface area ratio is related to the gradient σ at each level of filtering. Within a given section dy Eq. (13.15) is then replaced by

$$\frac{dS^\nu}{dS^{\nu+1}} = \frac{\sigma^\nu}{\sigma^{\nu+1}}, \quad (13.16)$$

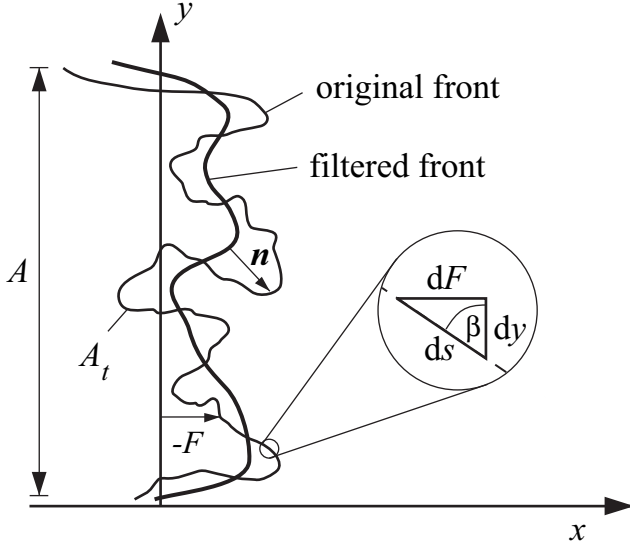


Figure 13.3: Illustration of the filtering of flame front corrugations showing that (13.15) remains valid even if multiple crossings occur.

where ν is an iteration index of successive filtering. The quantities dS^0 and σ^0 correspond to the instantaneous differential flame surface area dS and the respective gradient σ , and dS^1 and σ^1 to those of the first filtering level. At the next iteration one has $dS^1/dS^2 = \sigma^1/\sigma^2$ and so on. At the last filtering level for $\nu \rightarrow \infty$ the flame surface becomes parallel to the y -co-ordinate, so that $dS^\infty = dy$ and $\sigma^\infty = 1$. Canceling all intermediate iterations we obtain again Eq. (13.15).

This analysis assumes that the original flame surface is unique and continuous. There may be situations where pockets are formed, as shown in the 2D-simulation by Chen and Im (1998) [17]. In a subsequent paper Kollmann and Chen (1998) [18] have shown, however, that singularities in the source terms of the σ -equation, to be presented next, cancel out exactly even during pocket formation.

We now want to derive a modeled equation for the flame surface area ratio $\bar{\sigma}$ in order to determine the turbulent burning velocity. An earlier attempt in this direction is due to Rutland et al. (1990) [19]. An equation for σ can be derived from Eq. (12.33). For illustration purpose we assume constant density and constant values of s_L^0 and D . Applying the ∇ -operator to both sides

of the resulting equation and multiplying this with $-\mathbf{n} = \nabla G/\sigma$ one obtains

$$\frac{\partial \sigma}{\partial t} + \mathbf{v} \cdot \nabla \sigma = -\mathbf{n} \cdot \nabla \mathbf{v} \cdot \mathbf{n} \sigma + s_L^0 (\kappa \sigma + \nabla^2 G) + D \mathbf{n} \cdot \nabla (\kappa \sigma). \quad (13.17)$$

The terms on the l.h.s. of this equation describe the unsteady change and convection of σ . The first term on the r.h.s accounts for straining by the flow field which amounts to a production of flame surface area. The next term containing the laminar burning velocity has a similar effect as kinematic restoration has in the variance equation. The last term is proportional to D and its effect is similar to that of scalar dissipation in the variance equation.

In order to derive a model equation for the mean value $\bar{\sigma}$ we could, in principle, take the appropriate averages of Eq. (13.17). There is, however, no standard two-point closure procedure of such an equation, as there is none for deriving the ε -equation from an equation for the viscous dissipation. Therefore another approach was adopted in Peters (1999) [4]: The scaling relations between $\bar{\sigma}$, \tilde{k} , $\tilde{\varepsilon}$, and $\widetilde{G''^2}$ were used separately in both regimes to derive equations for $\bar{\sigma}$ from a combination of the \tilde{k} -, $\tilde{\varepsilon}$ - and $\widetilde{G''^2}$ -equations. The resulting equations contain the local change and convection of $\bar{\sigma}$, a production term by mean gradients and another due to turbulence. However, each of them contains a different sink term: In the corrugated flamelets regime the sink term is proportional to $s_L^0 \bar{\sigma}^2$ and in the thin reaction zones it is proportional to $D \bar{\sigma}^3$. Finally, in order to obtain a common equation for $\bar{\sigma}$ valid in both regimes, the two sink terms are assumed to be additive as are the two terms in Eq. (13.17) which also are proportional to s_L^0 and D .

Since proportionality between the turbulent burning velocity and $\bar{\sigma}$ is valid only in the limit of large values of v'/s_L , it accounts only for the increase of the flame surface area ratio due to turbulence, beyond the laminar value $\bar{\sigma} = |\nabla \widetilde{G}|$ for $v' \rightarrow 0$. We will therefore simply add the laminar contribution and write $\bar{\sigma}$ as

$$\bar{\sigma} = |\nabla \widetilde{G}| + \bar{\sigma}_t, \quad (13.18)$$

where $\bar{\sigma}_t$ now is the turbulent contribution to the flame surface area ratio $\bar{\sigma}$.

The resulting model equation for the unconditional quantity $\bar{\sigma}_t$ from Peters (1999) [4], that

covers both regimes, is written as

$$\begin{aligned} \bar{\rho} \frac{\partial \bar{\sigma}_t}{\partial t} + \bar{\rho} \tilde{\mathbf{v}} \cdot \nabla \bar{\sigma}_t &= \nabla_{||} \cdot (\bar{\rho} D_t \nabla_{||} \bar{\sigma}_t) \\ &+ c_0 \bar{\rho} \frac{(-\widetilde{\mathbf{v}'' \mathbf{v}''}) : \nabla \tilde{\mathbf{v}}}{\tilde{k}} \bar{\sigma}_t + c_1 \bar{\rho} \frac{D_t (\nabla \widetilde{G})^2}{\widetilde{G''^2}} \bar{\sigma}_t \\ &- c_2 \bar{\rho} \frac{s_L^0 \bar{\sigma}_t^2}{(\widetilde{G''^2})^{1/2}} - c_3 \bar{\rho} \frac{D \bar{\sigma}_t^3}{\widetilde{G''^2}}. \end{aligned} \quad (13.19)$$

The terms on the r.h.s. represent the local change and convection. Turbulent transport is modeled here by gradient transport in tangential direction only, since similar arguments as in the variance equation Eq. (12.47) apply with respect to the necessity of avoiding turbulent diffusion in direction normal to the turbulent flame surface. This is the first term on the r.h.s. of Eq. (13.20). The second term models production of the flame surface area ratio due to mean velocity gradients. The constant $c_0 = c_{\varepsilon_1} - 1 = 0.44$ originates from the $\tilde{\varepsilon}$ -equation Eq. (10.31). The last three terms in Eq. (13.20) represent turbulent production, kinematic restoration and scalar dissipation of the flame surface area ratio, respectively, and correspond to the three terms on the r.h.s of Eq. (13.17).

We now want to determine values for the modeling constants c_1 , c_2 , c_3 , and c_4 in Eq. (13.20). The average of the production term in Eq. (13.17) is equal to $-\overline{S\sigma}$. Wenzel (2000) [20] has performed DNS of the constant density G -equation in an isotropic homogeneous field of turbulence (cf. also Wenzel (1998) [21]), which show that the strain rate at the flame surface is statistically independent of σ and that the mean strain on the flame surface is always negative. The latter reflects the alignment of scalar gradients with the most compressive (negative) strain rate, as shown by Ashurst et al. (1987) [22] in analyzing DNS data of isotropic and homogeneous shear turbulence. When $-\overline{S\sigma}$, divided by $s_L^0 \bar{\sigma}$ is plotted over v'/s_L^0 one obtains a linear dependence. This leads to the closure model

$$-\overline{S\sigma} \sim \frac{v'}{\ell} \bar{\sigma}. \quad (13.20)$$

By comparing the production terms in Eqs. (13.17) and (13.20) the modeling constant c_1 in Eq. (13.20) was determined by Wenzel (2000) [20] as $c_1 = 4.63$.

In order to determine the remaining constants c_2 and c_3 we consider again the steady planar flame. In the planar case the convective term on the l.h.s. and the turbulent transport term on the r.h.s. of Eq. (13.20) vanish and since the flame is steady, so does the unsteady term. The production term due to velocity gradients, being in general much smaller than production by turbulence, may also be neglected. In terms of conditional quantities defined at the mean flame front, using

the definition Eq. (12.48) for the flame brush thickness $\ell_{F,t}$, the balance of turbulent production, kinematic restoration and scalar dissipation in Eq. (13.20) leads to the algebraic equation

$$c_1 \frac{D_t}{\ell_{F,t}^2} - c_2 \frac{s_L^0}{\ell_{F,t}} \frac{\bar{\sigma}_t}{|\nabla \tilde{G}|} - c_3 \frac{D}{\ell_{F,t}^2} \frac{\bar{\sigma}_t^2}{|\nabla \tilde{G}|^2} = 0. \quad (13.21)$$

In the limit of a steady state planar flame the flame brush thickness $\ell_{F,t}$ is proportional to the integral length scale ℓ . We may therefore use $\ell_{F,t} = b_2 \ell$ obtained from Eq. (12.51) in that limit and write Eq. (13.21) as

$$c_1 \frac{D_t}{\ell^2} - c_2 b_2 \frac{s_L^0}{\ell} \frac{\bar{\sigma}_t}{|\nabla \tilde{G}|} - c_3 \frac{D}{\ell^2} \frac{\bar{\sigma}_t^2}{|\nabla \tilde{G}|^2} = 0. \quad (13.22)$$

This equation covers two limits: In the corrugated flamelets regime the first two terms balance, while in the thin reaction zones regime there is a balance of the first and the last term. Using $D_t = a_4 v' \ell$ from Tab. 13.1 below it follows for the corrugated flamelets regime

$$c_2 b_2 s_L^0 \bar{\sigma}_t = a_4 c_1 v' |\nabla \tilde{G}|. \quad (13.23)$$

Experimental data (cf. Abdel-Gayed and Bradley (1981) [7]) for fully developed turbulent flames in that regime show that for $\text{Re} \rightarrow \infty$ and $v'/s_L \rightarrow \infty$ the turbulent burning velocity is $s_T^0 = b_1 v'$ where $b_1 = 2.0$. In Peters (2000) [23] it is shown that the turbulent burning velocity s_T is related to the mean flame surface area ratio as

$$(\rho s_T^0) |\nabla \tilde{G}| = (\rho s_L^0) \bar{\sigma}_t. \quad (13.24)$$

If the burning velocities s_T^0 and s_L^0 are evaluated at a constant density it follows in that limit that $s_L^0 \bar{\sigma}_t = b_1 v' |\nabla \tilde{G}|$ and therefore one obtains by comparison with Eq. (13.23)

$$b_1 b_2 c_2 = a_4 c_1 \quad (13.25)$$

which leads to $c_2 = 1.01$ using the constants from Tab. 13.1.

Similarly, for the thin reaction zones regime we obtain from Eq. (13.21) the balance

$$c_3 D \bar{\sigma}_t^2 = c_1 D_t |\nabla \tilde{G}|^2. \quad (13.26)$$

This must be compared with Eq. (13.8) written as

$$\frac{s_T^0}{s_L^0} = b_3 \left(\frac{D_t}{D} \right)^{1/2}. \quad (13.27)$$

Damköhler (1940) [2] believed that the constant of proportionality b_3 should be unity. Wenzel (1997) [21] has performed DNS simulations similar to those of Kerstein et al. (1988) [13] based on Eq. (12.33) in order to calculate $\bar{\sigma}$ in the thin reaction zones regime. He finds $b_3 = 1.07$ which is very close to Damköhler's suggestion. Therefore we will use $b_3 = 1.0$ which leads with $b_3^2 = c_1/c_3$ to

$$c_3 = c_1. \quad (13.28)$$

For consistency the diffusivity D is defined as $(\lambda/c_p)_0/\rho_u$. Then, with $\ell_F = D/s_L^0$ and the relations in Tab. 13.1, Eq. (13.21) leads to the quadratic equation

$$\frac{\bar{\sigma}_t^2}{|\nabla \tilde{G}|^2} + \frac{a_4 b_3^2}{b_1} \frac{\ell}{\ell_F} \frac{\bar{\sigma}_t}{|\nabla \tilde{G}|} - a_4 b_3^2 \frac{v' \ell}{s_L^0 \ell_F} = 0. \quad (13.29)$$

Using Eqs. (13.18) and (13.24) evaluated at a constant density, the difference Δs between the turbulent and the laminar burning velocity is

$$\Delta s = s_T^0 - s_L^0 = s_L^0 \frac{\bar{\sigma}_t}{|\nabla \tilde{G}|}. \quad (13.30)$$

Taking only the positive root in the solution of Eq. (13.29) this leads to an algebraic expression for Δs

$$\frac{\Delta s}{s_L^0} = -\frac{a_4 b_3^2}{2 b_1} \frac{\ell}{\ell_F} + \left[\left(\frac{a_4 b_3^2}{2 b_1} \frac{\ell}{\ell_F} \right)^2 + a_4 b_3^2 \frac{v' \ell}{s_L^0 \ell_F} \right]^{1/2}. \quad (13.31)$$

This expression corresponds in the limit $\ell/\ell_F \rightarrow \infty$ to the corrugated flamelets regime and in the limit $\ell/\ell_F \rightarrow 0$ to the thin reaction zones regime.

The modeling constants used in the final equations for \tilde{G} , $\widetilde{G''^2}$ and $\bar{\sigma}_t$ are summarized in Tab. 13.1. Note that b_1 is the only constant that has been adjusted using experimental data from turbulent burning velocity while the constant b_3 was suggested by Damköhler (1940) [2]. The constant c_1 was obtained from DNS and all other constants are related to constants in standard turbulence models.

If Eq. (13.31) is compared with experimental data as in the burning velocity diagram in Fig. 13.2, the turbulent Reynolds number $\text{Re}_t = v' \ell / s_L^0 \ell_F$ appears as a parameter. From the view-

constant	equation	suggested value	origin
a_1	$\tilde{\varepsilon} = a_1 v'^3 / \ell$	0.37	Bray (1990)
a_2	$\tilde{k} = a_2 v'^2$	1.5	definition
a_3	$\tau = a_3 \ell / v'$	4.05	$\tau = \tilde{k} / \tilde{\varepsilon}$
a_4	$D_t = a_4 v' \ell$	0.78	$D_t = \nu_t / 0.7$
b_1	$s_T = b_1 v'$	2.0	experimental data
b_2	$\ell_{F,t} = b_2 \ell$	1.78	$(2a_3 a_4 / c_s)^{1/2}$
b_3	$s_T^0 / s_L^0 = b_3 (D_t / D)^{1/2}$	1.0	Damköhler (1940)
c_0	$c_0 = c_{\varepsilon 1} - 1$	0.44	standard value
c_1	Eq. (13.18)	4.63	DNS
c_2	Eq. (13.18)	1.01	$a_4 c_1 / (b_1 b_2)$
c_3	Eq. (13.18)	4.63	$c_1 = c_3$
c_s	Eq. (12.47)	2.0	spectral closure

Table 13.1: Constants used in the modeling of premixed and partially premixed turbulent combustion.

point of turbulence modeling this seems disturbing, since in free shear flows any turbulent quantity should be independent of the Reynolds number in the large Reynolds number limit. The apparent Reynolds number dependence of Eq. (13.31) turns out to be an artifact, resulting from the normalization of Δs by s_L^0 , which is a molecular quantity whose influence should disappear in the limit of large Reynolds numbers and large values of v'/s_L . If the burning velocity difference Δs is normalized by v' rather than by s_L^0 , Eq. (13.31) may be expressed as a function of the turbulent Damköhler number $\text{Da}_t = s_L^0 \ell / v' \ell_F$ instead, and one obtains the form

$$\frac{\Delta s}{v'} = -\frac{a_4 b_3^2}{2 b_1} \text{Da}_t + \left[\left(\frac{a_4 b_3^2}{2 b_1} \text{Da}_t \right)^2 + a_4 b_3^2 \text{Da}_t \right]^{1/2}. \quad (13.32)$$

This is Reynolds number independent and only a function of a single parameter, the turbulent Damköhler number. In the limit of large scale turbulence ($\ell/\ell_F \rightarrow \infty$, or $\text{Da}_t \rightarrow \infty$) it becomes Damköhler number independent. In the small scale turbulence limit ($\ell/\ell_F \rightarrow 0$ or $\text{Da}_t \rightarrow 0$), it is proportional to the square root of the Damköhler number.

A Damköhler number scaling has also been suggested by Gülder (1990b) who has proposed

$$\frac{\Delta s}{v'} = 0.62 \text{Da}_t^{1/4} \quad (13.33)$$

as an empirical fit to a large number of burning velocity data. A similar correlation with the same Damköhler number dependence, but a constant of 0.51 instead of 0.62 was proposed by Zimont

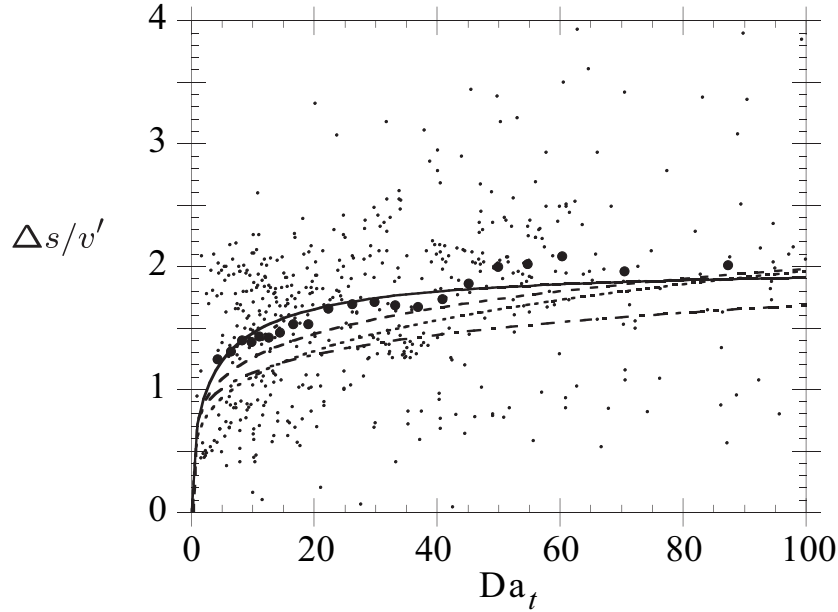


Figure 13.4: The burning velocity difference $\Delta = s_T - s_L$, normalized by v' , as a function of the turbulent Damköhler number. — Eq. (13.32), Eq. (13.33), - - - Eq. (13.36) with $v'/s_L = 2$, - · - - Eq. (13.36) with $v'/s_L = 5$.

and Lipatnikov (1995) [10].

Bradley et al. (1992) [6], pointing at flame stretch as a determinant of the turbulent burning velocity, propose to use the product of the Karlovitz stretch factor K and the Lewis number as the appropriate scaling parameter

$$\frac{s_T^0}{v'} = 0.88(K \text{Le})^{-0.3}, \quad (13.34)$$

where the Karlovitz stretch factor is related to the Damköhler number by

$$K = 0.157 \frac{v'}{s_L^0} \text{Da}_t^{-1/2}. \quad (13.35)$$

This leads to the expression

$$\frac{\Delta s}{v'} = 1.53 \left(\frac{s_L^0}{v'} \right)^{0.3} \text{Da}_t^{0.15} \text{Le}^{-0.3} - \frac{s_L^0}{v'}. \quad (13.36)$$

The correlations Eqs. (13.32), (13.33) and (13.36) are compared in Fig. 13.4 among each

other and with data from the experimental data collection used by Bradley et al. (1992) [6], which was kindly provided to us by M. Lawes. The data points show a large scatter, which is due to the fact that the experimental conditions were not always well defined. Since unsteady effects have been neglected in deriving Eq. (13.31), only data based on steady state experiments were retained from this collection. These 598 data points and their averages within fixed ranges of the turbulent Damköhler number are shown in Fig. 13.4 as small and large dots, respectively. In order to make such a comparison possible, the Lewis number was assumed equal to unity in Eq. (13.36) and two values of v'/s_L^0 were chosen. As a common feature of all three correlations one may note that $\Delta s/v'$ strongly increases in the range of turbulent Damköhler numbers up to ten, but levels off for larger turbulent Damköhler numbers. The correlation Eq. (13.32) is the only one that predicts Damköhler number independence in the large Damköhler number limit.

The model for the turbulent burning velocity derived here is based on Eq. (12.33) in which the mass diffusivity D (rather than the Markstein diffusivity) appears. As a consequence, flame stretch and thereby the Lewis number effects do not enter into the model. Lewis number effects are often found to influence the turbulent burning velocity (cf. Abdel-Gayed et al. (1984) [24]). This is supported by two-dimensional numerical simulations by Ashurst et al. (1987) [22] and Haworth and Poinsot (1992) [25], and by three-dimensional simulations by Rutland and Trouv   (1993) [26], all being based on simplified chemistry. There are additional experimental data on Lewis number effects in turbulent flames at moderate intensities by Lee et al. (1993) [27] and Lee et al. (1995) [28].

Bibliography

- [1] P. Clavin. Dynamic behaviour of premixed flame fronts in laminar and turbulent flows. *Progr. Energy Combust. Sci.*, 11:1–59, 1985.
- [2] G. Damköhler. Der einfluß der turbulenz auf die flammengeschwindigkeit in gasgemischen. *Z. Elektrochem.* 1947, *English translation NASA Tech. Mem.*, 1112., 46, 1940.
- [3] F. A. Williams. *Combustion Theory, Second Edition*. The Benjamin Cummings Publishing Co. Menlo Park, 1985.
- [4] N. Peters. The turbulent burning velocity for large scale and small scale turbulence. *J. Fluid Mech.*, 384:107–132, 1999.
- [5] K. N. C. Bray. Studies of the turbulent burning velocity. *Proc. Roy. Soc. Lond.*, A431:315–335, 1990.
- [6] D. Bradley. How fast can we burn? *Twenty-Fourth Symposium (International) on Combustion, The Combustion Institute, Pittsburgh*, pages 247–262, 1992.
- [7] R. G. Abdel-Gayed and D. Bradley. A two-eddy theory of premixed turbulent flame propagation. *Phil. Trans. Roy. Soc. Lond.*, 301:1–25, 1981.
- [8] Bradley D. Abdel-Gayed, R. G. and M. Lawes. Turbulent burning velocities: a general correlation in terms of strain rates. *Proc. Roy. Soc. Lond.*, A414:389–413, 1987.
- [9] Ö. L. Gülder. Turbulent premixed flame propagation models for different combustion regimes. *Twenty-Third Symposium (International) on Combustion, The Combustion Institute, Pittsburgh*, pages 743–750, 1990.
- [10] V. L. Zimont and A. N. Lipatnikov. A numerical model of premixed turbulent combustion of gases. *Chem. Phys. Reports*, 14:993–1025, 1995.

- [11] F. C. Gouldin. An application of fractals to modeling premixed turbulent flames. *Combust. Flame*, 68:249–266, 1987.
- [12] N. Peters. Laminar flamelet concepts in turbulent combustion. *Twenty-First Symposium (International) on Combustion, The Combustion Institute, Pittsburgh*, pages 1231–1250, 1986.
- [13] A. R. Kerstein. Fractal dimension of turbulent premixed flames. *Combust. Sci. and Tech.*, 60:441–445, 1988.
- [14] Ö. L. Gülder. Turbulent premixed combustion modelling using fractal geometry. *Twenty-Third Symposium (International) on Combustion, The Combustion Institute, Pittsburgh*, pages 835–842, 1990.
- [15] Ö. L. Gülder. Fractal characteristics and surface density of flame fronts in turbulent premixed combustion. *Mediterranean Combustion Symposium 99, Antalya, Turkey*, pages 130–154, 1999.
- [16] Kawabata Y. Maruta K. Kobayashi, H. Experimental study on general correlation of turbulent burning velocity at high pressure. *Twenty-Seventh Symposium (International) on Combustion, The Combustion Institute, Pittsburgh*, 1998.
- [17] J. H. Chen and H. G. Im. Correlation of flame speed with stretch in turbulent premixed methane/air flames. *Twenty-Seventh Symposium (International) on Combustion, The Combustion Institute, Pittsburgh*, pages 819–826, 1998.
- [18] W. Kollmann and J. H. Chen. Pocket formation and the flame surface density equation. *Twenty-Seventh Symposium (International) on Combustion, The Combustion Institute, Pittsburgh*, pages 927–934, 1998.
- [19] Ferziger J. H. Rutland, C. J. and S. H. El Tahry. Full numerical simulation and modelling of turbulent premixed flames. *Twenty-Third Symposium (International) on Combustion, The Combustion Institute, Pittsburgh*, pages 621–627, 1990.
- [20] H. Wenzel. *Direkte numerische Simulation der Ausbreitung einer Flammenfront in einem homogenen Turbulenzfeld*. Dissertation, RWTH Aachen University, Germany, 2000.
- [21] H. Wenzel. Turbulent premixed combustion in the laminar flamelet and the thin reaction zones regime. *Annual Research Briefs, Center for Turbulence Research*, pages 237–252, 1997.

- [22] Wm. T. Ashurst, A. R. Kerstein, R. M. Kerr, and C. H. Gibson. Alignment of vorticity and scalar gradient with strain rate in simulated Navier-Stokes turbulence. *Phys. Fluids*, 30:2343–2353, 1987.
- [23] N. Peters. *Turbulent Combustion*. Cambridge University Press, 2000.
- [24] Bradley D. Hamid M. N. Abdel-Gayed, R. G. and M. Lawes. Lewis number effects on turbulent burning velocity. *Twentieth Symposium (International) on Combustion, The Combustion Institute, Pittsburgh*, 100:505–512, 1984.
- [25] D.C. Haworth and T. J. Poinsot. The importance of time dependent flame structures in stretched laminar flamelet models for turbulent jet diffusion flames, journal= J. Fluid Mech., year = 1992 volume = 224, pages = 405-437.
- [26] C. J Rutland and A. Trouv . Direct simulations of premixed turbulent flames with non-unity lewis number. *Combust. Flame*, 94:41–57, 1993.
- [27] North G. L. Lee, J. G. and D. A. Santavicca. Surface properties of turbulent premixed propane/air flames at various lewis numbers. *Combust. Flame*, 93:445–456, 1993.
- [28] Lee T. W. Nye D. A. Lee, J. G. and D. A. Santavicca. Lewis number effects on premixed flames interacting with turbulent k rm n vortex streets. *Combust. Flame*, 100:161–168, 1995.

Lecture 14

Non-Premixed Turbulent Combustion: The Flamelet Concept

Models in nonpremixed turbulent combustion are often based on the presumed shape pdf approach. This requires the knowledge of the Favre mean mixture fraction \tilde{Z} and its variance $\widetilde{Z''^2}$ at position x and time t . As shown in Section 10.7 of Lecture 10 averaging of the mixture fraction equation Eq. (3.58) and using the gradient transport assumption Eq. (10.59) leads to the equation for the Favre mean mixture fraction \tilde{Z} Eq. (10.61)

$$\bar{\rho} \frac{\partial \tilde{Z}}{\partial t} + \bar{\rho} \tilde{\mathbf{v}} \cdot \nabla \tilde{Z} = \nabla \cdot (\bar{\rho} D_t \nabla \tilde{Z}). \quad (14.1)$$

The molecular diffusivity D in Eq. (3.58) is much smaller than the turbulent diffusivity D_t , and has therefore been neglected in Eq. (14.1). In addition to the mean mixture fraction in Section 10.7 of Lecture 10 we have derived an equation for the Favre variance $\widetilde{Z''^2}$ Eq. (10.63)

$$\bar{\rho} \frac{\partial \widetilde{Z''^2}}{\partial t} + \bar{\rho} \tilde{\mathbf{v}} \cdot \nabla \widetilde{Z''^2} = -\nabla \cdot (\bar{\rho} \widetilde{\mathbf{v}'' Z''^2}) + 2\bar{\rho} D_t (\nabla \tilde{Z})^2 - \bar{\rho} \tilde{\chi}, \quad (14.2)$$

where for $-\widetilde{\mathbf{v}'' Z''}$ the gradient transport assumption Eq. (10.59) has again been used in the third term on the r.h.s., the production term. For the turbulent flux of the mixture fraction variance the gradient transport assumption

$$-\widetilde{\mathbf{v}'' Z''^2} = D_t \nabla \widetilde{Z''^2} \quad (14.3)$$

can also be used in Eq. (14.2). In Eq. (14.2) the mean scalar dissipation rate appears, which will be modeled (10.66) as

$$\tilde{\chi} = c_\chi \frac{\tilde{\varepsilon}}{k} \widetilde{Z''^2} \quad (14.4)$$

where the time scale ratio c_χ is assumed to be a constant. Jones (1994) [1] suggests a value of $c_\chi = 1.0$, while Janicka and Peters (1982) [2] found that a value of $c_\chi = 2.0$ would predict the decay of scalar variance in an inert jet of methane very well. Overholt and Pope (1996) [3] and Juneja and Pope (1996) [4] performing DNS studies of one and two passive scalar mixing find an increase of c_χ with Reynolds number and steady state values around 2.0 and 3.0, respectively. In the numerical simulations of Diesel engine combustion, to be presented in Lecture 15, Section 15.2, a value of $c_\chi = 2.0$ has been used.

In many cases, as in turbulent jet diffusion flames in air, zero gradient boundary conditions, except at the inlet, can be imposed. If the simplifying assumptions mentioned in Section 3.9 of Lecture 3 can be introduced the enthalpy h can be related to the mixture fraction by the linear coupling relation

$$h = h_2 + Z(h_1 - h_2) \quad (14.5)$$

which also holds for the mean values

$$\tilde{h} = h_2 + \tilde{Z}(h_1 - h_2) \quad (14.6)$$

and no additional equation for the enthalpy is required. In Eqs. (14.5) and (14.6) h_2 is the enthalpy of the air and h_1 that of the fuel.

A more general formulation is needed, if different boundary conditions have to be applied for \tilde{Z} and \tilde{h} or if heat loss due to radiation or unsteady pressure changes must be accounted for. Then an equation for the Favre mean enthalpy \tilde{h} as an additional variable must be solved. An equation for \tilde{h} can be obtained from Eq. (3.43) by averaging

$$\bar{\rho} \frac{\partial \tilde{h}}{\partial t} + \bar{\rho} \tilde{\mathbf{v}} \cdot \nabla \tilde{h} = \frac{\partial \bar{p}}{\partial t} + \nabla \cdot (\bar{\rho} D_t \nabla \tilde{h}) + \bar{q}_R. \quad (14.7)$$

Again a gradient transport equation for $-\widetilde{\mathbf{v}''h''}$ has been introduced. The terms containing the mean spatial pressure gradient have been neglected in this equation by applying the limit of zero Mach number, where fast acoustic waves are rapidly homogenizing the pressure field. The term describing temporal mean pressure changes $\partial \bar{p} / \partial t$ has been retained, because it is important

for the modeling of combustion in internal combustion engines operating under nonpremixed conditions, such as the Diesel engine. The mean volumetric heat exchange term $\overline{\dot{q}_R}$ must also be retained in many applications where radiative heat exchange has an influence on the local enthalpy balance. Marracino and Lentini (1997) [5] have used the Stretched Laminar Flamelet Model to calculate the radiative heat flux from buoyant turbulent methane-air diffusion flames. Temperature changes due to radiation within the flamelet structure also have a strong influence on the prediction of NO_x formation (cf. Pitsch et al. (1998) [6]). Changes of the mean enthalpy also occur due to convective heat transfer at the boundaries or due to the evaporation of a liquid fuel. As in Eqs. (14.1) and (14.2) the transport term containing the molecular diffusivity has been neglected in Eq. (14.7) as being small compared to the turbulent transport term. Effects due to non-unity Lewis numbers have also been neglected.

No equation for enthalpy fluctuations is presented here, because in nonpremixed turbulent combustion, it is often assumed that fluctuations of the enthalpy are mainly due to mixture fraction fluctuations and are described by those.

14.1 The Presumed Shape Pdf Approach

Eqs. (14.1)-(14.3) can be used to calculate the mean mixture fraction and the mixture fraction variance at each point of the turbulent flow field, provided that the density field is known. In addition, of course, equations for the turbulent flow field, the Reynolds stress equations (or the equation for the turbulent kinetic energy \tilde{k}) and the equation for the dissipation $\tilde{\varepsilon}$ must be solved. If the assumption of fast chemistry is introduced and the coupling between the mixture fraction and the enthalpy Eq. (14.5) can be used, the Burke-Schumann solution or the equilibrium solution relates all reactive scalars to the local mixture fraction. Using these relations the easiest way to obtain mean values of the reactive scalars is to use the presumed shape pdf approach. This is called the Conserved Scalar Equilibrium Model. In this approach a suitable two-parameter probability density function is “presumed” in advance, thereby fixing the functional form of the pdf by relating the two parameters in terms of the known values of \tilde{Z} and $\widetilde{Z''^2}$ at each point of the flow field.

Since in a two-feed system the mixture fraction Z varies between $Z = 0$ and $Z = 1$, the beta function pdf is widely used for the Favre pdf in nonpremixed turbulent combustion. The beta-

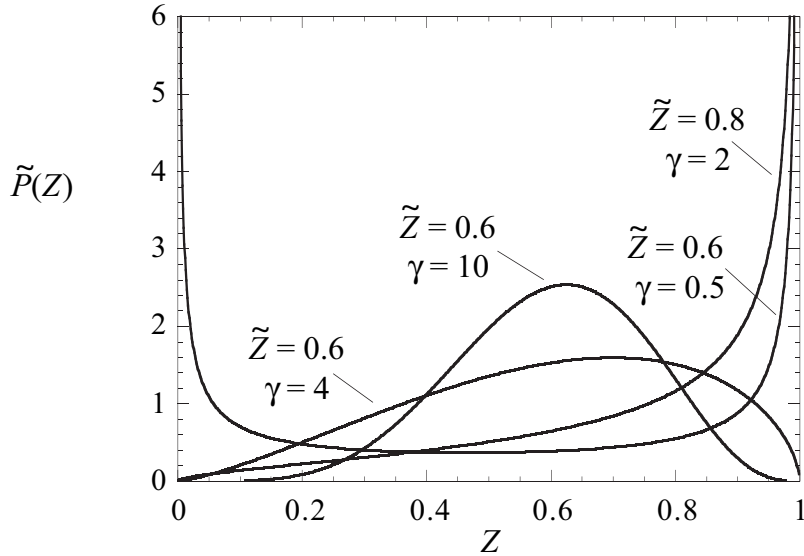


Figure 14.1: Shapes of the beta-function pdf for different parameters \tilde{Z} and γ .

function pdf has the form

$$\tilde{P}(Z; x, t) = \frac{Z^{\alpha-1}(1-Z)^{\beta-1} \Gamma(\alpha + \beta)}{\Gamma(\alpha)\Gamma(\beta)} \quad (14.8)$$

Here Γ is the gamma function. The two parameters α and β are related to the Favre mean $\tilde{Z}(x, t)$ and variance $\widetilde{Z''^2}(x, t)$ by

$$\alpha = \tilde{Z}\gamma, \quad \beta = (1 - \tilde{Z})\gamma, \quad (14.9)$$

where

$$\gamma = \frac{\tilde{Z}(1 - \tilde{Z})}{\widetilde{Z''^2}} - 1 \geq 0. \quad (14.10)$$

The beta-function is plotted for different combinations of the parameters \tilde{Z} and γ in Fig. 14.1. It can be shown that in the limit of very small $\widetilde{Z''^2}$ (large γ) it approaches a Gaussian distribution. For $\alpha < 1$ it develops a singularity at $Z = 0$ and for $\beta < 1$ a singularity at $Z = 1$. Despite of its surprising flexibility, it is unable to describe distributions with a singularity at $Z = 0$ or $Z = 1$ and an additional intermediate maximum in the range $0 < Z < 1$. For such shapes, which have been found in jets and shear layers, a composite model has been developed by Effelsberg and Peters (1983) [7]. It identifies three different contributions to the pdf: a fully turbulent part, an outer flow

part and a part which was related to the viscous superlayer between the outer flow and the fully turbulent flow region. The model shows that the intermediate maximum is due to the contribution from the fully turbulent part of the scalar field.

By the presumed shape pdf approach means of any quantity that depends only on the mixture fraction can be calculated. For instance, the mean value of ψ_i can be obtained from

$$\tilde{\psi}_i(\mathbf{x}, t) = \int_0^1 \psi_i(Z) \tilde{P}(Z; \mathbf{x}, t) dZ. \quad (14.11)$$

A further quantity of interest is the mean density $\bar{\rho}$. Since Favre averages are considered, one must take the Favre average of ρ^{-1} , which leads to

$$\widetilde{\rho^{-1}} = \frac{1}{\bar{\rho}} = \int_0^1 \rho^{-1}(Z) \tilde{P}(Z) dZ. \quad (14.12)$$

With Eqs. (14.8)-(14.12) and the Burke-Schumann solution or the equilibrium solution the Conserved Scalar Equilibrium Model for nonpremixed combustion is formulated. It is based on a closed set of equations which do not require any further chemical input other than the assumption of infinitely fast chemistry. It may therefore be used as an initial guess in a calculation where the Burke-Schumann solution or the equilibrium solution later on is replaced by the solution of the flamelet equations to account for non-equilibrium effects.

14.2 The Round Turbulent Jet Diffusion Flame

In many applications fuel enters into the combustion chamber as a turbulent jet, with or without swirl. To provide an understanding of the basic properties of jet diffusion flames, we will consider here the easiest case, the axisymmetric jet flame without buoyancy, for which we can obtain approximate analytical solutions. This will enable us to determine, for instance, the flame length. The flame length is defined as the distance from the nozzle to the point on the centerline of the flame where the mean mixture fraction is equal to Z_{st} . The flow configuration and the flame contour of a vertical jet diffusion flame have already been shown schematically in Fig. 9.5 but for a laminar jet flame.

Using Favre averaging and the boundary layer assumption we obtain a system of two-dimensional axisymmetric equations, similar to Eqs. (9.22-9.24) but for Favre averages. These will be in terms of the axial co-ordinate x and the radial co-ordinate r , for

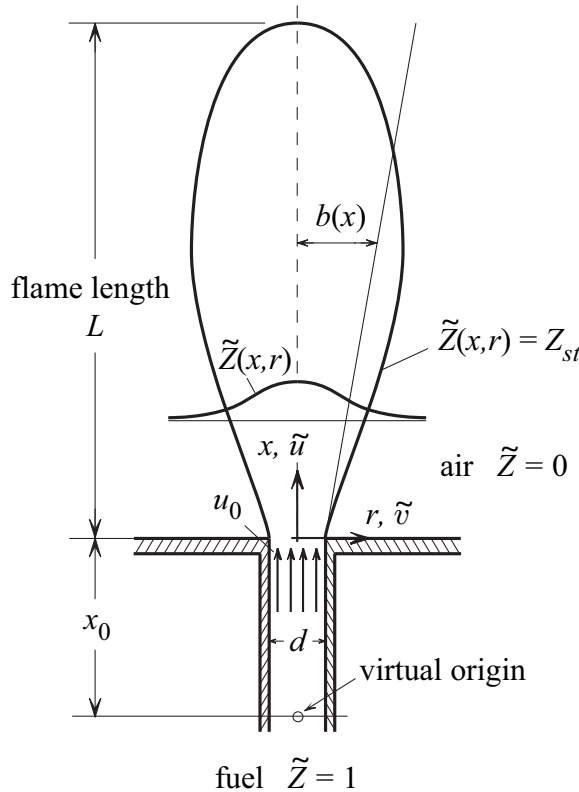


Figure 14.2: Schematic representation of a vertical jet flame into quiescent air.

continuity

$$\frac{\partial}{\partial x} (\bar{\rho} \tilde{u} r) + \frac{\partial}{\partial r} (\bar{\rho} \tilde{v} r) = 0, \quad (14.13)$$

momentum in x -direction

$$\bar{\rho} \tilde{u} r \frac{\partial \tilde{u}}{\partial x} + \bar{\rho} \tilde{v} r \frac{\partial \tilde{u}}{\partial r} = \frac{\partial}{\partial r} \left(\bar{\rho} \nu_t r \frac{\partial \tilde{u}}{\partial r} \right), \quad (14.14)$$

mean mixture fraction

$$\bar{\rho} \tilde{u} r \frac{\partial \tilde{Z}}{\partial x} + \bar{\rho} \tilde{v} r \frac{\partial \tilde{Z}}{\partial r} = \frac{\partial}{\partial r} \left(\frac{\bar{\rho} \nu_t r}{\text{Sc}_t} \frac{\partial \tilde{Z}}{\partial r} \right). \quad (14.15)$$

We have neglected molecular as compared to turbulent transport terms. Turbulent transport was modeled by the gradient flux approximation. For the scalar flux we have replaced D_t by introducing

the turbulent Schmidt number $Sc_t = \nu_t/D_t$.

For simplicity, we will not consider equations for \tilde{k} and $\tilde{\varepsilon}$ or the mixture fraction variance but seek an approximate solution by introducing a model for the turbulent viscosity ν_t . Details may be found in Peters and Donnerhack (1981) [8]. As in Section 9.2 for the laminar round diffusion flame the dimensionality of the problem will again be reduced by introducing the similarity transformation

$$\eta = \frac{\bar{r}}{\xi}, \quad \bar{r}^2 = 2 \int_0^r \frac{\bar{\rho}}{\rho_\infty} r \, dr, \quad \xi = x + x_0, \quad (14.16)$$

which contains a density transformation defining the density weighted radial co-ordinate \bar{r} . The new axial co-ordinate ξ starts from the virtual origin of the jet located at $x = -x_0$. Introducing a stream function ψ by

$$\bar{\rho}\tilde{u}r = \partial\psi/\partial r, \quad \bar{\rho}\tilde{v}r = -\partial\psi/\partial x \quad (14.17)$$

the continuity equation Eq. (14.13) is satisfied. In terms of the non-dimensional stream function $F(\eta)$ defined by

$$F(\eta) = \frac{\psi}{\rho_\infty \nu_{tr} \xi} \quad (14.18)$$

the axial and radial velocity components may now be expressed as

$$\tilde{u} = \frac{\frac{dF}{d\eta}}{\eta} \frac{\nu_{tr}}{\xi}, \quad \bar{\rho}\tilde{v}r = -\rho_\infty \nu_{tr} \left(F - \frac{dF}{d\eta} \eta \right). \quad (14.19)$$

Here ν_{tr} is the eddy viscosity of a constant density jet, used as a reference value. Differently from the laminar flame, where ν is a molecular property, ν_{tr} has been fitted (cf. Peters and Donnerhack (1981) [8] to experimental data as

$$\nu_{tr} = \frac{u_0 d}{70}. \quad (14.20)$$

For the mixture fraction the ansatz

$$\tilde{Z} = \tilde{Z}_{CL}(\xi) \tilde{\omega}(\eta) \quad (14.21)$$

is introduced, where \tilde{Z}_{CL} stands for the Favre mean mixture fraction on the centerline.

The system of equation for the turbulent round jet has the same similarity solution as the one derived in Section 9.2 of Lecture 9. Here we approximate the Chapman-Rubesin parameter, however, as:

$$C = \frac{\bar{\rho}^2 \nu_t r^2}{\rho_\infty^2 \nu_{tr} \bar{r}^2}. \quad (14.22)$$

In order to derive an analytical solution it must be assumed that C is a constant in the entire jet. With a constant value of C one obtains the system of differential equations as Eqs. (9.34) and its solution Eq. (9.35), if only the Schmidt number is replaced by a turbulent Schmidt number Sc_t . The solution reads

$$\tilde{u} = \frac{2C\gamma^2\nu_{tr}}{\xi} \left(\frac{1}{1 + (\gamma\eta/2)^2} \right)^2, \quad \tilde{\omega} = \left(\frac{1}{1 + (\gamma\eta/2)^2} \right)^{2Sc_t}, \quad (14.23)$$

where the jet spreading parameter is again

$$\gamma^2 = \frac{3 \cdot 70^2}{64} \frac{\rho_0}{\rho_\infty C^2} \quad (14.24)$$

obtained from the requirement of integral momentum conservation along the axial direction. Similarly, conservation of the mixture fraction integral across the jet yields the mixture fraction on the centerline

$$\tilde{Z}_{CL} = \frac{70(1 + 2Sc_t)}{32} \frac{\rho_0}{\rho_\infty C} \frac{d}{\xi} \quad (14.25)$$

such that the mixture fraction profile is given by

$$\tilde{Z} = \frac{2.19(1 + 2Sc_t)d}{x + x_0} \frac{\rho_0}{\rho_\infty C} \left(1 + \frac{1}{1 + (\gamma\eta/2)^2} \right)^{2Sc_t}. \quad (14.26)$$

From this equation the flame length L can be calculated by setting $\tilde{Z} = Z_{st}$ at $x = L, r = 0$

$$\frac{L + x_0}{d} = \frac{2.19(1 + 2Sc_t)}{Z_{st}} \frac{\rho_0}{\rho_\infty C}. \quad (14.27)$$

Experimental data by Hawthorne et al. (1949) [9] suggest that the flame length L should scale as

$$\frac{L + x_0}{d} = \frac{5.3}{Z_{st}} \left(\frac{\rho_0}{\rho_{st}} \right)^{1/2}. \quad (14.28)$$

This fixes the turbulent Schmidt number as $Sc_t = 0.71$ and the Chapman-Rubesin parameter as

$$C = \frac{(\rho_0\rho_{st})^{1/2}}{\rho_\infty}. \quad (14.29)$$

When this is introduced into Eqs. (14.23) and (14.24) one obtains the centerline velocity as

$$\frac{\tilde{u}_{CL}}{u_0} = \frac{6.56d}{x + x_0} \left(\frac{\rho_0}{\rho_{st}} \right)^{1/2}. \quad (14.30)$$

The distance of the virtual origin from $x = 0$ may be estimated by setting $\tilde{u}_{CL} = u_0$ at $x = 0$ in Eq. (14.30) so that

$$x_0 = 6.56 d \left(\frac{\rho_0}{\rho_{st}} \right)^{1/2}. \quad (14.31)$$

As an example for the flame length, we set the molecular weight at stoichiometric mixture equal to that of nitrogen, thereby estimating the density ratio ρ_0/ρ_{st} from

$$\frac{\rho_0}{\rho_{st}} = \frac{W_0}{W_{N_2}} \frac{T_{st}}{T_0}. \quad (14.32)$$

The flame length may then be calculated from Eq. (14.28) with $Z_{st} = 0.055$ as $L \sim 200 d$.

In large turbulent diffusion flames buoyancy influences the turbulent flow field and thereby the flame length. In order to derive a scaling law for that case, Peters and Göttgens (1991) [10] have integrated the boundary layer equations for momentum and mixture fraction for a vertical jet flame over the radial direction in order to obtain first order differential equations in terms of the axial coordinate for cross-sectional averages of the axial velocity and the mixture fraction. Since turbulent transport disappears entirely due to averaging, an empirical model for the entrainment coefficient β is needed, which relates the half-width b of the jet to the axial co-ordinate as

$$b(x) = \beta x. \quad (14.33)$$

By comparison with the similarity solution for a non-buoyant jet β was determined as

$$\beta = 0.23 \left(\frac{\rho_{st}}{\rho_0} \right)^{1/2}. \quad (14.34)$$

For the buoyant jet flame a closed form solution for the flame length could be derived which reads

$$\left(\frac{3}{4} \beta \text{Fr}^* - \frac{1}{8} \right) \left(\frac{\beta L}{d_{\text{eff}}} \right)^2 + \left(\frac{\beta L}{d_{\text{eff}}} \right)^5 = \frac{3\beta\alpha_1^2}{16 Z_{st}^2} \text{Fr}^*. \quad (14.35)$$

Here Fr^* is the modified Froude number

$$\text{Fr}^* = \text{Fr} \left(\frac{\rho_0}{\rho_\infty} \right)^{1/2} \frac{\rho_\infty}{\alpha_2(\rho_\infty - \rho_{st})}, \quad \text{Fr} = \frac{u_0^2}{gd} \quad (14.36)$$

and

$$d_{\text{eff}} = d \left(\frac{\rho_0}{\rho_\infty} \right)^{1/2} \quad (14.37)$$

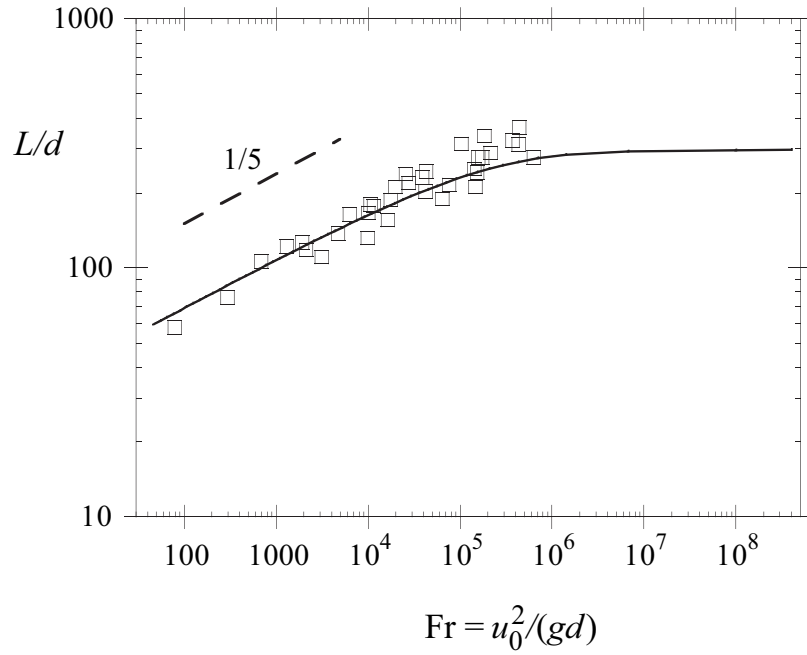


Figure 14.3: Dimensionless flame length, L/d , versus Froude number for propane-air flames. Comparison is made with experimental data of Sønju and Hustad (1984) [11].

is the effective nozzle diameter. The constants in Eqs. (14.35) and (14.36) are determined as $\alpha_1 = 1 + 2 \text{Sc}_t$ and $\alpha_2 = 1.0$. Details of the derivation may be found in Peters and Göttgens (1991) [10].

The flame length of propane flames calculated from Eq. (14.35) is compared with measurements from Sønju and Hustad (1984) [11] in Fig. 14.3. For Froude numbers smaller than 10^5 the data show a Froude number scaling as $\text{Fr}^{1/5}$, which corresponds to a balance of the second term on the l.h.s. with the term on the r.h.s. in Eq. (14.35). For Froude numbers larger than 10^6 the flame length becomes Froude number independent equal to the value calculated from Eq. (14.27).

14.3 Experimental Data from Turbulent Jet Diffusion Flames

While the flame length may be calculated on the basis of the fast chemistry assumption using the solution for mean mixture fraction field alone, more details on scalars are needed if one wants to determine chemical effects and pollutant formation in turbulent jet flames. For that purpose

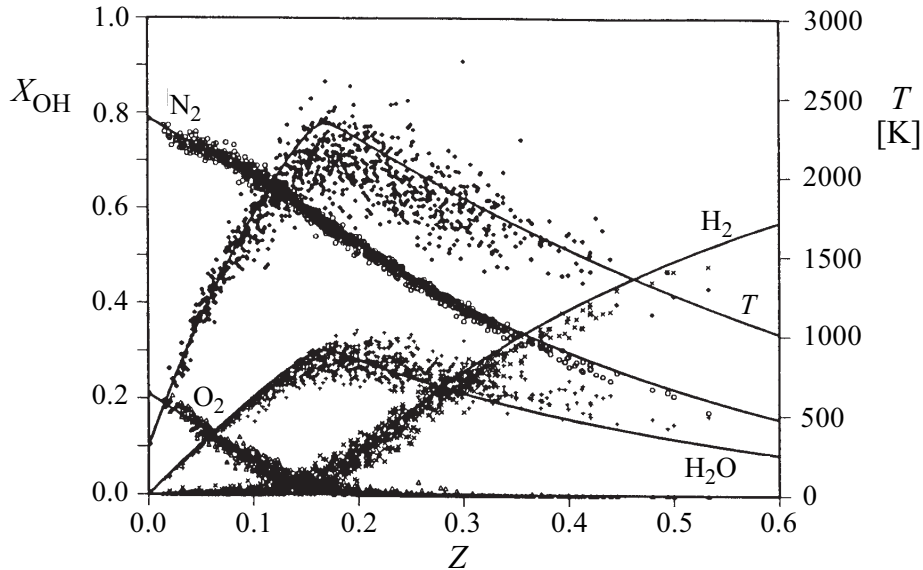


Figure 14.4: Ensemble of Raman scattering measurements of major species concentrations and temperatures at $x/d = 30, r/D = 2$. The solid curves show equilibrium conditions. (From Barlow et al. (1990) [12].

we want to discuss data taken locally within turbulent jet flames by non-intrusive laser-diagnostic techniques. There is a large body of experimental data on single point measurements using Laser Rayleigh and Raman scattering techniques combined with Laser-Induced Fluorescence (LIF). Since a comprehensive review on the subject by Masri et al. (1996) [13] is available, it suffices to present as an example the results by Barlow et al. (1990) [12] obtained by the combined Raman-Rayleigh-LIF technique. This paper has set a landmark not only due to the diagnostics that were used but also because of the interpretation of the chemical structure in terms of laminar flamelet profiles. The fuel stream of the two flames that were investigated consisted of a mixture of 78 mole% H_2 and 22 mole% argon, the nozzle inner diameter d was 5.2 mm and the co-flow air velocity was 9.2 m/s. The resulting flame length was approximately $L = 60d$. Two cases of exit velocities were analyzed, but only the case B with $u_0 = 150$ m/s will be considered here. The stable species H_2 , O_2 , N_2 , and H_2O were measured using Raman-scattering at a single point with light from a flash-lamp pumped dye laser. In addition, quantitative OH radical concentrations from LIF measurements were obtained by using the instantaneous one-point Raman data to calculate quenching corrections for each laser shot. The correction factor was close to unity for stoichio-

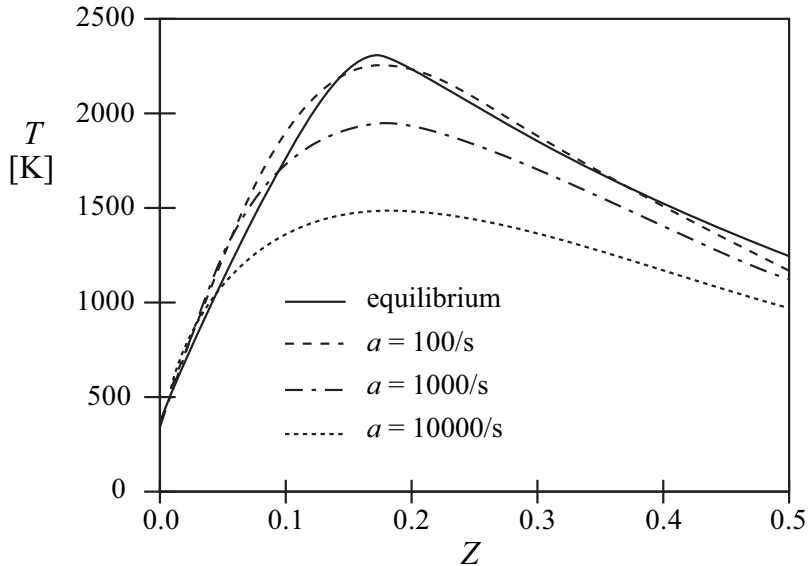


Figure 14.5: Temperature profiles from flamelet calculations at different strain rates. (From Barlow et al. (1990)[12].

metric and moderately lean conditions but increased rapidly for very lean and moderately rich mixtures. The temperature was calculated for each laser shot by adding number densities of the major species and using the perfect gas law. The mixture fraction was calculated from the stable species concentrations using Eq. (1.47).

An ensemble of one-point, one-time Raman-scattering measurements of major species and temperature plotted over mixture fraction are shown in Fig. 14.4. They were taken at $x/d = 30$, $r/d = 2$ in the case B flame. Also shown are calculations based on the assumption of chemical equilibrium.

The overall agreement between the experimental data and the equilibrium solution is quite good. This is often observed for hydrogen flames where chemistry is typically very fast. On the contrary, hydrocarbon flames at high exit velocities and small nozzle diameters are likely to exhibit local extinction and non-equilibrium effects. A discussion on localized extinction observed in turbulent jet flames may be found in Masri et al. (1996) [13]. Fig. 14.5 shows temperature profiles versus mixture fraction calculated for counterflow diffusion flames at different strain rates. These steady state flamelet profiles display the characteristic decrease of the maximum temperature with increasing strain rates (which corresponds to decreasing Damköhler numbers) as shown schemat-

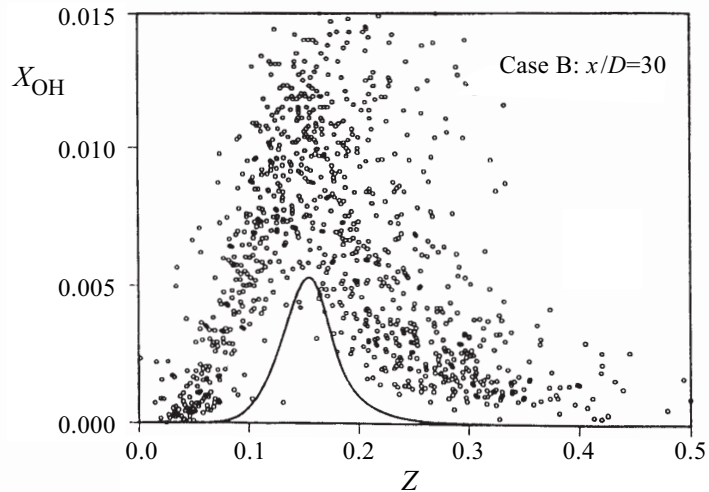


Figure 14.6: Ensemble of LIF measurements of OH mole fractions at $x/d = 30$, $r/D = 2$. The solid curve shows equilibrium solution.

ically by the upper branch of the S-shaped curve in Fig. 10.1. The strain rates vary here between $a = 100/\text{s}$ which is close to chemical equilibrium and $a = 10000/\text{s}$.

Data of OH-concentrations are shown in Fig. 14.6. They are to be compared to flamelet calculations in Fig. 14.7 for the different strain rates mentioned before. It is evident from Fig. 14.6 that the local OH-concentrations exceed those of the equilibrium profile by a factor up to 3. The flamelet calculations in Fig. 14.7 show an increase of the maximum values by a factor of 3 already at the low strain rates $a = 100/\text{s}$ and $a = 1000/\text{s}$. The maximum value of $a = 10000/\text{s}$ shown in Fig. 14.7 is close to extinction and does not represent conditions in the turbulent hydrogen flame considered here.

In summary, it may be concluded that one-point, one-time experimental data in turbulent flames, when plotted as a function of mixture fraction, show qualitatively similar tendencies as laminar flamelet profiles in counterflow diffusion flames. Non-equilibrium effects are evident in both cases and lead to an increase of radical concentrations and a decrease of temperatures. This has an important influence on NO_x formation in turbulent diffusion flames.

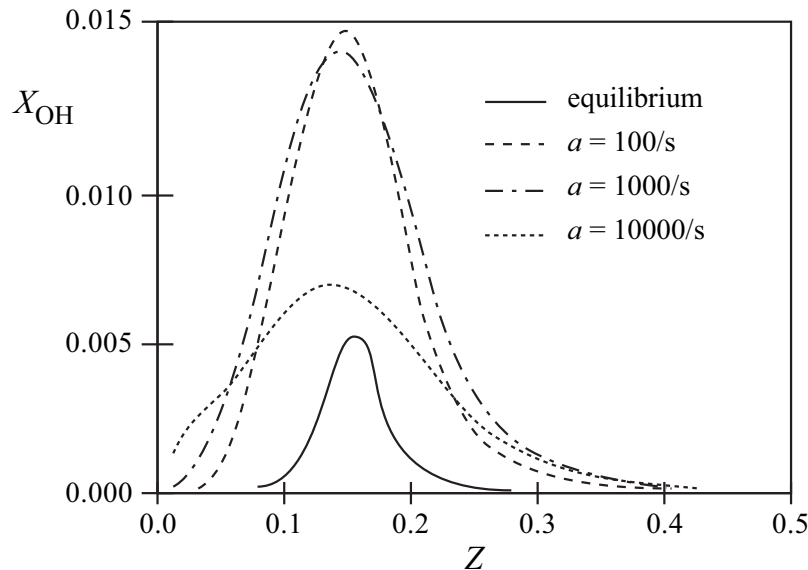


Figure 14.7: OH mole fractions from flamelet calculations at different strain rates.

14.4 Laminar Flamelet Equations for Nonpremixed Combustion

Based on the laminar flamelet concept introduced in Lecture 8 the flame surface is defined as the surface of stoichiometric mixture which is obtained by setting

$$Z(\boldsymbol{x}, t) = Z_{st} \quad (14.38)$$

as shown in Fig. 8.2. In the vicinity of that surface the reactive-diffusive structure can be described by the flamelet equations Eqs. 8.7, here written

$$\rho \frac{\partial \psi_i}{\partial t} = \frac{\rho}{Le_i} \frac{\chi}{2} \frac{\partial^2 \psi_i}{\partial Z^2} + \omega_i \quad (14.39)$$

In these equations the instantaneous scalar dissipation rate has been introduced. At the flame surface, it takes the value χ_{st} . If χ is assumed to be a function of Z , this functional dependence can be parameterized by χ_{st} . It acts as an external parameter that is imposed on the flamelet structure by the mixture fraction field. The scalar dissipation rate χ has the dimension of an inverse

time and therefore represents the inverse of a diffusion time scale. It also can be thought of as a diffusivity in mixture fraction space.

Eq. (14.39) shows that ψ_i depends on the mixture fraction Z , on the scalar dissipation rate χ , and on time t . This implies that the reactive scalars are constant along iso-mixture fraction surfaces at a given time and a prescribed functional form of the scalar dissipation rate. Thereby the fields of the reactive scalars are aligned to that of the mixture fraction and are transported together with it by the flow field.

In principle, both the mixture fraction Z and the scalar dissipation rate χ are fluctuating quantities and their statistical distribution needs to be considered, if one wants to calculate statistical moments of the reactive scalars (cf. Peters (1984) [14]).

If the joint pdf $\tilde{P}(Z, \chi_{st})$ surface, is known, and the steady state flamelet equations are solved to obtain ψ_i as a function of Z and χ_{st} , point x and the time t . The Favre mean $\tilde{\psi}_i$ can be obtained from

$$\tilde{\psi}_i(x, t) = \int_0^1 \int_0^\infty \psi_i(Z, \chi_{st}) P(Z, \chi_{st}; x, t) d\chi_{st} dZ. \quad (14.40)$$

For further reading see Peters (1984) [14].

If the unsteady term in the flamelet equation must be retained, joint statistics of Z and χ_{st} become impractical. Then, in order to reduce the dimension of the statistics, it is useful to introduce multiple flamelets, each representing a different range of the χ -distribution. Such multiple flamelets are used in the Eulerian Particle Flamelet Model (EPFM) by Barths et al. (1998) [15].

Then the scalar dissipation rate can be formulated as a function of the mixture fraction. Such a formulation can be used in modeling the conditional Favre mean scalar dissipation rate $\tilde{\chi}_Z$ defined by

$$\tilde{\chi}_Z = \frac{\langle \rho \chi | Z \rangle}{\langle \rho | Z \rangle}. \quad (14.41)$$

Then the flamelet equations in a turbulent flow field take the form

$$\rho \frac{\partial \psi_i}{\partial t} = \frac{\rho}{Le_i} \frac{\tilde{\chi}_Z}{2} \frac{\partial^2 \psi_i}{\partial Z^2} + \omega_i. \quad (14.42)$$

A mean scalar dissipation rate, however, is unable to account for those ignition and extinction events that are triggered by small and large values of χ , respectively. This is where LES, as discussed in Lecture 10, must be used.

With $\psi_i(Z, \tilde{\chi}_Z, t)$ obtained from solving Eq. (14.42), Favre mean values $\tilde{\psi}_i$ can be obtained at

any point x and time t in the flow field by

$$\tilde{\psi}_i(\mathbf{x}, t) = \int_0^1 \psi_i(Z, \tilde{\chi}_Z, t) \tilde{P}(Z; \mathbf{x}, t) dZ. \quad (14.43)$$

Here the presumed shape of the pdf $\tilde{P}(Z; \mathbf{x}, t)$ can be calculated from the mean and the variance of the turbulent mixture fraction field, as discussed in Section 14.1.

Then there remains the problem on how to model the conditional scalar dissipation rate $\tilde{\chi}_Z$. One way to solve that problem is to use the procedure by Janicka and Peters (1982) [2], where $\tilde{\chi}_Z$ is determined from the pdf transport equation for the mixture fraction. Another possibility is to construct $\tilde{\chi}_Z$ from a model. One then relates the conditional scalar dissipation rate $\tilde{\chi}_Z$ to that at a fixed value, say Z_{st} , by

$$\tilde{\chi}_Z = \tilde{\chi}_{st} \frac{f(Z)}{f(Z_{st})}, \quad (14.44)$$

where $f(Z)$ is a function as in Eq. (8.24) and $\tilde{\chi}_{st}$ is the conditional mean scalar dissipation rate at $Z = Z_{st}$. Then, with the presumed pdf $\tilde{P}(Z)$ being known, the unconditional average can be written as

$$\tilde{\chi} = \int_0^1 \tilde{\chi}_Z \tilde{P}(Z) dZ = \tilde{\chi}_{st} \int_0^1 \frac{f(Z)}{f(Z_{st})} \tilde{P}(Z) dZ. \quad (14.45)$$

Therefore, using the model Eq. (14.4) for $\tilde{\chi}$, the conditional mean scalar dissipation rate $\tilde{\chi}_{st}$ can be expressed as

$$\tilde{\chi}_{st} = \frac{\tilde{\chi} f(Z_{st})}{\int_0^1 f(Z) \tilde{P}(Z) dZ} \quad (14.46)$$

which is to be used in Eq. (14.44) to calculate $\tilde{\chi}_Z$.

Flamelet equations can also be used to describe ignition in a nonpremixed system. If fuel and oxidizer are initially at the unburnt temperature $T_u(Z)$, as was shown in Fig. 2.1, but the scalar dissipation rate is still large enough, so that heat loss out of the reaction zone exceeds the heat release by chemical reactions, a thermal runaway is not possible. This corresponds to the steady state lower branch in Fig. 10.1. As the scalar dissipation rate decreases, as for instance in a Diesel engine after injection, heat release by chemical reactions will exceed heat loss out of the reaction zone, leading to auto-ignition. The scalar dissipation rate at auto-ignition is denoted by

$$\chi_i = \chi_{st, ign}. \quad (14.47)$$

For ignition under Diesel engine conditions this has been investigated by Pitsch and Peters (1998b)

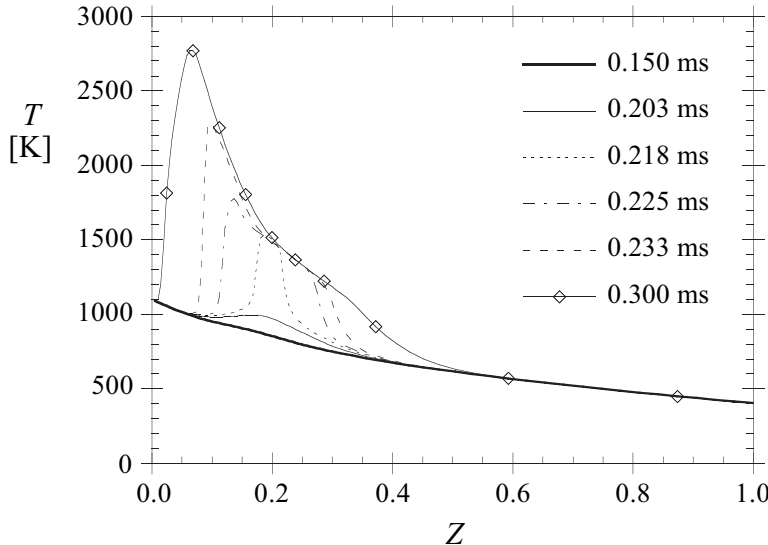


Figure 14.8: Auto-ignition of a *n*-heptane-air mixture calculated in mixture fraction space by solving the flamelet equations (cf. Paczko et al. (1999) [16]).

[17]. An example of auto-ignition of a *n*-heptane-air mixture calculated with the Representative Interactive Flamelets code (RIF, cf. Paczko et al. (1999) [16] is shown in Fig. 14.8. The initial air temperature is 1100 K and the initial fuel temperature is 400 K. Mixing of fuel and air leads to a straight line for the enthalpy in mixture fraction space, but not for the temperature $T_u(Z)$ in Fig. 14.8, since the heat capacity c_p depends on temperature. A linear decrease of the scalar dissipation rate from $\chi_{st} = 30 \text{ l/s}$ to $\chi_{st} = 10 \text{ l/s}$ within a time interval of 0.3 ms was prescribed. It is seen that auto-ignition starts after 0.203 ms, when the temperature profile shows already a small increase over a broad region around $Z = 0.2$. At $t = 0.218 \text{ ms}$ there has been a fast thermal runaway in that region, with a peak at the adiabatic flame temperature. From thereon, the temperature profile broadens, which may be interpreted as a propagation of two fronts in mixture fraction space, one towards the lean and the other towards the rich mixture. Although the transport term in Eq. (14.39) contributes to this propagation, it should be kept in mind that the mixture is close to auto-ignition everywhere. The propagation of an ignition front in mixture fraction space therefore differs considerably from premixed flame propagation. At $t = 0.3 \text{ ms}$ most of the mixture, except for a region beyond $Z = 0.4$ in mixture fraction space, has reached the equilibrium temperature. A maximum value of $T = 2750 \text{ K}$ is found close to stoichiometric mixture.

The ignition of *n*-heptane mixtures under Diesel engine condition has been discussed in detail

by Pitsch and Peters (1998b) [17]. There it is shown that auto-ignition under nonpremixed conditions occurs predominantly at locations in a turbulent flow field where the scalar dissipation rate is low. Turbulent combustion models have also been used to predict NO_x formation in turbulent diffusion flames. This is a problem of great practical importance, but due to the many physical aspects involved, it is also a very demanding test for any combustion model. A very knowledgeable review on the various aspects of the problem has been given by Turns (1995) [18].

A global scaling law for NO production in turbulent jet flames has been derived by Peters and Donnerhack (1981) [8] assuming equilibrium combustion chemistry and thin NO reaction zone around the maximum temperature in mixture fraction space. An asymptotic solution for the mean turbulent NO production rate can be obtained by realizing that in the expression

$$\bar{\omega}_{\text{NO}} = \bar{\rho} \tilde{S}_{\text{NO}} = \bar{\rho} \int_0^1 S_{\text{NO}}(Z) \tilde{P}(Z) dZ \quad (14.48)$$

the function $S_{\text{NO}}(Z)$ has a very strong peak in the vicinity of the maximum temperature, but decreases very rapidly to both sides. This is shown in Fig. 14.9 for the case of a hydrogen flame. The NO reaction rate acts nearly like a δ -function underneath the integral in Eq. (14.48). It has been shown by Peters (1978) [19] and Janicka and Peters (1982) [2] that an asymptotic expansion of the reaction rate around the maximum temperature leads to

$$\bar{\omega}_{\text{NO}} = \bar{\rho} \tilde{P}(Z_b) \varepsilon S_{\text{NO}}(Z_b), \quad (14.49)$$

where Z_b is the mixture fraction at the maximum temperature T_b and $S_{\text{NO}}(Z_b)$ is the maximum reaction rate. The quantity ε represents the reaction zone thickness of NO production in mixture fraction space. That quantity was derived from the asymptotic theory as

$$\varepsilon = \left(\frac{-2RT_b^2}{Z_b^2 E_{\text{NO}} (d^2 T / dZ^2)_{T_b}} \right)^{1/2}. \quad (14.50)$$

Here E_{NO} is the activation energy of the NO production rate. Finally, Peters and Donnerhack (1981) [8] predicted the NO emission index EINO, which represents the total mass flow rate of NO produced per mass flow rate of fuel, as being proportional to

$$\text{EINO} \sim S_{\text{NO}}(Z_b) \varepsilon \left(\frac{L}{d} \right)^3 \frac{d}{u_0}. \quad (14.51)$$

Here L is the flame length, d the nozzle diameter and u_0 the jet exit velocity. The normalized

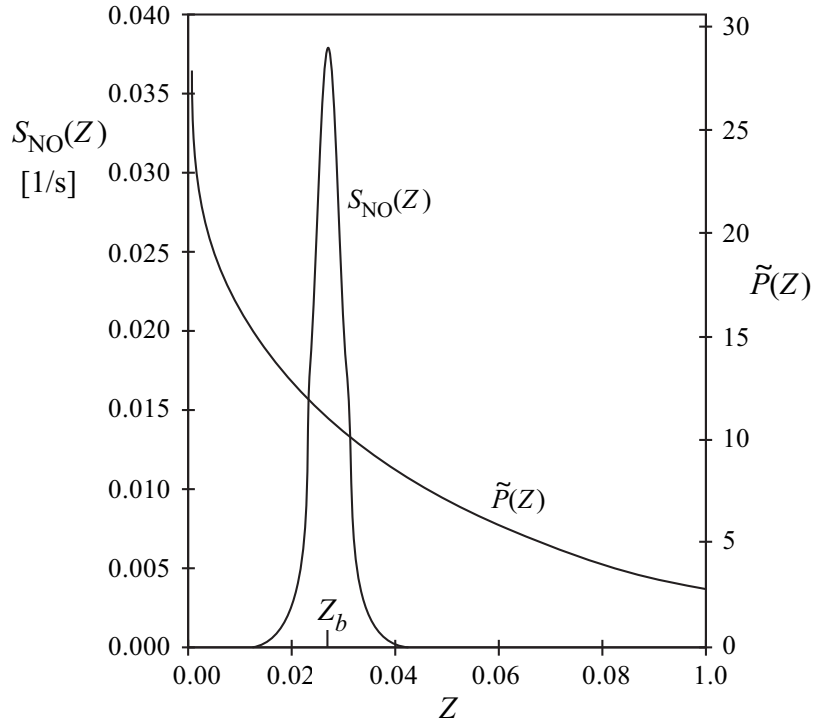


Figure 14.9: NO-reaction rate and pdf for a hydrogen-air mixture. From Peters and Donnerhack (1981) [8].

flame length L/d is constant for momentum dominated jets but scales with the Froude number $\text{Fr} = u_0^2/(gd)$ as $L/d \sim \text{Fr}^{1/5}$ for buoyancy dominated jets as shown in Fig. 14.3. This explains, for instance, the $\text{Fr}^{3/5}$ dependence of the emission index found in the buoyancy dominated propane jet diffusion flames of Røkke et al. (1992) [20]. These data are reproduced in Fig. 14.10 together with the prediction of the NO_x emission index (expressed here in terms of NO_2)

$$\frac{\text{EINO}_x}{d/u_0} = 22 \text{Fr}^{3/5} \left[\frac{\text{gNO}_2}{\text{kg fuel s}} \right]. \quad (14.52)$$

It is interesting to note that by taking the values $S_{\text{NO}}(Z_b) = 10.8 \times 10^{-3}/\text{s}$ and $\varepsilon = 0.109$ for propane from Peters and Donnerhack (1981) [8] and using Eq. (14.35) in the buoyancy dominated limit one calculates a factor of 27.2 rather than 22 in Eq. (14.52). Since Peters and Donnerhack (1981) [8] had assumed equilibrium combustion chemistry, the second derivative of the temperature in Eq. (14.50) was calculated from an equilibrium temperature profile as the one shown in Fig. 14.4.

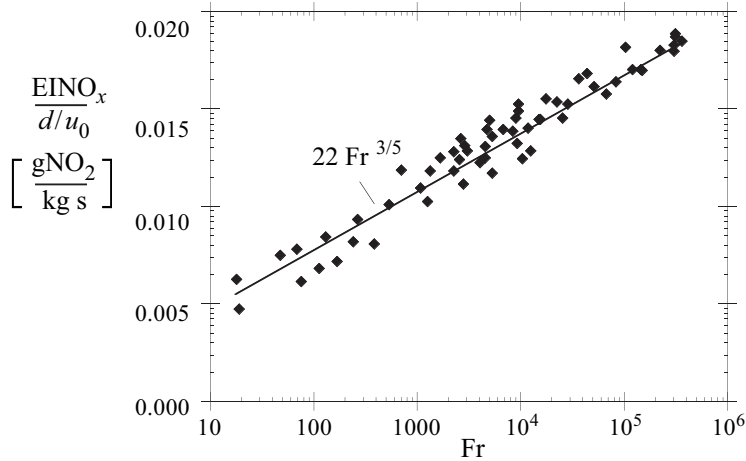


Figure 14.10: Emission index versus Froude number for buoyant jet diffusion flames of propane in air. Experimental data and prediction from Røkke et al.(1992) [20].

Therefore ε was tabulated as a constant for each fuel. If the quantity $S_{\text{NO}}(Z_b)d/u_0$ is interpreted as a Damköhler number the rescaled emission index from Eq. (14.51) is

$$\frac{\text{EINO}}{(L/d)^3} \sim \varepsilon \text{Da} \quad (14.53)$$

proportional to that Damköhler number.

An interesting set of experimental data are those by Chen and Driscoll (1990) [21] and Driscoll et al. (1992) [22] for diluted hydrogen flames. These data show a square root dependence of the rescaled emission index on the Damköhler number. This $\text{Da}^{1/2}$ dependence had been reproduced by Chen and Kollmann (1992) [23] using the transported pdf approach and by Smith et al. (1992) [24] with the CMC method. An explanation for this scaling may be found by using the steady state flamelet equation for the second derivative of temperature in Eq. (14.50) rather than the equilibrium profile. This may be written as

$$\frac{d^2T}{dZ^2} \sim \frac{\omega_T}{\chi}. \quad (14.54)$$

Here the term on the r.h.s., evaluated at and divided by the maximum temperature, may also be interpreted as a Damköhler number. This becomes evident, if one realizes that in a turbulent jet diffusion flame χ scales with u_0/d . Inserting this into Eq. (14.50) the quantity ε becomes

proportional to $\text{Da}^{-1/2}$. This finally leads with Eq. (14.53) to

$$\frac{\text{EINO}}{(L/d)^3} \sim \text{Da}^{1/2}. \quad (14.55)$$

This scaling law indicates that the experimentally observed $(d/u_0)^{1/2}$ dependence of the rescaled NO emission index is a residence time effect, modified by the temperature sensitivity of the NO reaction rate, on which the asymptotic theory by Peters and Donnerhack (1981) [8] was built. It also shows that unsteady effects of the flame structure and super-equilibrium O-concentrations may be of less importance than is generally assumed.

Sanders et al. (1997) [25] have reexamined steady state flamelet modeling using the two variable presumed shape pdf model for the mixture fractions and, either the scalar dissipation rate or the strain rate as second variable. Their study revealed that only the formulation using the scalar dissipation rate as the second variable was able to predict the $\text{Da}^{1/2}$ dependence of the data of Driscoll et al. (1992) [22]. This is in agreement with results of Ferreira (1996) [26]. In addition Sanders et al. (1997) [25] examined whether there is a difference between using a lognormal pdf of χ_{st} with a variance of unity and a delta function pdf and found that both assumptions gave similar results. Their predictions improved with increasing Damköhler number and their results also suggest that $\text{Le}_i = 1$ is the best choice for these hydrogen flames.

For a turbulent jet flame with a fuel mixture of 31% methane and 69% hydrogen Chen and Chang (1996) [27] performed a detailed comparison between steady state flamelet and pdf modeling. They found that radiative heat loss becomes increasingly important for NO predictions further downstream in the flame. This is in agreement with the comparison of time scales by Pitsch et al. (1998) [28] who found that radiation is too slow to be effective as far as the combustion reactions are concerned, but that it effects NO levels considerably.

Bibliography

- [1] W. P. Jones. Turbulence modeling and numerical solution methods for variable density and combusting flows. In *Turbulent Reacting Flows*, publisher = Academic Press, year = 1994, editor = P. A. Libby and F. A. Williams, Eds., volume = , series = , pages = 309–374,.
- [2] J. Janicka and N. Peters. Prediction of turbulent jet diffusion flame lift-off using a pdf transport equation. *Nineteenth Symposium (International) on Combustion, The Combustion Institute, Pittsburgh*, pages 367–374, 1982.
- [3] M. R. Overholz and S. B. Pope. Direct numerical simulation of a passive scalar with imposed mean gradient in isotropic turbulence. *Phys. Fluids*, 8:3128–3148, 1996.
- [4] A. Juneja and S. B. Pope. A dns study of turbulent mixing of two passive scalars, journal= *Phys. Fluids*, year = 1996, volume = 8, pages = 2177–2184.
- [5] B. Marracino and D. Lentini. Radiation modelling in non-luminous nonpremixed turbulent flames, journal= *Combust. Sci. and Tech.*, year = 1997, volume = 8, pages = 23–48.
- [6] H. Pitsch. *Modellierung der Zündung und Schadstoffbildung*. PhD thesis.
- [7] E. Effelsberg and N. Peters. A composite model for the conserved scalar pdf. *Combust. Flame*, 50:351–360, 1983.
- [8] N. Peters and S. Donnerhack. Structure and similarity of nitric oxide production in turbulent diffusion flames. *Eighteenth Symposium (International) on Combustion, The Combustion Institute, Pittsburgh*, 1981.
- [9] Weddell D. S. Hawthorne, W. R. and H. C. Hottel. Mixing and combustion of turbulent gas jets. *Third Symposium on Combustion, Flame and Explosion Phenomena, Williams and Wilkins, Baltimore*, pages 266–288, 1949.

- [10] N. Peters. Length scales in laminar and turbulent flames. In E.S. Oran and J.A. Boris, editors, *Numerical Approaches to Combustion Modeling*, volume 135, pages 155–182. Prog. Astronautics and Aeronautics, AIAA, 1991.
- [11] O. K. Sønju and J. E. Hustad. An experimental study of turbulent jet diffusion flames. In *Dynamics of Flames and Reactive Systems*, volume 95, pages 320–339. Prog. Astronautics and Aeronautics, 1984.
- [12] Dibble R. W. Chen J.-Y. Barlow, R. S. and R. P. Lucht. Effect of the damköhler number on super-equilibrium oh concentration in turbulent nonpremixed jet flames. *Combust. Flame*, 1990.
- [13] Dibble R. W. Masri, A. R. and R. S. Barlow. Turbulent nonpremixed flames stabilized on a piloted jet burner. In R. S. Barlow, editor, *International Workshop on Measurements and Computation of Turbulent Nonpremixed Flames, Naples, Italy*. Prog. Astronautics and Aeronautics, 1996.
- [14] N. Peters. *Progress in Energy and Combustion Science*, 10:319–339, 1984.
- [15] Antoni C. Barths, H. and N. Peters. Three-dimensional simulation of pollutant formation in a di-diesel engine using multiple interactive flamelets. *SAE paper 982459*, 1998.
- [16] Barths H. Miculic I. Paczko, G. and N. Peters. Demo-rif user guide, version 1.0. <http://www.flamelets.com/RIFUG.pdf>, 1999.
- [17] H. Pitsch, M. Chen, and N. Peters. Unsteady flamelet modeling of turbulent hydrogen/air diffusion flames. *Proc. Combust. Inst.*, 27:1057–64, 1998.
- [18] S. R. Turns. Understanding NO_x formation in nonpremixed flames: Experiments and modeling. *Prog. Energy Combust. Sci.*, 21:361–385, 1995.
- [19] N. Peters. An asymptotic analysis of nitric oxide formation in turbulent diffusion flames. *Combust. Sci. and Tech.*, 19:39–49, 1978.
- [20] Hustad J. E. Sønju O. K. Rø kke, N. A. and F. A. Williams. Scaling of nitric oxide emissions from buoyancy-dominated hydrocarbon turbulent jet diffusion flames. *Twenty-Fourth Symposium (International) on Combustion, The Combustion Institute, Pittsburgh*, pages 385–393, 1992.

- [21] Dibble R. W. Chen, J.-Y. and R. W. Bilger. Pdf modeling of turbulent nonpremixed CO/H₂/N₂ jet flames with reduced mechanisms. *Twenty-Third Symposium (International) on Combustion, The Combustion Institute, Pittsburgh*, pages 775–780, 1990.
- [22] Chen R.-H. Driscoll, J. F and Y. Yoon. Nitric oxide levels of turbulent jet diffusion flames: Effects of residence time and damköhler number. *Combust. Flame*, 88:37–49, 1992.
- [23] J.-Y. Chen and W. Kollmann. Pdf modeling and analysis of thermal no formation in turbulent nonpremixed hydrogen-air jet flames. *Combust. Flame*, 88:397–412, 1992.
- [24] Bilger-R. W. Smith, N. S. A. and J.-Y. Chen. Modelling nonpremixed hydrogen jet flames using a conditional moment closure method. *Twenty-Fourth Symposium (International) on Combustion, The Combustion Institute, Pittsburgh*, pages 263–269, 1992.
- [25] Chen-J.-Y. Sanders, J. P. H. and I. Gökalp. Flamelet-based modeling of no formation in turbulent hydrogen jet diffusion flames. *Combust. Flame*, pages 1–15, 1997.
- [26] J. C. Ferreira. *Flamelet modelling of stabilization in turbulent non-premixed combustion*. Dissertation, ETH Zürich, Switzerland, Nr. 11984, 1996.
- [27] J.-Y. Chen and W.-C. Chang. Flamelet and pdf modeling of co and no_x emissions from a turbulent, methane hydrogen jet nonpremixed flame. *Twenty-Sixth Symposium (International) on Combustion, The Combustion Institute, Pittsburgh*, pages 2207–2214, 1996.
- [28] H. Pitsch and N. Peters. A consistent flamelet formulation for non-premixed combustion considering differential diffusion effects. *Combust. Flame*, 114:26–40, 1998.

Lecture 15

Applications in Internal Combustion Engines

15.1 Spray-Guided Spark-Ignition Combustion

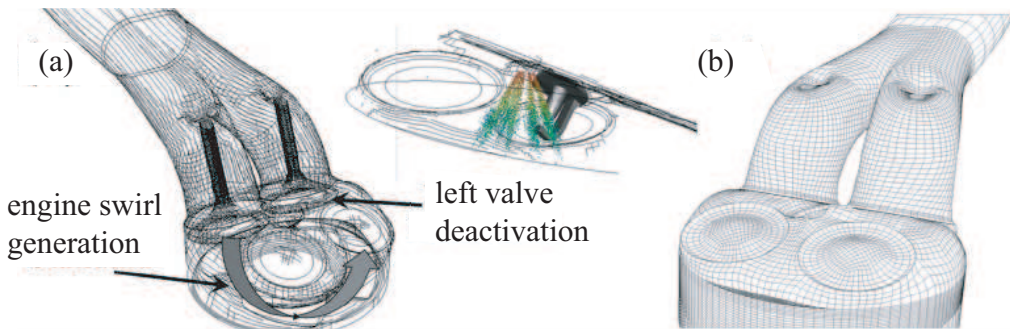


Figure 15.1: (a) Visualization of the mixture preparation process. A detailed 3D numerical simulation of the intake process with a deactivated left intake valve for enhanced swirl generation is performed. The direct fuel spray injection is modeled using a Lagrangian spray model. The spark plug is included in the engine mesh. (b) Unstructured computational grid ($\sim 222,000$ grid cells) of the engine including the model for the intake runner and the siamese port. (Reprinted with permission by R. Dahms.)

An important application of the G -equation flamelet theory is given by the simulation of turbulent combustion in spray-guided spark-ignition direct-injection (SG-SIDI) gasoline engines. These

		Cases		
		I	II	III
Intake air temperature	°C	91	95	103
Engine speed	rpm	1000	2000	3000
Ignition timing	° CA ATDC	-29	-34	-40
Start of injection	° CA ATDC	-32.3	-43	-59.5
End of injection	° CA ATDC	-29	-35	-39.9
Injected fuel mass	mg	5.6	9.3	12.93
Mean air/fuel ratio	[–]	43	27	22
Mean EGR	%	49.8	44	36.2
Dilution mass fraction	[–]	0.183	0.268	0.273

Table 15.1: Specifications of the investigated engine operating points. The dilution mass fraction is defined as $Y_{\text{dil}} = Y_{\text{inert,EGR}} - Y_{\text{air,EGR}}$.

engines offer substantially improved fuel economy and pollutant emission reductions compared to stratified charge wall-guided and homogeneous charge spark-ignition systems. The closeness of the fuel spray and the spark electrodes, shown in Fig. 15.1(a), can cause, however, unfavorable conditions for ignition and combustion.

A novel development of flamelet models to obtain a more comprehensive understanding of these SG-SIDI ignition processes is presented by the SparkCIMM model, recently developed by Dahms, Fansler, Drake, Kuo, Lippert, and Peters (2009) [1]. The setup and the experimental data of the investigated SG-SIDI gasoline engine were provided by the R&D department of the General Motors Company in Warren, MI, U.S.A. The specifications of the investigated engine operating points are summarized in Tab. 15.1. They differ in engine speed and load, applied level of exhaust gas recirculation, and in the timings of fuel injection and spark-ignition. The engine is equipped with a siamese port, a four-valve pent-roof head, and a contoured combustion bowl in the piston. The preparation of the combustible mixture at spark-timing is calculated with a three-dimensional CFD simulation of the gas exchange process, using a standard $k - \varepsilon$ turbulence model. The intake runner, the siamese port, and the spark plug are included in the engine model to capture the interactions of the fuel spray with the spark electrodes, shown in Fig. 15.1(b). The computational grids for the gas exchange and the spray-guided spark-ignition combustion process comprise $\sim 222,000$ and $\sim 97,000$ grid cells, respectively. An enhanced swirl field is generated by the deactivation of the left intake valve as presented in Fig. 15.1(a). The direct spray-injection is modeled with 25,000 stochastic Lagrangian spray parcels coupled to the gas phase via source terms. An initial droplet size distribution ($SMD = 15 \mu\text{m}$) is assumed instead of modeling the primary breakup. More details

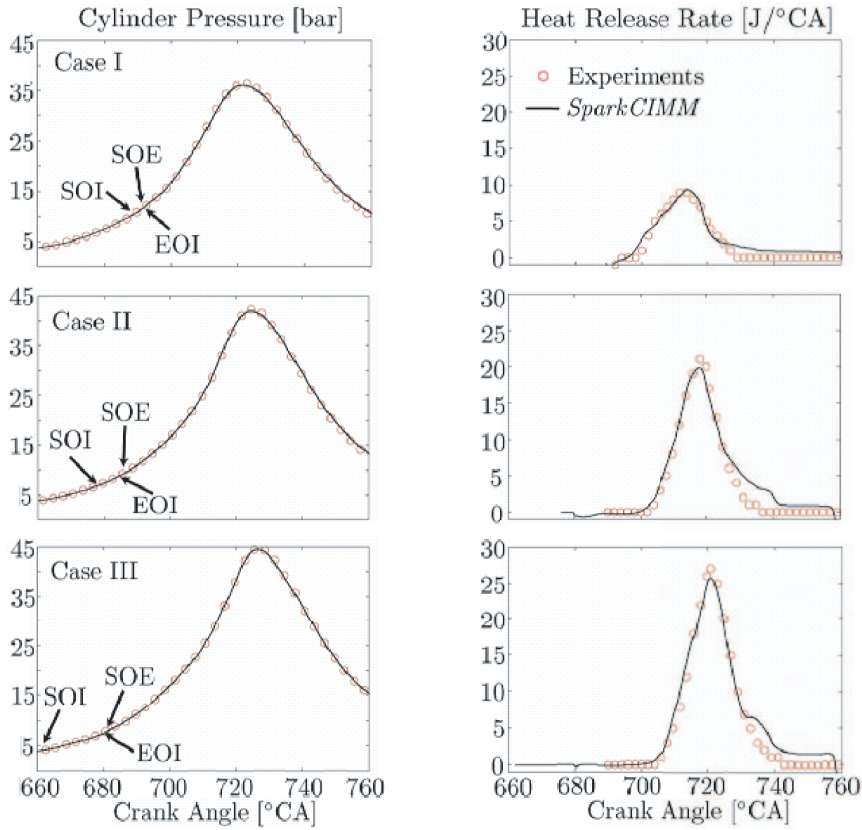


Figure 15.2: Comparison of simulated (lines) and measured (symbols) pressure traces (left) and heat release rates (right) for the investigated cases. For exemplification, the timings of the start/end of injection (SOI/EOI) and the start of energizing (SOE) are highlighted. (Reprinted with permission by R. Dahms.)

can be found in Dahms et al. (2009) [1].

The pressure traces and heat release rates, processed from the numerical simulation, are compared to experimental data and presented in Fig. 15.2. The flame-development angle $\Delta\theta$ (0 – 10% burnt fuel mass fraction, Heywood (1988) [2]) of the spark advance and the phase of main combustion are well predicted by the SparkCIMM/G-equation combustion model.

The complicated patterns of turbulent flame front propagation, induced by the high flow velocity and the stratified charge mixture preparation process from direct fuel-injection are presented in Fig. 15.3. It shows the three-dimensional visualization of the spray injection and the development of the early non-spherical turbulent flame front. Fig. 15.3 illustrates the substantial differences in the progression of turbulent combustion among the investigated engine operating points.

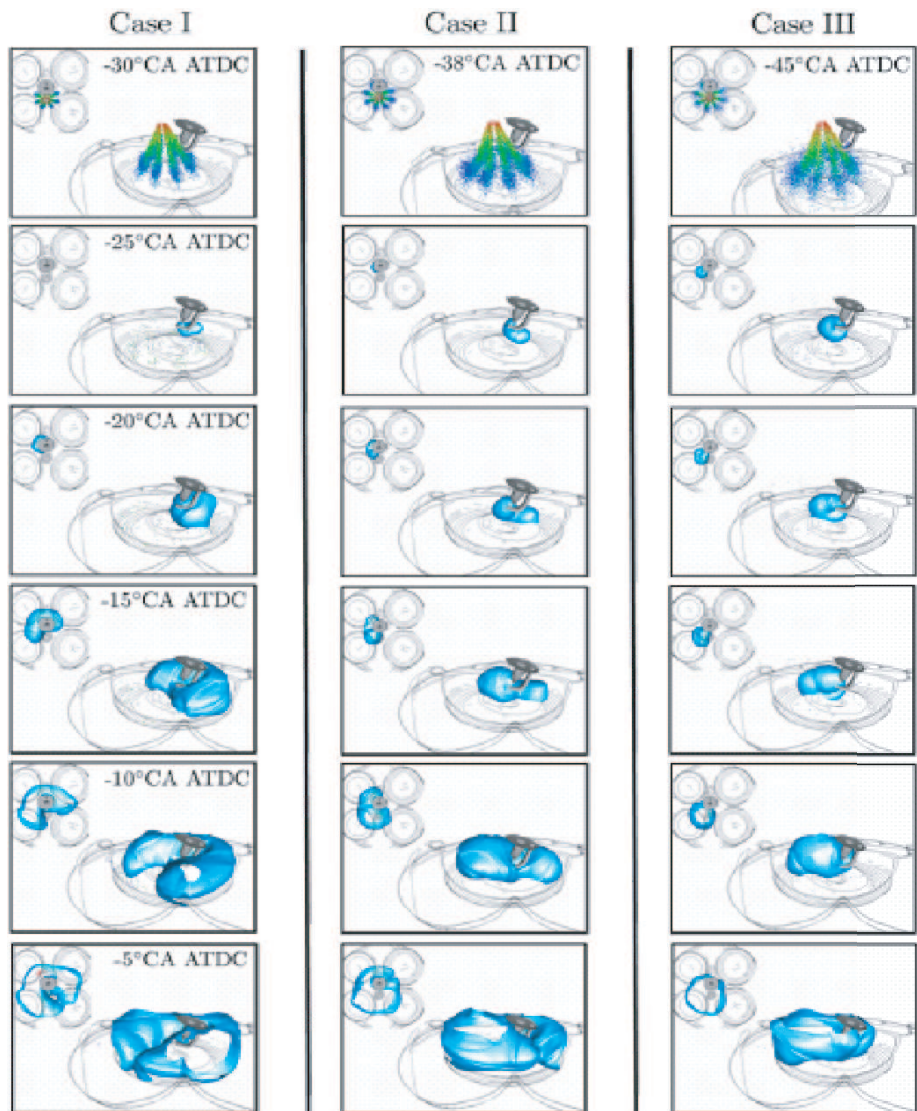


Figure 15.3: 3D visualization of the fuel spray injection (top row) and the turbulent flame front propagation for all investigated cases of the spray-guided gasoline engine. (Reprinted with permission by R. Dahms.)

The applied engine load and mixture dilution result in significant variations of the turbulent burning velocity. The temporal distribution of its flame front-averaged value is presented in Fig. 15.4. Local flame front values show a substantial deviation from these averaged quantities due to distinctive mixture stratification induced in this engine operating mode.

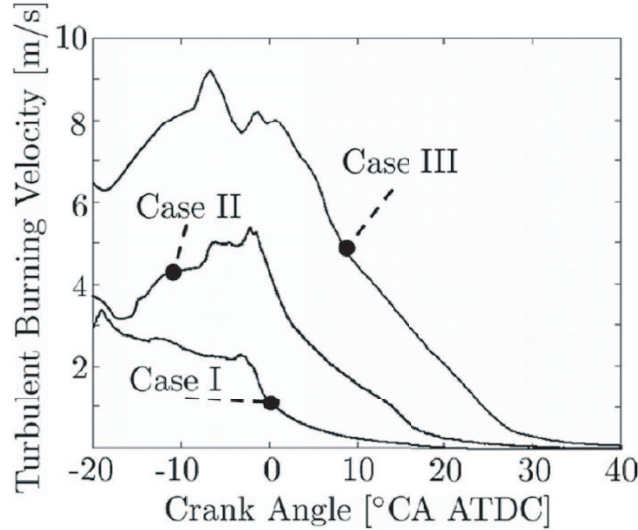


Figure 15.4: Turbulent burning velocity distribution for all investigated cases. Quantities are averaged over the mean turbulent flame front. (Reprinted with permission by R. Dahms.)

In Fig. 15.5, the partially-premixed combustion process of the investigated spray-guided gasoline engine is classified, using the regime diagram for premixed turbulent combustion by Peters (2000) [3], depicted for Case III. Although substantial temporal variations of turbulence and flame front velocity and length scales are observed, Fig. 15.5 shows that the operating conditions are located within the thin reaction zone regime throughout the whole combustion process. There, the increase of the turbulent burning velocity with the turbulence intensity approaches the square root dependence according to Damköhler (1940) [4]. In this regime, the Kolmogorov eddies do not perturb the inner layer reaction zone of the flame front so that the chemical time scales remain unaffected by turbulence. This confirms the underlying flamelet assumption of scale separation between the chemical kinetics and the turbulence, and demonstrates the validity of the G -equation flamelet model to predict turbulent partially-premixed combustion in spray-guided spark-ignition direct-injection engines.

In the following, a more detailed analysis, performed for Case II, is presented. At first, the velocity field close to the spark plug and at spark timing is investigated in Fig. 15.6. The flow

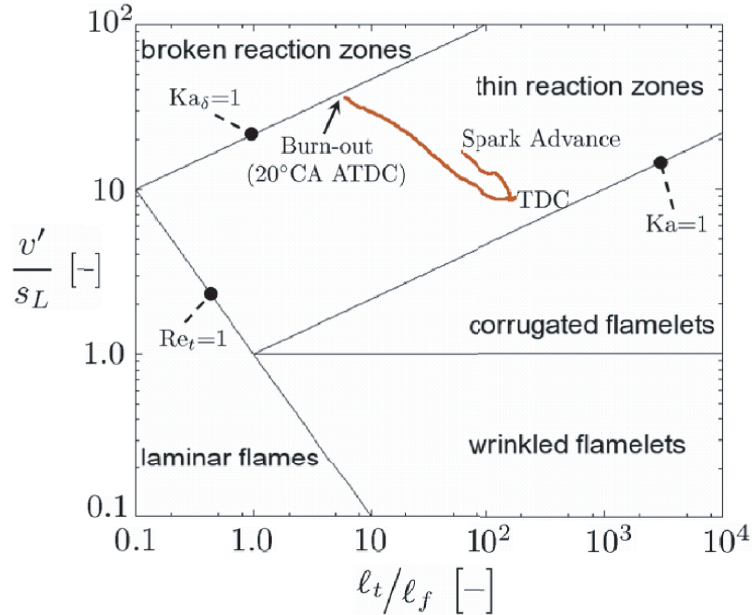


Figure 15.5: Location of turbulent combustion of the investigated spray-guided spark-ignition direct-injection gasoline engine, depicted for Case III, within the regime diagram. The timings of spark advance, top dead center (TDC), and burn-out are highlighted. Quantities are averaged over the mean turbulent flame front surface. (Reprinted with permission by R. Dahms.)

field results from the direct fuel injection and the gas exchange process, which generates an intensive swirl by the deactivation of the left intake valve. Local flow velocity magnitudes approach $||\tilde{u}|| = 50 \text{ m/s}$. Also steep gradients in the local velocities are shown in Fig. 15.6, indicating high turbulence intensities.

In Fig. 15.7, high-speed (24,000 frames/s) broadband visible luminosity images of the spark channel for two different individual engine cycles are presented. They show the formation and the turbulent corrugation of the spark channel due to the local high-velocity flow, compare Fig. 15.6. Also, localized ignition spots along the spark channel are observed, which subsequently lead to flame kernel formations and flame front propagations. Characteristic length scales are identified as the spark channel thickness ($\sim 0.05 \text{ mm}$) and the flame kernel length scale ($\sim 0.5 \text{ mm}$). The spark can stretch up to $\sim 10 \text{ mm}$ from the spark plug before a restrike occurs. The gas voltage has reached the breakdown voltage, which typically resets the spark channel to its original position between the spark electrodes. Such a restrike is tracked between the third and fourth image of cycle 41 in Fig. 15.7. However, such a restrike has no apparent influence on combustion, which

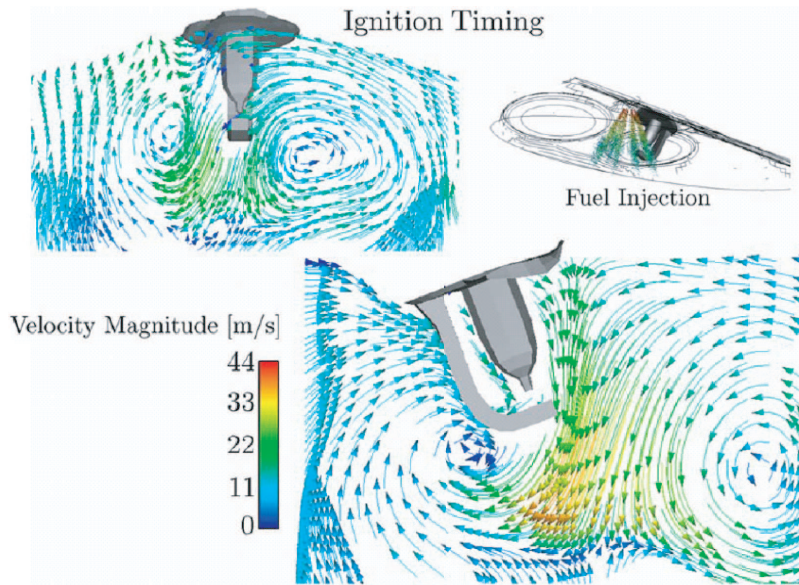


Figure 15.6: Velocity field around the spark gap at ignition timing induced by the intake swirl flow and the direct fuel spray-injection (top right). Local flow velocity magnitudes approach $||\tilde{u}|| = 50$ m/s. (Reprinted with permission by R. Dahms.)

proceeds due to the local conditions.

Fig. 15.8 present the distinctive scalar dissipation rates, conditioned on stoichiometric mixture fraction, along this stretched and wrinkled spark channel at ignition timing. It is seen that the initial high values of the scalar dissipation rate decay shortly after the start of energizing, but remain on substantial values during the spark duration. The distribution also shows discontinuities at simulated spark channel restrike events. If such an event is detected, the spark channel is set to a different location. Then, fresh mixture, characterized by different scalar dissipation rates, gets excited from that time on.

Fig. 15.9 presents a three-dimensional visualization of the distribution of the equivalence ratio, turbulence intensity, and velocity magnitude along the spark channel at three different times after the start of energizing. These auto-ignition and flame front propagation related quantities are used to detect the location and time of successful flame kernel formation. Such a successful local flame kernel propagation is predicted within the presented time-frame at $t \approx 470 \mu s$, using a combined extended flamelet and Karlovitz-number criterion as discussed in Dahms (2010) [5].

The SparkCIMM analysis has shown that advecting and merging flame kernels, launched during multiple ignition events along the restriking spark channel, result in non-spherical early turbu-

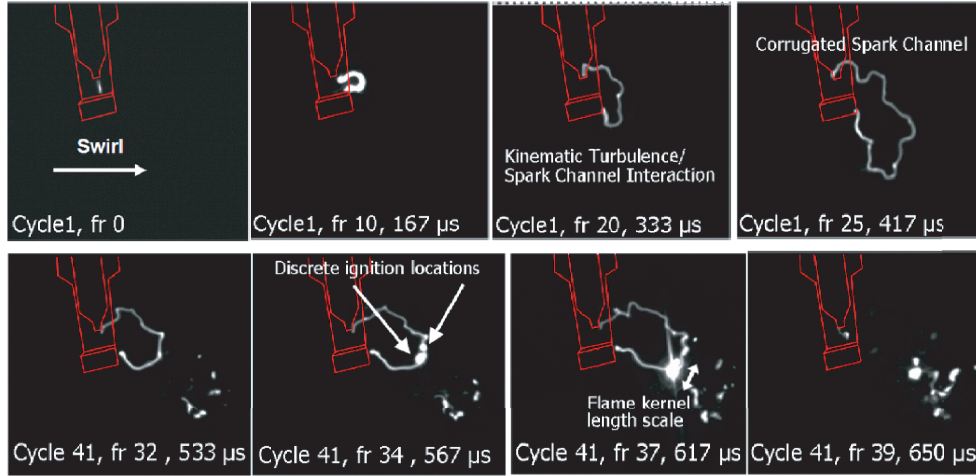


Figure 15.7: High-speed (24,000 frames/s) broadband visible (rich combustion) luminosity images of the spark-channel for two different individual engine cycles, Dahms et al. (2009) [1].

Top (Cycle 1): Formation, advection, and turbulent corrugation of the spark-channel due to the local flow field.

Bottom (Cycle 41): Localized ignition and flame kernel formation along the spark-channel. The restrike, tracked between the third and fourth image, has no apparent influence on the propagating flame kernel, Dahms et al. (2009) [1].

lent flame fronts. This characteristic feature of spray-guided spark-ignition systems is presented in Fig. 15.10, showing a side-view comparison of probabilities of finding an instantaneous flame front, processed from a classical single flame kernel model, high-speed laser-sheet Mie-scattering imaging data, averaged over 200 consecutive engine cycles, and the SparkCIMM model. Apparently, without the physical complexity of a detailed spark channel model, the characteristic non-spherical early flame shape cannot be reproduced, which leads to subsequent deficiencies in numerical simulation results.

The turbulent Damköhler number, averaged over the early non-spherical mean turbulent flame front after spark advance, is analyzed and highlighted in Fig. 15.11. The initial small Damköhler numbers result from rich and small scale turbulent mixtures, induced by the direct spray injection process, leading to low laminar burning velocities and thick laminar flame thicknesses. In this regime, highlighted in Fig. 15.11, the contribution of the turbulence intensity to the turbulent burning velocity is significantly reduced, which in turn largely depends on molecular fuel properties.

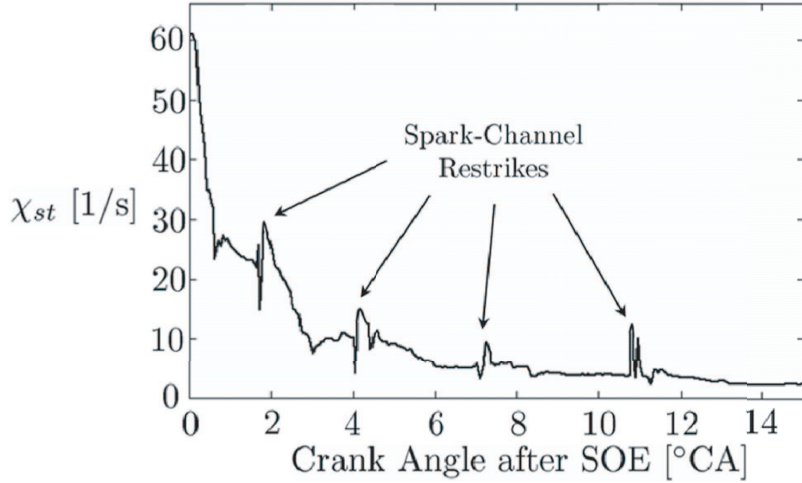


Figure 15.8: Scalar dissipation rate χ_{st} , conditioned on stoichiometric mixture fraction along the spark-channel as defined in Eq. (14.46) after the start of energizing (SOE). The distribution shows discontinuities at simulated spark-channel restrike events. (Reprinted with permission by R. Dahms.)

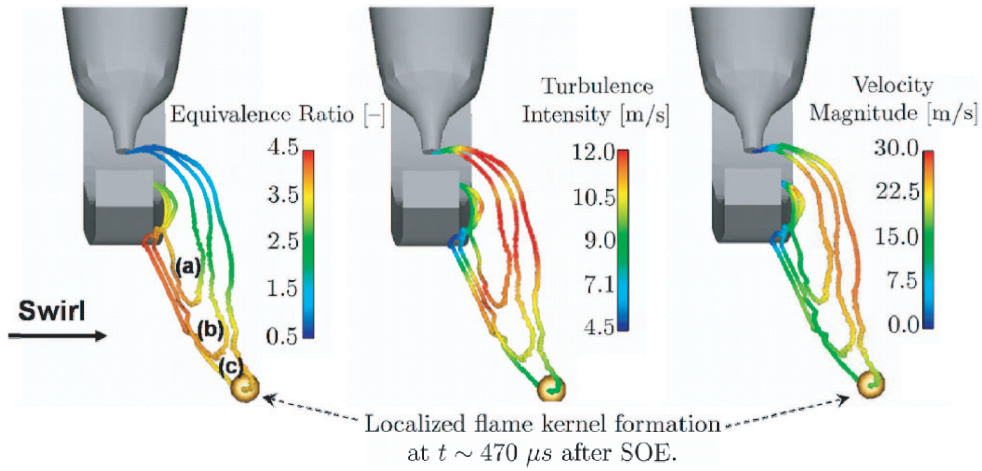


Figure 15.9: 3D visualization of (left) equivalence ratio ϕ , (middle) turbulence intensity v' , and (right) velocity magnitude $||\tilde{u}||$ along the spark channel at different timings after the start of energizing (SOE), computed by the SparkCIMM model [a: $t = 220 \mu s$, b: $t = 330 \mu s$, and c: $t = 550 \mu s$]. Localized ignition and subsequent successful flame kernel formation is detected within the presented time-frame at $t \sim 470 \mu s$, using extended flamelet and Karlovitz-number criterions. Then, a small (~ 0.5 mm, Maly (1978) [6]) spherical flame kernel (yellow sphere) is initialized at the corresponding position Dahms et al. (2009) [1].

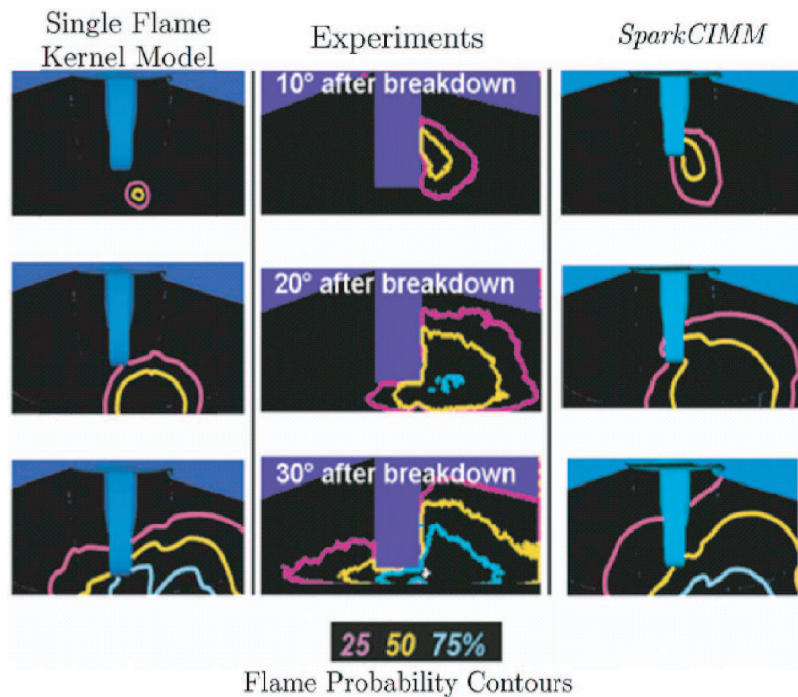


Figure 15.10: Side-view comparison of probabilities of finding an instantaneous flame front processed from results of (left) a single flame kernel model, (middle) experiments, and (right) the *SparkCIMM* model at three times after spark breakdown, Dahms et al. (2009) [1]. A Gaussian distribution of the flame location is used to calculate the flame-location probability for the *G*-equation simulations.

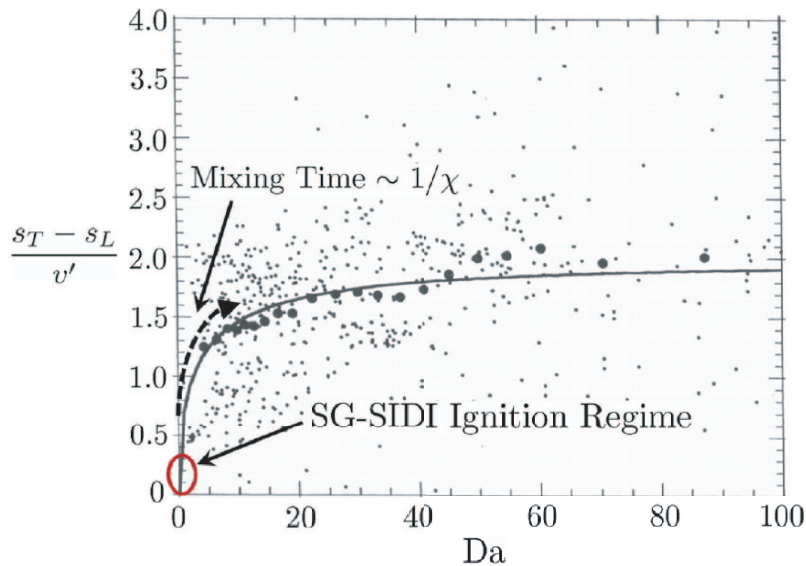


Figure 15.11: Regime of low turbulent Damköhler numbers during early non-spherical flame kernel propagation in spray-guided spark-ignition direct-injection (SG-PICT/PICT/Lecture15/SIDI) gasoline engines. In this regime, the effect of the turbulence intensity on the turbulent burning velocity is reduced and molecular fuel properties have a substantial meaning on flame front propagation. After a characteristic mixing time τ_χ , the Damköhler number increases distinctively. The small dots denote experimental data by Bradley (1992) [7] and the large dots their localized average. The line results according to Eq. (13.32), assuming a fully developed and a in the mean planar turbulent flame front. (Reprinted with permission by R. Dahms.)

15.2 Injection-Rate Shaping in Diesel Engine Combustion

The concept of flamelet equations and Representative Interactive Flamelets (RIF) prove valuable in the simulation of turbulent combustion in diesel engines. In this example, the concept is applied to study the effect of top-hat and boot-shaped injection-rate shapes on ignition, combustion, and pollutant formation as an advanced technology to achieve the stringent emission standards in the near future.

It is considered that boot-shaped rate comprises two different stages of injection as exemplarily shown in Fig. 15.12. The dashed-line on the figure marks the separation between the two stages. In the first stage, fuel injection starts and the injection rate increases to its first peak and remains nearly constant until the beginning of the second stage. In this second stage, the injection rate further increases from the first peak to the second peak, and then decreases till the end of injection time. The peak injection-rate (referred to as height) in both stages of the boot injection-rate shape is the parameter of variation in this study. Owing to a constant total injected mass and spray momentum (and nearly constant overall injection duration), three different boot-shaped rates, defined in Fig. 15.13, were analyzed.

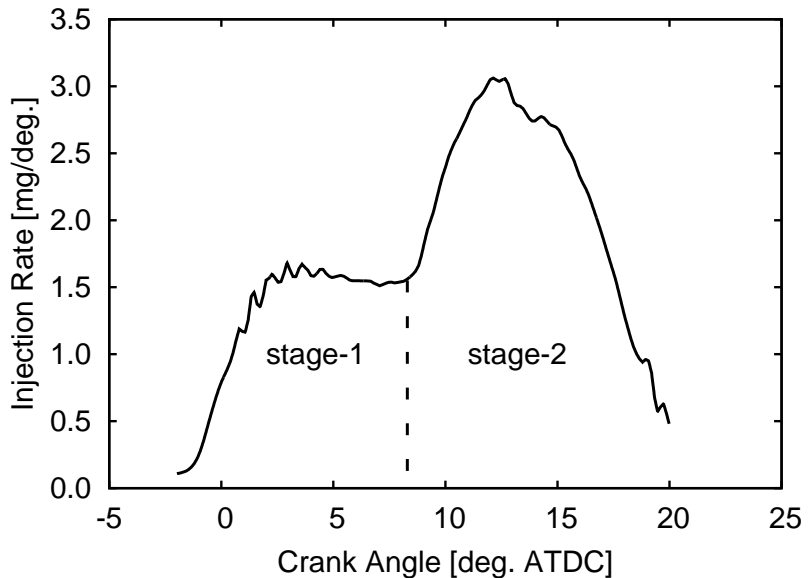


Figure 15.12: An example of a boot injection-rate shape; both stages of the rate shape are also shown in Luckhchoura (2010) [8].

Fig. 15.13 shows the injection rate (in mg per degree CA) of the investigated boot-shaped rates over crank angle. The increase in the injection rates of the first stage meant the decrease in the injection rates of the second stage of a rate shape. The rate shapes are named as BH1, BH2, and BH3 according to their peak injection-rate (height) in the first stage. Test case BH1 has the lowest peak injection-rate in the first stage and the highest peak injection-rate in the second stage among all the rate shapes. Whereas, BH3 has the highest peak injection-rate in the first stage and the lowest peak injection-rate in the second stage, respectively. Test case BH2 is in the middle of BH1 and BH3.

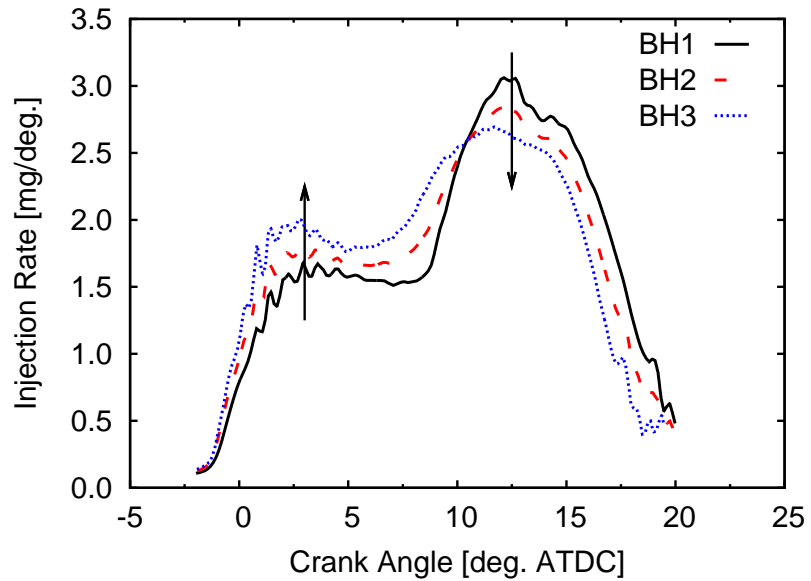


Figure 15.13: Injection profiles showing variation in the height of the first stage and the second stage of the boot-shaped rates , Luckhchoura (2010) [8].

Simulations were performed using the multiple-flamelet (M-RIF) model, shown in Fig. 15.14, for all the rate shapes. In the case of multiple-flamelets, several flamelets could be found at the same location due to the turbulent mixing process. Therefore, the contribution of each flamelet in the same computational cell, \tilde{I}_n , is calculated from the ratio of its mean mixture fraction and the total value of mixture fraction in the cell. Turbulent mean values of these scalars are then obtained by using the pre-assumed shape PDF in each cell:

$$\tilde{I}_n = \frac{\tilde{Z}_n(x_\alpha, t)}{\tilde{Z}(x_\alpha, t)} \quad n = 1, 2 \quad (15.1)$$

$$\tilde{Y}_i(x_n, t) = \sum \tilde{I}_n \left(\int_{Z=0}^1 \tilde{P}(Z; x_\alpha, t) Y_{i,n}(Z, t) dZ \right), \quad n = 1, 2 \quad (15.2)$$

Here, Y_i represents the species mass fraction. For this work, the multiple-flamelet concept has been coupled to a multi-dimensional CFD solver as shown in Fig. 15.14. The surrogate fuel (IDEA) of diesel used in this work is a mixture of 70% n -decane and 30% α -methylnapthalene (liquid volume).

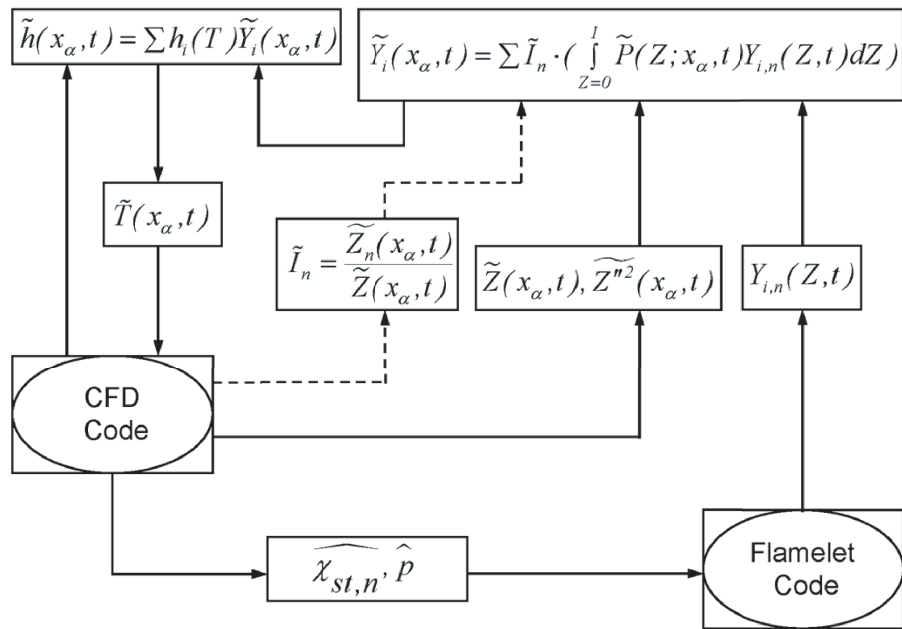


Figure 15.14: Interaction between the CFD code and the Flamelet code, using the multiple Representative Interactive Flamelets (M-RIF) model, Luckhchoura (2010) [8].

The specifications of the investigated single-cylinder engine, along with the applied computational grid at top dead center are shown in Fig. 15.15. For the CFD simulation, a sector mesh representing 1/7th of the combustion was used by taking advantage of the circumferential symmetry of the centrally located injector equipped with a 7-hole nozzle. During the piston stroke, seven different computational meshes were used. A remap of solutions was done before switching between different meshes. The different wall temperatures, color-coded in Fig. 15.15, were set based on the experimental experience and held constant during the simulation.

Details of the flow and mixing field are shown on a vertical center plane cut through the engine.

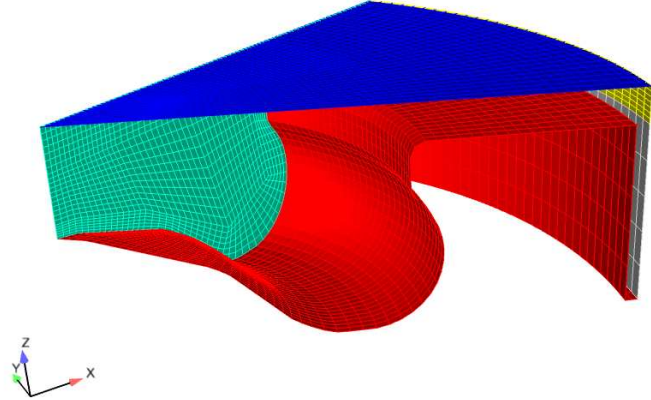


Figure 15.15: Engine specifications and computational grid of the 1/7th sector mesh of a single-cylinder diesel engine at top dead center.

Fig. 15.16 shows the instantaneous gaseous velocity field. The entrainment vortices generated by the spray plume can be clearly observed from the velocity field at 8° CA ATDC for both rate-shapes. The piston is traveling down and a strong squish flow is directed into the squish volume (reverse squish) from the piston bowl in both cases of top-hat and boot-shape injection profiles, respectively. At this crank angle, about 39% of the total fuel has been injected in the top-hat compared to about 32% of the total fuel in the boot case. The corresponding cumulative spray momentum is about 38.5% of the total spray momentum in the case of the boot shape. As a result, the top-hat case has a higher spray center-line velocity. The entrainment vortices induce mixing of the relatively cold fuel vapor with the surrounding hot gases, leading to the molecular mixing necessary for chemical reactions.

Corresponding spatial distributions of the mean mixture fraction are shown in Fig. 15.17. It is noticed that the spray has already impinged on the piston wall and has split between the squish volume and the bowl volume for the top-hat shape, whereas the boot case shows lower penetration due to lower injection rates. Thus, at this crank angle higher spray momentum and penetration in the top-hat case would enhance the mixing compared to the boot case. In the top-hat, the initial mixing was superior due to the higher velocities (and spray momentum) and hence the vortex has moved deeper inside the bowl and the leading edges of the spray plume are better mixed and leaner compared to the boot case at this crank angle. At the end of injection, both shapes ended

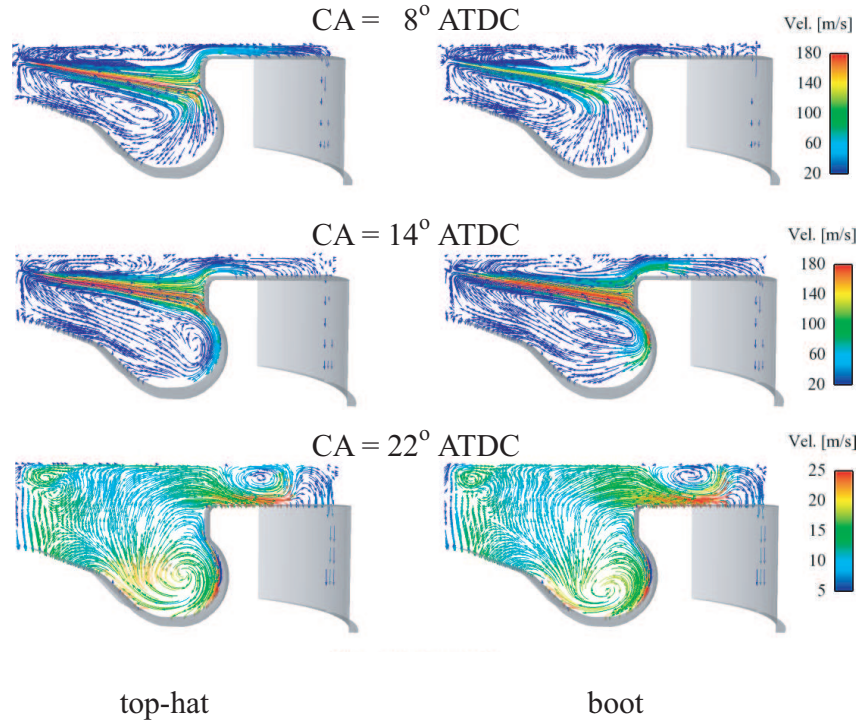


Figure 15.16: Velocity fields for top-hat shape (left) and boot shape (BH1, right) at three specific crank angles.

up with almost the same fuel mass and the injected spray momentum. Thus, in the beginning, the fuel has entered the cylinder with much higher injection velocities in the top-hat, and for the boot shape it happened in the latter crank angles. A higher transport of fuel for a lower increment in the squish volume results in the richer fuel mixtures in the squish region for the boot case. At 22° CA ATDC, a comparison of the mixing field for both shapes shows that the fuel distribution is better for the boot shape allowing the higher mixing with the surrounding air.

The discussed injection, mixing, and evaporation characteristics are also reflected in the temperature fields for top-hat and boot shape injection profiles as shown in Figs. 15.18 and 15.19, respectively. The latter shows the computed heat release rates for both injection-rate shapes. The effect of evaporation is evident in the heat release for both shapes. Earlier start of evaporation in the boot shape shows also early rise in the heat release rates. The top-hat shape shows the highest premixed peak in heat release rate due to higher evaporation rates during that period. Higher evaporation rates after 10° CA ATDC in the boot shape results in the highest peak during

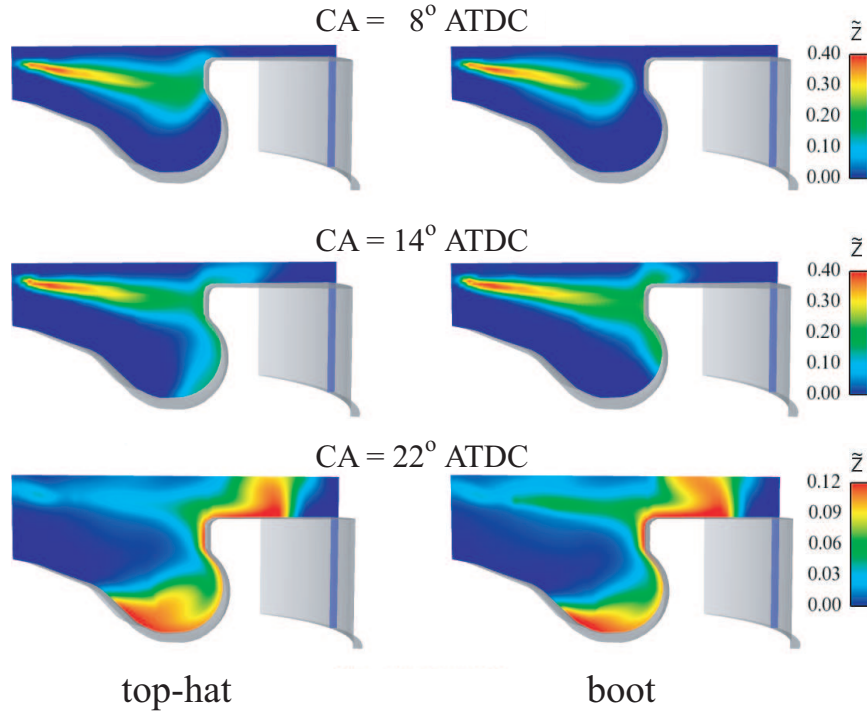


Figure 15.17: Mixing fields for top-hat shape (left) and boot shape (BH1, right) at three specific crank angles.

diffusion-controlled combustion.

Fig. 15.20 shows the comparison of the simulated and experimentally measured pressures for both shapes over crank angle. The measured and computed pressure evolutions show the same trends and good agreement. The model predicts an earlier ignition in the boot case as also seen in the experiments. This trend could be associated with the early start of injection and fuel evaporation leading to early molecular level mixing for the boot case. The pressure rise due to combustion is faster in the top-hat case. In addition, the peak pressure is also higher in the top-hat case. This is a result of the higher evaporation rate for the top-hat shape between 2° and 10° CA ATDC.

Fig. 15.21 shows a qualitative comparison of the simulated and measured soot (top) and CO (below) emissions at exhaust valve opening (EVO). The indicated concentrations are scaled to one in the top-hat case. Similar to the experiments, the model predicts a significant reduction in both soot and CO emissions at EVO for the boot shape.

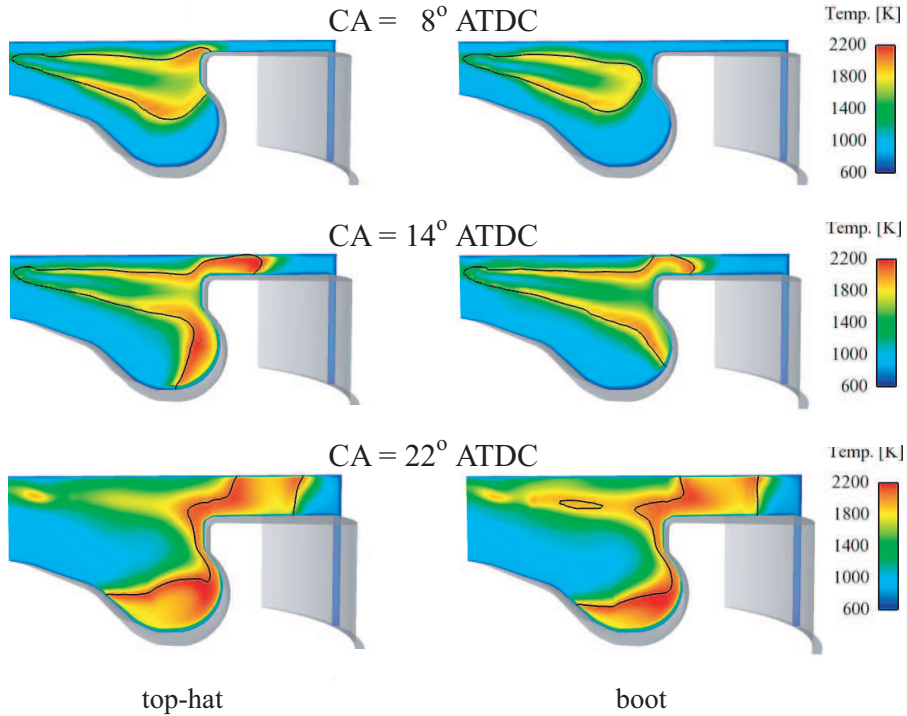


Figure 15.18: Temperature fields for top-hat shape (left) and boot shape (BH1, right) at three specific crank angles. The iso-line denotes the location of stoichiometric mixture fraction.

Fig. 15.22 compares the normalized soot values (scaled to 1.0) at exhaust valve opening in the experiments and simulations. In the experiments, lowering the injection rates in the first stage (i.e. increasing the rates in the second stage) total in-cylinder soot decreased at exhaust valve opening. This trend is satisfactorily captured in the simulations, though the level of reduction, with increasing injection rates in the first stage, is lower. With increasing the injection rates in the first stage (BH1 to BH3), the contribution from the first flamelet increases, and at the same time due to lower injection rates in the second stage, the second flamelet contributed more. Overall, the model-predicted results are in good agreement with the measurements.

Fig. 15.23 (left) shows the history of soot formation for the mass belonging to the first stage over crank angle in all the test cases. The figure provides the temporal distribution of the soot formation in each test case. In the figure, BH3 has the lowest, and BH1 has the highest peak soot formation. One can conclude that the higher injection rates in the first stage results in a lower peak in soot formation. However, at exhaust valve opening BH3 predicted higher soot emissions among

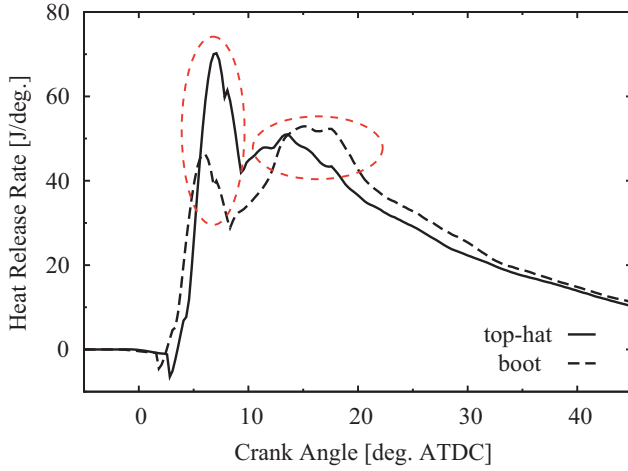


Figure 15.19: Computed heat release rates for the top-hat and boot (BH1) injection profiles, Luckhchoura (2010) [9].

all test cases. In the second stage, shown in Fig. 15.23 (right), the soot formation started earlier for BH3 due to the early start of ignition. The peak in soot formation shows a rather weak dependence on the injection rates compared to the first stage. Compared to the first stage, higher soot was formed in the second stage. Owing to the better mixing, the oxidation of the soot formed was also efficient. Overall, rate shape corresponding to BH1 shows the improved soot oxidation among the rate shapes. The soot formation in the cylinder is mainly a result of two factors: the first is the soot chemistry and the second is the state of the mixture. Therefore, it is important to quantify the effect of both factors in the soot formation for both stages as performed in Fig. 15.24. The mass weighted PDF of the mixture fraction describes the state of the mixture, and the first soot moment relates to the soot chemistry. The region of overlap between the profiles of the PDF and the soot moment contributes to the soot concentration in the cylinder. Fig. 15.24 corresponds to the crank angle where soot formation reaches its peak in all the cases for the stage-1 and stage-2. In Fig. 15.24 (left), in the region of overlap soot concentration in the cases is nearly the same but the profile of PDF is different in each case. This indicates the different levels of mixing in each case. In the case of BH3, the region of overlap is smaller compared to the other cases, which results in the lowest peak in soot formation. In Fig. 15.24 (right), profiles of PDF and soot moment are quite the same in all the cases. This explains the nearly same peak of soot formation in the second stage for all the cases. Therefore, one can conclude that in the first stage mixing plays a significant role in determining the soot formation, whereas in the second stage mixing as well as soot chemistry

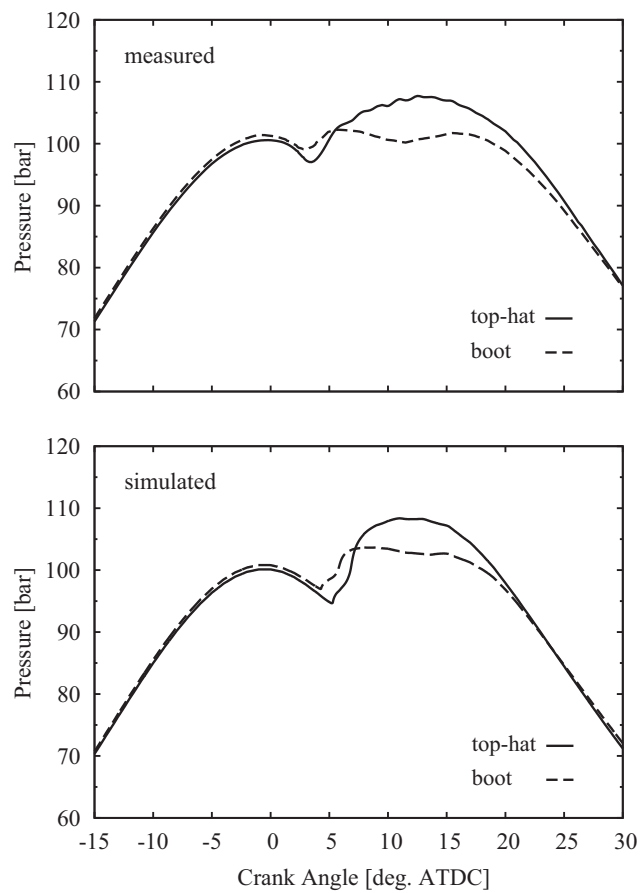


Figure 15.20: Comparison between the measured and the simulated pressure traces.

are controlling mechanisms for the soot formation.

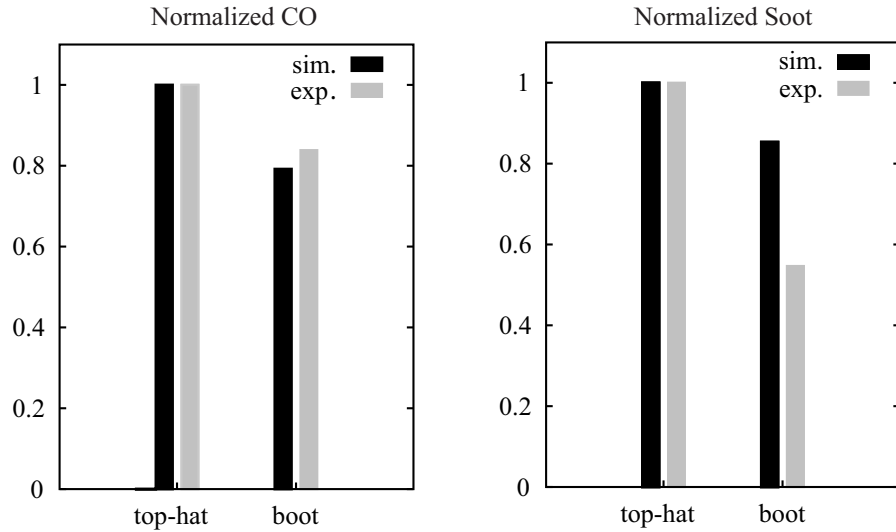


Figure 15.21: Comparison between the measured and simulated soot and CO emissions at exhaust valve opening (scaled to one in top-hat shape, BH1 boot-shape), Luckhchoura (2010) [9].

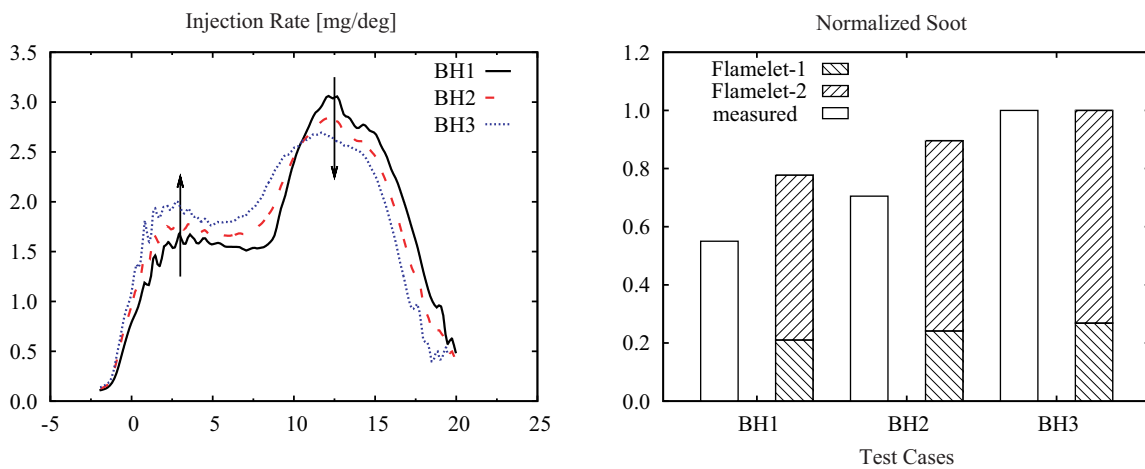


Figure 15.22: Model-predicted and measured soot emissions at exhaust valve opening in all the cases (scaled to 1.0), Luckhchoura (2010) [8].

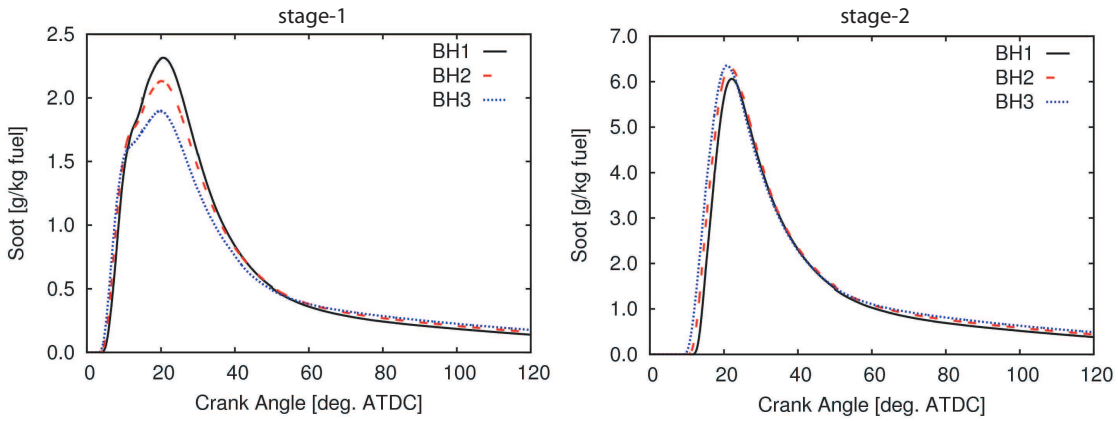


Figure 15.23: Soot formation history for both stages in all the test cases, Luckhchoura (2010) [8].

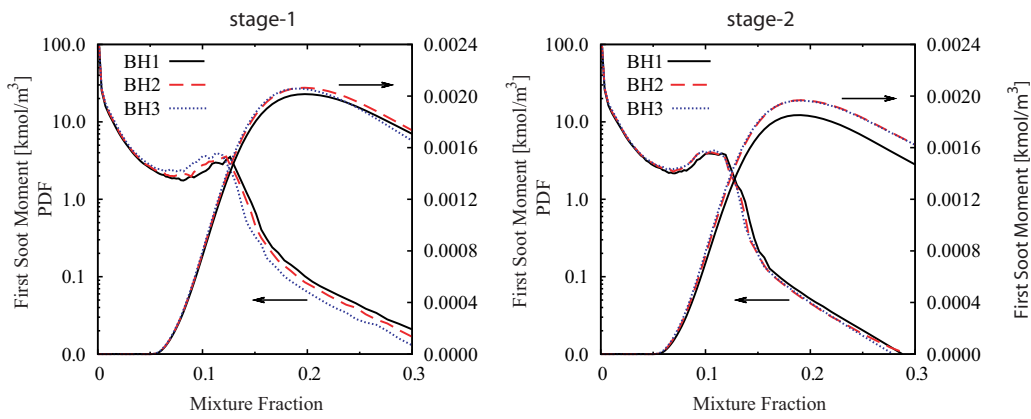


Figure 15.24: Mass weighted PDF of the mixture fraction in the cylinder with the profile of the first soot moment; crank angles correspond to their peak in the soot formation, Luckhchoura (2010) [8].

Bibliography

- [1] R. Dahms, T.D. Fansler, M.C. Drake, T.W. Kuo, A.M. Lippert, and N. Peters. Modeling ignition phenoman in spray-guided spark-ignited engines. *Proc. Combust. Inst.*, 32:2743–2750, 2009.
- [2] J.B. Heywood. *Internal Combustion Engine Fundamentals*. McGraw Hill, 1988.
- [3] N. Peters. *Turbulent Combustion*. Cambridge University Press, 2000.
- [4] G. Damköhler. Der Einfluss der Turbulenz auf die Flammengeschwindigkeit in Gasgemischen. *Zeitschr. f. Elektrochemie*, 46:601–626, 1940.
- [5] R. N. U. Dahms. *Modeling of Combustion in Spray-Guided Spark-Ignition Engines*. Dissertation, RWTH Aachen University, Germany, 2010.
- [6] R. Maly and M. Vogel. Initiation and Propagation of Flame Fronts in Lean CH₄-Air Mixtures by the Three Modes of the Ignition Spark. *Proc. Combust. Inst.*, 17:821–831, 1978.
- [7] D. Bradley, A.K.C. Lau, and M. Lawes. Flame stretch as a determinant of turbulent burning velocity. *Phil. Trans. Roy. Soc. Lond.*, 338:359–387, 1992.
- [8] V. Luckhchoura. *Modeling of Injection-Rate Shaping in Diesel Engine Combustion*. Dissertation, RWTH Aachen University, Germany, 2010.
- [9] V. Luckhchoura, F.-X. Robert, N. Peters, M. Rottmann, and S. Pischinger. Experimental and Numerical Investigation of Injection Rate Shaping in a Small-Bore Direct-Injection Diesel Engine. *Seventh Intl. Symp. Towards Clean Diesel Engines*, 2009.